universität wien

DISSERTATION | DOCTORAL THESIS

Titel | Title

Inverse modeling of greenhouse gases

verfasst von | submitted by

Martin Vojta BSc MSc

angestrebter akademischer Grad | in partial fulfilment of the requirements for the degree of

Doktor der Naturwissenschaften (Dr.rer.nat.)

Wien | Vienna, 2024

Studienkennzahl lt. Studienblatt | Degree programme code as it appears on the student record sheet:	UA 796 605 415
Dissertationsgebiet lt. Studienblatt | Field of study as it appears on the student record sheet:	Meteorologie
Betreut von | Supervisor:	Univ.-Prof. Mag. Dr. Andreas Stohl

Abstract

In recent decades, the substantial rise in anthropogenic greenhouse gas (GHG) emissions has become a worldwide concern. Enhancing our understanding of these emissions is crucial to assist policymakers in implementing effective mitigation strategies. A powerful tool to constrain GHG emissions is inverse modeling, where atmospheric measurements are used along with an atmospheric transport model to optimize an *a priori* estimate of these emissions. This thesis focuses on developing the inverse modeling framework and applying it to determine the global distribution of sulfur hexafluoride (SF_6) emissions, the GHG with the highest known global warming potential.

In the first part of this thesis, I investigate the uncertainties of atmospheric inversions, when utilizing Lagrangian Particle Dispersion Models (LPDMs) to model the atmospheric transport between emissions and measurements. In this approach, a large number of virtual particles is released from the measurement sites and followed backwards in time to establish a relationship between the measurements and emission sources within a chosen simulation period. As this simulation period is limited due to computational costs, a baseline has to be defined that accounts for all emissions that occur prior to the simulation period, representing a large source of uncertainty. I put a main emphasis on assessing the influence of different baseline methods and different LPDM backward simulation periods on the inversion results. I demonstrate, that commonly employed statistical baseline methods can encounter substantial problems and present the advantages of a Global-Distribution-Based (GDB) approach, that leads to more robust inversion results, accounts for meteorological variability, and allows the inclusion of low-frequency flask measurements in the inversion. I further propose to employ relatively long backward simulation periods, beyond 5–10 days, as this can improve the performance of the LPDM and the inversion.

In the second part of this thesis, I employ a global inversion setup that is based on the methodological findings of the first part, to globally determine the distribution of regionally resolved SF_6 emissions between 2005 and 2021. My findings show a substantial decline in U.S. SF_6 emissions, indicating the positive effects of national regulation measures. I also find a decreasing emission trend in the EU, with a substantial drop after 2017, likely a result of the EU's 2014 F-gas regulation. Chinese emissions, however, show a strong positive trend, that is even higher than the average global total emission trend. I further demonstrate that national reports to the United Nations Framework Convention on Climate Change underestimated the SF_6 emissions in the U.S., EU, and China throughout the whole study period. The aggregation of all the regionally resolved emissions shows a relatively good agreement with total global emissions, however, results are sensitive to the employed *a priori* emission fields, likely due to the challenges in constraining emissions in regions

poorly covered by the observation network. Lastly, monthly inversion results show higher SF_6 emissions in summer than in winter in the Northern Hemisphere.

This thesis contributes to the development of inverse modeling and globally enhances the knowledge about regionally resolved SF_6 emissions. The developed set-up for atmospheric inversions provides various advantages and is suitable for estimating GHG emissions on global, regional, and local scales.

Zusammenfassung

Der starke Anstieg von anthropogenen Treibhausgasemissionen über die letzten Jahrzehnte ist zu einer ernsthaften Bedrohung für die Umwelt geworden. Damit effektive Klimaschutzmaßnahmen getroffen werden können, ist die Bestimmung von Treibhausgasemissionen von größter Bedeutung. Die inverse Modellierung ist eine wichtige Methode um Emissionen zu bestimmen. Hierbei wird eine erste Schätzung der Emissionen (*a priori* Emissionen) mit Hilfe von atmosphärische Konzentrationsmessungen und einem atmosphärischen Transportmodell optimiert. Der Fokus dieser Arbeit liegt in der Entwicklung der inversen Modellierungsmethode und ihrer Anwendung, um Emissionen des potenten Treibhausgases Schwefelhexafluorid (SF_6) global zu bestimmen.

Im ersten Teil der Arbeit untersuche ich atmosphärische Inversionen, bei denen der atmosphärische Transport zwischen Emissionen und Messungen mit "Lagrangian-Particle-Dispersion-Models" (LPDMs) modelliert wird. Bei diesem Ansatz werden eine große Anzahl virtueller Teilchen an den Beobachtungsstellen freigesetzt und zeitlich rückwärts verfolgt, um eine Beziehung zwischen den Beobachtungen und den Emissionsquellen innerhalb eines gewählten Simulationszeitraums herzustellen. Da dieser Simulationszeitraum aufgrund der Rechenkapazitäten begrenzt ist, muss eine sogenannte "Baseline" definiert werden, die diejenigen Emissionen berücksichtigt, die vor dem Simulationszeitraum auftreten. In diesem ersten Teil der Arbeit untersuche ich, wie sich verschiedenen Methoden zur Bestimmung der Baseline auf die Inversionsresultate auswirken und welchen Einfluss unterschiedliche LPDM-Simulationszeiträume haben. Ich zeige, dass oft verwendete statistische Baseline Methoden erhebliche Probleme verursachen können und präsentiere die Vorteile einer "Global-Distribution-Based" (GDB) Methode, die zu robusteren Inversionsergebnissen führt, meteorologische Variabilität berücksichtigt und die Einbeziehung von niederfrequenten Messungen ermöglicht. Ich schlage weiters vor, relativ lange LPDM-Simulationszeiträume von mehr als 5–10 Tagen zu verwenden, da dies zu einer besseren Modellierung der Beobachtungen führen und die Inversionsergebnisse verbessern kann.

Im zweiten Teil der Arbeit verwende ich die inverse Modellierung, um die Verteilung regional aufgelöster SF_6-Emissionen zwischen 2005 und 2021 global zu bestimmen. Meine Ergebnisse zeigen einen deutlichen Rückgang der SF_6-Emissionen in den USA, welcher auf die positiven Auswirkungen nationaler Regulierungsmaßnahmen hinweist. Meine Ergebnisse zeigen ebenfalls einen negativen Emissionstrend in der Europäischen Union, mit einem deutlichen Rückgang nach 2017, der wahrscheinlich eine Folge der EU-Verordnung zu F-Gasen von 2014 ist. Chinesische Emissionen zeigen jedoch einen stark positiven Trend, der sogar den durchschnittlichen globalen Trend übertrifft. Ich zeige weiters, dass die nationalen Berichte an die Vereinten Nationen die SF_6-Emissionen in den USA, der EU und China

von 2005 bis 2021 unterschätzt haben. Die Summe aller regional aufgelösten Emissionen zeigt eine relativ gute Übereinstimmung mit den globalen Gesamtemissionen, wobei die Ergebnisse eine Abhängigkeit gegenüber den verwendeten *a priori* Emissionen aufweisen. Dies lässt sich darauf zurückführen, dass Emissionen in Gebieten, die schlecht vom Beobachtungsnetzwerk abgedeckt sind, schwer zu bestimmen sind. Weiters zeigen meine monatliche Inversionsergebnisse für die Nordhalbkugel höhere SF_6-Emissionen im Sommer als im Winter.

Diese Arbeit trägt zur Weiterentwicklung der inversen Modellierung bei und erweitert das Wissen über die globale Verteilung von SF_6-Emissionen. Die entwickelte Methode bietet verschiedene Vorteile und eignet sich zur Abschätzung von Treibhausgasemissionen auf globaler, regionaler und lokaler Ebene.

Contents

Chapter 1

Introduction

1.1 Greenhouse gases

"It is unequivocal that human influence has warmed the atmosphere, ocean, and land" (IPCC 2021). Human influence refers to all the human-driven activities that lead to perturbations in the Earth's energy budget, which describes the balance between incoming and outgoing radiation and controls the Earth's climate (Fig. 1.1).

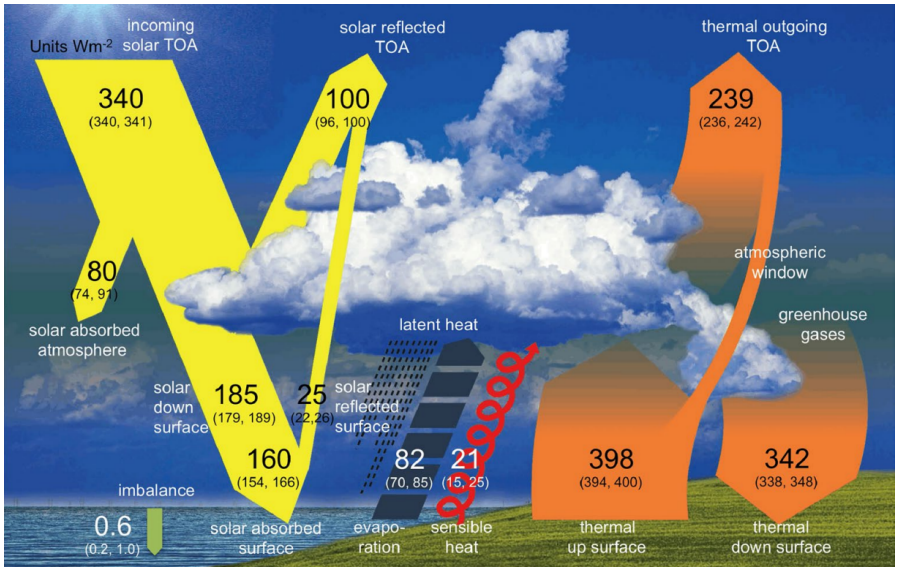

Figure 1.1: Illustration of the Earth's global annual mean energy balance (Wild et al. 2015). The numbers refer to the best estimates for the respective energy flows [in Wm^{-2}] of individual components.

Incoming solar radiation includes visible, ultraviolet and infrared wavelengths, collectively referred to as short-wave radiation. Approximately 30% of the solar radiation that reaches the Earth is reflected by the surface, clouds, and atmosphere while the rest is absorbed and re-emitted, mainly in the form of infrared radiation. While only a small fraction is directly re-emitted to space, most of the infrared radiation is absorbed by greenhouse gases (GHGs), which results in a warming of the Earth's surface and lower atmosphere. This is often

referred to as the greenhouse gas effect. The change in energy balance caused by a certain GHG is quantified by its radiative forcing, measured in Wm^{-2}. The strength of a GHG is most prominently quantified by its global warming potential (GWP). It is defined as the, over a chosen time horizon (typically 100 years, GWP-100), integrated radiative forcing from the emission of a GHG unit mass, compared to that of CO_2. While the natural greenhouse gas effect maintains the Earth's temperature at levels suitable for life, the emissions of anthropogenic GHGs enhance the greenhouse effect and lead to additional warming of the climate. Over the industrial era, atmospheric GHG concentrations have grown substantially due to anthropogenic emissions, increasing the global surface temperature by more than 1°C since the 19^{th} century (IPCC 2021). This warming trend manifests in many ways, such as altered weather patterns, increased frequency of extreme weather events, sea level rise, biodiversity loss, and disruptions in the ecosystem.

1.1.1 Anthropogenic greenhouse gases

The main anthropogenic GHGs in the atmosphere are carbon dioxide (CO_2), methane (CH_4), nitrous oxide (N_2O), and halogenated gases, including fluorinated gases (F-gases). CO_2 has the largest impact on the climate, due to its high atmospheric concentrations and its long atmospheric lifetime. The gas is primarily emitted from fossil fuel combustion and cement production, but also from land use, land-use change, and forestry (IPCC 2022), while the ocean (e.g. Sabine et al. 2004), terrestrial ecosystems (e.g. Pan et al. 2011) and soils (e.g. Lal 2004) have been identified as sinks. Methane is the second most abundant anthropogenic GHG. It has a relatively short atmospheric lifetime of 11.8 years, and GWPs of 81 and 28 over a 20- and 100-year time horizon respectively (Smith et al. 2021), which makes it attractive for mitigation strategies, limiting near-term warming. Its anthropogenic sources include agriculture, fossil fuel production, landfills, coal mining, oil and gas industry, and biomass burning, while wetlands represent the major natural sources (Canadell et al. 2021). The major CH_4 sink is the destructive reaction with the hydroxyl radical (OH) in the atmosphere. N_2O has a GWP-100 of 273 and an atmospheric lifetime of approximately 109 years (Smith et al. 2021). Anthropogenic N_2O is primarily emitted from agricultural activities such as fertilizer application and livestock manure management, while microbial activities in soils are the largest natural source. Soils can also act as a net N_2O sink although this impact is minor in comparison to the overall emissions (Canadell et al. 2021). Besides these three GHGs, less abundant halogenated gases, and especially F-gases, also significantly impact the climate due to their high GWPs and long atmospheric lifetimes. Figure 1.2 illustrates the global net anthropogenic GHG emissions 1990-2019 by the discussed groups of gases, reported in gigatonnes of CO_2-equivalent. While F-gases contribute roughly 2% to the total emissions, they have undergone rapid growth since the 1990s, and their future impact is expected to increase.

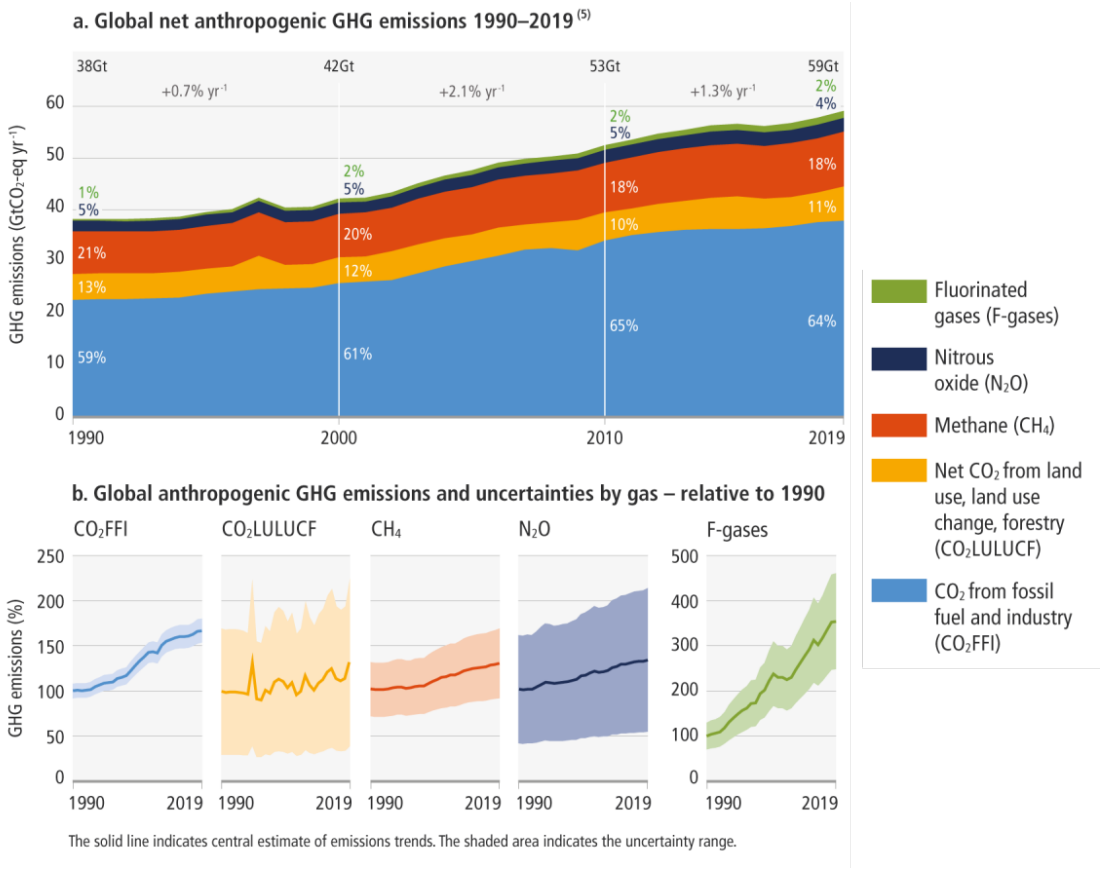

Figure 1.2: Global net anthropogenic GHG emissions 1990 - 2019 by groups of gases, adapted from IPCC (2022). Panel a) illustrates aggregate annual global net anthropogenic GHG emissions reported in gigatonnes of CO_2-equivalent, which were converted based on respective GWP-100 values. The proportion of global emissions attributed to each gas is displayed for the years 1990, 2000, 2010, and 2019, alongside the average annual growth rate across these decades. Panel b) shows global anthropogenic emissions, individually for every group of GHGs (normalized relative to 100 in 1990).

1.1.2 Fluorinated gases

F-gases are a class of synthetic, volatile molecules that are defined by the inclusion of at least one fluorine atom and their low boiling point (Sheldon and Crimmin 2022), including chlorofluorocarbons (CFCs), hydrochlorofluorocarbons (HCFCs), hydrofluorocarbons (HFCs), perfluorocarbons (PFCs), and sulfur hexafluoride (SF_6). CFCs, once widely used in refrigerants, aerosol propellants, and blowing agents, have been largely phased out due to their significant contribution to ozone depletion in the Earth's stratosphere (Powell 2002).

HCFCs served as temporary replacements for CFCs in refrigeration and air conditioning applications, due to their shorter atmospheric lifetime and lower ozone depletion potential. Consumption and production grew rapidly in developed countries until the mid-1990s (Simmonds et al. 2017), while especially HCFC-22 ($CHClF_2$) was extensively used (Saikawa et al. 2012). As HCFCs are ozone-depleting substances too, they were included in the Montreal Protocol and its amendments, requiring developed countries to halt HCFC consumption by 2030. HFCs were identified as direct replacements for CFCs and HCFCs, given that they do not deplete ozone while having similar chemical and thermal properties (Sheldon and Crimmin 2022). Consequently, their emissions have grown substantially in the past 2 decades, which introduced another environmental concern, as HFCs are potent GHGs. In 2019, the Kigali Amendment to the Montreal Protocol entered into force aiming to globally decrease both production and consumption of HFCs, while national regulations limit the use of HFCs in several countries. While total (CO_2-equivalent inferred) HFC emissions continue to increase, they were about 20% lower than previously projected for 2017–2019, indicating that companies might transition away from some species, such as the very potent HFC-143a ($C_2H_3F_3$) (Velders et al. 2022). PFCs are amongst the most potent and long-lived GHGs listed under the United Nations Framework, with atmospheric lifetimes ranging from thousands to tens of thousands of years. Despite being regulated under the Kyoto Protocol, PFCs are extensively used in the semi-conductor and electronics industry while also emitted as a by-product of aluminum smelting. Although abatement measures were introduced in these industries, global mean mole fractions of important PFCs, such as PFC-14 (CF_4), PFC-116 (C_2F_6), and PFC-218 (C_3F_8) continue to grow, with global annual growth rates increasing again after a period of decline (Say et al. 2021). In my thesis, I focus on SF_6, the GHG with the highest known GWP and high impact on the future climate.

1.2 Sulfur hexafluoride

1.2.1 A brief history of sulfur hexafluoride

SF_6 was initially produced in 1900, at the laboratories of the Faculté de Pharmacie de Paris by Henri Moissan and Paul Lebeau. The synthesis involved a highly exothermic reaction of fluorine with sulfur, which was obtained by electrolysis, resulting in the formation of an exceptionally stable gas (Assael et al. 2012). Subsequently, a series of publications studied the physical and chemical properties of SF_6 (e.g. Klemm and Henkel 1932, 1933; Prideaux 1906; Schumb 1947). The remarkable gas inertness and the chemical and dielectric properties caused the General Electric Company in 1937 to suggest its use in electrical equipment (Heise et al. 1997). By 1939, Thomson-Houston patented the concept of utilizing SF_6 in insulating cables and capacitors (Zavattoni 2014). After World War II, a broad spectrum of SF_6 applications emerged. In 1947, efforts began to use SF_6 for the insolation of transformers (Assael et al. 2012). SF_6 industrial production began in 1953 in the United States, with the introduction of SF_6-insulated circuit breakers (Maiss and Brenninkmeijer 1998). Following the market debut of gas-insulated switch gear (GIS) in the

1960s, SF_6 was widely manufactured for the use in electrical plant construction in Europe and the U.S. As companies initiated a transition from oil-based systems to SF_6, the gas was adopted in many applications as an arc-quenching and insulation medium (Rabie and Franck 2018).

1.2.2 Properties

SF_6 is a color- and odorless gas with a density of 6.139 $\frac{kg}{m^3}$ (at standard temperature and pressure), and a molecular weight of 146 $\frac{g}{mol}$, making it five times heavier than air (IEEE 2012). It has low solubility in fresh and seawater. Depending on the temperature and salinity, its solubility coefficient ranges from 1 to 6 $\cdot 10^{-4} \frac{mol}{l \cdot atm}$ (Bullister et al. 2002), which is roughly 2 magnitudes lower than of CO_2 (Weiss 1974). SF_6 is composed of one sulfur atom surrounded by six fluorine atoms arranged in a highly symmetrical octahedral geometry (see Fig. 1.3).

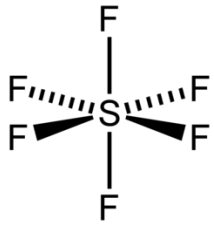

Figure 1.3: Illustration of the octahedral geometry of an SF6 molecule, consisting of six fluorine atoms attached to a central sulfur atom (Benjah-bmm27 2007).

The symmetrical arrangement of the six fluorine atoms around the central sulfur atom and the stable covalent bonds between the sulfur and fluorine atoms, lead to high chemical stability, making SF_6 resistant to chemical reactions under a wide range of conditions (e.g. Shida 2013). The structure also leads to high thermal stability, with reported decomposition temperatures between 500 and 600°C under normal atmospheric pressure (Camilli et al. 1952). However, in instances of overheated electrical equipment, SF_6 may initiate decomposition at temperatures exceeding 200°C, with substantial decomposition observed from 350°C onwards (Wang et al. 2011). When pressurized, SF_6 can exhibit the same dielectric strength as liquid insulators, withstanding high electric fields without electric break down (Giardini-Guidoni et al. 1979). At the same time, it possesses low thermal conductivity, restricting the transfer of heat energy within the gas. Both, the high dielectric strength and the low heat conductivity give rise to the exceptional arc-quenching capacity of SF_6 (Leeds et al. 1957), enabling it to extinguish or suppress electrical arc that forms during a fault condition in electrical equipment, which makes it an excellent insulator. In addition, SF_6 is non-explosive, non-flammable, and non-toxic. However, SF_6 can undergo reactions with gas impurities at arc temperatures, leading to the formation of by-products, which can be highly toxic (DeHope et al. 2007). While the chemical structure of SF_6 leads to favorable insulating properties, it also enables it to absorb infrared radiation at various

wavelengths, with a broad absorption band centered around 948 cm^{-1} wavelength (Harrison 2020), which renders SF_6 an extremely potent GHG with the highest known GWP-100 value of 24,300, as listed in the recent IPCC AR6 report (Smith et al. 2021). In addition, SF_6 is one of the longest-lived GHGs in the atmosphere, due to its chemical inertness.

1.2.3 Applications and emissions

1.2.3.1 Electrical equipment

SF_6 is primarily used in high-voltage electrical equipment in the electrical power industry, including GIS, transmission lines, high-voltage cables, and transformers.

Gas-insulated switch gears

SF_6 is used in high and medium-voltage switch gears, where it serves as an effective insulating medium between electrical components within the switch gear, preventing electrical breakdown. This includes circuit breakers (illustrated in Fig. 1.4), but also busbars, disconnectors, and other switching devices (depending on the specific switch gear configurations) (IEEE 2012). It also serves as a quenching gas to rapidly suppress or extinguish arcs that may occur during the opening or closing of electrical circuits, ensuring safe and reliable operation of the switch gear. Due to its high dielectric strength SF_6 enables the design of compact and space-saving switch gear configurations, occupying only 10–15% of the space required by conventional air-insulated units (Solvay 2018).

Figure 1.4: SF_6 gas circuit breakers in a 420 kV switchyard (Dingy 2007).

Gas-insulated transmission lines

Gas-insulated transmission lines are transmission systems that use a gas-insulated conductor to transmit high-voltage electricity (Koch 2011). Conventional designs are filled with pure SF_6, which serves as an insulating and arc-quenching medium (Koch 2008). New systems are designed for managing longer distances and use a mixture of SF_6 and N_2, where SF_6 can be diminished by up to 71%. With only 20% of SF_6 content, the insulation capability reaches 69% of that of pure SF_6 under identical gas pressure conditions. To offset the reduced dielectric strength relative to pure SF_6, a pressure increase of approximately 45% proves adequate (Koch et al. 2018).

High-voltage cables and tubular transmission lines

SF_6 also serves as an insulating and arc-quenching medium in gas-insulated high-voltage cables and tubular transmission lines, which are used for power transmission at high and extra high voltage in heavily concentrated industrial areas (Solvay 2018). Tubular transmission lines serve to link power stations with transformers or switching stations and can permit high current levels with minimal electric loss, when filled with pressurized SF_6 or SF_6/N_2 mixtures (Kunze et al. 2007).

Transformers

In transformers, the insulating medium serves the dual purpose of providing insulation and transferring heat from the winding and core assembly to the surrounding environment (Gouda et al. 2012). Gas-insulated transformers use SF_6 because of its excellent heat-transfer capacity, non-flammability, and non-toxicity (Toda 2002). This is an advantage over oil-insulated transformers which have limitations including the need for fire-extinguishing equipment, long clearance length, low ignition value, costly and toxic soil remediation, as well as the danger of explosions (Özgönenel et al. 2018). Due to their superior operational safety, SF_6-insulated transformers are commonly installed in mines and department stores (Solvay 2018).

Emissions from electrical equipment

The electrical equipment in the power industry is considered to be the largest source of SF_6 emissions. Sales data from Europe, Japan, the U.S., and South Africa (1996 - 2003) indicate that electric utilities and equipment manufacturers for power systems consumed 80% of the produced SF_6 (Simmonds et al. 2020). In China, emissions from the electrical equipment sector contributed to about 70% of total SF_6 emissions from 1990 to 2010 (Fang et al. 2013). In this sector, emissions occur primarily through leakage, maintenance, and retirement of the equipment (Xu et al. 2011). Emissions during the production process are considered negligible (Zhou et al. 2018). The emission levels of SF_6 are influenced by various factors, including the age of the equipment, where older models tend to have higher leakage rates compared to newer ones, as well as the scale of the transmission network

and the recycling practices for outdated equipment (Gambhir et al. 2017; Purohit and Höglund-Isaksson 2017). The typical lifespan of electrical equipment in the power sector is 30–40 years, leading to a delay between SF_6 consumptions and emissions (Zhou et al. 2018). In recent years, studies have shown that less potent alternative gases, such as NOVEC-4710 and NOVEC-5110 can be used to replace SF_6 in mid- and high-voltage electrical switch gear (e.g. Billen et al. 2020; Owens et al. 2021; Yedinak et al. 2023) and several manufacturers, such as Siemens, General Electric, and ABB have announced the expansion of SF_6-free technologies (Billen et al. 2020). Nevertheless, SF_6 can not be replaced completely, and especially not in the short term (Zhou et al. 2018).

1.2.3.2 Magnesium and aluminum metal industry

SF_6 is used for blanketing or degassing for molten reactive metals, such as magnesium and aluminum (Maiss and Brenninkmeijer 1998). In particular, the magnesium industry uses SF_6 to prevent high-flammable liquid magnesium from oxidation and surface burning during the production of primary magnesium, die casting, and recycling operations (Bartos et al. 2003). In the aluminum industry, SF_6 is primarily used for degassing, removing dissolved gases like hydrogen from molten aluminum before it solidifies into a casting, to improve mechanical properties (Schwarz and Gschrey 2009).

The magnesium industry is recognized as a significant source of SF_6 emissions, especially in China, the world's largest magnesium producer and exporter. Between 1990 to 2010 Fang et al. (2013) found its contribution to be about 10% of the total Chinese emissions, with a consumption factor of 1.65kg SF_6 per ton of magnesium. In the magnesium sector, all consumption of SF_6 is considered equal to its emissions to the atmosphere, as only a minor fraction of the blanketing gas undergoes chemical reactions and thermal degradation while the major part escapes through leakages and openings of the melting furnace (Eggleston et al. 2006). After 2010, the consumption of SF_6 as a blanketing gas in Chinese magnesium production was halted and largely replaced with SO_2 (Simmonds et al. 2020; Zhou et al. 2018). In 2006, SF_6 emissions from EU magnesium industry equaled almost 20% of the total SF_6 emissions (Schwarz and Gschrey 2009). While the 2006 EU F-gas regulation restricted SF_6 usage in magnesium die-casting, the 2014 EU F-gas regulation banned SF_6 also in recycling magnesium die-casting. Alongside with SO_2, HFC-134a emerged as an accepted alternative to SF_6. Additionally, NOVEC-612 started being used in the U.S. and Japan in 2008, and is now available worldwide (Hort et al. 2015; Schwarz and Gschrey 2009).

1.2.3.3 Semiconductor industry

In the semiconductor sector, thin film transistor liquid crystal display manufacturing is the major source of SF_6 emissions (Cheng et al. 2013), in which it is used for the cleaning of chemical vapor deposition chambers (Rößler et al. 2005) and for plasma etching (Lee et al. 2004). Here, the gas is ionized, dissociating into sulfur and fluorine radicals and ions, which react and remove material from the substrate surface (mostly silicon) to create specific patterns (Hodak et al. 2008). In photovoltaic manufacturing, SF_6 is also used in etching

processes and to remove damages to the wafers, which are slices of silicon, the building blocks of solar panels (Andersen et al. 2014).

Between 2000 and 2010, Fang et al. (2013) found the contribution of the semiconductor industry to the total Chinese SF_6 emissions ranging from 10% to 20% and documented emissions of 0.15 Gg in 2005 and 0.4 Gg in 2010. Cheng et al. (2013) reported Chinese SF_6 emissions of roughly 0.2 Gg/yr between 2004 and 2011. According to Zhou et al. (2018) there is a phase-out of Chinese SF_6 emissions in semiconductor production. Global annual consumption by the semiconductor industry was reported to range between 0.41–0.55 Gg/yr from 2012 to 2018 (Simmonds et al. 2020). In recent years mainly NF_3, but also other gases such as CF4 or HFC-134a have been used as a substitute for SF_6 in the semiconductor industry. Further, F_2 produced onsite from hydrogen fluoride (HF) and SF_4 have been proven as an alternative (Cui et al. 2024).

1.2.3.4 Sulfur hexafluoride production

There are two main methods for SF_6 production: direct synthesis and electrolysis. In the direct synthesis, fluorine gas is introduced directly into molten sulfur at temperatures of 120 to 180 °C. In the electrolysis method, fluorine gas is generated through the electrolysis of fluorine-containing substances, which is then combined with elemental sulfur or sulfides at high temperatures (Cui et al. 2024). Between 2000 and 2010, emissions from the SF_6 production accounted for 6-10 % of the total SF_6 emissions in China (Fang et al. 2013), who is globally the main producer of SF_6. Simmonds et al. (2020) estimated annual SF_6 loss from production of 0.1 Gg/yr between 1990 and 2018, using an emission factor (see Sec. 1.3.1) of 2.2% for China (Fang et al. 2013) and 0.5% for the rest of the world.

1.2.3.5 Particle accelerators

SF_6 is used in research-operated, industrial (low and high voltage), and medical particle accelerators (clinical linear accelerators) to prevent electrical breakdown, suppress electrical arcs, and maintain stable electric fields (Schwarz 2005). In clinical linear accelerators SF_6 is pressurized in the waveguide, a hollow metal tube that accelerates charged particles, such as electrons, utilizing high-frequency electromagnetic waves (Lichter et al. 2023). In the industry, SF_6 insulated accelerators serve as electron beam systems for manufacturing purposes (e.g. polymer cross-linking) (Cleland 2006). In research, the accelerator is typically placed together with a high-voltage generator in an SF_6 insulated tank where charges can vary from five to more than ten thousand kilograms (Zille et al. 2019). These tanks must be opened for adjustment and repair of the equipment, where SF_6 is pumped into a storage tank (illustrated in Fig. 1.5), entailing considerable gas losses with emission factors up to 7% (German Environment Agency 2023; Schwarz 2005). Between 1995 and 2021 German SF_6 emissions from particle accelerators were estimated to be between 4 and 5 tonnes per year (German Environment Agency 2023).

Figure 1.5: SF_6 storage tank at the university of Dresden (Yeti-Hunter 2018).

1.2.3.6 Soundproof windows

In Western Europe, starting in 1975, SF_6 was filled in double-glazing windows to damp acoustic pressure and improve the sound-insulating effect. In Germany, six percent of the manufactured and installed glazing contained SF_6 in 1990. Since the end of the 1990s, a change in glazing structures made the sound-insulating effect of SF_6 dispensable, and the entire interspace between the glasses could be used for thermal insulating with the gas argon (Schwarz 2005). Since 2007, the EU banned the use of F-gases in windows, for residential uses, and expanded the ban to all windows in 2008. However soundproof windows have a relatively long lifetime of about 25 years, and therefore emissions have been expected to continue growing until 2020 and are still substantial in Germany and Austria (Purohit 2024).

1.2.3.7 Car tires

From 1984, Germany has utilized SF_6 as a filling gas in automobile tires to maintain stable tire pressure. It takes over 1 kg of SF_6 to fill a complete set of four tires. The consumption of SF_6 for this purpose increased to 125 tons between 1984 and 1995 and dropped afterward as a result of the awareness of the gas's GWP (Schwaab 2000). As emissions occur around 3 years after the filling, SF_6 emissions from car tyres substantially decreased between 1995 and 2002 (German Environment Agency 2023).

1.2.3.8 Sport shoes

From 1996 to 1997, SF_6 was used in Nike's Air model shoes, according to a letter from the director for Nike Environmental Action Team to Greenpeace Denmark, with a total SF_6

consumption of around 288 tones. However, Nike announced phasing out its use of SF_6 and replacing it with nitrogen from 2001 at the latest (Pedersen 2000).

1.2.3.9 Military applications

The military has many critical uses for SF_6. It is used as an insulator in ground and airborne radar systems, preventing electrical arcing in the antenna's hollow conductors during the transmission of high-frequency energy pulses at high voltages (Zille et al. 2019). Annual emissions of SF_6 from radar systems of the German NAEWF (NATO - Airborne Early Warning and Control Force) aircraft were estimated to be 12.5 t/yr between 1995 and 2002 (Schwarz 2005). SF_6 also serves as an oxidant for lithium in Stored Chemical Energy Propulsion Systems, like infrared decoys or torpedos (Koch 2004). The usage of SF_6 to reduce the noise from torpedo propellers has also been documented (Christophorou et al. 1997). SF_6 is also assumed to be emitted as a by-product during the production of nuclear fuel and nuclear warheads (Zille et al. 2019).

1.2.3.10 Medical applications

SF_6 is used as a contrast agent for ultrasound imaging (Lee et al. 2017), and for dynamic pulmonary ventilation (Schreiber et al. 2001). Furthermore, it is used for eye surgical procedures, where the SF_6 bubbles are injected into the eye, to increase its volume (Brinton and Wilkinson 2009). In many medical applications, SF_6 is considered to be emitted within one year of its purchase (Zille et al. 2019).

1.2.3.11 Tracer gas

In addition to the non-toxic and inert nature of SF_6, it is detectable at very low concentrations and has low atmospheric background concentrations, which makes it suitable as an atmospheric tracer gas. It has been used as a tracer in environmental studies, to investigate atmospheric dispersion, circulation patterns, and pollution transport (Maiss et al. 1996; Martin et al. 2011) and for leakage detection (Wan et al. 2024). In addition, it has also been used as a tracer in groundwater (e.g. Okofo et al. 2022), rivers (e.g. Ho et al. 2002), and oceans (e.g. Tanhua et al. 2004). Simmonds et al. (2020) estimated a total release of 4 Mg from historical SF_6 tracer studies

1.2.3.12 Wind turbines

SF_6 is used in GIS within the offshore wind sector (Eastern Research Group, Inc. 2023). Due to a recent BBC article (McGrath 2019) the use of SF_6 in the renewable energy sector got a lot of media attention. According to an article by WindEurope (2019), leakage emissions from Europe's 100,000 wind turbines accounted for about 900kg of SF_6 between 2013 and 2019.

1.2.3.13 Natural sources

SF_6 was detected in granites where fluorite is an accessory mineral. Outgassing from these materials was estimated to lead to a natural SF_6 background atmospheric abundance of 0.01 ppt (Harnisch and Eisenhauer 1998).

1.2.4 Atmospheric lifetime

To determine the atmospheric lifetime of a tracer gas, its annual loss can be derived either through measurements or modeling. In the case of measurements, one can utilize multiple trace gases to correlate the loss of one gas with a known lifetime to that of another. In the context of model-derived estimations, the loss from considered removal processes can be computed at each model time step (Ray et al. 2017). SF_6 remains highly unreactive from the troposphere to the middle stratosphere and is only slowly removed in the upper stratosphere and mesosphere. Ravishankara et al. (1993) estimated an atmospheric lifetime of 3,200 years, using a two-dimensional atmospheric model, considering loss processes through dissociative electron attachment ($SF_6 \rightarrow SF_5^- + F$), photolysis by Lyman-$alpha$ radiation, and O(1D) reaction. Morris et al. (1995) expanded the model with ion chemistry and found that associative electron attachment ($SF_6 + e^- \rightarrow SF_6^-$) is the major loss process, which can reduce the atmospheric lifetime of 3,200 down to 800 years, and under certain conditions even to 600 years. These values were, however, presented as lower limits. Two years later Patra et al. (1997) presented a value of 1,937$\pm$432 years, computed from measured SF_6 mixing ratio correlations with simultaneous measurements of N_2O, and CFC-12. Nevertheless, the value of 3,200 years by Ravishankara et al. (1993) became the most prominent one and was used in all of the climate and stratospheric ozone assessments and State of the Climate report, even making it into the IPCC AR5 report (Myhre et al. 2013). A more recent study by Kovács et al. (2017) determined a SF_6 lifetime ranging from 1,120 to 1,475 years, by using the Whole Atmosphere Community Climate Model, including complex formalism for both associative and dissociative electron attachment and a comprehensive model of ion chemistry in the lower ionosphere to account for partitioning of electrons and negative ions below 80 km. In the same year, Ray et al. (2017) utilized in situ measurements in the Arctic polar vortex that sampled air with up to 50% SF_6 loss to compute a lifetime ranging from 580 to 1,400 years. Due to these two studies, the IPCC AR6 report (Smith et al. 2021) revised the value of SF_6 atmospheric lifetime from 3,200 to 1,000 years.

1.2.5 Oceanic sink

In addition to atmospheric loss, the ocean potentially serves as an SF_6 sink. Atmospheric SF_6 can enter the ocean through air-sea exchange, with the rate of gas exchange correlating with wind speed (Wanninkhof et al. 1985). The concentrations in the ocean's surface layer depend upon various factors including gas solubility, as well as atmospheric and oceanic concentrations (Fine 2011). As SF_6 has low atmospheric concentration and solubility, the concentration in surface seawater is less than $10^{-15} \frac{mol}{l}$ (Cai et al. 2016). Ko et al. (1993)

suggested that, in addition to atmospheric removal processes, oceanic SF_6 sinks should be considered, but nevertheless, estimated the effect to be very small. They stated that the SF_6 lifetime due to the ocean removal would be of the order of 10^4 years and longer. Therefore, in many studies, oceanic SF_6 sinks have been neglected (e.g. Levin et al. 2010; Rigby et al. 2010; Simmonds et al. 2020). However, a recent study by Ni et al. (2023) suggested, that the ocean is an important atmospheric SF_6 sink, removing about 7% of the annual anthropogenic emissions. They based their estimation on calculated sea-air fluxes of SF_6, derived from simultaneous measurements of SF_6 concentrations in both the atmosphere and surface seawater of the Western Pacific and Eastern Indian Ocean.

1.2.6 Impact on the climate

SF_6 is the gas with the highest known GWP, with values of 18,200, 24,300, and 29,000 for a 20-, 100-, and 500-year time horizon, respectively (Smith et al. 2021). Given its very long atmospheric lifetime, emitted SF_6 accumulates in the atmosphere, and warms the climate for centuries. Since the late 1990s, global concentrations of SF_6 have undergone rapid growth, increasing from 4.2 ppt in 1998 to 11.0 ppt in 2022 (see Fig 1.6).

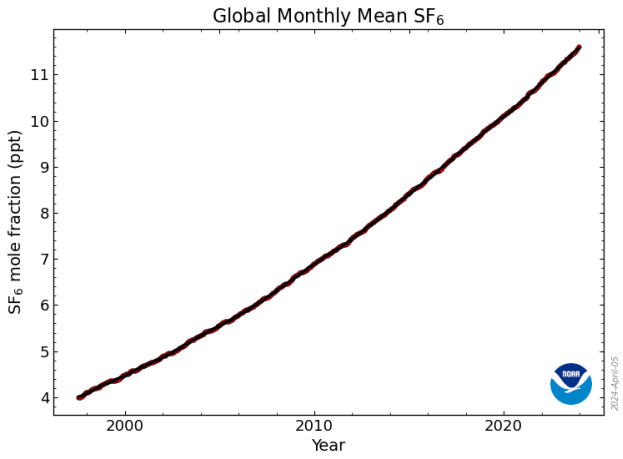

Figure 1.6: Globally-averaged, monthly mean atmospheric SF_6 abundance determined from marine surface sites (Lan et al. 2024).

Radiative forcing increased from roughly 2.4 $\frac{mW}{m^2}$ (1998) to 6.2 $\frac{mW}{m^2}$ (2022), given SF_6's large radiative efficiency of 0.567 $\frac{W}{m^2 \cdot ppb}$ (Smith et al. 2021). By the end of the 21st century, radiative forcing of SF_6 could surge tenfold if the current trend in global SF_6 emissions prevails (Hu et al. 2023). The global emission trend is positive, which can be deduced from the increasing global-averaged atmospheric SF_6 growth rates, which represent the sum of all SF_6 annually added to the atmosphere by human activities. Since 1998, atmospheric growth rates have almost doubled, increasing from 0.20 ppt/yr in 1998 to 0.37 ppt/yr 2022 (Lan et al. 2024).

1.2.7 Sulfur hexafluoride regulations

SF_6 is regulated under the Kyoto Protocol, ratified in 1997, where it was listed as one of the six categories of major GHGs, initializing the efforts to reduce emissions. For the first commitment period (2008-2012) the Kyoto Protocol set individual binding GHG emission reduction targets for 37 countries, adding up to an average reduction of about 5% compared to levels in 1990 (United Nations Framework Convention on Climate Change 1997). During the Bali Roadmap in 2007, many countries aimed for abatement reduction targets between 25 and 40% below 1990 levels by the year 2020, which, however, were not committed in the action plan, but inserted as a footnote (Jingmin and Dong 2008; United Nations Framework Convention on Climate Change 2007). The 15^{th} Conference of the Parties (COP 15), brought a political agreement for the establishment of emission reduction targets for developed countries and financial assistance for climate change mitigation to developing countries (United Nations Framework Convention on Climate Change 2009). The Paris Agreement mandated each participating nation to prepare, communicate, and maintain nationally determined contributions (NDCs) for the reduction of GHG emissions to limit the temperature increase to 1.5°C above pre-industrial levels (United Nations Framework Convention on Climate Change 2015). Following the Paris Agreement, several governments and organizations set ambitious emissions goals for realizing net zero in 2050 or earlier. Cui et al. (2024) provide a comprehensive summary of woldwide implementations of SF_6 reduction efforts.

China

Since 2012, China implemented GHG reduction policies, including regulations like GB/T-28537-2012 and GB/T-32151.2-2015, setting standards for using SF_6 in high-voltage switch gear, specifying the installation, maintenance, and disposal of the equipment, and addressing SF_6 emission accounting rules (Cui et al. 2024). In addition, environmentally friendly switch gear technologies have been introduced (An et al. 2024). The demand for SF_6 emission reduction is also addressed in China's net-zero goal by 2060.

U.S.

In 1999, the U.S. Environmental Protection Agency (EPA) established an emission reduction partnership with the electric power industry to reduce SF_6 emissions. In 2009, the EPA published a regulation under the Greenhouse Gas Reporting Program, for the mandatory reporting of GHG emissions from sources typically emitting more than 25,000 CO_2 equivalent metric tons per year, requiring the large SF_6 users to report annual emissions (Ottinger et al. 2015). California's Global Warming Solutions Act of 2006 (California State Legislature 2006) mandates SF_6 emissions to be reduced to 1990 levels by the year 2020. The 310 CMR 7.72 regulation in Massachusetts mitigates SF_6 emissions from GIS. It imposes a maximum annual SF_6 leak rate of 1% for GIS acquisitions after 2015, while GIS owners are required to outline measures for cutting emission rates (Massachusetts 2021). In 2021, the U.S. State of Maine passed the LD 1503 law "An Act To Stop Perfluoroalkyl and Polyfluoroalkyl

Substances Pollution", which requires manufacturers of products with intentionally added PFAS (per- and polyfluoroalkyl substances, including SF_6) to report the presence of PFAS in those products from 2025 and prohibits the sale of products containing intentionally added PFAS from 2030 (State of Maine 2021).

European Union

To achieve the reduction targets for the first commitment period to the Kyoto Protocol, the EU passed regulation No. 842/2006 in 2006, which set rules for the containment, recovery, use, and reporting of F-gases. In particular, the use of SF_6 for the filling of vehicle tyres was prohibited from 2007 and the SF_6 use in magnesium die-casting (above 850 kg) was prohibited from 2008. In addition, F-gas-filled windows and footwear were prohibited from being put on the market (European Parliament and Council of the European Union 2006). In 2014, EU's F-gas regulation 517/2014 further tightened the rules, banning the use of SF_6 for recycling magnesium die-casting alloys from 2018 and requiring leak detection systems for electrical switch gear from 2017 (European Parliament and Council of the European Union 2014). In 2024, the EU parliament adopted a new regulation for F-gases, where the consumption of HFCs will be completely phased out by 2050 (European Parliament and Council of the European Union 2024). The regulation requires the phase-out of F-gases in medium-voltage switch gears by 2030 and high-voltage switch gears by 2032. Further, the use of SF_6 for the maintenance or servicing of electrical switch gear equipment is prohibited from 2035 (unless it is reclaimed or recycled).

1.3 Emission monitoring

A crucial element of the Kyoto Protocol was the establishment of a system for reporting and monitoring GHG emissions by participating countries, to assess the progress in meeting their emission reduction targets. Industrial countries classified as Annex-I nations are required to annually submit reports detailing their GHG emissions to the UNFCCC, including SF_6. These national GHG inventories are almost exclusively calculated by so-called bottom-up methods.

1.3.1 Bottom-up methods

In bottom-up methods, individual emission sources are identified and categorized, and a large number of statistical activity data (e.g. industrial production and consumption) is gathered, to quantify the amount of gas, which is used or produced in the different source sectors. By applying emission factors, that represent the emissions generated by a certain activity, total emissions from each source sector are calculated and aggregated to obtain an emissions inventory for a specific country. However, the reliability of this complex self-reporting system, based on bottom-up methods, has been questioned (e.g. Nilsson et al. 2001). On one hand, its effectiveness will primarily depend on the way individual countries implement their obligations into practice (Gupta et al. 2003). Certainly, emissions

from spurious or even illegal activities will not be reported. And even if inventories are prepared according to good practice and guidelines by the UNFCCC, intrinsic uncertainties are high (Rypdal et al. 2005). The emissions from individual source sectors are based on an assumption about the relationship between a particular activity and the resulting emissions. These emission-producing activities are variable in space and time, making it hard to come up with an appropriate estimate. Some processes might also be poorly understood, or not recognized as an important source. For other activities, appropriate data is missing and the estimates rely on approximations. Finally, the complex systems of creating and processing data for the inventory give rise to a range of possibilities for human errors (Rypdal and Winiwarter 2001). All of these uncertainties present large obstacles to efficient emission reduction strategies. In the recent IPCC AR6 report (Dhakal et al. 2022), uncertainties of aggregated F-gas emissions are estimated to be 30%. For SF_6, the aggregation of bottom-up based reports to the UNFCCC has been shown to strongly underestimate global emissions, leaving a substantial gap of 70% to 80% of non-reported emissions in the 2000s (Levin et al. 2010). Thus, there is a growing need for independent verification of these bottom-up estimates, which can be provided by atmospheric observation-based top-down methods such as inverse modeling (e.g. Nisbet and Weiss 2010; Rypdal et al. 2005).

1.3.2 Inverse modeling

Inverse modeling provides a tool to optimize GHG emissions based on atmospheric measurements of a certain gas. Gases released into the atmosphere disperse through atmospheric turbulence and are transported by winds, while they are globally mixed through large-scale circulation patterns. The atmospheric transport can be simulated by atmospheric transport models. For inversion purposes, typically Eulerian or Lagrangian Particle Dispersion models (LPDMs) are used. Eulerian models solve the equations of fluid dynamics on a fixed grid system to derive the movement of pollutants, while LPDMs simulate the dispersion of pollutants by releasing a large number of virtual particles and tracking their individual trajectories over time, as they move through the atmosphere (see Sec. 2.1). In the inverse model approach, atmospheric models are used to relate the changes in atmospheric mole fractions (e.g. at a measurement station) to GHG fluxes from the surface. These relationships are then used together with the observed atmospheric mole fractions and *a priori* information on the emissions in an optimization process, to find the best estimate of emissions (*a posteriori* emissions), that minimizes the mismatch between modeled and observed mole fractions (see Sec. 2.2.3). Inverse modeling can be applied at different scales, from national to continental or even global scale. Recent advancements in numerical algorithms, computer capacity, transport models, and atmospheric observations have substantially improved this methodology (Leip et al. 2017). Consequently, it was suggested, that the emphasis for emission estimation should be shifted away from bottom-up and towards top-down methods (Leip et al. 2017), and that atmospheric inversion estimates should supplement the traditional inventories, in particular in the case of F-gases (Rypdal et al. 2005). Until now, only Switzerland, the United Kingdom, and Australia have been using top-down methods as part of their national GHG reports. Several countries have shown

initiatives to follow their example, however, in many cases insufficient observational data hinders the implication of inverse modeling estimates. Generally, the lack of observations is a big problem in the global emission monitoring of GHG emissions, as there are big gaps in detection networks (Weiss et al. 2021). While areas such as central North America, eastern Asia, and western Europe are relatively well-sampled for the main GHGs, South America, central, southern, and western Asia, eastern Europe, parts of Southeast Asia and North America, New Zealand, Australia and most of Africa are covered poorly (see Fig. 1.7 for the example of SF_6). In many of these regions, emissions are expected to grow due to industrial and economic development. Less prominent GHGs are sampled only by a few observation stations. Thus substantial effort is required to further develop surface measurement networks, with emphasis on the southern hemisphere and tropics. Leip et al. (2017) estimated that roughly 500 million dollars would be required in the next 20 years to provide a good in-situ network of about 500 stations globally, sufficient to resolve most countries, a small amount, compared to investments in global carbon-equivalent trading markets (Nisbet and Weiss 2010; Weiss and Prinn 2011).

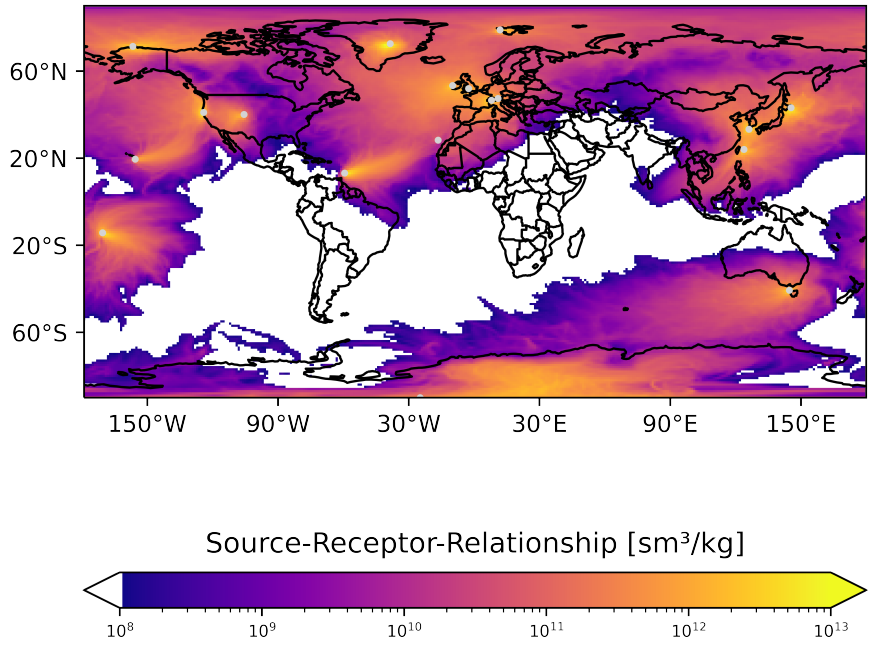

Figure 1.7: Networks of continuous SF_6 measurement stations (grey dots) can be used in an inverse modeling approach to quantify regional emissions. The shown annual-averaged emission sensitivity (also known as Source-Receptor Relationship (SRR), see Sec. 2.1.3), which illustrates how well regions are covered by the existing network, shows big gaps. More sites are needed to cover the global South and large parts of the northern Hemisphere.

.

1.4 Uncertainties of the inverse modeling approach

The recent IPCC AR6 report states that top-down methods are useful, but "not yet capable of verifying emission levels or trends" (Dhakal et al. 2022). Partly, this can be attributed to the discussed lack in observation networks, however, the inverse modeling approach itself has been argued to provide insufficient accuracy (e.g. Rypdal et al. 2005). Inverse modeling comes with substantial uncertainties, and "most systems are not at the level of transparency, flexibility, and accessibility needed to provide the scientific community and policy makers with a comprehensive and robust view of the uncertainties associated with the inverse estimation of GHG and reactive species fluxes" as stated by Berchet et al. (2021). Traditionally, the uncertainties of inversion-derived emissions are based on Gaussian error statistics within a Bayesian framework, using a single transport model and inversion set-up, potentially missing major contributions to the true uncertainties (Brunner et al. 2017). Several studies (e.g., Bergamaschi et al. 2015; Chevallier et al. 2019; Locatelli et al. 2013) have shown that the range of inversion-derived emissions using different inversion systems or set-ups can be considerably larger than the uncertainties calculated by the individual inversions. Therefore, a better understanding of the uncertainties is crucial. Errors in the simulated atmospheric transport play a substantial role in the overall uncertainties of emission estimates from inverse modeling, particularly at smaller spatial scales (e.g. Chevallier et al. 2019; Gurney et al. 2003; Locatelli et al. 2013). These can be errors in the meteorological fields, or errors in the models themselves. Another source of uncertainty is the aggregation error, arising from the limited spatial resolution of the emission grid, when the assumption that fluxes within the resolved area do not deviate substantially from the area's mean, becomes invalid (e.g. Kaminski et al. 2001). Major errors can also emerge from insufficient knowledge about the observation and *a priori* emission uncertainties, and their respective correlations, which all have to be estimated prior to the inversion process (e.g. Berchet et al. 2013; Ganesan et al. 2014; Michalak et al. 2005). When using LPDMs for inverse modeling, the definition of the baseline is one of the largest sources of uncertainties (Henne et al. 2016; Katharopoulos et al. 2023; Thompson and Stohl 2014). Further uncertainties arise from the subjective choice of the LPDM backward simulation length.

1.4.1 The baseline definition

When utilizing LPDMs for inverse modeling applications, a large number of virtual particles are usually released from the measurement site and traced backward in time for a chosen simulation period. The model output provides the sensitivity of the measured atmospheric mole fractions to the emissions that occur during the chosen backtracking simulation period. Using Lagrangian models has many benefits, such as subgrid-scale information at the measurement point (see Sec. 2.1). A drawback, however, is that virtual particles can be followed backward only for a limited period, due to computational constraints. The LPDM can, therefore, only relate emissions occurring within this simulation window to observed mole fraction values. In contrast, any emissions preceding the chosen simulation period can not be captured by the LPDM, however, they still have to be considered when modeling the mole fraction values. Therefore, all these emission contributions are aggregated in a

so-called baseline that has to be added to the modeled emission contributions. Given that errors in the baseline propagate to errors in the resulting *a posteriori* emissions, an accurate baseline definition is crucial for the inversion. Numerous approaches have been proposed for establishing this baseline.

One approach is to use statistical filter methods. These methods define the baseline through low mole fraction measurements which are statistically selected at individual measurement sites and which are assumed to be unaffected by emissions within the LPDM simulation period. Baseline mole fractions have been defined as the minimum measured values (e.g. Ganesan et al. 2014; Zeng et al. 2012) or by excluding measurement outliers, outside a Gaussian distribution (e.g. Kim et al. 2021; Saito et al. 2010) in a selected time interval. Similarly, Graziosi et al. (2015) and Maione et al. (2014) decomposed the overall observed probability distribution function into a Gaussian and a Gamma distribution part, where the Gaussian distribution part was used as the baseline. Shirai et al. (2010) determined the baseline by using a peak analysis tool, where a rectangle is manually positioned over each observation peak and the baseline is drawn within the two outermost points included in that rectangle. A widely used statistical method (e.g Annadate et al. 2023; Henne et al. 2016; Schoenenberger et al. 2018; Vollmer et al. 2016) is the robust estimation of baseline signal (REBS) method, introduced by Ruckstuhl et al. (2012) which employs a local linear regression model. For some stations, a statistically derived baseline from a nearby background station was taken to estimate the baseline (Oney et al. 2017). Some statistical baseline methods also include model information for the selection of measurements. The UK Met Office analyzes the history of air entering the regional inversion domain as selection criteria (see e.g. Manning et al. 2021). Stohl et al. (2009) suggested subtracting *a priori* simulated mole fractions from pre-selected measurements, in order to avoid a baseline overestimation.

A totally different baseline approach was presented by Rödenbeck et al. (2009), where a regional transport model is nested into a global model, providing external information beyond the boundaries of the spatial-temporal inversion domain. In such an approach, the baseline is based on the output of the global model, which is why I refer to it as global distribution based (GDB) approach. Trusilova et al. (2010) and Ganshin et al. (2012) showed, that embedding a regional Lagrangian model into a global Eulerian model improved the correlation between modeled and measured CO_2 mole fractions, in comparison to using the Eulerian model alone. Rigby et al. (2011) and Monteil and Scholze (2021) developed such an Eulerian-Lagrangian coupled system to optimize SF_6 and CO_2 emissions, respectively. In many regional LPDM-based inversion studies the baseline is computed by coupling the LPDM trajectories to a global model at the location where particles leave the spatial inversion domain (e.g. Ganesan et al. 2017; Lunt et al. 2016; Ramsden et al. 2022; Say et al. 2019). Another possibility is to do the coupling at the end of the LPDM simulation period, where back-trajectories terminate (e.g. Thompson and Stohl 2014).

Although the treatment of the baseline is crucial for LPDM-based inversions, the influence of chosen baseline approaches on inversion results is unclear. A systematic comparison of various methods across different model configurations, such as the LPDM backward simulation period, is missing.

1.4.2 The backward simulation period

Another source of uncertainty regarding LPDM-based inversion methods is the choice of the LPDM backward simulation period. It must be decided how long particles are traced back in the LPDM simulation before they are terminated, as there are limitations due to computational costs. This decision sets the temporal boundaries of the inversion, determining which emissions can be directly related to the mole fraction measurements and are accessible to the inversion (emissions occurring within this period) and which emissions must be accounted for in the baseline (emissions occurring before this period). For regional inversions, these choices are usually made, such that the majority of particles have left the region of interest before getting terminated. For global GHG inversions, the emission sensitivities are usually spread over large areas of the globe after 10-20 days. However, observations are most sensitive to emissions occurring during the first few days of the backward simulation. In practical terms this means that the biggest part of the observed variability (e.g. pollution events) can be explained by emissions occurring within a few days before the respective measurements. The spatially resolved information content however decreases with temporal distance to the measurements, as virtual particles are spread over larger areas. While, with longer simulation periods, more emissions become accessible to the inversion, it also becomes more difficult to extract information on individual emission sources (Stohl et al. 2009). The benefit obtained from every additional simulation day will therefore typically decrease, while computational costs grow. Consequently, LPDM-based inversion studies constrain the backward simulation to relatively short periods, while the choice remains subjective. The range of simulation periods used by different studies is therefore large, e.g., 5 days (e.g. Keller et al. 2012; Vollmer et al. 2009; Zhao et al. 2009), 7 days (e.g. Koyama et al. 2011), 10 days (e.g. Schoenenberger et al. 2018; Simmonds et al. 2018; Thompson et al. 2017), 20 days (e.g. Fang et al. 2014; Maione et al. 2014; Stohl et al. 2009) or 30 days (maximum, e.g. An et al. 2024; Ganesan et al. 2017). Here, Koyama et al. (2011) and Stohl et al. (2009) are global inversion studies, while the other listed studies apply regional inversions. A systematic analysis of the impact of the backward simulation period is missing.

1.5 Top-down sulfur hexafluoride emissions

In 2020, Simmonds et al. (2020) published a comprehensive SF_6 study, where they employed a global box model (AGAGE 12-box model; Rigby et al. 2013) together with an inversion system, to estimate global SF_6 emissions between 1980 and 2018 (Fig. 1.8). Similar to earlier studies by Levin et al. (2010) and Rigby et al. (2010), they found that, after a peak around 1995 (6.2 Gg/yr), global SF_6 emissions exhibited a decreasing trend until 2000 (5.0 Gg/yr), after which they started to grow again, with a persistent positive trend until the end of the study period (9.0 Gg/yr). The emission growth after 2000 could be primarily attributed to emissions from non-Annex-I Asian countries (Rigby et al. 2010), due to the expansion in electrical power, electronics, and metal industries. Specifically, East Asian countries have been identified, to substantially contribute to the overall global SF_6

emissions (45%-49% between 2009 and 2012), with China emerging as the main contributor (Fang et al. 2014). Between 2011 and 2021, Chinese emissions have almost doubled (from 2.6 Gg/yr to 5.1 Gg/yr) and accounted on average to about 46% of the global emissions (An et al. 2024). Employing regional inversion systems, Simmonds et al. (2020) found, that Western Europe emissions were around 10 times lower than those in China. In their contribution to the UK annual report to the UNFCCC, Manning et al. (2022) presented inversion-derived SF_6 emissions for North-West Europe, revealing a declining trend (0.37 Gg/yr in 2004 to 0.18 Gg/yr in 2021). A declining SF_6 emission trend was also found for the United States of America between 2007 (0.83 Gg/yr) and 2018 (0.39 Gg/yr), where emissions were suggested to be higher in the winter than in summer (Hu et al. 2023). The SF_6 emissions in other regions such as Africa, Oceania or South America have been studied on a continental scale between 2004 and 2008 by Rigby et al. (2010), however no trends could be derived due to the poor observational constraint.

Although global SF_6 emissions can be well constrained by global box models, and regional inversion systems have been used to estimate SF_6 emissions in specific regions, there is no clear link between regional and global emissions and an updated, comprehensive, top-down perspective of the global SF_6 emission distribution is missing. Additionally, many inversion studies rely solely on high-frequency tower measurements or observations from specific networks, potentially missing information. Further, the seasonality of SF_6 emissions, which could help to identify seasonally dependent sources, is poorly understood.

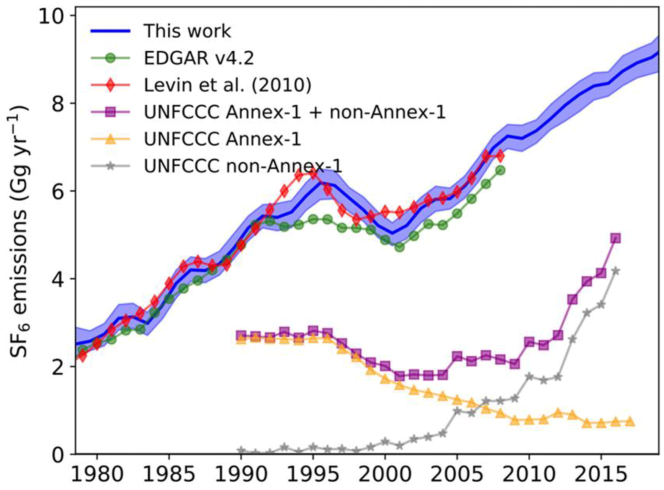

Figure 1.8: Global SF_6 emission trend (Simmonds et al. 2020). The solid blue line represents the global emissions derived with the AGAGE 12-box model, while the red diamonds and green circles show global emissions from Levin et al. (2010) and the EDGAR 4.2 inventory, respectively. While reported emissions from Annex-I countries (orange triangles) decrease after 1995, emissions from non-Annex-I countries (grey stars) grow substantially, resulting in an increase in combined non-Annex-I and Annex-I emissions (purple squares) from the beginning of the 20^{th} century.

1.6 Research objectives

The overarching objectives of my thesis are:

(1) **evaluating the use of LPDMs for inverse modeling of GHGs to develop an optimal set-up for atmospheric inversions**

(2) **determining the global distribution of SF_6 emissions for the period 2005-2021**

They are further discussed and refined within the following two subsections.

1.6.1 Evaluating the use of LPDMs for inverse modeling of GHGs

When using LPDMs as a basis for inverse modeling, virtual particles are released from observation sites and traced backward in time to establish a relationship between atmospheric concentrations and emission sources within the simulation period (see Sec. 2.1.3). The fact, that this simulation period is limited due to computational costs, raises two essential research questions, investigated in this thesis:

(i) *How to best define a baseline, that accounts for all emissions occurring prior to the simulation period?*

(ii) *Which period length should be chosen for the backward-simulation?*

To address these questions a global inverse modeling approach is applied to estimate emissions for the example of SF_6 for the year 2012, while investigating:

(a) **the effect of different LPDM backward simulation periods:**
I employ various simulation periods, including 1, 5, 10, 20, and 50 days, for backtracking virtual particles in the LPDM simulation. I then analyze the model-measurement agreement at the individual measurement sites and the inversion results across these different periods.

(b) **the impact of the baseline definition:**
I compare three different baseline methods - the REBS method, the method proposed by Stohl et al. (2009), and the GDB method (see Sec. 1.4.1) and explore their impact on the model-measurement agreement and inversion results, while also investigating their sensitivity to the backward simulation period.

(c) **the consistency with known global total emissions:**
The true SF_6 emission distribution is unknown, and it is therefore challenging to decide which baseline method produces the best inversion results. However, for long-lived gases, such as SF_6, the total global emissions can be relatively accurately determined by considering their atmospheric growth rates. I, therefore, investigate the consistency with global total emissions using different baseline methods and backward simulation periods.

(d) **the influence of biases in the baseline and a priori emissions:**
I introduce artificial biases in the *a priori* emission fields and the baseline to explore their influence on inversion results for the different backward simulation periods.

(e) **the value of different observation types:**
With the GDB method it is possible to include low-frequency measurements (e.g. flask measurements) from fixed sites or measurements from moving platforms in the inversion. Statistical baseline methods require short measurement intervals at fixed sites for the statistical baseline calculation, and thus it is not possible to include low-frequency measurements or measurements from moving platforms. I therefore explore their value to the inversion.

1.6.2 Determining the global emission distribution of sulfur hexafluoride for the period 2005-2021

Based on the methodological results of the first research objective, I perform global inversions for SF_6, to determine its global emission distribution from 2005 to 2021. The inversions are based on 50-days LPDM backward simulations, the GDB baseline method, and a comprehensive observation data set, combining continuous with flask measurements sampled at fixed surface locations, and observations from aircraft and ship campaigns. I investigate regional and national SF_6 emission trends with annual and also monthly resolution, and compare my results with the existing regional studies (see Sec. 1.5). I further discuss the derived global total emission trend and compare it to results from the AGAGE 12-box model and to global emissions directly calculated from annual increases in globally averaged atmospheric SF_6 mole fractions. This approach aims to answer the following research questions, regarding:

(a) **annual emissions in relatively well-monitored regions, such as Europe, the U.S., and China:**
What are the annual SF_6 emission trends in Europe, China, and the U.S.? Do they change over time? How well do the results of such a global inversion approach agree with the existing regional inversion studies? Do emission trends show any effects of emission regulations? How do the inverse modeling results compare to the reported bottom-up emissions and other emission inventories?

(b) **annual emissions from poorly-monitored regions, such as Africa, South America, Australia, and India:**
Can a global inversion approach help to constrain the SF_6 emissions in poorly-monitored regions? If yes, to which extent? Can any trends be derived in those regions? How do the inverse modeling results compare to bottom-up emission inventories?

(c) **annual global emissions:**
How do the global inversion results agree with the relatively well-known global emissions based on observed atmospheric growth rates? Can regionally resolved inversion results reflect the global emission trend?

(d) **monthly SF_6 emissions:**
Do SF_6 emissions follow any seasonal pattern? Do well-monitored countries, such as Europe, China, and the U.S. show similar seasonal patterns?

(e) **GDB baseline method**
Can the multi-year global atmospheric inversion confirm the advantages of using the GDB method for defining a baseline?

Chapter 2

Theory & Methods

In this chapter I present the models used in my research and provide the relevant theoretical background. Starting with an overview about atmospheric transport modeling, I focus on LPDMs and discuss their use for atmospheric inversions. I introduce the LPDM FLEXPART and its chemistry transport model extension FLEXPART CTM. Subsequently, I discuss the general inverse model problem, its relation to Bayes theorem and present common approaches to solve the problem, with a focus on analytic solutions which are used in this thesis. Finally, I introduce the inversion framework FLEXINVERT+, utilized in my research.

2.1 Atmospheric transport modeling

Atmospheric transport modeling (ATM) aims to understand, predict, and simulate the evolution of atmospheric components or tracers in the atmosphere, which can be formulated by the advection-diffusion equation (Eq.2.1, e.g. Jacob 1999).

$$\frac{\partial C}{\partial t} = \nabla(D\nabla C) - \nabla(\mathbf{v}C) + R \tag{2.1}$$

The equation represents the continuity equation for an atmospheric component or tracer C, describing its evolution by a diffusion term $\nabla(D\nabla C)$ with diffusion coefficient D, and an advection term $\nabla(\mathbf{v}C)$ with the mean wind velocity vector $\mathbf{v}$, while also considering sources and sinks represented by R. ATMs can be classified in Eulerian and Lagrangian models. Eulerian models solve Eq. 2.1 on a fixed coordinate system, and fluid properties are defined within each model grid cell as functions of time. Offline models such as CHIMERE (Menut et al. 2021) or DEHM (Christensen 1997) integrate meteorological data from external models, while in online models such as COSMO-GHG (Jähn et al. 2020) or WRF-Chem (Grell et al. 2005) Eq. 2.1 is typically solved together with the primitive equations. Online models benefit from the interplay between meteorology and chemistry, however, they are more complex and computationally more expensive than offline models (Katharopoulos 2022). Lagrangian models use a reference frame that follows individual air parcel. These air parcels represent a portion of the atmosphere, large enough to encompass sufficient molecules to represent macroscopic properties like temperature or pollutant concentration, yet small enough to be considered as a point in space that represents a single value for properties like temperature, density, humidity or pollutant concentration (Lin 2012). The parcel's boundaries are not well defined and an imagined surface surrounding the parcels

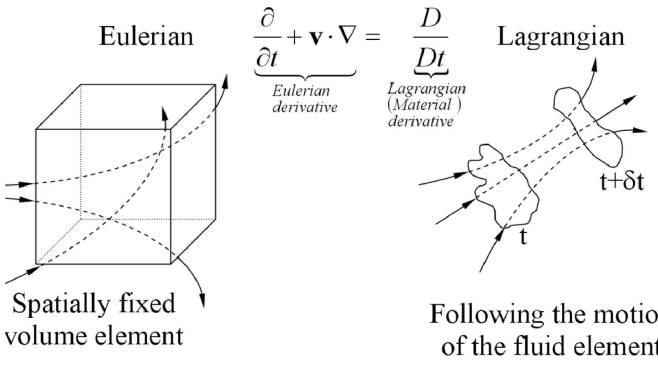

Figure 2.1: Visualization of the difference between Eulerian and Lagrangian models (Shadloo et al. 2016). Eulerian models (a) solve the equations of fluid dynamics on a fixed grid system, while Lagrangian models (b) refer to a reference frame that follows the atmospheric flow of an air parcel. Lagrangian derivatives present the link between the Eulerian and Lagrangian view.

would constantly be deformed due to molecular and turbulent diffusion. The link between the Eulerian and the Lagrangian perspective (Fig. 2.1) can mathematically be expressed by introducing the Lagrangian derivatives $\frac{D}{Dt}$, acting on an air parcel quantity ψ

$$\frac{D\psi}{Dt} \equiv \frac{\partial\psi}{\partial t} + \mathbf{v}\cdot\nabla\psi, \tag{2.2}$$

The left hand side of Eq. 2.2 describes the change of the quantity in a reference frame following the parcel in a velocity field $\mathbf{v}$ (Lagrangian perspective), which can be related to the local change $\frac{\partial\psi}{\partial t}$ (Eulerian perspective) with the advection term $\mathbf{v}\cdot\nabla\psi$.
Using the Lagrangian derivatives, the temporal change in a parcel's position $\mathbf{x}$, can therefore be defined as

$$\frac{D\mathbf{x}}{Dt} = \mathbf{v} \tag{2.3}$$

representing the trajectory. By integrating the velocity $\mathbf{v}$ over time, the parcel's position $\mathbf{x}$ can be determined at various time steps. The first order solution reads

$$\mathbf{x}(t_0 + \Delta t) = \mathbf{x}(t_0) + \mathbf{v}(t_0)\Delta t. \tag{2.4}$$

which allows the approximation of the parcel's trajectory for short integration time steps, given that its velocity is known at each time step. By integrating Eq. 2.3 backward in time

$$\mathbf{x}(t_0 - \Delta t) = \mathbf{x}(t_0) - \mathbf{v}(t_0)\Delta t \tag{2.5}$$

trajectories can be also followed backwards in time, which is an important feature, especially for inverse modeling applications.

Lagrangian models have many advantages but also disadvantages compared to Eulerian models (Lin 2012). By simulating the transport of a large number of particles, the Lagrangian approach comes closer to the true nature of atmospheric flows and processes (e.g. turbulent eddies, mixing, convection). The approach of particle tracking, also automatically ensures the conservation of physical properties, such as mass, which is not always the case for Eulerian models. Lagrangian models can distinguish between near-field and far-field dispersion characteristics, a capability lacking in Eulerian models. Lagrangian models, further, exhibit much less numerical diffusion compared to Eulerian models, enabling models to maintain the distribution of certain properties with sharp atmospheric gradients. As Lagrangian models are not tied to a regular grid, air parcels possess subgrid-scale information, which, for inverse modeling applications, are particularly valuable close to the release point in the backward mode. However, the irregularity of the grid requires additional interpolation procedures (e.g. counting of particles within regular grid cells). Additionally, Lagrangian models operate offline and therefore depend on the quality and resolution of meteorological fields provided by an Eulerian model. Thus, they can not account for any interaction between meteorology and chemistry, in contrast to online Eulerian models. Lastly, specific Lagrangian applications with large particle ensembles and small time steps can be computationally very expensive.

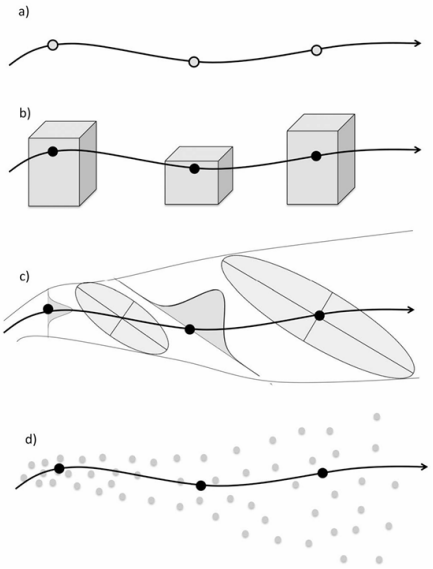

Figure 2.2: Visualization of different Lagrangian models (Lin 2012): (a) Mean trajectory models, (b) Box models, (c) Puff Models, (d) LPDMs

There are different Lagrangian approaches, as illustrated in Fig. 2.2. Mean trajectory Lagrangian models (e.g. Danielsen 1961) neglect diffusion and simulate the movement of air parcels based only on the mean wind. They are better suited to model trajectories under laminar flow conditions, however poorly simulate the transport within the planetary boundary layer (Stohl and Wotawa 1995). Box models (e.g. CiTTyCAT, Pugh et al. 2012) aggregate parcels in one or more boxes, following a mean trajectory, while the box volume describes

the extent of mixing. They are often used to simulate atmospheric chemistry and model the concentration of a species at a specific location, from where a back trajectory is computed, along which the box is then tracked forward, while concentration changes are calculated (Stohl 1998). Puff models (e.g. CALPUFF, Levy et al. 2002) account for turbulent dispersion, leading to an expansion of the air parcels, modeled with a three dimensional Gaussian distribution. They perform best when the mean winds and turbulence remain relatively constant (Lin 2012). LPDMs are the most sophisticated, but also computationally expensive models, representing air parcels by a large number of particles with equal mass. Due to the large number of particles, stochastic effects of turbulence can be accounted for.

2.1.1 Lagrangian particle dispersion models

LPDMs are stochastic Lagrangian models, simulating the trajectories for a large number of infinitesimally small virtual particles. Each of these particles carries an attributed mass, which can be influenced by loss processes, such as chemical loss, radioactive decay, or dry and wet deposition. At each model time step, the transport of individual particles is simulated based on the sum of the mean wind velocity $\overline{\mathbf{v}}$ and the turbulent velocity $\mathbf{v}'$. The determination of $\mathbf{v}'$ represents the core problem of LPDMs and is based on the stochastic particle movement in a turbulent flow, and originates in the Langevin equation. The so-called "general Langevin equation" describes turbulent dispersion as a Markov chain, a stochastic process, where the future state depends solely on the present state:

$$dv_i' = a_i(\mathbf{x}, \mathbf{v}', t)\, dt + b_{ij}(\mathbf{x}, \mathbf{v}', t)\, d\xi_j \tag{2.6}$$

Eq. 2.6 describes the change in the particle's turbulent velocity as the sum of a deterministic term, with acceleration a_i (drift term), and a stochastic term, where $d\xi_j$ represents random Gaussian forcing, (with $\overline{d\xi_i} = 0$ and $\overline{d\xi_i d\xi_j} = dt\delta_{ij}$), scaled by the coefficient b_{ij}. The specification of the coefficients a_i and b_{ij} is referred to as the selection problem. Thomson (1987) established a comprehensive set of criteria, that have to be fulfilled by Lagrangian stochastic models. He showed, that those criteria are met if the so-called well-mixed condition is satisfied. The well-mixed condition ensures the compliance with the second law of thermodynamics and demands that a well-mixed distribution of particles stays in a well-mixed state throughout the entire simulation period. The condition serves as the basis for deriving the parameters in Eq. 2.6 and for ensuring the model's consistency. It induces a unique model in one dimension as well as in three dimensions if variables in each dimension are considered to be independent from those in the other dimensions. Following the work of Thomson (1987), numerous specialized model formulations and applications have been developed. A prominent application is the modeling of emission sensitivities, forming the basis for inversion frameworks. The Hybrid Single-Particle Lagrangian Integrated Trajectory (HYSPLIT) model (Stein et al. 2015), the Numerical Atmospheric dispersion Modelling Environment (NAME) model (Jones et al. 2007), the Stochastic Time-Inverted Lagrangian Transport (STILT) model (Lin 2012) and the FLEXiblePARTicle (FLEXPART) model (Pisso et al. 2019; Stohl 1998) have been widely used in various inversion studies.

2.1.2 FLEXPART

The open-source model FLEXPART is one of the most commonly used LPDMs (Pisso et al. 2019). It simulates the atmospheric transport of tracers and atmospheric components, considering turbulence, radioactive decay, dry and wet deposition, gravitational settling, and linear chemical reactions. The implemented turbulence parameterization for the general Langevin equation regarding the turbulent vertical wind component w has the form (Stohl et al. 2005):

$$dw = -\frac{w}{\tau_L}dt + \frac{\partial \sigma_w^2}{\partial z}dt + \frac{\sigma_w^2}{\rho}\frac{\partial \rho}{\partial z}dt + \left(\frac{2}{\tau_L}\right)^{1/2}\sigma_w dW \tag{2.7}$$

where ρ is the density, σ_w is the standard deviation of w, and τ_L is the Lagrangian time scale for the autocorrelation of the vertical velocity. dW refers to a Wiener process, representing random Gaussian forcing with zero mean and variance dt. σ_w and τ_L are parametrized by the Hanna scheme (Hanna 1984) for different meteorological conditions, based on boundary layer parameters. The second and third term on the right hand side of Eq. 2.7 represent the drift correction (McNider et al. 1988) and density correction (Stohl and Thomson 1999), respectively, ensuring compliance with the well-mixed criterion.

FLEXPART was developed in the mid-1990s to simulate the dispersion of chemical species and radionuclides from nuclear accidents. Since its inception it has undergone various developments and now covers a wide range of atmospheric research applications. It was used to simulate the atmospheric transport of: wildfire (e.g. Paris et al. 2009) and volcanic plumes (Sellitto et al. 2023); dust (e.g. Groot Zwaaftink et al. 2017); heat and water (e.g. Baier et al. 2022); aerosols such as microplastics (e.g. Evangeliou et al. 2020), black carbon (e.g. Zhu et al. 2020), or biogenic aerosols (e.g. Martinsson et al. 2017); radionuclides after nuclear desasters (e.g. Arnold et al. 2015); and for ice core interpretations (e.g. Eckhardt et al. 2023). One major application is the simulation of emission sensitivities (e.g. Annadate et al. 2023), which build the basis for inverse modeling.

2.1.3 Emission sensitivity

If a GHG is emitted into the atmosphere, and transported towards an observation station which measures the gas, the measured value can be related to that emission. If the emission source is nearby and the gas is quickly transported to the station, it will produce a large change in the measured mole fraction. Such a signal is often referred to as a pollution event. Emissions from very distant sources will mix with a large air volume due to diffusion, before they reach the station, and therefore only contribute to the background concentration. In any case, there is a relationship between the emission and the measurement, which is determined by the atmospheric transport between the source and the measurement station. This relationship is called emissions sensitivity or Source-Receptor Relationship (SRR). To simulate this relationship LPDMs can be operated in a backward mode, as this is computationally more efficient if the number of emission grid cells exceeds the number of observation sites. A large number of virtual particles is released from every measurement site, which are tracked backwards for a chosen simulation period, while the particles' residence

time spent in every emission grid cell is recorded. If atmospheric loss processes can be neglected on the timescale of the simulation period, the SRR between the mole fraction measurement y and the emission in a certain spatio-temporal grid cell $x_{i,n}$ can be expressed as:

$$\frac{\partial y}{\partial x_{i,n}} = \frac{1}{J} \sum_{j=1}^{J} \frac{\Delta t_{i,j,n}}{\rho_{j,n}} \tag{2.8}$$

where J is the total number of particles, $\rho_{j,n}$ is the air density, and $\Delta t_{i,j,n}$ is the residence time of the j^{th} particle in the spatio-temporal grid cell (i,n) (Seibert and Frank 2004). Thus, the sensitivity is proportional to the average residence time particles spend in the spatio-temporal grid cell of the emission, during the backward simulation. If loss processes have to be considered, a transmission function, quantifying the loss, has to be included on the right hand side of Eq. 2.8.

2.1.4 FLEXPART CTM

The FLEXPART CTM (chemistry transport model) is an extension of the FLEXPART LPDM and was designed to model global 3-dimensional mole fraction fields of species, for which atmospheric loss can be characterized as a linear process (e.g. OH reactions). The model can be run in a domain-filling mode, where the global domain is filled with a large number of virtual particles, proportionally to air density. These particles can carry an air tracer and different chemical species at the same time, while they are transported throughout the atmosphere. The model is able to account for the emissions of the species, which are added to virtual particles, when they reside near the surface. Therefore, emission fields have to be provided as model input, together with meteorological wind field data. As inaccurate input data and model errors lead to biases in the global modeled fields, FLEXPART CTM provides a nudging routine, which adjusts simulated mole fractions to measurements. Around each observation, a symmetrical kernel is defined in which modeled values are pushed towards the observation, while the weight of each kernel is characterized by its spatial and temporal size. The spatial kernel weight w_s for each pair of measurement (i) and particle (j) is defined by:

$$w_{s,ij} = \begin{cases} 1 - r_{ij}^2 & \text{for } r_{ij}^2 < 1 \\ 0 & \text{otherwise} \end{cases} \tag{2.9}$$

where r_{ij} is defined by the kernel dimensions ($h_{x,i}$, $h_{y,i}$, $h_{z,i}$)

$$r_{ij}^2 = \left(\frac{x_j - X_i}{h_{x,i}}\right)^2 + \left(\frac{y_j - Y_i}{h_{y,i}}\right)^2 + \left(\frac{z_j - Z_i}{h_{z,i}}\right)^2 \tag{2.10}$$

with x_j, y_j, z_j and X_i, Y_i, Z_i representing location of the particle and measurement, respectively. The temporal kernel weight is represented by a tricubic weight function

$$w_{t,ij} = \left(1 - \left|\frac{t_j - t_i}{h_t}\right|^3\right)^3 \tag{2.11}$$

where h_t represents the temporal kernel width and t_i is the measurement time closest to the model time t_j. The nudging tendency Δm_{ji}, representing the adjustment to the modeled particles mass m_j according to the observed mass M_i (calculated from the measured mole fractions), is computed as:

$$\Delta m_{ji} = w_{s,ij} w_{t,ij} \frac{M_i - m_j}{\tau_i} \Delta t \tag{2.12}$$

where Δt represents the model synchronization time step and τ_i is the nudging relaxation timescale. Groot Zwaaftink et al. (2018) used the FLEXPART CTM for modeling global CH_4 mole fraction fields, while I apply it to SF_6.

2.2 Inverse Modeling

2.2.1 The general inverse problem

Physical theories enable us to make predictions. If the physical system is completely described one can predict the results of a certain measurement, using a model, usually called the forward model. The forward problem aims to determine the consequence to a specific cause, and has a unique solution. Inverse modeling is a method that uses the observations of a physical system, to better quantify the variables that characterize that system (Brasseur and Jacob 2017). The inverse problem aims to trace the consequence back to the cause, and does not necessarily have a unique solution (Tarantola 2005). As for the example of atmospheric inversions, if the emission distribution of a certain gas would be known, a perfect transport model could predict the concentration at a certain location. However there are different emission distributions possible that would result in the exact same concentration at that location. Thus, this inverse problem has multiple solutions. It therefore becomes necessary to include any available *a priori* information regarding the model parameters in addition to the observational information. Inverse approaches have found application across different fields, such as medicine (e.g. Ezhov et al. 2023), geoscience (e.g. de Campos Velho et al. 2013), biology (e.g. Guzzi et al. 2018), or economy (e.g. Horowitz 2014), among others. The main applications in atmospheric science are remote sensing of atmospheric composition to retrieve vertical concentration profiles, chemical data assimilation to achieve gridded 3-D concentration fields, and the application of top down constraints on surface fluxes (Brasseur and Jacob 2017).

2.2.2 Bayes theorem

The inverse modeling theory has its origin in Bayesian statistics, which treats parameters as random variables, described by probability distributions. In Bayesian statistics probability is interpreted as degree of belief or uncertainty about an event, instead of long-run relative

frequency of an event occurring over repeated trials (Fornacon-Wood et al. 2022). The essence of Baysian theory is the Bayes' theorem, which provides a mathematical formula to update probabilities based on new evidence and past knowledge. For a vector $\mathbf{x}$, whose elements represent the variables driving a system, and a vector $\mathbf{y}$ whose elements represent measurements of that system, Bayes' theorem can be formulated as:

$$P(\mathbf{x}|\mathbf{y}) = \frac{P(\mathbf{y}|\mathbf{x}) \cdot P(\mathbf{x})}{P(\mathbf{y})}, \tag{2.13}$$

- $P(\mathbf{x})$ represents the *a priori* probability distribution function (PDF) of $\mathbf{x}$, which represents the best knowledge of the driving variables before including new information from the observations.
- $P(\mathbf{y})$ is the marginal PDF of $\mathbf{y}$, representing the total probability of observing $\mathbf{y}$ over all possible values of $\mathbf{x}$.
- $P(\mathbf{y}|\mathbf{x})$ represents the likelihood of observing vector $\mathbf{y}$ given the driving variables $\mathbf{x}$
- $P(\mathbf{x}|\mathbf{y})$ represents the *a posteriori* PDF of $\mathbf{x}$ updated through the measurements $\mathbf{y}$.

Inverse modeling aims to find the best estimate for $\mathbf{x}$, by considering the observational information of $\mathbf{y}$, and the *a priori* information of the driving variables. This best estimate is defined by the maximum of the *a posteriori* PDF:

$$\nabla_x[P(\mathbf{x}|\mathbf{y})] = 0 \tag{2.14}$$

2.2.3 The analytical inversion

The application of Bayes' theorem for inverse modeling, requires the formulation of PDFs to describe the treated variables. As the error distribution of these variables is usually unknown, one has to make an assumption. Commonly, the PDFs of all treated variables are assumed to be Gaussian. For an n-dimensional vector $\mathbf{x}$ the Gaussian PDF can be fully described by the expectation value $E[\mathbf{x}]$ and the error covariance matrix $\mathbf{S}$:

$$P(\mathbf{x}) = \frac{1}{(2\pi)^{\frac{n}{2}}|\mathbf{S}|^{\frac{1}{2}}} \exp\left(-\frac{1}{2}(\mathbf{x} - E[\mathbf{x}])^T\mathbf{S}^{-1}(\mathbf{x} - E[\mathbf{x}])\right) \tag{2.15}$$

where $|\mathbf{S}|$ refers to the determinant of $\mathbf{S}$. If $\mathbf{e}$ is the error of $\mathbf{x}$, $\mathbf{S}$ can be defined by $E\left[(\mathbf{e} - E[\mathbf{e}])(\mathbf{e} - E[\mathbf{e}])^T\right]$, which simplifies to $E\left[\mathbf{e}\mathbf{e}^T\right]$ for unbiased errors. The diagonal elements $\mathbf{S}_{\mathrm{i,i}}$ refer to the variance of the i^{th} error component and the off-diagonal elements $\mathbf{S}_{i,j}$ correspond to the covariance between the i^{th} and the j^{th} error element.Gaussian distributions have the big advantage, that the combination (i.e. product) of two Gaussian PDFs results in another Gaussian distribution, allowing for an easy formalism and an analytical solution to Eq. 2.14. Let now

- $\mathbf{x} \in \mathbb{R}^N$ be the vector of variables that drive the physical system. $\mathbf{x}$ is called the state vector and is an element of the state space $\mathbb{R}^N$. In case of atmospheric inversions it refers to all the GHG emissions on a spatio-temporal grid that should be optimized by the inversion. However also other parameters to be optimized can be added to $\mathbf{x}$ (e.g. baseline mole fractions).

- $\mathbf{x}_a \in \mathbb{R}^N$ be the vector of *a priori* estimated values for the driving variables. It represents the additional information included to the inverse problem. $\mathbf{x}_a$ is called the *a priori* state vector and has the same number of elements as $\mathbf{x}$. In case of atmospheric inversion, it refers to a first estimate for emissions, often taken from bottom-up inventories.

- $\mathbf{B} \in \mathbb{R}^{N \times N}$ be the *a priori* error covariance matrix, representing the uncertainties of the *a priori* state. If $\mathbf{e}_\mathrm{a}$ is the error of $\mathbf{x}_a$, it can be expressed by $\mathbf{e}_\mathrm{a} = \mathbf{x} - \mathbf{x}_a$ and is assumed to be unbiased. $\mathbf{B}$ is therefore defined as $E\left[\mathbf{e}_a {\mathbf{e}_a}^T\right]$. The uncertainties of the *a priori* state are usually unknown and have to be estimated together with their correlation.

- $\mathbf{y} \in \mathbb{R}^M$ be the vector of measurements that are used to optimize the state variables. $\mathbf{y}$ is called the observation vector and is an element of the observation space $\mathbb{R}^M$. In case of atmospheric inversions, it refers to the measured mole fraction values.

- $\mathbf{R} \in \mathbb{R}^{M \times M}$ be the error covariance matrix, representing the observation error $\mathbf{e}_o$. The observation error is assumed to be unbiased and can be expressed by $\mathbf{e}_o = \mathbf{y} - \mathbf{H}\mathbf{x}$. It includes the measurement error $\mathbf{e}_m$, the forward model error $\mathbf{e}_f$ and the representation error $\mathbf{e}_r$, which reflects the mismatch between the measurement location and the model resolution. These errors are assumed to be unbiased and uncorrelated and their covariance matrices are therefore additive: $\mathbf{R} = E\left[\mathbf{e}_\mathrm{m}{\mathbf{e}_\mathrm{m}}^T\right] + E\left[\mathbf{e}_\mathrm{f}{\mathbf{e}_\mathrm{f}}^T\right] + E\left[\mathbf{e}_\mathrm{r}{\mathbf{e}_\mathrm{r}}^T\right]$. Given that the forward model error and the representation error are typically unknown, $\mathbf{R}$ has to be estimated.

- $\mathbf{H} \in \mathbb{R}^{M \times N}$ be the forward operator. It maps the variables of the state space to the elements of the observation space: $\mathbf{H} : \mathbb{R}^N \rightarrow \mathbb{R}^M$, and can be represented by a Jacobian matrix, if linear. In case of atmospheric inversions, $\mathbf{H}$ is also called the atmospheric transport operator linking the emissions to the measured mole fractions. Each element is a partial derivative of the change in mole fractions at the measurement location with respect to the emission change in a certain grid cell and can be built from the SRRs (see Sec. 2.1.3).

The Gaussian *a priori* PDF $P(\mathbf{x})$ and the likelihood $P(\mathbf{y}|\mathbf{x})$ can be written as:

$$P(\mathbf{x}) = Const. \exp\left(-\frac{1}{2}(\mathbf{x} - \mathbf{x}_a)^T \mathbf{B}^{-1}(\mathbf{x} - \mathbf{x}_a)\right), \tag{2.16}$$

$$P(\mathbf{y}|\mathbf{x}) = Const. \exp\left(-\frac{1}{2}(\mathbf{y} - \mathbf{H}\mathbf{x})^T \mathbf{R}^{-1}(\mathbf{y} - \mathbf{H}\mathbf{x})\right), \tag{2.17}$$

Applying Bayes' theorem gives an expression for the *a posteriori* PDF $P(\mathbf{x}|\mathbf{y})$:

$$P(\mathbf{x}|\mathbf{y}) = Const. \exp\left(-\frac{1}{2}(\mathbf{x}-\mathbf{x}_a)^T\mathbf{B}^{-1}(\mathbf{x}-\mathbf{x}_a) - \frac{1}{2}(\mathbf{y}-\mathbf{H}\mathbf{x})^T\mathbf{R}^{-1}(\mathbf{y}-\mathbf{H}\mathbf{x})\right) \quad (2.18)$$

The most probable solution for $\mathbf{x}$ is represented by the maximum of $P(\mathbf{x}|\mathbf{y})$, thus the minimum of the negative exponent in Eq. 2.18. Therefore a cost function $J(\mathbf{x})$ can be defined, whose minimum represents the solution of the inverse problem:

$$J(\mathbf{x}) = (\mathbf{x}-\mathbf{x}_a)^T\mathbf{B}^{-1}(\mathbf{x}-\mathbf{x}_a) + (\mathbf{y}-\mathbf{H}\mathbf{x})^T\mathbf{R}^{-1}(\mathbf{y}-\mathbf{H}\mathbf{x}) \quad (2.19)$$

The minimum $\hat{x}$ can analytically be found by solving

$$\nabla_x J(\hat{\mathbf{x}}) = 0 \quad (2.20)$$

The solution of the inverse problem reads

$$\hat{\mathbf{x}} = \mathbf{x}_a + \mathbf{B}\mathbf{H}^T(\mathbf{H}\mathbf{B}\mathbf{H}^T + \mathbf{R})^{-1}(\mathbf{y}-\mathbf{H}\mathbf{x}_a) \quad (2.21)$$

and can be expressed in a compact form as

$$\hat{\mathbf{x}} = \mathbf{x}_a + \mathbf{G}(\mathbf{y}-\mathbf{H}\mathbf{x}_a) \quad (2.22)$$

by defining the Gain matrix

$$\mathbf{G} = \mathbf{B}\mathbf{H}^T(\mathbf{H}\mathbf{B}\mathbf{H}^T + \mathbf{R})^{-1} \quad (2.23)$$

The Gain matrix characterizes the sensitivity of the *a posteriori* state to the observations $\mathbf{G} = \frac{\partial\hat{\mathbf{x}}}{\partial y}$. It can be understood as the gain that each measurement contributes to the estimation of the state, showing the weight that is attributed to each observation. For some applications, where the state space is larger than the observation space and inverting $\mathbf{R}$ is computationally cheap, it can be convenient to rewrite Eq.2.21 in the form (Tarantola 2005):

$$\hat{\mathbf{x}} = \mathbf{x}_a + (\mathbf{H}^T\mathbf{R}^{-1}\mathbf{H} + \mathbf{B}^{-1})^{-1}\mathbf{H}^T\mathbf{R}^{-1}(\mathbf{y}-\mathbf{H}\mathbf{x}_a) \quad (2.24)$$

A big advantage of the analytical solution is that the uncertainties of the *a posteriori* estimate, described by the *a posteriori* error covariance $\hat{\mathbf{B}}$, can be calculated:

$$\hat{\mathbf{B}} = (\mathbf{H}^T\mathbf{R}^{-1}\mathbf{H} + \mathbf{B}^{-1})^{-1} = \mathbf{B} - \mathbf{G}\mathbf{H}\mathbf{B} \quad (2.25)$$

2.2.4 Variational methods

The analytical solution to the minimization of the cost function (Eq. 2.20) exists only for linear forward operators and under the assumption of Gaussian distributed errors. Further, there are practical computational limits to the analytical solution, if the size of the problem becomes too large. These restrictions can be overcome by minimizing the cost function numerically, instead of using the analytical solution. Such methods are often referred to as variational methods. In principle, variational methods can be seen as totally independent from the Bayesian approach, with the general aim of finding the optimal state by minimize a cost function that quantifies the difference between the state vector and both, its *a priori* values, and the observations. However the most commonly used cost function is the least squares approach, which takes exactly the form of the Bayesian approach in Eq. 2.19, with the difference, that discussed limitations (linearity of the forward operator and Gaussian distributed errors) can be lifted.

Variational methods obtain the gradient of J, which is employed to find the minimum of the cost function. Often a steepest-descent algorithm is used, where a sequence of the state vector x_k is built, that is updated at each iteration by taking a small step (with step size α) in the direction opposite to the gradient, subsequently approaching the minimum.

$$\mathbf{x}_{k+1} = \mathbf{x}_k - \alpha \nabla J(\mathbf{x}_\mathrm{k},) \tag{2.26}$$

In conjugate gradient method the state vector update is made in a direction that is orthogonal to the directions of the previous updates. For a linear forward operator, the $\nabla J(x_k)$ takes the form:

$$\nabla J(\mathbf{x}_k) = 2\mathbf{B}^{-1}(\mathbf{x}_k - \mathbf{x}_a) + 2\mathbf{H}^T\mathbf{R}^{-1}(\mathbf{H}\mathbf{x}_k - \mathbf{y}) \tag{2.27}$$

A drawback of variational methods is that the posterior error covariance matrix is not provided as part of the solution. While some algorithms allow the approximation of the Hessian matrix $\nabla^2 J(\mathbf{x})$ representing the reciprocal of the posterior error covariance matrix, others need the use of Monte Carlos methods to estimate the *a posteriori* uncertainties.

2.2.5 Markov Chain Monte Carlo methods

Markov Chain Monte Carlo (MCMC) methods offer another approach to solve the inverse problem. MCMCs are also based on Bayes' theorem and obtain the *a posteriori* PDF $P(\mathbf{x}|\mathbf{y})$ by modeling P($\mathbf{x}$) and $P(\mathbf{y}|\mathbf{x})$ directly, using a large ensemble of state vector values. They use a Markov chain, to iteratively propose new state vector values $\mathbf{x}'$, based on the current state $\mathbf{x}$ which is randomly perturbed according to a transition PDF, which is often assumed to be Gaussian. These iteratively proposed new values are then either accepted or rejected based on a defined acceptance criterion, comparing $P(\mathbf{y}|\mathbf{x})$ with $P(\mathbf{y}|\mathbf{x}')$. MCMCs have the advantage, that they can employ any observational and prior PDFs, and allow for non-Gaussian errors distributions, non-linear forward operators and any additional constrains on the *a priori* emissions. They, further, enable the inclusion of hyperparameters in the joint probability distribution, which allows the estimation of state and observation uncertainties (e.g. An et al. 2024; Ganesan et al. 2014; Lunt et al. 2016). However, MCMC algorithms

can be computationally expensive, convergence must be ensured, and the initial choice of parameter values is a source of uncertainty.

2.2.6 FLEXINVERT+

Flexinvert+ (Thompson and Stohl 2014) is a Bayesian inversion framework for the optimization of emissions of tracer species, such as GHGs or aerosols. It is applicable to any species, provided that the atmospheric loss can be characterized as a linear process. The model can be employed to global, regional, and local problems. FLEXINVERT+ can solve Eq. 2.20 analytically to find the state vector minimizing the cost function Eq. 2.19, using either Eq. 2.21 or Eq. 2.24, depending on the dimensions of the state and observation vector. As the analytical solution allows for the computation of the *a posteriori* error covariance matrix (Sec. 2.2.3), FLEXINVERT+ can therefore also provide *a posteriori* emission uncertainties. Alternatively, the framework offers two variational methods to iteratively minimize the cost function. One option is to use the conjugate gradient method, where the cost function's Hessian matrix ($\mathbf{H}^T\mathbf{R}^1\mathbf{H} + \mathbf{B}^{-1}$) is approximated using the Lanczos algorithm and used alongside the cost function gradient to find the minimum. A second option is to use the M1QN3 algorithm, which uses a Quasi-Newton method for the minimization, and is designed for large numerical problems. FLEXINVERT+ optimizes emissions on a grid with varying cell size, which is based on the emission sensitivities regarding the employed observation network. The framework accounts for spatial and temporal emission error correlations using a simple exponential decay model, however does not consider correlations of observational errors. Baseline values can be computed by coupling the LPDM back trajectories to a global model, and the baseline can optionally be optimized in the inversion. FLEXINVERT+ can be run directly with the emission sensitivity output from FLEXPART, but in principle any other LPDM could be used. In my thesis I employ the FLEXINVERT+ framework based on FLEXPART emission sensitivites, and use the analytical solution (see Sec. 2.2.3) to minimize the cost function.

Chapter 3

A comprehensive evaluation of the use of Lagrangian particle dispersion models for inverse modeling of greenhouse gas emissions

Overview

This publication applies a global inverse modeling approach for the example of SF_6 and the year 2012, to investigate the use of LPDMs for atmospheric inversions. The main emphasis of this study lies on assessing the influence of different baseline methods and different LPDM backward simulations periods on the inversion results. I therefore employ two statistical and one GDB approach to determine a baseline for the global inversion, while also considering different LPDM backward simulation periods between 1 and 50 days. I investigate the model-measurement agreement at individual measurement sites and compare the aggregated *a posteriori* emissions with relatively well known global total emissions. I further explore the influence of biases in the baseline and *a priori* emissions for different LPDM simulation periods and examine the use of low-frequency flask measurements for the inversion.

Own contributions

Conceptualization, investigation, methodology, modeling, formal analysis, visualization, writing. My contribution to this publication is estimated to be about 90%.

Publication details

Vojta, M., Plach, A., Thompson, R. L., and Stohl, A.: A comprehensive evaluation of the use of Lagrangian particle dispersion models for inverse modeling of greenhouse gas emissions, Geosci. Model Dev., 15, 8295–8323, https://doi.org/10.5194/gmd-15-8295-2022, 2022

Geosci. Model Dev., 15, 8295–8323, 2022
https://doi.org/10.5194/gmd-15-8295-2022

Geoscientific Model Development
Open Access
EGU

A comprehensive evaluation of the use of Lagrangian particle dispersion models for inverse modeling of greenhouse gas emissions

Martin Vojta[1], **Andreas Plach**[1,2], **Rona L. Thompson**[3], **and Andreas Stohl**[1]

[1]Department of Meteorology and Geophysics, University of Vienna, Vienna, Austria
[2]Physics Institute, Climate and Environmental Physics, University of Bern, Bern, Switzerland
[3]Norwegian Institute for Air Research NILU, Kjeller, Norway

Correspondence: Martin Vojta (martin.vojta@univie.ac.at)

Received: 28 April 2022 – Discussion started: 16 June 2022
Revised: 28 September 2022 – Accepted: 21 October 2022 – Published: 18 November 2022

Abstract. Using the example of sulfur hexafluoride (SF_6), we investigate the use of Lagrangian particle dispersion models (LPDMs) for inverse modeling of greenhouse gas (GHG) emissions and explore the limitations of this approach. We put the main focus on the impacts of baseline methods and the LPDM backward simulation period on the a posteriori emissions determined by the inversion. We consider baseline methods that are based on a statistical selection of observations at individual measurement sites and a global-distribution-based (GDB) approach, where global mixing ratio fields are coupled to the LPDM back-trajectories at their termination points. We show that purely statistical baseline methods can cause large systematic errors, which lead to inversion results that are sensitive to the LPDM backward simulation period and can generate unrealistic global total a posteriori emissions. The GDB method produces a posteriori emissions that are far less sensitive to the backward simulation period and that show a better agreement with recognized global total emissions. Our results show that longer backward simulation periods, beyond the often used 5 to 10 d, reduce the mean squared error and increase the correlation between a priori modeled and observed mixing ratios. Also, the inversion becomes less sensitive to biases in the a priori emissions and the global mixing ratio fields for longer backward simulation periods. Further, longer periods might help to better constrain emissions in regions poorly covered by the global SF_6 monitoring network. We find that the inclusion of existing flask measurements in the inversion helps to further close these gaps and suggest that a few additional and well-placed flask sampling sites would have great value for improving global a posteriori emission fields.

1 Introduction

Over the last few decades, the sharp increase of anthropogenic greenhouse gas (GHG) emissions has become a global concern, as it affects the Earth's climate with possible dangerous consequences for human health, infrastructure, and ecosystems (IPCC, 2018). In order to prevent dangerous human interference with the climate system, the United Nations Framework Convention on Climate Change (UNFCCC) was established. As an important commitment to the convention, Annex-I countries (industrialized nations that are legally bound to reduce GHG emissions) are required to report their national emissions for regulated GHGs. These inventories are compiled by applying bottom-up methods, where statistical economic production or consumption data and source-specific emission factors are used to estimate national emissions. However, bottom-up estimates are suspected to suffer from significant uncertainties, and there is a growing need for independent verification of these estimates (e.g., Rypdal et al., 2005; Weiss et al., 2021). Independent verification can be provided by top-down methods, such as inverse modeling (e.g., Leip et al., 2017; Weiss and Prinn, 2011).

Inverse modeling requires the use of atmospheric transport models, either Eulerian models or Lagrangian particle dispersion models (LPDMs). LPDMs are usually run backward in time. They release a large number of virtual particles from a given observation location and time and trace them backward for a limited simulation period. The model output gives the sensitivity of the atmospheric mixing ratio to emissions during the backtracking time. In the inversion al-

Published by Copernicus Publications on behalf of the European Geosciences Union.

gorithm, the sensitivities for a large number of observations are used to optimize a priori emission estimates such that (with the obtained a posteriori emissions) the simulated mixing ratios better fit the atmospheric observations. Most studies only use continuous in situ observations for this purpose; however flask measurements with low sampling frequency can be included as well (e.g., Villani et al., 2010). For certain species, satellite measurements could also be used.

Previous studies argue that inversion methods have insufficient accuracy (e.g., Rypdal et al., 2005) and problems with reproducibility (Berchet et al., 2021). In order to enhance the credibility of inverse modeling, a better knowledge of the associated uncertainties is required (Brunner et al., 2017). An important source of uncertainty regarding LPDM-based inversion methods is the fact that they are often run backward in time only for a few days, e.g., 5 d (Keller et al., 2012; Vollmer et al., 2009; Zhao et al., 2009), 7 d (Koyama et al., 2011), 10 d (Schoenenberger et al., 2018; Simmonds et al., 2018; Thompson et al., 2017), or 20 d (Fang et al., 2014; Maione et al., 2014; Stohl et al., 2009). Koyama et al. (2011) and Stohl et al. (2009) are global inversion studies, while the other listed studies apply regional inversions. The choices of the backward simulation period used made by different authors seem arbitrary, and a systematic analysis of the impact of the backward simulation period is lacking.

The inversions can only account for the emissions that have occurred during the backward simulation period. By contrast, the emission contributions prior to the limited LPDM backward simulation period are not explicitly modeled but must still be accounted for in order to compare the model results with the observations. These contributions must be collected in a so-called baseline that is added to the modeled contributions. As errors in the baseline translate to errors in the a posteriori emissions, the baseline needs to be as accurate as possible. Many different methods have been suggested to determine this baseline.

Investigating halocarbons or fluorinated gases (F-gases) most studies use statistical methods to calculate the baseline by selecting low mixing ratio observations at individual stations (e.g., Ganesan et al., 2014; Prinn et al., 2000; Saito et al., 2010; Zeng et al., 2012). Such statistical methods have been operationally applied within observation networks, such as the Georgia Institute of Technology method (O'Doherty et al., 2001) used within the AGAGE community. The general idea is to statistically identify observations which are assumed to be unaffected by emissions within the LPDM simulation period. A widely used statistical method is the robust estimation of baseline signal (REBS) method, introduced by Ruckstuhl et al. (2012), which applies a robust local linear regression model. Statistical methods, however, always involve subjective data selection and treatment decisions, which can lead to problems. For instance, they will by definition wrongly classify measurements during longer lasting pollution episodes as baseline observations and therefore overestimate the baseline – a problem that is likely to occur frequently in polluted areas. It is also unclear to which degree these methods distinguish between lightly polluted air and measurement noise (Ryall et al., 2001). Furthermore, they fail to identify correct baseline mixing ratios when they are below the lowest observations (Rigby et al., 2011), especially at polluted continental sites which virtually never receive air masses unaffected by emissions within the backward simulation period. In addition to the statistical selection some methods also use model information to improve the baseline. A method applied by the UK Met Office and commonly used within the AGAGE network (see, e.g., Manning et al., 2021) identifies baseline measurements by analyzing the direction and height of air entering the regional inversion domain. A baseline method introduced by Stohl et al. (2009), further termed "Stohl's method", uses model information to subtract prior simulated mixing ratios from preselected observations, in order to avoid an overestimation of the baseline. Nevertheless, this preselection is subjective, and prior simulated mixing ratios depend on a priori emission estimates.

Apart from using observations at each individual station to maintain a baseline, Rödenbeck et al. (2009) suggested a general "nesting" scheme, where a regional transport model – either a Eulerian or Lagrangian model – is embedded into a global model providing information from outside the spatiotemporal inversion domain. Such a global-distribution-based (GDB) approach was used by many authors: Trusilova et al. (2010) and Monteil and Scholze (2021) used Rödenbeck's approach to estimate CO_2 emissions. Similarly, Rigby et al. (2011) and Ganshin et al. (2012) developed approaches to nest a Lagrangian model into a Eulerian model and tested it for SF_6 and CO_2, respectively. Estimating CO_2 baseline mole fractions for inverse modeling, Hu et al. (2019) applied two GDB approaches and a statistical method, where a subset of observations with minimal sensitivity was selected to correct a GDB baseline. Lunt et al. (2016) and Thompson and Stohl (2014) applied GDB approaches to model CH_4. While Thompson and Stohl (2014) coupled the LPDM back-trajectories with the global model at the end of the trajectories (which are terminated after a defined time), Lunt et al. (2016) used the exit location of the particles, leaving the inversion domain for the coupling. The GDB method defines the baseline exactly in the way it is needed for the inversion and can account for meteorological variability (i.e., transport of air from regions with lower or higher mixing ratios, respectively), which may cause sudden changes in the baseline. The accuracy of the GDB method, however, depends on how well the global field of mixing ratios can be modeled.

The treatment of the baseline is critical when using LPDMs as a basis for atmospheric inversions. Still, it is unclear what influence the choice of a certain baseline approach has on inversion results. Previous studies indicated that different approaches lead to significant mismatches in simulated emissions (Thompson and Stohl, 2014; Henne et al., 2016). However, different methods were never compared systemati-

Table 1. Sites of continuous surface measurements used in the inversion and in the reanalysis.

Site ID	Station	Organization	Calibration scale	Latitude	Longitude	Altitude[a]	Frequency
CGO	Cape Grim, Tasmania	AGAGE	SIO-2005	40.7° S	144.7° E	94	2 h
JFJ*	Jungfraujoch, Switzerland	AGAGE	SIO-2005	46.5° N	8.0° E	3580	2 h
MHD	Mace Head, Ireland	AGAGE	SIO-2005	53.3° N	9.9° W	5	2 h
RPB	Ragged Point, Barbados	AGAGE	SIO-2005	13.2° N	59.4° W	45	2 h
SMO	Cape Matatula, American Samoa	AGAGE	SIO-2005	14.2° S	170.6° W	77	2 h
THD	Trinidad Head, USA	AGAGE	SIO-2005	41.0° N	124.1° W	107	2 h
ZEP	Zeppelin, Ny-Ålesund, Norway	AGAGE	SIO-2005	78.9° N	11.9° E	474	2 h
GSN	Gosan, South Korea	KNU/AGAGE	SIO-2005	33.3° N	126.2° E	89	2 h
RGL	Ridge Hill, UK	UNIVBRIS	SIO-2005	52.0° N	2.5° W	204	30 min
ZSF*	Zugspitze-Schneefernerhaus, Germany	UBAG	WMO SF6 X2006	47.4° N	11.0° E	2671	1 h
BRW	Barrow (now Utqiaġvik), Alaska, USA	NOAA	WMO SF6 X2014	71.3° N	156.6° E	11	1 h
MLO*	Mauna Loa, USA	NOAA	WMO SF6 X2014	19.5° N	155.6° W	3397	1 h
NWR*	Niwot Ridge, USA	NOAA	WMO SF6 X2014	40.0° N	105.6° W	3523	1 h
SPO	South Pole, Antarctic	NOAA	WMO SF6 X2014	90.0° S	24.8° W	2841	1 h
SUM	Summit, Greenland	NOAA	WMO SF6 X2014	72.6° N	38.5° W	3238	1 h
IZO*	Izaña, Tenerife, Spain	AEMET	WMO SF6 X2014	28.3° N	16.5° W	2373	1 h
COI	Cape Ochiishi, Japan	NIES	NIES-2008	43.2° N	145.5° E	49	1 h
HAT	Hateruma, Japan	NIES	NIES-2008	24.1° N	123.8° E	47	1 h

[a] The altitude specifies the sampling height in meters above sea level. Stations considered as mountain sites are marked with an asterisk.

cally and tested for different model setups such as the length of the LPDM backward simulations.

Another problem of LPDM-based inversion studies is the general lack of consistency between regional emission estimates and the global emissions of a GHG. Given that the LPDMs are only usually run backward in time for a few days, the inversions only constrain the emissions in regions where observation stations exist (Rigby et al., 2011). This can lead to substantial deviations of the derived emissions from, often well-known, global totals, a problem shared with regional inversion studies based on Eulerian models.

In this study we (i) investigate the effect of the backward simulation time period within the range of 0–50 d, (ii) analyze the impact of the baseline definition on inversion results, (iii) examine their consistency with known global total emissions, (iv) explore the influence of biases in the baseline and a priori emissions on inversion results for different backward simulation periods, and (v) compare the value of different observation types (flask vs. continuous) for the inversion. We compare three different baseline methods – the REBS method, Stohl's method, and the GDB method – and apply inverse modeling to the species sulfur hexafluoride (SF_6). SF_6 is the most potent GHG regulated under the Kyoto Protocol, with a high global warming potential of approximately 23 500 over a 100-year time horizon (Myhre et al., 2013) and an estimated atmospheric lifetime of 3200 years (Ravishankara et al., 1993). SF_6 is a convenient choice for our studies because it has no negative sources (as, e.g., CO_2), a very long lifetime in the atmosphere, and well-known global emissions, and there are relatively many measurements available. However, we expect our findings to also hold for other species and be informative for inverse modeling of GHGs with LPDMs in general.

2 Methods

2.1 Measurement data

The inversion (Sect. 2.2) is performed using continuous atmospheric observations of SF_6 dry-air mole fractions from 18 observation sites, distributed around the globe. Those measurements were provided by the Advanced Global Atmospheric Gases Experiment (AGAGE; Prinn et al., 2018) network, the NOAA/ESRL halocarbons in situ program (Dutton et al., 2017), and a number of independent organizations, whose data were partly included in the World Data Centre for Greenhouse Gases (WDCGG, 2018). Measurement sites are listed in Table 1, together with acronyms and other station-specific information.

At AGAGE stations, SF_6 mixing ratios are measured using Medusa gas chromatography followed by mass spectrometry (GC/MS; Miller et al., 2008). At the stations HAT and COI, the SF_6 measurement system is based on cryogenic preconcentration and capillary GC/MS (Yokouchi et al., 2006). At all other stations, gas chromatography followed by electron capture detection (GC-ECD) is used to measure SF_6 mole fractions. Observations were calibrated with four different SF_6 scales: SIO-2005, WMO SF6 X2006, WMO SF6 X2014, and NIES-2008. We converted all observations to the SIO-2005 calibration scale by dividing NIES-2008 calibrated data by the factor 1.013 (Takuya Saito, private communication, 5 February 2021) and WMO SF6 X2014 calibrated data by 1.002 (Guillevic et al., 2018). To convert mole

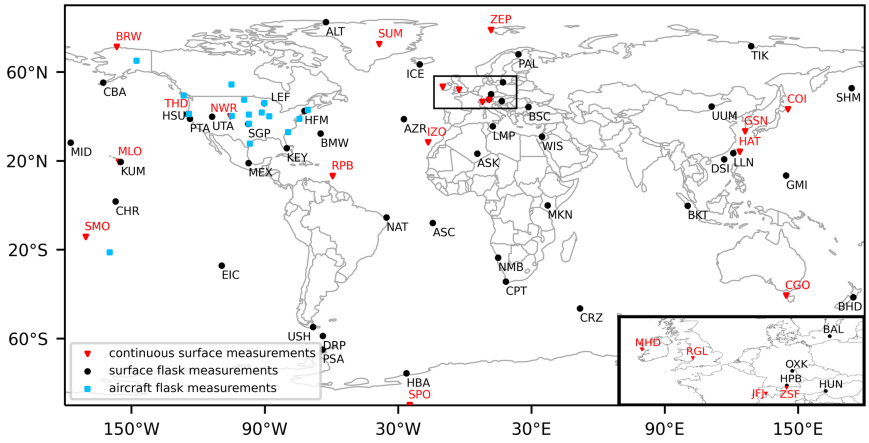

Figure 1. Map of sites with continuous surface measurements used for the inversion (red triangles) and flask measurements (surface: black dots, aircraft: blue squares) that were additionally used for the reanalysis of SF_6.

fractions from WMO SF6 X2006 to WMO SF6 X2014, we used $y = ax^2 + bx + c$, where y corresponds to SF_6 mole fractions on the X2014 scale and x to mole fractions on the X2006 scale. The coefficients a, b, and c have the values of 2.6821×10^{-3}, 9.7748×10^{-1}, and 3.5831×10^{-2} (NOAA ESRL, 2014), respectively.

We averaged all observation data over 3-hourly intervals. For stations at low altitudes, we selected afternoon values (12:00 to 16:00 LT), to only consider time periods with a well-mixed planetary boundary layer, when the smallest model errors can be expected. At mountain stations, we instead selected observations during nighttime (00:00 to 04:00 LT) to avoid larger errors due to daytime small-scale upslope winds in the complex topography around these sites, which are unresolved in the model. Additionally, we followed a method by Stohl et al. (2009) to identify observations that cannot be brought into agreement with modeled mixing ratios by the inversion, which we removed completely (in contrast to Stohl et al., 2009, who assigned larger uncertainties to these observations). For this, we used the kurtosis of the a posteriori error frequency distribution and iteratively excluded observations causing the largest absolute errors until the kurtosis of the remaining error values fell below 5 (close to a Gaussian distribution). This method removed 0.62 % (63 data points) of the whole dataset, affecting 0 % to 2.92 % of the observations at individual measurement sites. In total, 10 142 observations were used in the inversion for the year 2012.

In order to generate global SF_6 mixing ratio fields required by the GDB method, we performed a 2-year SF_6 reanalysis (for more details see Sect. 2.5), for which we used all the available 2011 and 2012 continuous measurements from the sites listed in Table 1. In addition, we included flask air samples from 44 surface observation stations (NOAA, Dlugokencky et al., 2020) and from 16 aircraft profiling stations (Sweeney et al., 2015; NOAA Carbon Cycle Group ObsPack Team, 2018). Surface flask measurements were available at intervals ranging from a few days up to months. Sampling flights were conducted irregularly with intervals between 2 and 5 weeks at individual sites. Aircraft measurements from individual flights provide vertical SF_6 mixing ratio profiles up to 8.5 km above sea level, where air samples are usually taken within less than an hour. With one exception, all aircraft samples were collected over North America. Additional information about the flask measurements from surface sites and aircraft programs can be found in Tables A1 and A2 (Appendix). All flask measurements were calibrated with the WMO SF6 X2014 calibration scale, and we converted them to the SIO-2005 calibration scale. For the reanalysis, we used 175 557 in situ, 3423 surface flask, and 5581 aircraft measurements amounting to 184 561 measurements in total in 2011 and 2012. Figure 1 provides an overview of all observation sites considered in the inversion and the reanalysis.

In one specific test case (see Sect. 3.2), we also used the 2012 surface flask measurements in addition to the continuous measurements for the inversion.

2.2 Inversion method

In this study we use the Bayesian inversion framework FLEXINVERT+, described in detail by Thompson and Stohl (2014), which was further developed since then, to make the code more modular and to include iterative solution methods. However, our results should be valid for all inversion methods based on LPDM calculations, and we thus only include a brief description of FLEXINVERT+. It is based on a linear forward operator **H** that represents the atmospheric transport,

so that the forward problem reads

$$\boldsymbol{y} = \mathbf{H}\boldsymbol{x} + \boldsymbol{\varepsilon}, \tag{1}$$

where $\boldsymbol{y}$ is the vector of observed mixing ratios, $\boldsymbol{x}$ the emission state vector, and $\boldsymbol{\varepsilon}$ the sum of observation and model error. Since $\mathbf{H}$ is ill-conditioned and has no unique inverse, a priori emission estimates can be added, in order to solve Eq. (1) for $\boldsymbol{x}$. The inversion method applies Bayes' theorem to calculate a posteriori emissions, which on the one hand minimize the difference between observed and modeled mixing ratios and on the other hand stay close to the a priori emissions and inside of predefined uncertainty bounds. Assumed uncertainties are Gaussian-distributed, resulting in a minimization of the cost function (e.g., Tarantola, 2005)

$$\begin{aligned}\mathbf{J}(\boldsymbol{x}) = &\frac{1}{2}(\boldsymbol{x}-\boldsymbol{x}_\mathrm{p})^\mathrm{T}\mathbf{B}^{-1}(\boldsymbol{x}-\boldsymbol{x}_\mathrm{p}) \\ &+\frac{1}{2}(\mathbf{H}\boldsymbol{x}-\boldsymbol{y})^\mathrm{T}\mathbf{R}^{-1}(\mathbf{H}\boldsymbol{x}-\boldsymbol{y}),\end{aligned} \tag{2}$$

where $\mathbf{B}$ is the a priori emission error covariance matrix, $\mathbf{R}$ the observation error covariance matrix, and $\boldsymbol{x}_\mathrm{p}$ the vector of the a priori emissions. This study uses the following analytical solution to minimize $\mathbf{J}(\boldsymbol{x})$:

$$\boldsymbol{x} = \boldsymbol{x}_\mathrm{p} + (\mathbf{H}^\mathrm{T}\mathbf{R}^{-1}\mathbf{H} + \mathbf{B}^{-1})^{-1}\mathbf{H}^\mathrm{T}\mathbf{R}^{-1}(\boldsymbol{y} - \mathbf{H}\boldsymbol{x}_\mathrm{p}). \tag{3}$$

We use a spatial emission grid (Fig. A1) with 6219 grid cells of varying size ranging from $1^\circ \times 1^\circ$ to $16^\circ \times 16^\circ$. We define the grid by using model information to aggregate grid cells with low emission contributions, as further described by Thompson and Stohl (2014). For this, the emission sensitivity is taken from the LPDM 50 d backward simulation, and the resulting inversion grid is used for all inversions. The output emission fields are saved at a spatial resolution of $1^\circ \times 1^\circ$. $\boldsymbol{x}$ is assumed to not vary with time.

SF_6 has no surface sinks, and its surface fluxes can therefore only be larger than or equal to zero. However, the inversion algorithm can produce negative a posteriori fluxes. To overcome this problem we follow Thompson et al. (2015) and apply an inequality constraint on the a posteriori emissions, using the truncated Gaussian approach by Thacker (2007). This approach, which applies inequality constraints as error-free observations, is described by the following equation:

$$\hat{\boldsymbol{x}} = \boldsymbol{x} + \mathbf{A}\mathbf{P}^\mathrm{T}(\mathbf{P}\mathbf{A}\mathbf{P}^\mathrm{T})^{-1}(\boldsymbol{c} - \mathbf{P}\boldsymbol{x}), \tag{4}$$

where $\mathbf{P}$ is a matrix operator selecting the fluxes violating the inequality constraint, and $\boldsymbol{c}$ a vector of the inequality constraint (zero in our case). $\boldsymbol{x}$ and $\mathbf{A}$ represent the a posteriori emissions and error covariance matrix precalculated in the inversion, respectively.

In contrast to many other studies (e.g., Henne et al., 2016; Rigby et al., 2011; Stohl et al., 2009; Thompson and Stohl, 2014), we do not use the option to optimize the baseline mixing ratios in the inversion, except for sensitivity tests. In any case, it is desirable to obtain a baseline that is as accurate as possible prior to any optimization, which is a purely statistical correction that may falsely compensate for errors elsewhere (e.g., in the emissions). Waiving this option further gives us the opportunity to better analyze the differences between investigated baseline methods and to study their impacts on the a posteriori emissions more systematically. For the baseline optimization of the sensitivity tests, we use a temporal window of 28 d and a baseline uncertainty of 0.1 ppt. Increasing the uncertainty up to 0.2 ppt did not show any significant changes in the results. For general details on the baseline optimization, see Thompson and Stohl (2014).

2.3 Atmospheric transport

$\mathbf{H}$ is the so-called source–receptor relationship (SRR) in the context of atmospheric transport. The SRR is an emission sensitivity that relates emission changes in a given grid cell to changes in modeled mixing ratios at a given receptor; for further details, see Seibert and Frank (2004). The SRR value in a specific grid cell (units of $1\,\mathrm{s\,m^3\,kg^{-1}}$) measures the simulated mixing ratio change at a receptor that a unit strength source ($1\,\mathrm{kg\,s^{-1}\,m^{-3}}$) in that grid cell would create (Stohl et al., 2009).

In this study, we use the LPDM FLEXPART 10.4 (Pisso et al., 2019; Stohl et al., 1998, 2005) to calculate the SRR. The model is run in backward mode as this is more efficient than forward calculations when the number of emission grid cells exceeds the number of observation sites. Available observations are averaged to 3-hourly means (see Sect. 2.1). For each of these means, 50 000 virtual particles are released continuously over the averaging period and followed backward in time. The SRR is calculated by determining the average time the particles spend in each grid cell of the $1^\circ \times 1^\circ$ output grid within the lowest 100 m above the ground, assuming that all emissions occur at or near the ground. FLEXPART is driven by the hourly reanalysis dataset ERA5 (Hersbach et al., 2018) from the European Centre for Medium-Range Weather Forecasts (ECMWF) at a resolution of $0.5^\circ \times 0.5^\circ$ and with 137 vertical levels. Since SF_6 is an almost nonreactive gas, removal processes are neglected in the calculation of the SRR.

In this study, five different backward calculation periods are investigated: 1, 5, 10, 20, and 50 d. At the end of these periods, particles are terminated, and the back trajectories end. Figure 2 shows the 2012 annual average emission sensitivities for the backward calculation period of 5 d (Fig. 2a) and 50 d (Fig. 2b), respectively. On the 5 d timescale large land areas in the Southern Hemisphere (northern Australia, South America, southern Africa) and also parts of the Northern Hemisphere (e.g., India, Iran) are sampled poorly or not at all. In these areas, emissions can therefore not be determined well by the inversion. High sensitivity can only be

found at land regions with many receptors, such as Europe. On the 50 d timescale, the SRR has higher values compared to the 5 d backward calculation. Large parts of the Northern Hemisphere are sampled quite well, and the emission sensitivities provide some information, even at areas that are far away from the observation stations. However, emission sensitivities are still low in the tropics, especially over Africa, South America, and northern Australia. Figure 2c shows the increase in the annual averaged SRR due to the use of flask measurements in addition to continuous measurements in the case of 50 d simulations. One can see substantial increases in the vicinity of the measurement sites that quickly decline with distance to the sites. Further SRR values increase in large parts of the Southern Hemisphere; however, the increases over southern continental areas are relatively low, as most flask measurements are not well located for inversion purposes.

2.4 The baseline definition

The transport model can only account for mixing ratio changes caused by emissions within the chosen backward calculation period. Consequently, a baseline representing the influence of all the emission contributions prior to this time period has to be defined.

2.4.1 The REBS method

The REBS method introduced by Ruckstuhl et al. (2012) is a statistical method using a robust local regression model to identify background observations from each individual observation station to estimate a baseline curve. In recent years it has been used in various studies to determine a baseline for atmospheric inversions of several GHG species (e.g., An et al., 2012; Brunner et al., 2017; Henne et al., 2016; Schoenenberger et al., 2018; Simmonds et al., 2016; Vollmer et al., 2016). The REBS method defines observed mixing ratios $y(t_i)$ at each time step t_i as the sum of a baseline signal $g(t_i)$, an enhancement due to polluted air masses $m(t_i)$, and the observational error E_i:

$$y(t_i) = g(t_i) + m(t_i) + E_i. \quad (5)$$

The method assumes that most observations are baseline observations and therefore not influenced during pollution episodes ($m(t_i) = 0$). It also assumes that the baseline curve g is smooth – so that it can be linearly approximated around any given time. The method then applies a local linear regression model that fits the observation data, giving more weight to data points close to the considered time and iteratively excluding data points outside a certain range. An advantage of the REBS method is that it is simple to implement. The code is freely available, and besides some parameters that need to be chosen, it only depends on the observation data. This simplicity, however, also means that the method is unable to take the length of the LPDM backward calculation into account.

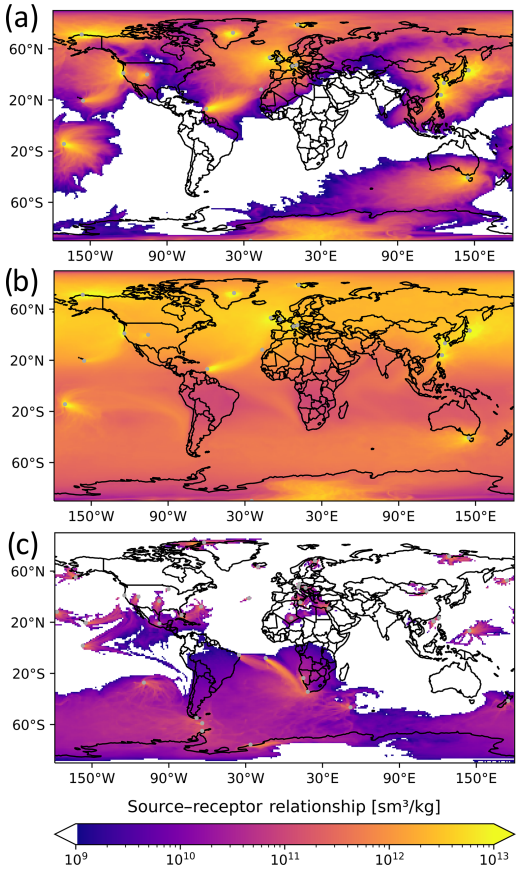

Figure 2. Source–receptor relationship obtained from FLEXPART backward simulations, averaged over the year 2012. The SRR is shown for all considered continuous measurement stations and for a simulation period of **(a)** 5 and **(b)** 50 d. Panel **(c)** shows the increase in the annual averaged SRR due to the use of flask measurements in addition to continuous measurements for the case of a 50 d backward simulation period.

As we shall see, this leads to systematic biases in the inversion results that depend on the length of the backward calculation. The method also assumes a smoothly varying baseline, which limits its ability to account for meteorological variability. Another disadvantage is the dependence on certain parameter settings. The settings used in this study are provided in Table A3. Finally, the method can only be used at sites with frequent observations, not for flask measurement sites or moving measurement platforms.

2.4.2 Stohl's method

The method introduced by Stohl et al. (2009) is primarily based on the selection of observed mixing ratios at individual observation stations but also uses the simulated SRR values and a priori emissions to determine the baseline. In the last few years, it has been used in several inversion studies (e.g., Brunner et al., 2017; Fang et al., 2014, 2015, 2019; Stohl et al., 2010; Thompson and Stohl, 2014). We apply the method and select the lowest 25 % of observations from individual stations in a moving time window of 30 d to only consider observations which are weakly influenced by emissions within the backward calculation period. Prior simulated mixing ratio enhancements are subtracted from the selected observations to eliminate the emission contributions from within the time interval of the LPDM simulation. In order to avoid an overestimation of their contribution, only the lower half of the prior simulated values and the corresponding observed data points are selected. In every time window, resulting mixing ratios are averaged and finally linearly interpolated to the timestamp of the observations. By subtracting prior simulated mixing ratios, the method takes the length of the LPDM backward calculation into account and aims to avoid an overestimation of the baseline. However, simulated mixing ratios are calculated using a priori emission estimates, making the method dependent on a priori information. Further, the subjective choice of the time window and the subjective selection of observations are problematic. As the REBS method, Stohl's method assumes a smooth baseline curve, and thus it cannot account for sudden changes in the baseline due to meteorological variability. Also, the method can only be used at sites with frequent observations.

2.4.3 The GDB method

The idea of the GDB approach (Thompson and Stohl, 2014) is to determine the baseline directly from a 3D global field of mixing ratios, e.g., from a reanalysis of the atmospheric chemical composition. The end points of the back-trajectories that are used by the LPDM to calculate the SRR are utilized to determine the sensitivity at the receptor to mixing ratios at the points in space and time where particles terminate (see Fig. 3 for a simplified illustration). This sensitivity (termed "termination sensitivity" hereafter) in a particular grid cell is calculated in the LPDM by dividing the number of particles terminating in that cell by the total number released at the receptor, while also including a transmission function to account for loss processes (not relevant for SF_6) during the backward simulation period. The termination sensitivity fields are saved in a 3D $1° \times 1°$ output grid with 16 vertical layers with interface heights at 0.1, 0.5, 1, 2, 3, 4, 5, 7, 9, 12, 15, 20, 25, 30, 40, and 50 km above ground level. For global inversions, baseline mixing ratios are then calculated by multiplying the termination sensitivity with the mixing ratios of the 3D global field and integrating the product over all grid cells. The GDB method can also be used for regional inversions (not done in this study). In this case, the emission contributions from outside the regional domain need to be added to the baseline (Thompson and Stohl, 2014), but otherwise the inversion procedure is identical as described here.

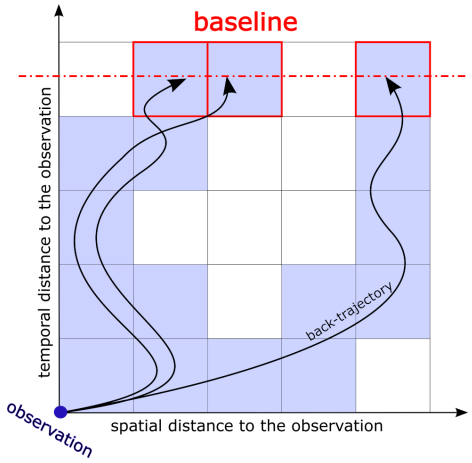

Figure 3. Simplified illustration of the global-distribution-based (GDB) method for baseline determination, where the backward simulation is represented by three back trajectories released at the time and space of a particular observation. The spatiotemporal grid is simplified to two dimensions with a vertical time and a horizontal space axis. Grid cells that contribute to the modeled mixing ratio through emissions are shaded blue; termination grid cells where termination sensitivity is stored are marked with red rectangles; the termination point is illustrated by a dashed red horizontal line.

The GDB method is independent of subjective data selection and choice of parameter settings. In contrast to the REBS method and Stohl's method, it does not assume a smooth baseline and has the potential to fully account for meteorological variability. As illustrated, it excludes emission contributions from within the backward simulation period and therefore provides a baseline that is fully consistent with the length of the backward simulation. Furthermore, contrary to the other two methods, it can also be used at measurement sites with infrequent observations or moving observation platforms. Its accuracy, however, is dependent on the ability to minimize errors and especially biases of the global 3D mixing ratio fields. We target this challenge using the FLEXible PARTicle dispersion chemical transport model (FLEXPART CTM; Henne et al., 2018) to perform a reanalysis of SF_6 as described in the next section.

2.5 Reanalysis of SF_6 using FLEXPART CTM

In this study the LPDM FLEXPART 8-CTM-1.1 is used to perform a reanalysis of SF_6 for the year 2012. It was de-

veloped by Henne et al. (2018) and is based on FLEXPART 8.0. Groot Zwaaftink et al. (2018) provide a detailed description of FLEXPART CTM and evaluate this model for the example of CH_4. FLEXPART CTM is run in a domain filling mode where 12 million particles are randomly distributed over the globe, proportional to the air density. In addition to an air tracer, particles also carry the chemical species SF_6. The initialization is based on a latitudinal SF_6 profile based on surface observations. We run the simulation from 2011 to 2012, using 2011 as a spin-up period. Particles are followed forward in time, and whenever a particle resides below the diagnosed boundary layer height, its mass is increased due to surface SF_6 emissions. The model is driven with the ECMWF ERA5 dataset and with emission fields calculated as described in Sect. 2.6. Mixing ratio fields are saved daily on a $3^\circ \times 2^\circ$ output grid and coupled to the backward simulations.

FLEXPART CTM uses a nudging routine to keep simulated SF_6 fields close to the observations of SF_6. With this simple data assimilation method, modeled fields of mixing ratios are relaxed towards observations within so-called nudging kernels around observation sites. For all surface observation stations in the Southern Hemisphere, we assign relatively large uniform kernel sizes, since the model tends to overestimate SF_6 mixing ratios in the Southern Hemisphere, and there are only few measurement stations to correct this bias. For the surface observation sites in the Northern Hemisphere, we assigned smaller kernel sizes to measurement stations with a large observation variability to conserve SF_6 spatial variability, especially over the continents (see Groot Zwaaftink et al., 2018). For the aircraft measurements we predefine vertical levels at 0.05, 0.15, 0.3, 0.5, 0.75, 0.1, 1.5, 2, 2.5, 3, 3.5, 4, 5, 6, 7, 8, and 9 km a.g.l., co-locate the individual measurements to the closest vertical level, and choose kernel sizes that increase with altitude. Specific kernel settings are detailed in Table A4.

2.6 A priori emissions

An a priori estimate of the spatial distribution of SF_6 emissions for the year 2012 is determined by collecting information on the emissions from individual countries. We use country emissions reported to the United Nations Framework Convention on Climate Change (UNFCCC, 2021) and for East Asian countries' emissions estimated by Fang et al. (2014). The sum of these individual country emissions is subtracted from the total global SF_6 emissions determined by Simmonds et al. (2020), and the remaining emissions are distributed to all other countries proportional to their electric power consumption (World Bank, 2021). Finally, total country emissions are disaggregated according to the gridded population density (CIESIN, 2018) within each country's borders. Note at this point that the a priori emissions as constructed agree with recognized global emissions, which should be kept in mind when the global total is used as a reference value in the discussion. The a priori emission uncertainty is estimated to be 50 % in each grid cell, with a minimal value of 1×10^{-13} kg m^{-2} h^{-1}. Spatial correlation between uncertainties is considered using an exponential decay model with a scale length of 250 km.

3 Results

3.1 Baselines and length of backward simulation

The three investigated baseline methods are discussed for the example of two measurement sites, Gosan and Ragged Point, and for five backward simulation time periods. The Gosan observation station is located on the southwestern tip of Jeju Island, South Korea, monitors the outflows from the Asian continent, and is representative of stations which frequently measure pollution events. The Ragged Point observation station is situated on the eastern edge of Barbados, with direct exposure to the Atlantic Ocean. Ragged Point is primarily influenced by easterly winds providing "clean" background air masses, uninfluenced by local emissions, and is therefore representative of background stations. Both Gosan and Ragged Point periodically intercept air from the Southern Hemisphere and therefore have a rather complex baseline.

Baseline mixing ratios are plotted together with respective observations and a priori mixing ratios for different LPDM backward simulation periods ranging from 1 to 50 d (Figs. 4–7). A priori mixing ratios are calculated as the sum of the baseline and the contribution originating from a priori emissions during the period of the backward simulation (termed "direct emissions contributions" hereafter). Ideally, the choice of the backward simulation period should have no systematic effect on the calculated a priori mixing ratios. By increasing the backward simulation time, and therefore enlarging the temporal domain, additional emission contributions are included in the optimization. Per definition, these contributions are not part of the baseline and should ideally be removed from it. As a result, the baseline should become lower and smoother when the simulation period is increased. We investigate the agreement between modeled and observed mixing ratios for the three methods with time series plots (Figs. 4–7), as well as statistical parameters (bias, mean squared error (MSE), and coefficient of determination (r^2)), summarized in Table 2.

Figure 4 shows the smooth baselines calculated with the REBS method and Stohl's method at the measurement station Gosan. In the case of 1 d backward simulations (Fig. 4a and d), both methods show a poor agreement between modeled and observed mixing ratios, as neither the smooth baselines nor the small direct emission contributions can reproduce the observed mixing ratios during pollution episodes. This agreement becomes much better with longer backward simulation periods (Fig. 4b and e). The REBS baseline stays completely unchanged for different backward simulation pe-

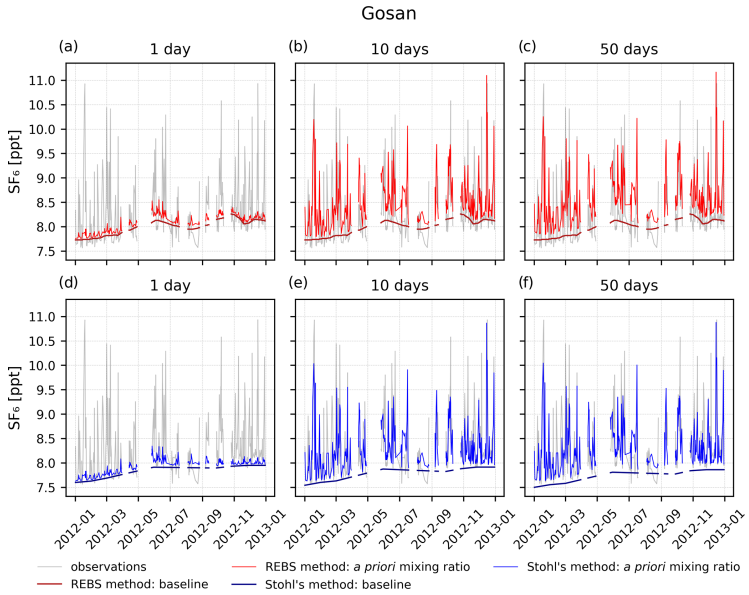

Figure 4. Baseline and a priori SF_6 mixing ratios calculated with the REBS method (panels **a–c**) and Stohl's method (panels **d–f**) at the Gosan observation station, compared to SF_6 observations. Model results are shown for backward simulations of 1 d (panels **a** and **d**), 10 d (panels **b** and **e**), and 50 d (panels **c** and **f**).

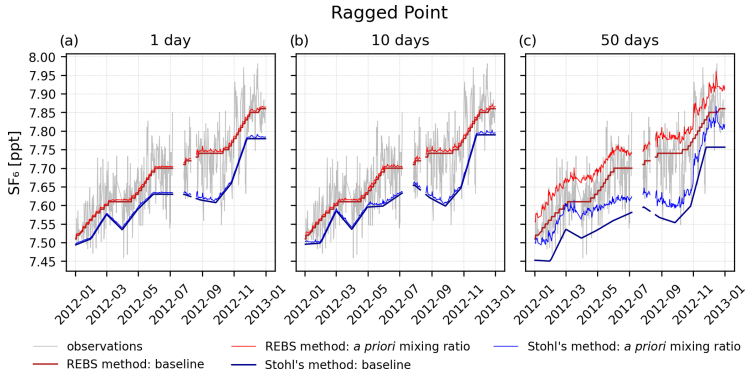

Figure 5. Baseline and a priori SF_6 mixing ratios determined by the REBS method and Stohl's method at the Ragged Point observation station for backward simulation times of 1 d (panel **a**), 10 d **(b)**, and 50 d **(c)**.

riods. Therefore, a priori mixing ratios grow with increasing simulation periods (Fig. 4b and c), as more direct emissions contribute to the calculated total mixing ratio. For Gosan, the bias is negative for the 1 d simulation period but becomes increasingly positive for longer simulation periods (Table 2). This systematically increasing bias is inherent to all purely observation-based baseline methods and cannot be corrected without adding model information. In contrast, Stohl's baseline level decreases with longer backward simulation periods as higher direct emission contributions are subtracted from the preselected observations. Consequently, the bias of the a priori mixing ratios changes less between 10 and 50 d of backward simulation (Fig. 4e and f). This is confirmed by statistical parameters in Table 2 also showing only little change between 10 and 50 d.

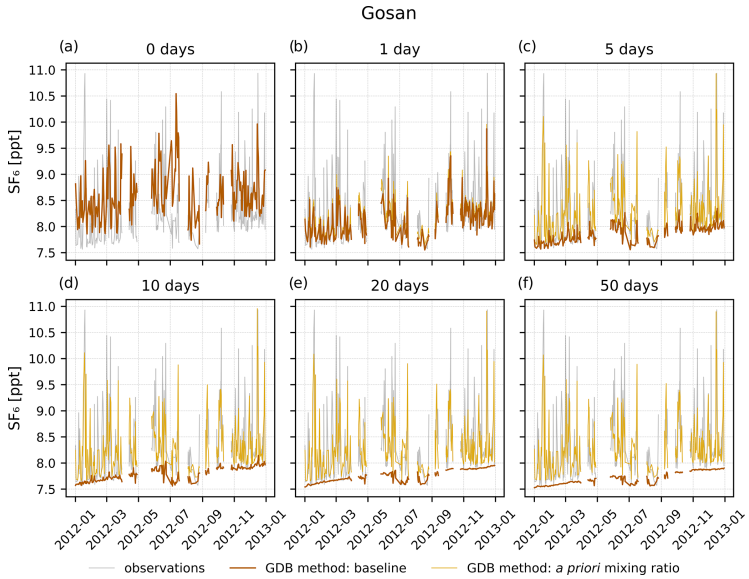

Figure 6. Baseline and a priori SF_6 mixing ratios calculated with the GDB method at the Gosan observation station for backward simulation times of 0 (panel **a**), 1 **(b)**, 5 **(c)**, 10 **(d)**, 20 **(e)**, and 50 d **(f)**.

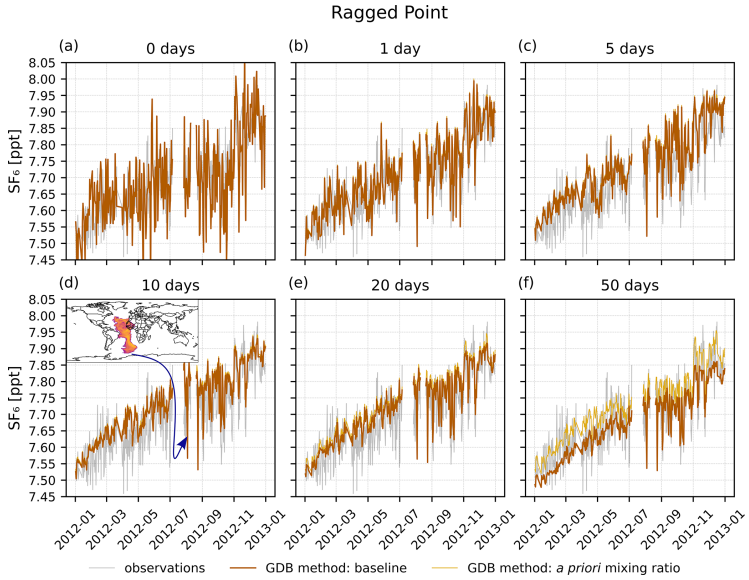

Figure 7. Baseline and a priori SF_6 mixing ratios calculated with the GDB method at the Ragged Point measurement station for backward simulation periods of 0 (panel **a**), 1 **(b)**, 5 **(c)**, 10 **(d)**, 20 **(e)**, and 50 d **(f)**. The inset in panel **(d)** shows the termination sensitivity averaged over all heights for the time of the marked observation low point, illustrating the method's ability to account for baseline changes due to episodic transport from the Southern Hemisphere.

Table 2. Bias, mean squared error (MSE), and coefficient of determination (r^2) of a priori SF_6 mixing ratios determined by the three investigated baseline methods with respect to observed mixing ratios. Statistical parameters are shown for three different backward calculation periods (1, 10, and 50 d) at the stations Gosan and Ragged Point. Also reported are the bias, MSE, and r^2, calculated separately for all stations listed in Table 1 and then averaged.

		Gosan			Ragged Point			All stations		
Parameter	Method	1 d	10 d	50 d	1 d	10 d	50 d	1 d	10 d	50 d
Bias [ppt]	REBS	−0.225	0.190	0.267	0.006	0.007	0.054	−0.028	0.012	0.061
	Stohl	−0.384	−0.016	0.008	−0.067	−0.068	−0.065	−0.103	−0.064	−0.051
	GDB	−0.090	−0.002	−0.006	0.023	0.044	0.033	0.022	0.016	0.007
MSE [ppt^2]	REBS	0.420	0.250	0.281	0.004	0.004	0.006	0.034	0.023	0.028
	Stohl	0.525	0.216	0.210	0.009	0.009	0.009	0.050	0.026	0.024
	GDB	0.303	0.206	0.205	0.005	0.005	0.004	0.034	0.022	0.021
r^2	REBS	0.085	0.482	0.495	0.671	0.670	0.712	0.584	0.647	0.651
	Stohl	0.068	0.474	0.490	0.649	0.629	0.623	0.548	0.616	0.623
	GDB	0.272	0.499	0.501	0.631	0.718	0.746	0.423	0.589	0.634

At Ragged Point (Fig. 5), the a priori mixing ratios determined by the REBS method fit the observation data very well for short backward simulation periods, where baseline and a priori mixing ratios overlap because of small direct emission contributions (Fig. 5a and b). This is expected, since the method determines the baseline by fitting the observation data while iteratively excluding outliers. Since regional pollution events captured at Ragged Point tend to be very small, no significant measurement peaks need to be excluded. Therefore, the REBS baseline fits well through the measurement data, resulting in a good statistical model–observation agreement (Table 2). However, the smooth baseline is unable to reproduce the observed variability. In the case of a simulation period of 50 d (Fig. 5c), more direct emission contributions give higher a priori mixing ratios, overestimating the measurements and causing a large bias. In contrast, due to its 25th percentile preselection of observations, Stohl's method shifts the baseline curve towards the lowest observations. In the case of Ragged Point, these lowest observations come from southern hemispheric air masses. Hence, Stohl's baseline is more representative of southern hemispheric conditions, which do not necessarily dominate at that site. Consequently, a priori mixing ratios underestimate the observations for low direct emission contributions (Fig. 5a and b). The resulting bias is almost unaffected by the different backward simulation periods (Table 2 and Fig. 5c), showing the method's ability to compensate for increasing direct emission contributions. However, the rather ad hoc 25th percentile preselection of data for the baseline is obviously not justified for a background station with few pollution episodes and southern hemispheric air interceptions, leading to a systematic underestimation of modeled a priori mixing ratios, irrespective of the length of the backward simulation.

The GDB method is illustrated for all backward simulation periods tested, including a case without any backward simulation (0 d). In this extreme case, the baseline is obtained directly from the value of the global mixing ratio field simulated with FLEXPART CTM in the spatiotemporal grid cell of the respective observation. At Gosan, FLEXPART CTM reproduces observed mixing ratios well, even capturing a few pollution events (Fig. 6a). This good agreement is however expected, since these observations were used for the nudging in the FLEXPART CTM model. In the 1 d backward simulation case (Fig. 6b), the method computes a highly variable baseline, partly representing the observed variability. This results in a much better agreement between a priori and observed mixing ratios than using the REBS method or Stohl's method (Table 2). The GDB baseline becomes smoother and lower with increasing backward simulation time. The loss of variability arises from the fact that the GDB method calculates the baseline from a weighted average of grid cell mixing ratios at the trajectory termination points. The longer particles are followed backward in time, the more widely dispersed over large geographical regions termination points become, thus resulting in a smoother baseline. The lowering of the GDB baseline is compensated for by the increase of the direct emission contributions (see Sect. 2.4.3 and Fig. 3), ensuring a seamless transition between forward (FLEXPART CTM) and backward simulations. As a result, a priori mixing ratios in Fig. 6 show no large systematic changes with an increasing simulation period between 5 and 50 d.

Figure 6 also demonstrates the advantage of the Lagrangian backward simulation. As FLEXPART CTM is limited in resolution and particle number, it can only reproduce a few pollution events at Gosan, and it underestimates the highest and overestimates the lowest measured SF_6 mixing ratios, as demonstrated in the 0 d case (Fig. 6a). The backward simulation is initiated at the exact location of the measurement point and provides much higher resolution (Fig. 6b–f). If the backward calculation period is long enough that back

trajectories reach important emission regions, mixing ratio spikes similar to the observed ones can be simulated. At the same time, the lowered baseline for intrusions of southern air masses during the Asian summer monsoon also allows the lowest observed values to be captured. Table 2 shows exclusively improving correlation between modeled and observed values with increasing backward simulation periods.

Figure 7 illustrates the GDB method at the Ragged Point station. FLEXPART CTM (Fig. 7a) reproduces the measured mixing ratios well. However, it generates more variability than observed at this station. This is partly due to the limited number of particles in the domain-filling simulation, which introduces noise into the model results. This is averaged out by the GDB method with increasing backward simulation time, as the baseline becomes a weighted average over many grid cells. Nevertheless, the baseline maintains variability for all tested simulation periods, fitting the observed signal well (Fig. 7b–e). It is noteworthy that at Ragged Point a substantial part of the observed SF_6 variability seems to be caused by transport from different latitudes/regions without direct emission contributions, exemplified by the quite variable baseline even for the 50 d backward simulation. In contrast, the direct emissions accumulated over the 50 d of the backward simulation are producing an almost constant enhancement over the baseline. This is very different from a station like Gosan that is strongly influenced by pollution episodes.

Notice also that for backward simulation times of 10 d and longer, the GDB method is able to reproduce short episodes of very low observed mixing ratios at Ragged Point that are caused by episodic transport from the Southern Hemisphere (see also inset in Fig. 7d). Neither the REBS method nor Stohl's method could correctly reproduce these negative SF_6 excursions.

Additional figures illustrating the three baseline methods at all investigated measurement sites can be found in the Supplement. Despite all the advantages of the GDB method, it does not work well if the modeled global mixing ratio fields are biased. At Mace Head and Zeppelin (see Figs. S17 and S33 in the Supplement), FLEXPART CTM overestimates the measurements, and thus the GDB method gives a baseline that partly exceeds the observations. Possible error sources include deficiencies in the emission assumptions driving the model that are impossible to be compensated for through nudging with the few available observations. It is also unclear whether the FLEXPART CTM nudging routine was able to properly correct mixing ratios at higher altitudes, as aircraft measurements were available only over North America (with one exception). On the other hand, statistical baseline methods might work better at observation stations, where the baseline termination is less complex. At Mace Head (Fig. S18 in the Supplement) for instance, both the REBS method and Stohl's method lead to a very high correlation between modeled and observed mixing ratios for the case of a 50 d backward simulation ($r^2 = 0.87$). Nevertheless, for the REBS method, the discussed growing negative bias with longer simulation periods can be observed.

Statistical parameters (bias, MSE, and r^2) were separately calculated for every observation station, and respective averages over all stations are shown in Table 2. One should keep in mind that the REBS method and Stohl's method are directly based on the observations themselves, and thus the dependency between observed and modeled a priori mixing ratios is likely higher than in the case of the GDB method, where observations are rather used to improve the mixing ratio fields. Therefore, it is remarkable that overall the GDB method obtains smaller bias and MSE values than the other two methods. The REBS method shows the highest r^2 values. The main reason for this good correlation is that the method captures the trend in the time series very well, which represents a considerable fraction of the total variability in the data. The GDB baseline may contain a fair fraction of noise, in contrast to the smooth baselines of the other two methods. This will lead to lower correlation. However, it is noteworthy that for the GDB method, the r^2 value improves systematically with growing backward simulation time and for 50 d even exceeds the value derived by Stohl's method. By extending the backward calculation period from 10 to 50 d, the GDB r^2 value increases by 0.045, meaning that an extra 4.5 % of the observed variability can be explained by the model. Notice also the improvement in bias and MSE, which can be observed for the GDB method and Stohl's method, when extending the simulation period from 10 to 50 d. The REBS method does not show these improvements due to its systematical increase of bias with backward simulation time.

3.2 Inversion results

Figure 8 illustrates (a) the global distribution of the SF_6 a priori emissions 2012 as well as (b–d) the emission increments (i.e., a posteriori minus a priori emissions) for the three investigated baseline methods using SRRs from 20 d backward calculations. A priori emissions are allocated to regions proportional to electricity use and population density. This implies large a priori emissions in South and East Asia, including China, which is estimated to be the biggest contributor to global SF_6 emissions. In general, much higher a priori emissions are allocated to the Northern Hemisphere than to the Southern Hemisphere. We should also note that the emission optimization of the inversion focuses on regions with large a priori emissions, where also assumed uncertainties are bigger (see Sect. 2.6), assigning more freedom to the algorithm.

The inversion increments in Fig. 8b–d show three very contrasting pictures, illustrating the huge impact of the choice of the baseline method on the inversion results. Using different baseline approaches completely changes the results of the inversions. When using the REBS method (Fig. 8b), the inversion produces negative emission increments in almost all areas of the globe. As the real emissions are unknown, this is not necessarily an unrealistic result. However,

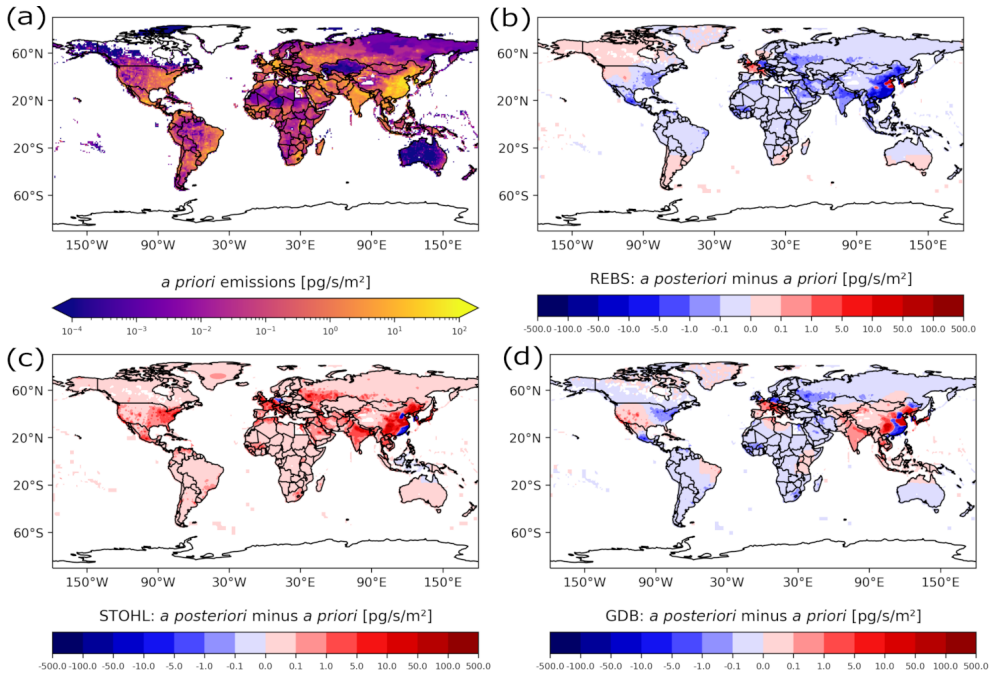

Figure 8. A priori SF_6 emissions **(a)** and SF_6 emission increments given by the inversion when using the REBS method **(b)**, Stohl's method **(c)**, and the GDB method **(d)** based on 20 d LPDM backward simulations.

when considering these mostly negative increments together with the discussed positive bias for REBS baselines in Table 2 (especially for longer backward simulation periods), there is reason to assume that the REBS method overestimates baselines and consequently underestimates the a posteriori emissions overall. In contrast, the inversion algorithm produces positive increments almost everywhere around the globe when applying Stohl's method (Fig. 8c). Again, considering this together with the discussed negative biases in Table 2, this might indicate an underestimation of the baselines and an overestimation of the a posteriori emissions overall. In the case of the GDB method (Fig. 8d), negative and positive increments are more balanced. Overall, the patterns are more similar to the ones of the REBS method, except in East Asia, where they rather resemble the patterns of Stohl's method. Large positive increments can be seen in East Asian regions and parts of Europe, whereas the inversion tends to produce slightly negative increments in the Southern Hemisphere.

National emissions

As the verification of emission reports to UNFCCC takes place on a national scale, the impact of baseline methods on national emissions is of great interest (Fig. 9). In countries with very low emission sensitivity (e.g., Brazil), inversion increments are very small in all three cases, and therefore the baseline choice has little impact. However, considering countries with higher emission sensitivities (e.g., China), the a posteriori emissions are very sensitive to the baseline definition. In almost all cases, the REBS method leads to smaller national emissions and Stohl's method to larger national emissions than the GDB method. Due to the large emissions in China, the differences in a posteriori emissions become especially apparent there, with almost a factor of 3 emission difference, corresponding to almost 30 % of the 2012 global SF_6 emissions.

Global emissions

The 2012 SF_6 global emissions are shown in Fig. 10. The bars represent inversion results using different backward calculation periods between 1 and 50 d (light to dark shading). The horizontal dashed line illustrates a reference value calculated by Simmonds et al. (2020) with the AGAGE 12-box model. Notice that this is the same value used to calculate the a priori emissions, so the line also represents the global a priori emissions, which should be kept in mind for the interpretation of the results. Since the uncertainty of the global emissions is relatively small, global emissions derived by the

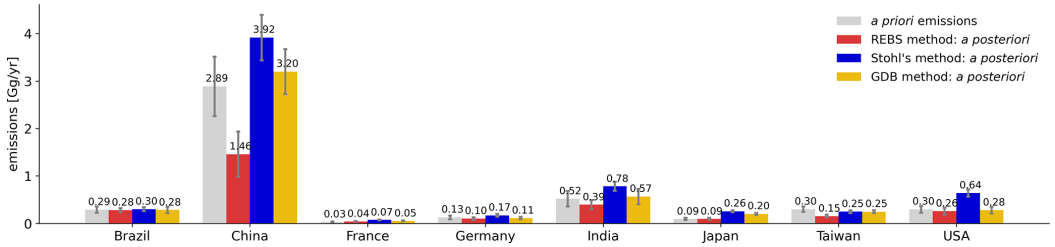

Figure 9. National SF_6 emissions for selected countries, based on 20 d LPDM backward calculations with different choices of the baseline method. Uncertainties represent a 1σ range.

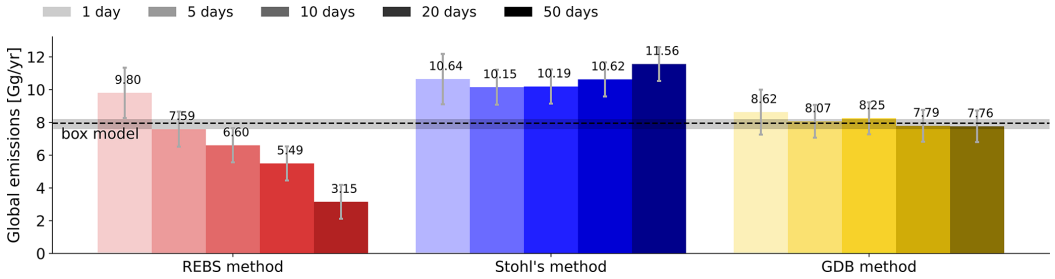

Figure 10. SF_6 global emissions derived by the inversions. Results are shown for the three applied baseline methods and for the five applied backward simulation periods between 1 and 50 d. The horizontal dashed line represents the reference value of the AGAGE 12-box model with shaded error bands. Uncertainties represent a 1σ range.

inversion should roughly match the value of the box model, regardless of which backward simulation period was used.

For the REBS method, calculated global emissions (red) decrease dramatically with growing backward simulation time, showing values between 3.15 and 9.80 Gg yr^{-1}. This is a consequence of the method's incapability to remove emission contributions from the baseline when the backward simulation period expands, leading to a systematical overestimation of the baseline and underestimation of the emissions. The resulting bias increases with growing simulation period, and as a result global emissions estimates deviate strongly from the box model.

In the case of Stohl's method (blue), derived global emissions do not show such a systematic decrease with longer backward simulation periods as observed for the REBS method. This is because Stohl's method not only selects low mixing ratio observations, but also uses model information to maintain the baseline. For longer backward simulation periods, higher simulated mixing ratios are subtracted from the preselected observations to compensate for more direct emission contributions. Nevertheless, global emissions significantly exceed the reference value of the box model for all applied simulation periods, implying a systematic overestimation of emissions through too low baselines. The overestimation of the global emissions increases with longer backward simulation times larger than 5 d. This suggests that the method overcompensates for additional direct emission contributions when the simulation period expands, subtracting values that are systematically too high from the preselected observations.

We further investigate whether the encountered biases can be reduced by optimizing the baseline in the inversion. Therefore, we repeated the inversion with exactly the same setup, except optimizing the REBS baseline and Stohl's baseline as part of the inversion. Results are shown in Fig. A2. In the case of the REBS method, the baseline optimization only has little effect on the global total a posteriori emissions for backward simulation periods between 1 and 10 d and only becomes noticeable after 20 d. The greatest improvements can be observed for the 50 d simulation, where the bias is almost halved. Still, for longer simulation periods the increasing improvements through the baseline optimization cannot compensate for the growing underestimation of the emissions and substantial biases remain. Optimizing Stohl's baseline shows great improvements, especially for longer simulation periods. These improvements increase systematically with growing backward simulation period, and results get very close to the box model outcome for the 20 and 50 d simulation case.

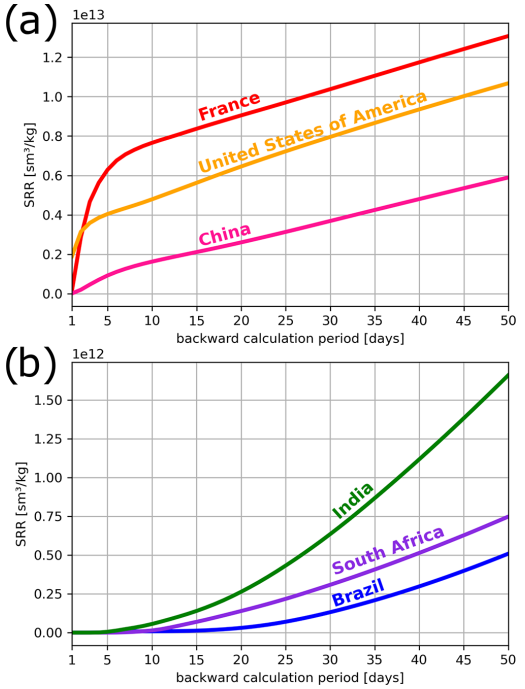

Figure 11. SRR for individual countries and different backward calculation periods between 1 to 50 d, considering all continuous measurement stations in Table 1. The values shown are averages over the grid cells of **(a)** France, USA, and China and **(b)** India, South Africa, and Brazil for the year 2012.

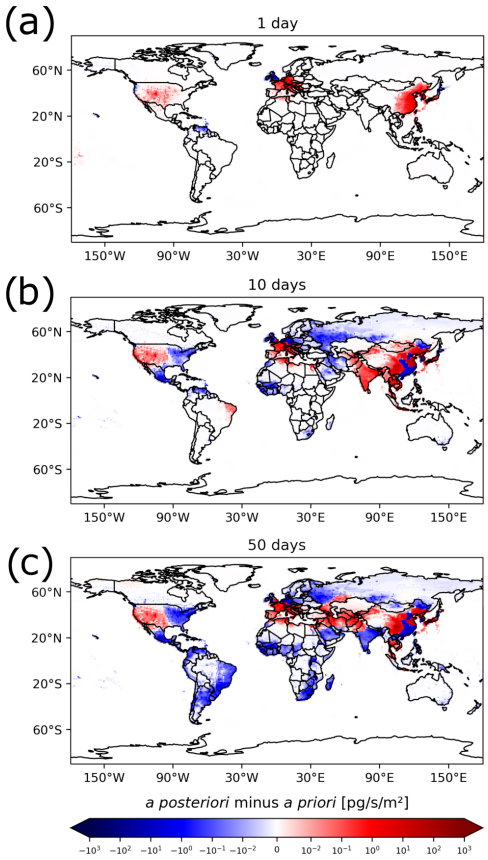

Figure 12. SF_6 emission increments calculated with the inversion by using the GDB method and a backward simulation period of **(a)** 1, **(b)** 10, and **(c)** 50 d.

Considering the inversion results based on the GDB method, global emissions are in good agreement with the box model result for all tested backward simulation periods, as the global a posteriori emissions stay close to the global a priori value. Furthermore, these global emissions stay almost unchanged for different backward simulation periods, demonstrating the method's ability to adjust the baseline according to the sampled emissions of different simulation periods.

The advantage of longer backward simulation periods

As an argument for a relatively short backward simulation period, Stohl et al. (2009) stated that "the value for the inversion of every additional simulation day decreases rapidly with time backward". Certainly, this is true for countries and regions that are well covered by the global monitoring network. For instance, for France the SRR increases rapidly in the first few backward simulation days but flattens to a linear increase for longer backward simulation periods (Fig. 11a). A similar behavior can be observed for many countries in the Northern Hemisphere, although the curve's slope for the first few days varies. For countries poorly covered by the monitoring network, however, the SRR is close to zero for the first 5 to 15 backward days, and only longer backward simulations might provide information for the inversion (see Fig. 11b). For these countries, the SRR increase with time only flattens to a linear increase for very long transport times, even beyond the 50 d used in this study.

Figure 12 further illustrates the impact of different backward simulation periods on the inversion, by showing emission increments for the GDB method and for backward simulation periods of 1, 10, and 50 d. In the case of 1 d backward calculations (Fig. 12a), the inversion only significantly optimizes a priori emissions in East Asia and parts of Europe. As the backward simulation period is extended to 10 d (Fig. 12b), the inversion optimizes emissions in larger parts

of the Northern Hemisphere, but in the Southern Hemisphere emission increments are still small. In the case of 50 d (Fig. 12c), the inversion optimizes emissions even far away from observation stations (e.g., South America or South Africa). In India, where SRR values are also small, and a priori emissions (and thus emission uncertainties) are high (see also Fig. 11b), the emission increments even switch from positive to negative by extending the period from 10 to 50 d. Also, the calculated relative uncertainty reduction increases by extending the backward simulation period (see Fig. A3a–c).

The use of flask samples

An advantage of the GDB method is the possibility to include flask measurements from fixed sites or moving platforms in the inversion. By contrast, the REBS method and Stohl's method require short measurement intervals at fixed sites for the statistical baseline calculation. Here, the baseline could be taken from nearby or same latitude continuous sites or represented through baselines at the domain border in case of regional inversions (Manning et al., 2021). Figure 13a shows the relative change in a posteriori emissions and Fig. 13b the additional relative error reduction when using flask measurements additionally to the continuous measurements for the 50 d backward simulation. One can see substantial differences in the USA, eastern Europe, South Africa, East Asia, and the Near East, where also an additional error reduction occurs. While this additional error reduction can be relatively large (up to 73 %) for grid cells in the vicinity of the measurement sites, it quickly decreases down to a few percent with larger distance to the measurements. Consequently, flask measurements only show a small influence on the total global emission estimate (< 1 %) but can have a large impact on calculated national emissions of specific countries (Fig. A4). For countries in the Near East, the additional use of flask measurements changes national emission estimates by 40 % to 100 %. South African and American emissions are modified by around 10 %.

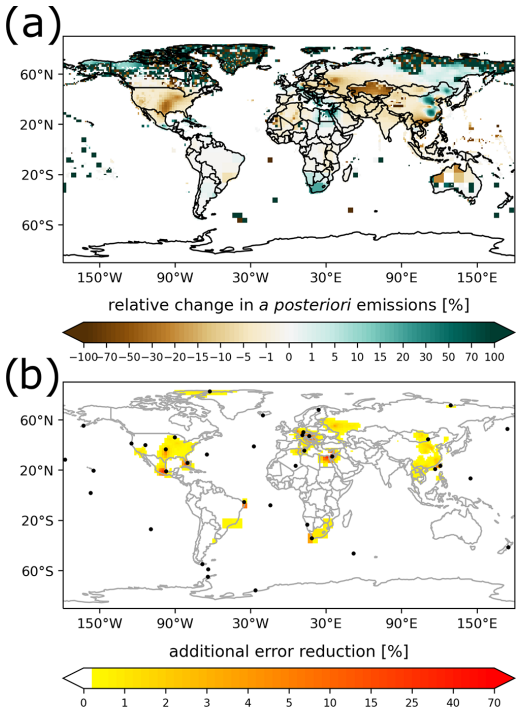

Figure 13. (a) Relative change in a posteriori emissions and **(b)** the additional error reduction when using flask measurements in addition to continuous measurements for the 50 d simulation. The locations of the flask measurements are marked with black dots.

Reliable global emissions can only be obtained with long backward simulation periods

In previous sections, we have used global mixing ratio fields from the GDB method, where great care has been taken to avoid biases that would affect the baseline, and we have used global a priori emissions that correspond to the rather well-known global SF_6 emissions. These are optimal conditions for the inversion that are rarely fulfilled for other species than SF_6. For many species, global emissions are less well known, and with fewer observations than for SF_6 the global distribution (and, thus, the baseline) is also more uncertain. However, a skillful inversion should tolerate such biases and still produce reliable results. While we lack information for verifying that regional emissions are reliable, for SF_6 we can at least test whether global emissions can be determined by our inversion in the presence of biases.

Figure 14 shows global a posteriori emissions when biases in (1) the a priori emissions and (2) global mixing ratio fields were added. This is shown for different backward simulation periods between 1 and 50 d and for the 50 d case with the inclusion of flask measurements. Note that for all these sensitivity cases shown in Fig. 14, we use the same absolute a priori emission uncertainties as for the original a priori emissions without any artificial bias.

Comparing the inversion results for doubled (Fig. 14a) and halved (Fig. 14b) a priori emissions clearly shows that the corresponding biases in the global a posteriori emissions are reduced substantially with increasing backward simulation period and converge towards the rather well-known global SF_6 emission from the box model. It seems an extension of the backward simulation period beyond 50 d would be required in order to further reduce the remaining bias. The inclusion of flask measurements leads to slight additional improvements.

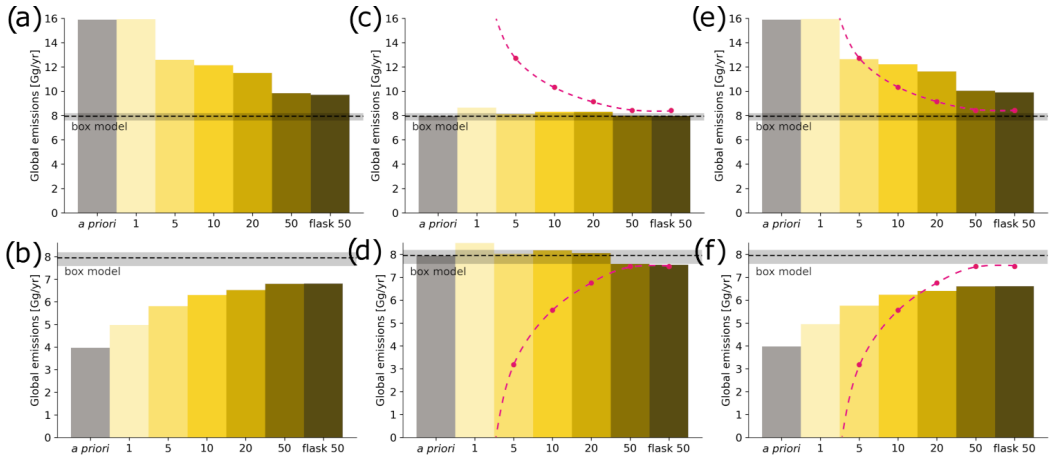

Figure 14. Global SF_6 emissions using the GDB method shown for different sensitivity cases, using backward simulation periods between 1 and 50 d and a 50 d backward simulation case in which flask measurements were also included in the inversion in addition to continuous measurements. The sensitivity cases include **(a)** doubled and **(b)** halved a priori emissions; biased global mixing ratio fields with a uniform bias of **(c)** −0.003 and **(d)** +0.003 ppt in every grid cell; and combinations of the two test types; **(e)** doubled a priori emissions plus −0.003 ppt global field bias; **(f)** halved a priori emissions plus +0.003 ppt global field bias. The dashed pink lines represent the expected relationship between the baseline bias and a resulting emission bias if a global box model was used and the bias attributed solely to emissions in different periods corresponding to the backward simulation times.

Another sensitivity test was performed with artificially biased global mixing ratio fields by subtracting (Fig. 14c) or adding (Fig. 14d) 0.003 ppt from/to the FLEXPART CTM model output in every grid cell of the 3D mixing ratio fields. 0.003 ppt is equivalent to roughly 1 % of the 2012 global mixing ratio increase and thus corresponds to about 3 d of global SF_6 emissions. To still fit the model to the observations, the inversion will try to compensate for such a bias in the baseline with a bias of the opposite sign in the emissions. As always, the inversion can only attribute this additional bias to emissions within the simulation period. Therefore, shorter backward simulation periods require a greater modification of emissions than longer periods, in order to compensate for the baseline bias. To fully compensate for the baseline bias equivalent to 3 d of emissions, global a posteriori emissions would need to deviate strongly from the reference value for the 1 d case but converge towards it with increasing backward simulation time. This is shown by the dashed pink line, which indicates the expected relationship between this baseline bias and a resulting emission bias if a global box model was used and the bias attributed solely to emissions in different periods corresponding to the backward simulation times. In fact, with a positive baseline bias, negative emissions would be required for backward simulation times of less than 3 d, as the baseline exceeds the observations. The inversion results do not show this extreme behavior, since for short backward simulation times high SRR values are only found in small regions, and the emission changes there are bound by the prescribed a priori uncertainties. Notice that in our case of a known added bias, this is rather a shortcoming, as this shows that the inversion is not able to compensate for the baseline bias for short backward simulation times. Only for the longest times do the emissions converge towards the expected global emissions (dashed pink lines), and only for such long backward simulation times do baseline biases equivalent to 3 d of emissions become negligible. We also investigated the inversion behavior for larger baseline biases, subtracting/adding (Fig. A5a and b) 0.05 ppt from/to the global fields, corresponding to roughly 50 d of the 2012 global SF_6 emissions. Here again, the results for short simulation times seem unpredictable; i.e., they do not follow the described expected behavior, indicated by the dashed pink lines. Only for the 50 d simulation periods do results converge to the expected global emissions, consistent with the respective baseline bias.

Finally, we also combined doubled a priori emissions with a −0.003 ppt bias in the global mixing ratio fields (Fig. 14e) and halved a priori emissions with a +0.003 ppt bias (Fig. 14f). For both cases, the inversion becomes less sensitive to biases in the a priori emissions and the global fields with longer backward simulation periods.

Final remark

In this study, we show many advantages of using relatively long backward simulation periods for the inversion. Nev-

ertheless, the improvement of regional emission patterns is still limited by the observation network. A lack of observations in one region cannot simply be compensated for by extending the simulations for stations in other regions to very long periods. For backward simulation times of 20–50 d, the emission sensitivity is distributed over large areas but usually still concentrated within broad latitude bands. The additional information to be gained from such long simulation times, on top of the information provided by the shorter simulation times, can probably best be compared with the inversions done with a multi-box model such as the AGAGE 12-box model (e.g., Rigby et al., 2013), which is capable of determining the emissions in broad latitude bands. Consequently, if the emissions in certain regions with a dense observation network are already well constrained by shorter simulation periods, the residual emission will be attributed correctly as an emission total to all other regions of the same latitude band with a poor station coverage. The effective resolution of the obtained emissions in such data-poor regions may be very coarse, but the result might still be informative. Furthermore, the emission sensitivity for the 20–50 d backward period is still not uniformly distributed over a latitude band and thus provides some limited regional information. Perhaps supported with a limited number of strategically located flask measurements, inversions with long backward simulation times could provide coarse but robust information on emissions in poorly sampled regions. Independently, the growing correlation between modeled and observed mixing ratios with increasing backward simulation length (Table 2; averaged over all stations) also shows that longer backward simulations hold additional information, even though the information gain decreases with every day added to the simulation length and probably becomes marginal for very long backward simulation times. However, we propose to make use of this additional information and apply longer periods whenever possible to make the best use of the existing observation network.

4 Conclusions

We have examined the use of LPDMs for inverse modeling of GHG emissions by varying the backward simulation period in the range of 1 to 50 d, testing several methods for estimating a baseline, investigating the influence of biases in the a priori emissions and the baseline, and exploring the value of flask measurements for the inversion. We found the following:

- A baseline method that is purely based on the observations at the observation site itself, such as the REBS method, may lead to unreliable inversion results that are highly sensitive to the length of the LPDM backward simulation and can lead to unrealistic a posteriori global total emissions. For instance, for the year 2012, inversions with the REBS method produce a posteriori global total SF_6 emissions ranging between 9.8 and 3.2 $Gg\,yr^{-1}$ for backward simulation periods between 1 and 50 d, compared to a well-known reference value of around 8.0 $Gg\,yr^{-1}$. Optimizing the baseline shows little effect for simulation periods between 1 and 20 d but could halve the bias in the 50 d simulation case. Although the improvements of the baseline optimization increase with growing backward simulation period, the simultaneously growing bias cannot be compensated for.

- A baseline method that is based on the observations at the site itself but corrects for emissions occurring during the LPDM backward simulation period leads to smaller sensitivity to the backward calculation time but may still lead to substantially biased emissions irrespective of the backward simulation period. For instance, inversions with Stohl's method overestimate the well-known 2012 SF_6 global total emissions by 2.2–3.6 $Gg\,yr^{-1}$ (28 %–45 %). Optimizing the baseline, however, shows great improvements, especially for longer simulation periods.

- A global-distribution-based (GDB) approach, where the LPDM backward simulation is nested into a global mixing ratio field, leads to a posteriori emissions that are less sensitive to LPDM backward calculation lengths and stay close to the global total emission value. In contrast to station-specific baselines, the GDB method allows for the inclusion of low-frequency measurements (e.g., flask samples) or data from mobile platforms into the inversion.

- Statistical comparisons of a priori modeled versus observed mixing ratios suggest that longer LPDM backward simulations outperform shorter simulations. In particular, extending the trajectory length from 5–10 to 50 d can reduce the mean squared error and increase the correlation.

- Inverse modeling is highly sensitive to biases in the a priori emissions as well as biases in the baseline. We could show that this sensitivity can decrease with the length of the backward simulation period, and we find that longer backward simulation periods can help to correct biased global emission fields. In the presented case, it is not possible to correct strongly biased global a priori emissions with backward simulation periods of 1–10 d, while they are captured quite accurately with 50 d backward simulations.

- The additional use of flask measurements has the potential to improve the observational constraint on SF_6 emissions, especially close to the measurement sites. However, existing flask sampling sites are often not well located for inversion purposes. Similar to Weiss et al. (2021), we suggest that placing a few additional flask

sampling sites downwind of potential emission regions in currently undersampled parts of the world (in particular, tropical South America, tropical Africa, India, Australia, and the Maritime Continent) would have disproportionately large value in improving regional and global a posteriori emission fields.

Following these results, we advise against the use of baseline methods that are purely based on the observations of individual sites. At least great care needs to be taken that problems such as those demonstrated in this paper do not occur. In order to reduce biases, the optimization of the baseline as part of the inversion might be necessary but would likely not be sufficient to avoid biases completely. We recommend also employing longer LPDM backward simulation periods, beyond 5–10 d, as this can lead to improvements in overall model performance, can produce more robust global emission estimates, and might help to constrain emissions, at least at a very coarse resolution, in regions poorly covered by the monitoring network. When consistency between regional and global emission estimates is important, even longer backward simulation periods than 50 d may be useful. Finally, we suggest taking additional flask measurements at continental sites in the tropics and the Southern Hemisphere as they would greatly enhance inversion-derived global emission fields.

Appendix A

Table A1. Surface flask measurement sites.

Site ID	Station	Latitude	Longitude	Altitude[a]
ALT	Alert, Canada	82.5° N	62.5° W	190
ASC	Ascension Island, UK	8.0° S	14.4° W	90
ASK	Assekrem, Algeria	23.3° N	5.6° E	2715
AZR	Serreta (Terceira), Portugal	38.8° N	27.4° W	24
BAL	Baltic Sea, Poland	55.4° N	17.2° E	28
BHD	Baring Head, New Zealand	41.4° S	174.9° E	90
BKT	Bukit Kototabang, Indonesia	0.2° S	100.3° E	875
BMW	Tudor Hill (Bermuda), UK	32.3° N	64.9° W	60
BSC	Constanta (Black Sea), Romania	44.2° N	28.7° E	5
CBA	Cold Bay (AK), USA	55.2° N	162.7° W	57
CHR	Christmas Island, Kiribati	1.7° N	157.2° W	5
CPT	Cape Point, South Africa	34.4° S	18.5° E	260
CRZ	Crozet, France	46.4° S	51.8° E	202
DRP	Drake Passage, USA	59.0° S	63.7° W	10
DSI	Dongsha Island, Taiwan	20.7° N	116.7° E	8
EIC	Easter Island, Chile	27.2° S	109.4° W	69
GMI	Guam (Mariana Island), USA	13.4° N	144.7° E	5
HBA	Halley, UK	75.6° S	26.2° W	35
HFM	Harvard Forest (MA), USA	42.5° N	72.2° W	1000
HPB	Hohenpeissenberg, Germany	47.8° N	11.0° E	941
HSU	Humboldt State University, USA	41.0° N	124.7° W	8
HUN	Hegyhatsal, Hungary	47.0° N	16.6° E	344
ICE	Storhofdi, Iceland	63.4° N	20.3° W	127
KEY	Key Biscane (FL), USA	25.7° N	80.2° W	6
KUM	Cape Kumukahi (HI), USA	19.5° N	154.8° W	8
LEF	Park Falls (WI), USA	45.9° N	90.3° W	868
LLN	Lulin, Taiwan, Province of China	23.5° N	120.9° E	2867
LMP	Lampedusa, Italy	35.5° N	12.6° E	50
MEX	Mex High Altitude Global Climate Observation Center, Mexico	19.0° N	97.3° W	4469
MID	Sand Island, USA	28.2° N	177.4° W	16
MKN	Mt. Kenya, Kenya	0.1° S	37.3° E	3649
NAT	Natal, Brazil	5.5° S	35.3° W	20
NMB	Gobabeb, Namibia	23.6° S	15.0° E	461
OXK	Ochsenkopf, Germany	50.0° N	11.8° E	1172
PAL	Pallas, Finland	68.0° N	24.1° E	570
PSA	Palmer Station, USA	64.9° S	64.0° W	15
PTA	Point Arena (CA), USA	39.0° N	123.7° W	22
SGP	Southern Great Plains E13 (OK), USA	36.6° N	97.5° W	374
SHM	Shemya Island, USA	52.7° N	174.1° E	28
TIK	Tiksi, Russian Federation	71.6° N	128.9° E	29
USH	Ushuaia, Argentina	54.8° S	68.3° W	32
UTA	Wendover (UT), USA	39.9° N	113.7° W	1332
UUM	Ulaan Uul, Mongolia	44.5° N	111.1° E	1012
WIS	Sede Boker, Israel	30.9° N	34.8° E	482

[a] The altitude specifies the sampling height in meters above sea level.

Table A2. Aircraft flask measurement programs.

Site ID	Aircraft programs	Latitude	Longitude	Altitude[a]
BNE	Beaver Crossing, Nebraska, USA	40.8° N	97.2° W	616–7855
CAR	Briggsdale, Colorado, USA	40.7° N	104.3° W	1795–8469
CMA	Cape May, New Jersey, USA	38.9° N	74.3° W	280–8010
DND	Dahlen, North Dakota, USA	47.5° N	99.1° W	587–8023
ESP	Estevan Point, British Columbia, Canada	49.4° N	126.4° W	246–5740
ETL	East Trout Lake, Saskatchewan, Canada	54.3° N	104.9° W	811–7823
HIL	Homer, Illinois, USA	40.0° N	87.9° W	555–8051
LEF	Park Falls, Wisconsin, USA	46.0° N	90.2° W	583–4018
NHA	Worcester, Massachusetts, USA	42.9° N	70.5° W	245–8069
PFA	Poker Flat, Alaska, USA	64.8° N	148.2° W	222–7444
RTA	Rarotonga, Cook Islands	21.2° S	159.8° W	15–6483
SCA	Charleston, South Carolina, USA	32.9° N	79.5° W	218–8070
SGP	Southern Great Plains, Oklahoma, USA	36.6° N	97.5° W	437–5716
TGC	Sinton, Texas, USA	27.7° N	96.7° W	250–8074
THD	Trinidad Head, California, USA	41.1° N	124.2° W	231–8034
WBI	West Branch, Iowa, USA	41.7° N	91.3° W	591–8204

[a] The altitude specifies the range of sampling heights in meters above sea level.

Table A3. Setting parameters of the REBS method. For more information, see Ruckstuhl et al. (2012).

Setting parameters	Description
$b = 2.5$	tuning factor which governs the weight of outliers in the baseline
span $= \frac{1}{6}$	the ratio of observation points used to compute one baseline value (the goal is a temporal window of 2 months), which regulates the amount of baseline smoothing
maxit $= c(10, 10)$	maximum number of iterations

Table A4. Nudging kernel settings for surface and aircraft measurement sites. The kernels are set to have an equal spatial length (in m) in the x and the y direction. For surface measurement sites in the Northern Hemisphere, an upper limit for h_y was set to 25°; σ_{obs} defines the standard deviation of measurements over the simulation period at each nudging location; σ_{max} describes the maximum value of σ_{obs} from all surface observation stations. For aircraft measurement sites, the kernel size depends on the height level above ground H. For additional information on the parameters, see Groot Zwaaftink et al. (2018).

Surface measurement sites				
Hemisphere	Spatial kernel width h_y [°]	Kernel height h_z [m]	Temporal kernel length h_t [s]	Kernel relaxation time τ [s]
Northern Hemisphere	$h_y = \frac{\sigma_{\text{max}}}{\sigma_{\text{obs}}} \cdot 2$	$h_z = 300$	$h_t = 86\,400 \cdot \frac{\sigma_{\text{max}}}{\sigma_{\text{obs}}}$	$\tau = 3600$
Southern Hemisphere	$h_y = 25$	$hz = 500$	$h_t = 86\,400 \cdot \frac{\sigma_{\text{max}}}{\sigma_{\text{obs}}}$	$\tau = 3600$
Aircraft measurement sites				
Height H [km above ground]	Spatial kernel width h_y [°]	Kernel height h_z [m]	Temporal kernel length h_t [s]	Kernel relaxation time τ [s]
$H \leqslant 0.5$	$h_y = 10$	$h_z = 100$	$h_t = 86\,400 \cdot \frac{h_y}{1°}$	$\tau = 3600$
$0.5 < H \leqslant 1$	$h_y = 20$	$h_z = 250$	$h_t = 86\,400 \cdot \frac{h_y}{1°}$	$\tau = 3600$
$1 < H \leqslant 2$	$h_y = 30$	$h_z = 500$	$h_t = 86\,400 \cdot \frac{h_y}{1°}$	$\tau = 3600$
$2 < H \leqslant 3$	$h_y = 40$	$h_z = 500$	$h_t = 86\,400 \cdot \frac{h_y}{1°}$	$\tau = 3600$
$3 < H \leqslant 4$	$h_y = 50$	$h_z = 500$	$h_t = 86\,400 \cdot \frac{h_y}{1°}$	$\tau = 3600$
$4 < H \leqslant 5$	$h_y = 60$	$h_z = 500$	$h_t = 86\,400 \cdot \frac{h_y}{1°}$	$\tau = 3600$
$5 < H \leqslant 6$	$h_y = 70$	$h_z = 1000$	$h_t = 86\,400 \cdot \frac{h_y}{1°}$	$\tau = 3600$
$6 < H \leqslant 7$	$h_y = 80$	$h_z = 1000$	$h_t = 86\,400 \cdot \frac{h_y}{1°}$	$\tau = 3600$
$7 < H \leqslant 8$	$h_y = 90$	$h_z = 1000$	$h_t = 86\,400 \cdot \frac{h_y}{1°}$	$\tau = 3600$
$8 < H \leqslant 9$	$h_y = 100$	$h_z = 1000$	$h_t = 86\,400 \cdot \frac{h_y}{1°}$	$\tau = 3600$

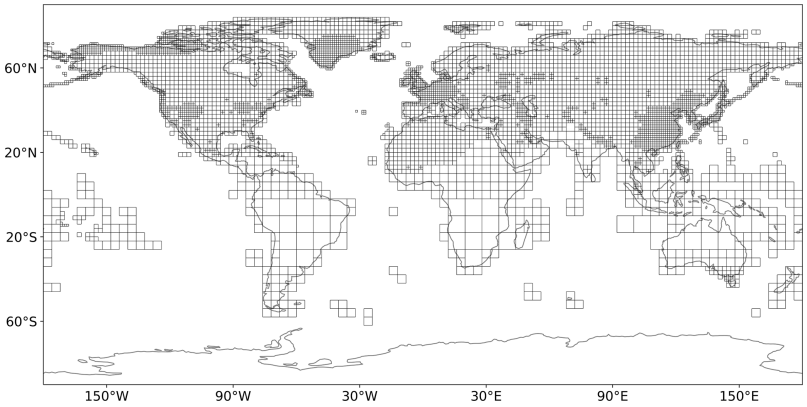

Figure A1. Variable-resolution grid on which emissions are optimized by the inversion.

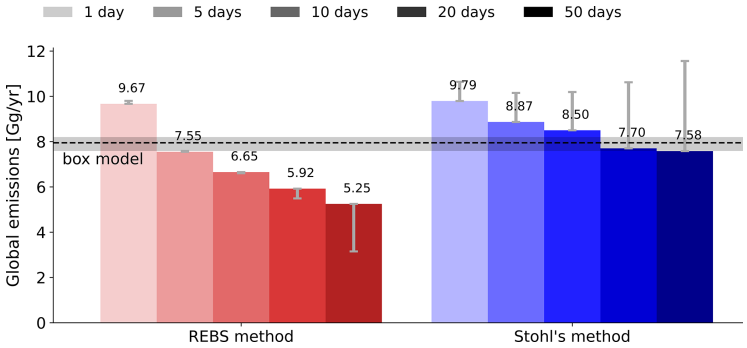

Figure A2. Calculated SF_6 global emissions when baseline concentrations are optimized as part of the inversion. Grey bars represent the improvements obtained by the baseline optimization. Results are shown for the REBS method and Stohl's method and for all five applied simulation periods between 1 and 50 d. The horizontal dashed line represents the reference value of the AGAGE 12-box model with shaded error bands.

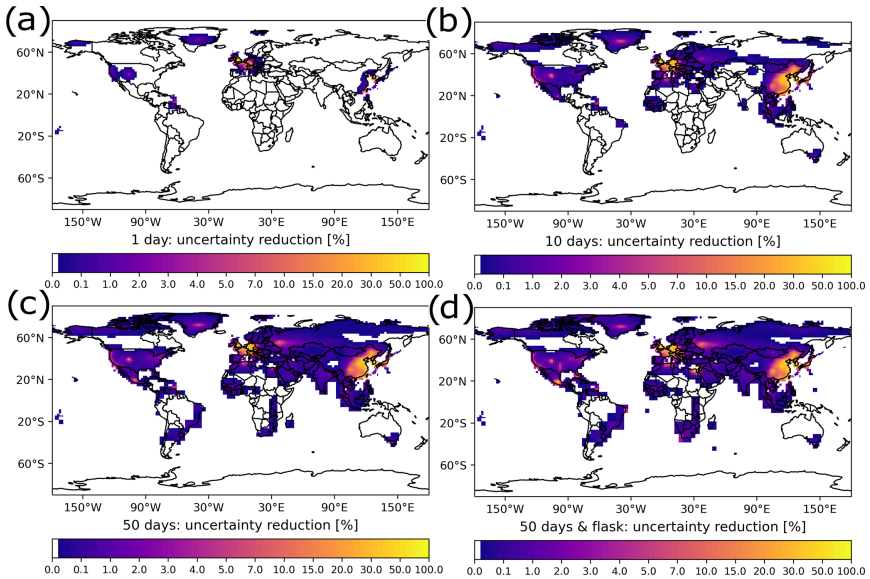

Figure A3. Relative uncertainty reductions $(1-u_{\mathrm{post}}/u_{\mathrm{pri}})$ calculated with the inversion by using the GDB method and a backward simulation period for **(a)** 1, **(b)** 10, and **(c)** 50 d and **(d)** for the 50 d case in which flask measurements were also included.

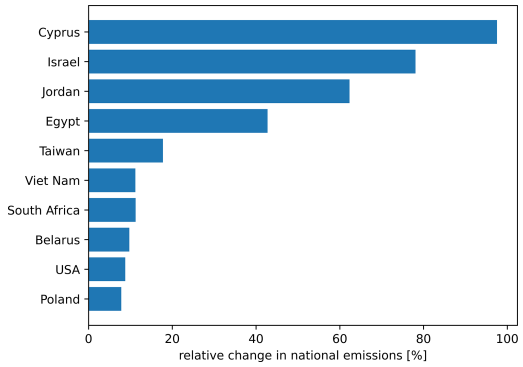

Figure A4. Relative change in national a posteriori emissions of selected countries, when flask measurements are used in addition to continuous measurements in the case of 50 d simulations.

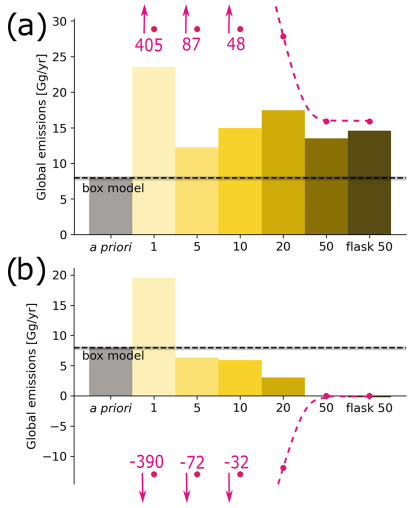

Figure A5. Global SF_6 emissions using the GDB method shown for two sensitivity tests, where a uniform bias of **(a)** −0.05 and **(b)** +0.05 ppt is added to every grid cell of the global mixing ratio fields. Results are shown for backward simulation periods between 1 and 50 d, and for a 50 d backward simulation case, where additionally to continuous measurements also flask measurements were included in the inversion. The dashed pink lines represent the expected relationship between the baseline bias and a resulting emission bias if a global box model was used and the bias attributed solely to emissions in different periods. For these two sensitivity tests, a priori uncertainties were set to 500 %.

Code and data availability. The source codes of FLEXPART 10.4 and FLEXINVERT+ used (with small modifications to the original version freely available at https://flexinvert.nilu.no/downloads/flexinvertplus.tar.gz; Thompson, 2022; downloaded in July 2020; described in detail by Thompson and Stohl, 2014) are provided at https://doi.org/10.25365/phaidra.339 (Vojta, 2022), together with input, setting, and output data. The source code of FLEXPART 8-CTM-1.1 together with a user's guide can be freely downloaded at https://doi.org/10.5281/zenodo.1249190 (Henne et al., 2018). The source code of FLEXPART 10.4 is also freely available on the FLEXPART website at https://www.flexpart.eu/downloads/66 (FLEXPART developer team, 2022) (described in detail by Pisso et al., 2019). Atmospheric measurements of SF_6 mixing ratios used in this study are freely available from the following sources: AGAGE data – https://agage2.eas.gatech.edu/data_archive/agage/gc-ms-medusa/complete/ (all stations, year 2011 and 2012; Advanced Global Atmospheric Gases Experiment, 2022), NOAA ESRL data – https://gml.noaa.gov/dv/data/index.php?parameter_name=Sulfur%2BHexafluoride&type=Insitu&frequency=Hourly%2BAverages (all stations, hourly data; NOAA ESRL, 2022), NOAA Carbon Cycle Group ObsPack data – https://doi.org/10.25925/20180817 (NOAA Carbon Cycle Group ObsPack Team, 2018), World Data Centre for Greenhouse Gases – https://gaw.kishou.go.jp/search/file/0077-6020-1004-01-01-9999 (World Meteorological Organization, 2022a) (https://gaw.kishou.go.jp/search/file/0071-6031-1004-01-01-9999, World Meteorological Organization, 2022b; https://gaw.kishou.go.jp/search/file/0003-1002-1004-01-01-9999, World Meteorological Organization, 2022c; https://gaw.kishou.go.jp/search/file/0053-2008-1004-01-01-9999, World Meteorological Organization, 2022d; https://gaw.kishou.go.jp/search/file/0002-4020-1004-01-02-3005, World Meteorological Organization, 2022e; year 2011 and 2012). All the listed websites were last accessed on 27 April 2022.

Supplement. The supplement related to this article is available online at: https://doi.org/10.5194/gmd-15-8295-2022-supplement.

Author contributions. MV and AS designed the study with contributions from RLT. MV performed the FLEXPART, FLEXPART CTM, and FLEXINVERT+ simulations. RLT helped with the FLEXINVERT+ setup and simulation issues. MV made the figures with help from AP. MV wrote the text with input from AS, AP, and RLT.

Competing interests. The contact author has declared that none of the authors has any competing interests.

Disclaimer. Publisher's note: Copernicus Publications remains neutral with regard to jurisdictional claims in published maps and institutional affiliations.

Acknowledgements. We thank the whole AGAGE team for providing measurement data, including Jens Mühle (Scripps Institution of Oceanography); Paul Krummel, Paul Fraser, and Paul Steele (CSIRO Oceans and Atmosphere); Ray Wang (Georgia Institute of Technology); Simon O'Doherty and Dickon Young (University of Bristol); Martin Vollmer and Stefan Reimann (EMPA: Swiss Federal Laboratories for Materials Science and Technology); and Chris René Lunder and Ove Hermansen (NILU: Norwegian Institute for Air Research). AGAGE operations at Mace Head, Trinidad Head, Cape Matatula, Ragged Point, and Cape Grim are supported by NASA (USA) grants to MIT (NAG5-12669, NNX07AE89G, NNX11AF17G, NNX16AC98G) and SIO (NNX07AE87G, NNX07AF09G, NNX11AF15G, NNX11AF16G, NNX16AC96G, NNX16AC97G) and also by the Department for Business, Energy & Industrial Strategy (BEIS, UK), contract no. 1537/06/2018, to the University of Bristol for Mace Head, and NOAA (USA), contract no. 1305M319CNRMJ0028, to the University of Bristol for Ragged Point. Further, AGAGE operations are supported by CSIRO and BoM (Australia), FOEN grants to Empa (Switzerland), NILU (Norway), SNU (S. Korea), CMA (China), NIES (Japan), and Urbino University (Italy). For Jungfraujoch, funding is acknowledged for the project HALCLIM/CLIMGAS-CH by the Swiss Federal Office for the Environment (FOEN) and for ICOS (Integrated Carbon Observation System) by the Swiss

National Science Foundation. In addition, measurements are supported by the International Foundation High Altitude Research Stations Jungfraujoch and Gornergrat (HFSJG). The Commonwealth Scientific and Industrial Research Organisation (CSIRO; Australia) and Bureau of Meteorology (Australia) are thanked for their ongoing long-term support and funding of the Cape Grim station and the Cape Grim science program. We also thank the NOAA Global Monitoring Laboratory for providing access to their data, including Geoff Dutton, Jim Elkins, Bradley Hall, Colm Sweeney, Ed Dlugokencky, Arlyn Andrews, and David Nance and key partners, Lin Huang (EC), Kenneth James Davis (PSU), and Sébastien Biraud (LBNL-ARM). We further acknowledge the following people and institutions for sharing their observation data: Takuya Saito (National Institute for Environmental Studies, Japan); Sunyoung Park and Mi-Kyung Park (Kyungpook National University – operations of the Gosan station on Jeju Island, South Korea, were supported by the National Research Foundation of Korea grant, funded by the MSIT of South Korea, grant no. 2020R1A2C3003774); Emilio Cuevas (State Meteorological Agency, Spain); and Daniel Say (University of Bristol). We also thank Christine Groot Zwaaftink, Sabine Eckhardt (NILU), and Stephan Henne (EMPA) for their provision and support of the FLEXPART CTM model. Further acknowledgement is made for the use of ECMWF's computing and archive facilities provided through a special project (spatvojt) in this research. We further thank Marina Dütsch, Lucie Bakels, Silvia Bucci, Katharina Baier, Daria Tatsii, and Perta Seibert for their support. Finally, we want to thank Andrea Stenke for editing our manuscript and the two anonymous reviewers for their constructive comments, which significantly improved our manuscript.

Review statement. This paper was edited by Andrea Stenke and reviewed by two anonymous referees.

References

Advanced Global Atmospheric Gases Experiment (AGAGE): Medusa GC-MS SF6 time series, AGAGE [data set], https://agage2.eas.gatech.edu/data_archive/agage/gc-ms-medusa/complete/, all stations, year 2011 and 2012, last access: 27 April 2022.

An, X., Henne, S., Yao, B., Vollmer, M. K., Zhou, L., and Li, Y.: Estimating emissions of HCFC-22 and CFC-11 in China by atmospheric observations and inverse modeling, Sci. China Chem., 55, 2233–2241, https://doi.org/10.1007/s11426-012-4624-8, 2012.

Berchet, A., Sollum, E., Thompson, R. L., Pison, I., Thanwerdas, J., Broquet, G., Chevallier, F., Aalto, T., Berchet, A., Bergamaschi, P., Brunner, D., Engelen, R., Fortems-Cheiney, A., Gerbig, C., Groot Zwaaftink, C. D., Haussaire, J.-M., Henne, S., Houweling, S., Karstens, U., Kutsch, W. L., Luijkx, I. T., Monteil, G., Palmer, P. I., van Peet, J. C. A., Peters, W., Peylin, P., Potier, E., Rödenbeck, C., Saunois, M., Scholze, M., Tsuruta, A., and Zhao, Y.: The Community Inversion Framework v1.0: a unified system for atmospheric inversion studies, Geosci. Model Dev., 14, 5331–5354, https://doi.org/10.5194/gmd-14-5331-2021, 2021.

Brunner, D., Arnold, T., Henne, S., Manning, A., Thompson, R. L., Maione, M., O'Doherty, S., and Reimann, S.: Comparison of four inverse modelling systems applied to the estimation of HFC-125, HFC-134a, and SF_6 emissions over Europe, Atmos. Chem. Phys., 17, 10651–10674, https://doi.org/10.5194/acp-17-10651-2017, 2017.

CIESIN: Center for International Earth Science Information Network, Columbia University, Gridded Population of the World, Version 4 (GPWv4): Population Density, Revision 11, NASA Socioeconomic Data and Applications Center (SEDAC), Palisades, NY, https://doi.org/10.7927/H49C6VHW (last access: 27 April 2022), 2018.

Dlugokencky, E., Crotwell, A., Mund, J., Crotwell, M., and Thoning, K.: Atmospheric Sulfur Hexafluoride Dry Air Mole Fractions from the NOAA GML Carbon Cycle Cooperative Global Air Sampling Network, 1997–2019, Version: 2020-07, https://doi.org/10.15138/p646-pa37, 2020.

Dutton, G., Elkins, J., Hall, B., and NOAA ESRL: Earth System Research Laboratory Halocarbons and Other Atmospheric Trace Gases Chromatograph for Atmospheric Trace Species (CATS) Measurements, Version 1, NOAA National Centers for Environmental Information, https://doi.org/10.7289/V5X0659V, 2017.

Fang, X., Thompson, R. L., Saito, T., Yokouchi, Y., Kim, J., Li, S., Kim, K. R., Park, S., Graziosi, F., and Stohl, A.: Sulfur hexafluoride (SF_6) emissions in East Asia determined by inverse modeling, Atmos. Chem. Phys., 14, 4779–4791, https://doi.org/10.5194/acp-14-4779-2014, 2014.

Fang, X., Stohl, A., Yokouchi, Y., Kim, J., Li, S., Saito, T., Park, S., and Hu, J.: Multiannual Top-Down Estimate of HFC-23 Emissions in East Asia, Environ. Sci. Technol., 49, 4345–4353, https://doi.org/10.1021/es505669j, 2015.

Fang, X., Yao, B., Vollmer, M. K., Reimann, S., Liu, L., Chen, L., Prinn, R. G., and Hu, J.: Changes in HCFC Emissions in China During 2011–2017, Geophys. Res. Lett., 46, 10034–10042, https://doi.org/10.1029/2019GL083169, 2019.

FLEXPART developer team: FLEXPART v10.4, FLEXPART [code], https://www.flexpart.eu/downloads/66, last access: 27 April 2022.

Ganesan, A. L., Rigby, M., Zammit-Mangion, A., Manning, A. J., Prinn, R. G., Fraser, P. J., Harth, C. M., Kim, K.-R., Krummel, P. B., Li, S., Mühle, J., O'Doherty, S. J., Park, S., Salameh, P. K., Steele, L. P., and Weiss, R. F.: Characterization of uncertainties in atmospheric trace gas inversions using hierarchical Bayesian methods, Atmos. Chem. Phys., 14, 3855–3864, https://doi.org/10.5194/acp-14-3855-2014, 2014.

Ganshin, A., Oda, T., Saito, M., Maksyutov, S., Valsala, V., Andres, R. J., Fisher, R. E., Lowry, D., Lukyanov, A., Matsueda, H., Nisbet, E. G., Rigby, M., Sawa, Y., Toumi, R., Tsuboi, K., Varlagin, A., and Zhuravlev, R.: A global coupled Eulerian-Lagrangian model and 1×1 km CO_2 surface flux dataset for high-resolution atmospheric CO_2 transport simulations, Geosci. Model Dev., 5, 231–243, https://doi.org/10.5194/gmd-5-231-2012, 2012.

Groot Zwaaftink, C. D., Henne, S., Thompson, R. L., Dlugokencky, E. J., Machida, T., Paris, J.-D., Sasakawa, M., Segers, A., Sweeney, C., and Stohl, A.: Three-dimensional methane distribution simulated with FLEXPART 8-CTM-1.1 constrained with observation data, Geosci. Model Dev., 11, 4469–4487, https://doi.org/10.5194/gmd-11-4469-2018, 2018.

Guillevic, M., Vollmer, M. K., Wyss, S. A., Leuenberger, D., Ackermann, A., Pascale, C., Niederhauser, B., and Reimann, S.: Dynamic–gravimetric preparation of metro-

logically traceable primary calibration standards for halogenated greenhouse gases, Atmos. Meas. Tech., 11, 3351–3372, https://doi.org/10.5194/amt-11-3351-2018, 2018.

Henne, S., Brunner, D., Oney, B., Leuenberger, M., Eugster, W., Bamberger, I., Meinhardt, F., Steinbacher, M., and Emmenegger, L.: Validation of the Swiss methane emission inventory by atmospheric observations and inverse modelling, Atmos. Chem. Phys., 16, 3683–3710, https://doi.org/10.5194/acp-16-3683-2016, 2016.

Henne, S., Brunner, D., Groot Zwaaftink, C., and Stohl, A.: FLEXPART 8-CTM-1.1: Atmospheric Lagrangian Particle Dispersion Model for global tracer transport (8-CTM-1.1), Zenodo [code], https://doi.org/10.5281/zenodo.1249190, 2018.

Hersbach, H., de Rosnay, P., Bell, B., Schepers, D., Simmons, A., Soci, C., Abdalla, S., Alonso-Balmaseda, M., Balsamo, G., Bechtold, P., Berrisford, P., Bidlot, J.-R., de Boisséson, E., Bonavita, M., Browne, P., Buizza, R., Dahlgren, P., Dee, D., Dragani, R., Diamantakis, M., Flemming, J., Forbes, R., Geer, A., Haiden, T., Hólm, E., Haimberger, L., Hogan, R., Horányi, A., Janiskova, M., Laloyaux, P., Lopez, P., Munoz-Sabater, J., Peubey, C., Radu, R., Richardson, D., Thépaut, J.-N., Vitart, F., Yang, X., Zsótér, E., and Zuo, H.: Operational global reanalysis: progress, future directions and synergies with NWP, ERA Report, https://doi.org/10.21957/tkic6g3wm, 2018.

Hu, L., Andrews, A. E., Thoning, K. W., Sweeney, C., Miller, J. B., Michalak, A. M., Dlugokencky, E., Tans, P. P., Shiga, Y. P., Mountain, M., Nehrkorn, T., Montzka, S. A., McKain, K., Kofler, J., Trudeau, M., Michel, S. E., Biraud, S. C., Fischer, M. L., Worthy, D. E. J., Vaughn, B. H., White, J. W. C., Yadav, V., Basu, S., and van der Velde, I. R.: Enhanced North American carbon uptake associated with El Niño, Science Advances, 5, eaaw0076, https://doi.org/10.1126/sciadv.aaw0076, 2019.

IPCC: Summary for Policymakers, in: Global Warming of 1.5 °C. An IPCC Special Report on the impacts of global warming of 1.5 °C above pre-industrial levels and related global greenhouse gas emissions pathways, in the context of strengthening the global response to the threat of climate change, sustianable development, and efforts to eradicate poverty, edited by: Masson-Delmotte, V., Zhai, P., Pörtner, H. O., Roberts, D., Skea, J., Shukla, P. R., Pirani, A., Moufouma-Okia, W., Péan, C., Pidcock, R., Connors, S., Matthews, J. B. R., Chen, Y., Zhou, X., Gomis, M. I., Lonnoy, E., Maycock, T., Tignor, M., and Waterfield, T., World Meteorological Organization, Geneva, Switzerland, 32, https://ipcc.ch/report/sr15 (last access: 27 April 2022), 2018.

Keller, C. A., Hill, M., Vollmer, M. K., Henne, S., Brunner, D., Reimann, S., O'Doherty, S., Arduini, J., Maione, M., Ferenczi, Z., Haszpra, L., Manning, A. J., and Peter, T.: European emissions of halogenated greenhouse gases inferred from atmospheric measurements, Environ. Sci. Technol., 46, 217–225, https://doi.org/10.1021/es202453j, 2012.

Koyama, Y., Maksyutov, S., Mukai, H., Thoning, K., and Tans, P.: Simulation of variability in atmospheric carbon dioxide using a global coupled Eulerian – Lagrangian transport model, Geosci. Model Dev., 4, 317–324, https://doi.org/10.5194/gmd-4-317-2011, 2011.

Leip, A., Skiba, U., Vermeulen, A., and Thompson, R. L.: A complete rethink is needed on how greenhouse gas emissions are quantified for national reporting, Atmos. Environ., 174, 237–240, https://doi.org/10.1016/j.atmosenv.2017.12.006, 2017.

Lunt, M. F., Rigby, M., Ganesan, A. L., and Manning, A. J.: Estimation of trace gas fluxes with objectively determined basis functions using reversible-jump Markov chain Monte Carlo, Geosci. Model Dev., 9, 3213–3229, https://doi.org/10.5194/gmd-9-3213-2016, 2016.

Maione, M., Graziosi, F., Arduini, J., Furlani, F., Giostra, U., Blake, D. R., Bonasoni, P., Fang, X., Montzka, S. A., O'Doherty, S. J., Reimann, S., Stohl, A., and Vollmer, M. K.: Estimates of European emissions of methyl chloroform using a Bayesian inversion method, Atmos. Chem. Phys., 14, 9755–9770, https://doi.org/10.5194/acp-14-9755-2014, 2014.

Manning, A. J., Redington, A. L., Say, D., O'Doherty, S., Young, D., Simmonds, P. G., Vollmer, M. K., Mühle, J., Arduini, J., Spain, G., Wisher, A., Maione, M., Schuck, T. J., Stanley, K., Reimann, S., Engel, A., Krummel, P. B., Fraser, P. J., Harth, C. M., Salameh, P. K., Weiss, R. F., Gluckman, R., Brown, P. N., Watterson, J. D., and Arnold, T.: Evidence of a recent decline in UK emissions of hydrofluorocarbons determined by the InTEM inverse model and atmospheric measurements, Atmos. Chem. Phys., 21, 12739–12755, https://doi.org/10.5194/acp-21-12739-2021, 2021.

Miller, B. R., Weiss, R. F., Salameh, P. K., Tanhua, T., Greally, B. R., Mühle, J., and Simmonds, P. G.: Medusa: A Sample Preconcentration and GC/MS Detector System for in Situ Measurements of Atmospheric Trace Halocarbons, Hydrocarbons, and Sulfur Compounds, Anal. Chem., 80, 1536–1545, https://doi.org/10.1021/ac702084k, 2008.

Monteil, G. and Scholze, M.: Regional CO_2 inversions with LUMIA, the Lund University Modular Inversion Algorithm, v1.0, Geosci. Model Dev., 14, 3383–3406, https://doi.org/10.5194/gmd-14-3383-2021, 2021.

Myhre, G., Shindell, D., Bréon, F.-M., Collins, W., Fuglestvedt, J., Huang, J., Koch, D., Lamarque, J.-F., Lee, D., Mendoza, B., Nakajima, T., Robock, A., Stephens, G., Takemura, T., and Zhang, H.: Anthropogenic and natural radiative forcing, Cambridge University Press, Cambridge, UK, 659–740, https://doi.org/10.1017/CBO9781107415324.018, 2013.

NOAA Carbon Cycle Group ObsPack Team: Multi-laboratory compilation of atmospheric sulfure hexafluoride data for the period 1983–2017; obspack_sf6_1_v2.1.1_2018-08-17; NOAA Earth System Research Laboratory, Global Monitoring Division [data set], https://doi.org/10.25925/20180817, 2018.

NOAA, Earth System Research Laboratory (ESRL): NOAA Earth System Research Laboratoriy: Sulfur Hexafluoride (SF6) WMO Scale, https://gml.noaa.gov/ccl/sf6_scale.html (last access: 27 May 2022), 2014.

NOAA, Earth System Research Laboratory (ESRL): SF6 time series, NOAA, Earth System Research Laboratories [data set], https://gml.noaa.gov/dv/data/index.php?parameter_name=Sulfur%2BHexafluoride&type=Insitu&frequency=Hourly%2BAverages, all stations, hourly data, last access: 27 April 2022.

O'Doherty, S., Simmonds, P., Cunnold, D., Wang, H., Sturrock, G., Fraser, P., Ryall, D., Derwent, R., Weiss, R., Salameh, P., Miller, B. R., and Prinn, R. G.: In situ chloroform measurements at Advanced Global Atmospheric Gases Experiment atmospheric research stations from 1994 to 1998, J. Geophys. Res.-Atmos., 106, 20429–20444, https://doi.org/10.1029/2000JD900792, 2001.

Pisso, I., Sollum, E., Grythe, H., Kristiansen, N. I., Cassiani, M., Eckhardt, S., Arnold, D., Morton, D., Thompson, R. L., Groot Zwaaftink, C. D., Evangeliou, N., Sodemann, H., Haimberger, L., Henne, S., Brunner, D., Burkhart, J. F., Fouilloux, A., Brioude, J., Philipp, A., Seibert, P., and Stohl, A.: The Lagrangian particle dispersion model FLEXPART version 10.4, Geosci. Model Dev., 12, 4955–4997, https://doi.org/10.5194/gmd-12-4955-2019, 2019.

Prinn, R. G., Weiss, R. F., Fraser, P. J., Simmonds, P. G., Cunnold, D. M., Alyea, F. N., O'Doherty, S., Salameh, P., Miller, B. R., Huang, J., Wang, R. H. J., Hartley, D. E., Harth, C., Steele, L. P., Sturrock, G., Midgley, P. M., and McCulloch, A.: A history of chemically and radiatively important gases in air deduced from ALE/GAGE/AGAGE, J. Geophys. Res.-Atmos., 105, 17751–17792, https://doi.org/10.1029/2000JD900141, 2000.

Prinn, R. G., Weiss, R. F., Arduini, J., Arnold, T., DeWitt, H. L., Fraser, P. J., Ganesan, A. L., Gasore, J., Harth, C. M., Hermansen, O., Kim, J., Krummel, P. B., Li, S., Loh, Z. M., Lunder, C. R., Maione, M., Manning, A. J., Miller, B. R., Mitrevski, B., Mühle, J., O'Doherty, S., Park, S., Reimann, S., Rigby, M., Saito, T., Salameh, P. K., Schmidt, R., Simmonds, P. G., Steele, L. P., Vollmer, M. K., Wang, R. H., Yao, B., Yokouchi, Y., Young, D., and Zhou, L.: History of chemically and radiatively important atmospheric gases from the Advanced Global Atmospheric Gases Experiment (AGAGE), Earth Syst. Sci. Data, 10, 985–1018, https://doi.org/10.5194/essd-10-985-2018, 2018.

Ravishankara, A. R., Solomon, S., Turnipseed, A. A., and Warren, R. F.: Atmospheric lifetimes of long-lived halogenated species, Science, 259, 194–199, https://doi.org/10.1126/science.259.5092.194, 1993.

Rigby, M., Manning, A. J., and Prinn, R. G.: Inversion of long-lived trace gas emissions using combined Eulerian and Lagrangian chemical transport models, Atmos. Chem. Phys., 11, 9887–9898, https://doi.org/10.5194/acp-11-9887-2011, 2011.

Rigby, M., Prinn, R. G., O'Doherty, S., Montzka, S. A., McCulloch, A., Harth, C. M., Mühle, J., Salameh, P. K., Weiss, R. F., Young, D., Simmonds, P. G., Hall, B. D., Dutton, G. S., Nance, D., Mondeel, D. J., Elkins, J. W., Krummel, P. B., Steele, L. P., and Fraser, P. J.: Re-evaluation of the lifetimes of the major CFCs and CH_3CCl_3 using atmospheric trends, Atmos. Chem. Phys., 13, 2691–2702, https://doi.org/10.5194/acp-13-2691-2013, 2013.

Rödenbeck, C., Gerbig, C., Trusilova, K., and Heimann, M.: A two-step scheme for high-resolution regional atmospheric trace gas inversions based on independent models, Atmos. Chem. Phys., 9, 5331–5342, https://doi.org/10.5194/acp-9-5331-2009, 2009.

Ruckstuhl, A. F., Henne, S., Reimann, S., Steinbacher, M., Vollmer, M. K., O'Doherty, S., Buchmann, B., and Hueglin, C.: Robust extraction of baseline signal of atmospheric trace species using local regression, Atmos. Meas. Tech., 5, 2613–2624, https://doi.org/10.5194/amt-5-2613-2012, 2012.

Ryall, D. B., Derwent, R. G., Manning, A. J., Simmonds, P. G., and O'Doherty, S.: Estimating source regions of European emissions of trace gases from observations at Mace Head, Atmos. Environ., 35, 2507–2523, https://doi.org/10.1016/S1352-2310(00)00433-7, 2001.

Rypdal, K., Stordal, F., Fuglestvedt, J., and Berntsen, T.: Introducing top-down methods in assessing compliance with the Kyoto Protocol, Clim. Policy, 5, 393–405, https://doi.org/10.1080/14693062.2005.9685565, 2005.

Saito, T., Yokouchi, Y., Stohl, A., Taguchi, S., and Mukai, H.: Large Emissions of Perfluorocarbons in East Asia Deduced from Continuous Atmospheric Measurements, Environ. Sci. Technol., 44, 4089–4095, https://doi.org/10.1021/es1001488, 2010.

Schoenenberger, F., Henne, S., Hill, M., Vollmer, M. K., Kouvarakis, G., Mihalopoulos, N., O'Doherty, S., Maione, M., Emmenegger, L., Peter, T., and Reimann, S.: Abundance and sources of atmospheric halocarbons in the Eastern Mediterranean, Atmos. Chem. Phys., 18, 4069–4092, https://doi.org/10.5194/acp-18-4069-2018, 2018.

Seibert, P. and Frank, A.: Source-receptor matrix calculation with a Lagrangian particle dispersion model in backward mode, Atmos. Chem. Phys., 4, 51–63, https://doi.org/10.5194/acp-4-51-2004, 2004.

Simmonds, P. G., Rigby, M., Manning, A. J., Lunt, M. F., O'Doherty, S., McCulloch, A., Fraser, P. J., Henne, S., Vollmer, M. K., Mühle, J., Weiss, R. F., Salameh, P. K., Young, D., Reimann, S., Wenger, A., Arnold, T., Harth, C. M., Krummel, P. B., Steele, L. P., Dunse, B. L., Miller, B. R., Lunder, C. R., Hermansen, O., Schmidbauer, N., Saito, T., Yokouchi, Y., Park, S., Li, S., Yao, B., Zhou, L. X., Arduini, J., Maione, M., Wang, R. H. J., Ivy, D., and Prinn, R. G.: Global and regional emissions estimates of 1,1-difluoroethane (HFC-152a, CH_3CHF_2) from in situ and air archive observations, Atmos. Chem. Phys., 16, 365–382, https://doi.org/10.5194/acp-16-365-2016, 2016.

Simmonds, P. G., Rigby, M., McCulloch, A., Vollmer, M. K., Henne, S., Mühle, J., O'Doherty, S., Manning, A. J., Krummel, P. B., Fraser, P. J., Young, D., Weiss, R. F., Salameh, P. K., Harth, C. M., Reimann, S., Trudinger, C. M., Steele, L. P., Wang, R. H. J., Ivy, D. J., Prinn, R. G., Mitrevski, B., and Etheridge, D. M.: Recent increases in the atmospheric growth rate and emissions of HFC-23 (CHF_3) and the link to HCFC-22 ($CHClF_2$) production, Atmos. Chem. Phys., 18, 4153–4169, https://doi.org/10.5194/acp-18-4153-2018, 2018.

Simmonds, P. G., Rigby, M., Manning, A. J., Park, S., Stanley, K. M., McCulloch, A., Henne, S., Graziosi, F., Maione, M., Arduini, J., Reimann, S., Vollmer, M. K., Mühle, J., O'Doherty, S., Young, D., Krummel, P. B., Fraser, P. J., Weiss, R. F., Salameh, P. K., Harth, C. M., Park, M.-K., Park, H., Arnold, T., Rennick, C., Steele, L. P., Mitrevski, B., Wang, R. H. J., and Prinn, R. G.: The increasing atmospheric burden of the greenhouse gas sulfur hexafluoride (SF_6), Atmos. Chem. Phys., 20, 7271–7290, https://doi.org/10.5194/acp-20-7271-2020, 2020.

Stohl, A., Hittenberger, M., and Wotawa, G.: Validation of the lagrangian particle dispersion model FLEXPART against large-scale tracer experiment data, Atmos. Environ., 32, 4245–4264, https://doi.org/10.1016/S1352-2310(98)00184-8, 1998.

Stohl, A., Forster, C., Frank, A., Seibert, P., and Wotawa, G.: Technical note: The Lagrangian particle dispersion model FLEXPART version 6.2, Atmos. Chem. Phys., 5, 2461–2474, https://doi.org/10.5194/acp-5-2461-2005, 2005.

Stohl, A., Seibert, P., Arduini, J., Eckhardt, S., Fraser, P., Greally, B. R., Lunder, C., Maione, M., Mühle, J., O'Doherty, S., Prinn, R. G., Reimann, S., Saito, T., Schmidbauer, N., Simmonds, P. G., Vollmer, M. K., Weiss, R. F., and Yokouchi, Y.: An analytical inversion method for determining regional and global emissions of greenhouse gases: Sensitivity studies and application to halocarbons, Atmos. Chem. Phys., 9, 1597–1620, https://doi.org/10.5194/acp-9-1597-2009, 2009.

Stohl, A., Kim, J., Li, S., O'Doherty, S., Mühle, J., Salameh, P. K., Saito, T., Vollmer, M. K., Wan, D., Weiss, R. F., Yao, B., Yokouchi, Y., and Zhou, L. X.: Hydrochlorofluorocarbon and hydrofluorocarbon emissions in East Asia determined by inverse modeling, Atmos. Chem. Phys., 10, 3545–3560, https://doi.org/10.5194/acp-10-3545-2010, 2010.

Sweeney, C., Karion, A., Wolter, S., Newberger, T., Guenther, D., Higgs, J. A., Andrews, A. E., Lang, P. M., Neff, D., Dlugokencky, E., Miller, J. B., Montzka, S. A., Miller, B. R., Masarie, K. A., Biraud, S. C., Novelli, P. C., Crotwell, M., Crotwell, A. M., Thoning, K., and Tans, P. P.: Seasonal Climatology of CO_2 across North America from Aircraft Measurements in the NOAA/ESRL Global Greenhouse Gas Reference Network, J. Geophys. Res.-Atmos., 120, 5155–5190, https://doi.org/10.1002/2014JD022591, 2015.

Tarantola, A.: Inverse Problem Theory and Methods for Model Parameter Estimation, Society for Industrial and Applied Mathematics, 1–67, https://doi.org/10.1137/1.9780898717921, 2005.

Thacker, W. C.: Data assimilation with inequality constraints, Ocean Model., 16, 264–276, https://doi.org/10.1016/j.ocemod.2006.11.001, 2007.

Thompson, R. L.: FLEXINVERT+, NILU [code], https://flexinvert.nilu.no/downloads/flexinvertplus.tar.gz, last access: 27 April 2022.

Thompson, R. L. and Stohl, A.: FLEXINVERT: an atmospheric Bayesian inversion framework for determining surface fluxes of trace species using an optimized grid, Geosci. Model Dev., 7, 2223–2242, https://doi.org/10.5194/gmd-7-2223-2014, 2014.

Thompson, R. L., Stohl, A., Zhou, L. X., Dlugokencky, E., Fukuyama, Y., Tohjima, Y., Kim, S.-Y., Lee, H., Nisbet, E. G., Fisher, R. E., Lowry, D., Weiss, R. F., Prinn, R. G., O'Doherty, S., Young, D., and White, J. W. C.: Methane emissions in East Asia for 2000–2011 estimated using an atmospheric Bayesian inversion, J. Geophys. Res.-Atmos., 120, 4352–4369, https://doi.org/10.1002/2014JD022394, 2015.

Thompson, R. L., Sasakawa, M., Machida, T., Aalto, T., Worthy, D., Lavric, J. V., Lund Myhre, C., and Stohl, A.: Methane fluxes in the high northern latitudes for 2005–2013 estimated using a Bayesian atmospheric inversion, Atmos. Chem. Phys., 17, 3553–3572, https://doi.org/10.5194/acp-17-3553-2017, 2017.

Trusilova, K., Rödenbeck, C., Gerbig, C., and Heimann, M.: Technical Note: A new coupled system for global-to-regional downscaling of CO_2 concentration estimation, Atmos. Chem. Phys., 10, 3205–3213, https://doi.org/10.5194/acp-10-3205-2010, 2010.

UNFCCC: United Nations Framework Convention on Climate Change, https://di.unfccc.int/time_series, last access: 10 March 2021.

Villani, M. G., Bergamaschi, P., Krol, M., Meirink, J. F., and Dentener, F.: Inverse modeling of European CH_4 emissions: sensitivity to the observational network, Atmos. Chem. Phys., 10, 1249–1267, https://doi.org/10.5194/acp-10-1249-2010, 2010.

Vojta, M.: Supplementary for Vojta et al., 2022, GMD, Universität Wien [code], https://doi.org/10.25365/phaidra.339, 2022.

Vollmer, M. K., Zhou, L. X., Greally, B. R., Henne, S., Yao, B., Reimann, S., Stordal, F., Cunnold, D. M., Zhang, X. C., Maione, M., Zhang, F., Huang, J., and Simmonds, P. G.: Emissions of ozone-depleting halocarbons from China, Geophys. Res. Lett., 36, L15823, https://doi.org/10.1029/2009GL038659, 2009.

Vollmer, M. K., Mühle, J., Trudinger, C. M., Rigby, M., Montzka, S. A., Harth, C. M., Miller, B. R., Henne, S., Krummel, P. B., Hall, B. D., Young, D., Kim, J., Arduini, J., Wenger, A., Yao, B., Reimann, S., O'Doherty, S., Maione, M., Etheridge, D. M., Li, S., Verdonik, D. P., Park, S., Dutton, G., Steele, L. P., Lunder, C. R., Rhee, T. S., Hermansen, O., Schmidbauer, N., Wang, R. H. J., Hill, M., Salameh, P. K., Langenfelds, R. L., Zhou, L., Blunier, T., Schwander, J., Elkins, J. W., Butler, J. H., Simmonds, P. G., Weiss, R. F., Prinn, R. G., and Fraser, P. J.: Atmospheric histories and global emissions of halons H-1211 ($CBrClF_2$), H-1301 ($CBrF_3$), and H-2402 ($CBrF_2CBrF_2$), J. Geophys. Res.-Atmos., 121, 3663–3686, https://doi.org/10.1002/2015JD024488, 2016.

WDCGG: World Data Centre for Greenhouse Gases, https://gaw.kishou.go.jp/ (last access: 27 April 2022), 2018.

Weiss, R. F. and Prinn, R. G.: Quantifying greenhouse-gas emissions from atmospheric measurements: a critical reality check for climate legislation, Philos. T. Roy. Soc. A, 369, 1925–1942, https://doi.org/10.1098/rsta.2011.0006, 2011.

Weiss, R. F., Ravishankara, A. R., and Newman, P. A.: Huge gaps in detection networks plague emissions monitoring, Nature, 595, 491–493, https://doi.org/10.1038/d41586-021-01967-z, 2021.

World Bank: Electric power consumption, https://data.worldbank.org/indicator/EG.USE.ELEC.KH.PC (last access: 27 April 2022), 2021.

World Meteorological Organization (WMO): World Data Centre of Greenhouse Gases – SF6 time series, WMO [data set], https://gaw.kishou.go.jp/search/file/0077-6020-1004-01-01-9999, year 2011 and 2012, last access: 27 April 2022a.

World Meteorological Organization (WMO): World Data Centre of Greenhouse Gases – SF6 time series, WMO [data set], https://gaw.kishou.go.jp/search/file/0071-6031-1004-01-01-9999, year 2011 and 2012, last access: 27 April 2022b.

World Meteorological Organization (WMO): World Data Centre of Greenhouse Gases – SF6 time series, WMO [data set], https://gaw.kishou.go.jp/search/file/0003-1002-1004-01-01-9999, year 2011 and 2012, last access: 27 April 2022c.

World Meteorological Organization (WMO): World Data Centre of Greenhouse Gases – SF6 time series, WMO [data set], https://gaw.kishou.go.jp/search/file/0053-2008-1004-01-01-9999, year 2011 and 2012, last access: 27 April 2022d.

World Meteorological Organization (WMO): World Data Centre of Greenhouse Gases – SF6 time series, WMO [data set], https://gaw.kishou.go.jp/search/file/0002-4020-1004-01-02-3005, year 2011 and 2012, last access: 27 April 2022e.

Yokouchi, Y., Taguchi, S., Saito, T., Tohjima, Y., Tanimoto, H., and Mukai, H.: High frequency measurements of HFCs at a remote site in east Asia and their implications for Chinese emissions, Geophys. Res. Lett., 33, L21814, https://doi.org/10.1029/2006GL026403, 2006.

Zeng, J., Nakajima, H., Matsunaga, T., Mukai, H., Hiraki, K., and Yokota, Y.: Linking carbon dioxide variability at Hateruma station to East Asia emissions by Bayesian inversion, in: Lagrangian Modeling of the Atmosphere, Geophys. Monogr. Ser., 200, 163–172, https://doi.org/10.1029/2012GM001245, 2012.

Zhao, C., Andrews, A. E., Bianco, L., Eluszkiewicz, J., Hirsch, A., MacDonald, C., Nehrkorn, T., and Fischer, M. L.: Atmospheric Inverse Estimates of Methane Emissions from Central California, J. Geophys. Res.-Atmos., 114, D16302, https://doi.org/10.1029/2008JD011671, 2009.

Chapter 4

A global re-analysis of regionally resolved emissions and atmospheric mole fractions of SF6 for the period 2005–2021

Overview

This atmospheric inversion study determines the global distribution of SF_6 emissions, analyzed at both global and regional levels between 2005 and 2021. The study is characterized by a large observational dataset employed, including continuous surface station measurements, flask measurements, and data from aircraft and ship campaigns, while also multiple *a priori* emission fields are considered for the inversion process. In order to determine initial conditions, global SF_6 measurements are assimilated into modeled global three-dimensional mole fraction fields, creating an atmospheric re-analysis spanning from 2005 to 2021. National, regional, and global SF_6 emission trends are discussed on an annual level, while also the seasonal variation in emissions is investigated.

Own contributions

Conceptualization, investigation, methodology, modeling, formal analysis, visualization, writing. My contribution to this publication is estimated to be about 90%.

Publication details

Vojta, M., Plach, A., Annadate, S., Park, S., Lee, G., Purohit, P., Lindl, F., Lan, X., Mühle, J., Thompson, R. L., and Stohl, A.: A global re-analysis of regionally resolved emissions and atmospheric mole fractions of SF6 for the period 2005–2021, EGUsphere [preprint], https://doi.org/10.5194/egusphere-2024-811, 2024.

https://doi.org/10.5194/egusphere-2024-811
Preprint. Discussion started: 11 April 2024

A global re-analysis of regionally resolved emissions and atmospheric mole fractions of SF_6 for the period 2005-2021

Martin Vojta[1], Andreas Plach[1], Saurabh Annadate[2,3], Sunyong Park[4], Gawon Lee[4], Pallav Purohit[6], Florian Lindl[6], Xin Lan[8], Jens Mühle[7], Rona L. Thompson[5], and Andreas Stohl[1]

[1]Department of Meteorology and Geophysics, University of Vienna, Vienna, Austria
[2]Department of Pure and Applied Sciences, University of Urbino "Carlo Bo", Urbino, Italy
[3]University School for Advanced Studies IUSS, 27100 Pavia, Italy
[4]Kyungpook National University, Department of Oceanography, School of Earth System Sciences, Daegu, South Korea
[5]NILU, Kjeller, Norway
[6]International Institute for Applied Systems Analysis (IIASA), Laxenburg, Austria
[7]Scripps Institution of Oceanography, University of California, San Diego, CA, 92037, USA
[8]NOAA Global Monitoring Laboratory, Boulder, CO, USA

Correspondence: Martin Vojta (martin.vojta@univie.ac.at)

Abstract. We determine the global emission distribution of the potent greenhouse gas sulfur hexafluoride (SF_6) for the period 2005-2021 using inverse modeling. The inversion is based on 50-day backward simulations with the Lagrangian Particle Dispersion Model (LPDM) FLEXPART and on a comprehensive observation data set of SF_6 mole fractions, in which we combine continuous with flask measurements sampled at fixed surface locations, and observations from aircraft and ship campaigns. We use a global distribution-based (GDB) approach to determine baseline mole fractions directly from global SF_6 mole fraction fields at the termination points of the backward trajectories. We compute these fields by performing an atmospheric SF_6 re-analysis, assimilating global SF_6 observations into modeled global three-dimensional mole fraction fields. Our inversion results are in excellent agreement with several regional inversion studies in the USA, Europe, and China. We find that (1) annual U.S. SF_6 emissions strongly decreased from 1.25 Gg in 2005 to 0.48 Gg in 2021, however, they were on average twice as high as the reported emissions to the United Nations. (2) SF_6 emissions from EU countries show an average decreasing trend of -0.006 Gg/yr during the period 2005 to 2021, including a substantial drop in 2018. This drop is likely a direct result of the EU's F-gas regulation 517/2014, which bans the use of SF_6 for recycling magnesium die-casting alloys from 2018 and requires leak detection systems for electrical switch gear. (3) Chinese annual emissions grew from 1.28 Gg in 2005 to 5.16 Gg in 2021, with a trend of 0.21 Gg/yr, which is even higher than the average global total emission trend of 0.20 Gg/yr. (4) National reports for the USA, Europe, and China all underestimated their SF_6 emissions. (5) The global total SF_6 emissions are captured well by the inversion, however, results are sensitive to the *a priori* emission estimates, given that substantial biases of these estimates in regions poorly covered by the measurement network (e.g. Africa, South America) can be improved but not entirely corrected. (6) Monthly inversions indicate that SF_6 emissions in the Northern Hemisphere were on average higher in summer than in winter throughout the study period.

https://doi.org/10.5194/egusphere-2024-811
Preprint. Discussion started: 11 April 2024

1 Introduction

Sulfur hexafluoride (SF_6) is the greenhouse gas (GHG) with the highest known Global Warming Potential (GWP), 24,300, over a 100-year time horizon (Smith et al., 2021). However, this GWP-100 value might still underplay the climate impact of this gas. Once emitted, SF_6 accumulates in the atmosphere, as it is only slowly degraded via photolysis and electron attachment (Ravishankara et al., 1993) resulting in a very long atmospheric lifetime, with estimates ranging from 580 to 3200 years (Kovács et al., 2017; Patra et al., 1997; Ravishankara et al., 1993; Ray et al., 2017). The ocean also acts as a sink for atmospheric SF_6, however, its magnitude is debated, with estimates ranging up to 7% of the global annual emissions (Ni et al., 2023). Regardless of its exact lifetime and possible ocean sink, SF_6 emissions will cause a positive radiative forcing for hundreds of years. Thus, GWPs, which are typically given for time horizons of 20 or 100 years, underestimate the climate impact of SF_6 on longer time scales.

Since the early 2000s, global concentrations of SF_6 have undergone a rapid increase, more than doubling from roughly 4.5 ppt in 2000 to 10 ppt in 2020 (Lan et al., 2024). In 2020, the radiative forcing of SF_6 was 5.9 mW/m^2 (Laube et al., 2023). This value could surge tenfold by the end of the 21st century if the upward trend in global SF_6 emissions persists, as pointed out by Hu et al. (2023).

SF_6 plays a crucial role in various industrial applications due to its remarkable insulating properties and chemical stability (e.g. Cui et al., 2024). It is primarily used in high-voltage electrical equipment in the power industry, such as gas-insulated switch gears (IEEE, 2012), transmission lines (Koch, 2008), and transformers (Gouda et al., 2012), where it acts as a dielectric and insulator. Here, emissions occur primarily during leakage, maintenance, and decommissioning of equipment (Zhou et al., 2018). Furthermore, SF_6 finds applications in semiconductor manufacturing, facilitating precise etching processes (Lee et al., 2004) and serves for blanketing or degassing in the magnesium or aluminum metal industry (Maiss and Brenninkmeijer, 1998). Moreover, it is used in medicine (Lee et al., 2017; Brinton and Wilkinson, 2009), photovoltaic manufacturing (Andersen et al., 2014), military applications (Koch, 2004), particle accelerators (Lichter et al., 2023), as a tracer gas (Martin et al., 2011), soundproof glazing (Schwarz, 2005), sports shoes (Pedersen, 2000), car tyres (Schwaab, 2000), wind turbines (EPA, 2023), and SF_6 measurements were used to determine OH radical concentrations in the stratosphere and troposphere (Li et al., 2018a).

SF_6 is regulated under the Kyoto Protocol. Thus, countries classified as ("developed") Annex-I nations must submit reports detailing their SF_6 emissions to the United Nations Framework Convention on Climate Change (UNFCCC). These national inventories are almost exclusively created by bottom-up methods, wherein statistical data of industrial production and consumption are used along with source-specific emission factors to estimate the emissions. However, SF_6 emissions have been shwn to be strongly underestimated by the bottom-up reports, underlining the need for independent verification methods (Levin et al., 2010). Therefore, bottom-up approaches such as inverse modeling on the basis of atmospheric measurements have been used in several studies to estimate SF_6 emissions (e.g., Brunner et al., 2017; Fang et al., 2014; Ganesan et al., 2014; Hu et al., 2023; Rigby et al., 2011; Simmonds et al., 2020; Vojta et al., 2022).

Around the year 2000, there was a notable shift in the global SF_6 emission pattern from a declining to an increasing trend, which has continued since then (Simmonds et al., 2020). This rising trend was primarily attributed to the increasing emissions

https://doi.org/10.5194/egusphere-2024-811
Preprint. Discussion started: 11 April 2024

from ("developing") non-Annex-I Asian countries (Rigby et al., 2010). An inversion study by Fang et al. (2014) confirmed a strong increase in East Asian SF_6 emissions between 2006 and 2009, and found its contribution to the global total emissions to be 45%-49% between 2009 and 2012, with China being the largest contributor. Several other inversion studies identified China as the major contributor to global SF_6 emissions (e.g., Ganesan et al., 2014; Rigby et al., 2011; Vojta et al., 2022). From 2007 to 2018 China's annual emissions increased from 1.4 to 3.2 Gg/yr accounting for 36% of the global total emissions in 2018, according to Simmonds et al. (2020). A recent inversion study by An et al. (2024) had access to data from a relatively dense monitoring network inside China and estimated even higher Chinese emissions, with an increase from 2.6 Gg/yr in 2011 to 5.1 Gg/yr in 2021. Simmonds et al. (2020) also constrained Western European SF_6 emissions for the years 2013-2018 using three different regional inversion systems. Two of these inversion systems closely matched the emissions reported to the UNFCCC, while the third one indicated substantially higher emissions. Brunner et al. (2017) found that Western European SF_6 emissions were 47% higher than reported to the UNFCCC for the year 2011. As part of the UK annual report to the UNFCCC, Manning et al. (2022) reported inversion results for SF_6 emissions in North-West Europe and found a decreasing trend, dropping from 0.37 Gg/yr in 2004 to 0.18 Gg/yr in 2021. An atmospheric inversion study by Hu et al. (2023) found that annual U.S. SF_6 emissions decreased between 2007 and 2018 but were on an annual basis 40 – 250% higher than calculated by the U.S. Environmental Protection Agency's national inventory submitted to UNFCCC. They also suggested that U.S. SF_6 emissions were substantially higher in the winter than in the summer.

Up to this point, SF_6 inversion studies have exclusively been focusing on specific geographical areas, i.e., using regional inversions only. Although global observation-based box models, such as the AGAGE 12-box model (e.g., Rigby et al., 2013) are considered to be capable of accurately determining the global total emissions, a comprehensive top-down perspective of the global SF_6 emission distribution is missing. Moreover, existing inversion studies often only use data from continuous surface station measurements or from specific observation networks, potentially missing valuable information from other available observations. In the absence of accurate global SF_6 mole fraction fields, many studies use statistical observation-based methods to determine initial conditions for their inversions, which are suspected of introducing systematic errors in the inversion results (Vojta et al., 2022). Lastly, the seasonality of SF_6 emissions has not been considered by inversion studies so far, with the exception of the recent study by Hu et al. (2023).

Our study offers a comprehensive global, regionally resolved top-down perspective of SF_6 emissions, using inverse modeling to determine the global emission distribution in the period between 2005 and 2021. We use all available SF_6 observations that we could track down by merging continuous surface station measurements, flask measurements, and observations from aircraft and ship campaigns. We consider multiple *a priori* emission fields for our inversion. For the initial conditions (Vojta et al., 2022), we assimilate global SF_6 observations into modeled global three-dimensional SF_6 concentration fields, resulting in an atmospheric SF_6 re-analysis for the period 2005-2021. We investigate regional and national SF_6 emission trends with annual and also monthly resolution, and compare our results to various existing regional studies. Finally, we discuss our global total emission trend and compare it to results from the AGAGE 12-box model and to global emissions directly calculated from annual increases in globally-averaged atmospheric SF_6 mole fractions provided by NOAA (Lan et al., 2024).

https://doi.org/10.5194/egusphere-2024-811
Preprint. Discussion started: 11 April 2024

2 Methods

2.1 Measurement data

The SF_6 re-analysis (Sec. 2.3) and the atmospheric inversion (Sec. 2.5) are based on globally distributed atmospheric observations of SF_6 dry-air mole fractions collected during the period 2005 to 2021. Our data set combines both continuous on-line and instantaneous flask sample measurements from surface stations, with observations from moving platforms. Figure 1 shows all surface station sites included in the inversion and the re-analysis. Figure A1 gives an overview of all the measurements from moving platforms, highlighting the measurement date and altitude with different colors. In addition, Section S3 as well as Tables S1 (continuous surface stations), S2, S3 (flask measurement stations), and S4 (moving platforms) list all the data sets used and give further details. The measurements were provided by several independent organizations, and by international observation networks such as AGAGE and NOAA. Table S5 lists all the individual providers and their acronyms. Most of the data can be found in databases like WDCGG (di Sarra et al., 2022), EBAS (Tørseth et al., 2012), and CEDA (CEDA, 2023). We standardize all observations to the SIO-2005 calibration scale, as described in section S4.

For the inversion, continuous surface measurements were averaged over 3-hour intervals. Observations from moving platforms were averaged on a spatio-temporal grid with a temporal resolution of 3 hours and a spatial resolution of 0.5° in latitude, 0.5° in longitude, and 300 m in height. No observation averaging was performed for the re-analysis. Our complete dataset consists of around 2.7 million observations, while the averaged dataset comprises roughly 800,000 observations. Figure S1 shows the total number of annual observations available for (a) the entire dataset and (b) the averaged dataset.

2.2 Atmospheric transport

We use the Lagrangian particle dispersion model (LPDM) FLEXPART 10.4 (Pisso et al., 2019) to simulate the atmospheric transport of SF_6 between the emission sources and the measurement locations. The model does not account for removal processes, as SF_6 is almost inert in the troposphere to middle stratosphere. We run FLEXPART in backward mode releasing 50,000 particles continuously over 3-hour intervals from the measurement locations and tracking them backward in time for 50 days. For the continuous and moving platform observations, the 3-hour intervals are identical to the 3-hour averaging windows mentioned above (Sec. 2.1). For the flask measurements, the 3-hour intervals are centered around the measurement time. FLEXPART determines emission sensitivities shown as linear operator $\mathbf{H_e}$, which allows us to relate mole fraction values at the measurement location $\mathbf{y}$ with the corresponding emissions $\mathbf{e}$ occurring during the 50-day simulation period. The emissions prior to the simulation cannot be directly related, but still contribute to the measured mole fraction value and thus must be accounted for in the model as well (Sec. 2.2.2). Therefore, FLEXPART also determines sensitivities to the initial conditions, which are shown as linear operator $\mathbf{H_i}$, which is multiplied by a 3-d SF_6 mole fraction field $\mathbf{y_i}$ (Sec. 2.3) 50 days before the respective measurement to obtain the baseline $\mathbf{H_i y_i}$. The relationship between receptor mole fractions $\mathbf{y}$, initial conditions $\mathbf{y_i}$ and emissions $\mathbf{e}$ is given by:

https://doi.org/10.5194/egusphere-2024-811
Preprint. Discussion started: 11 April 2024

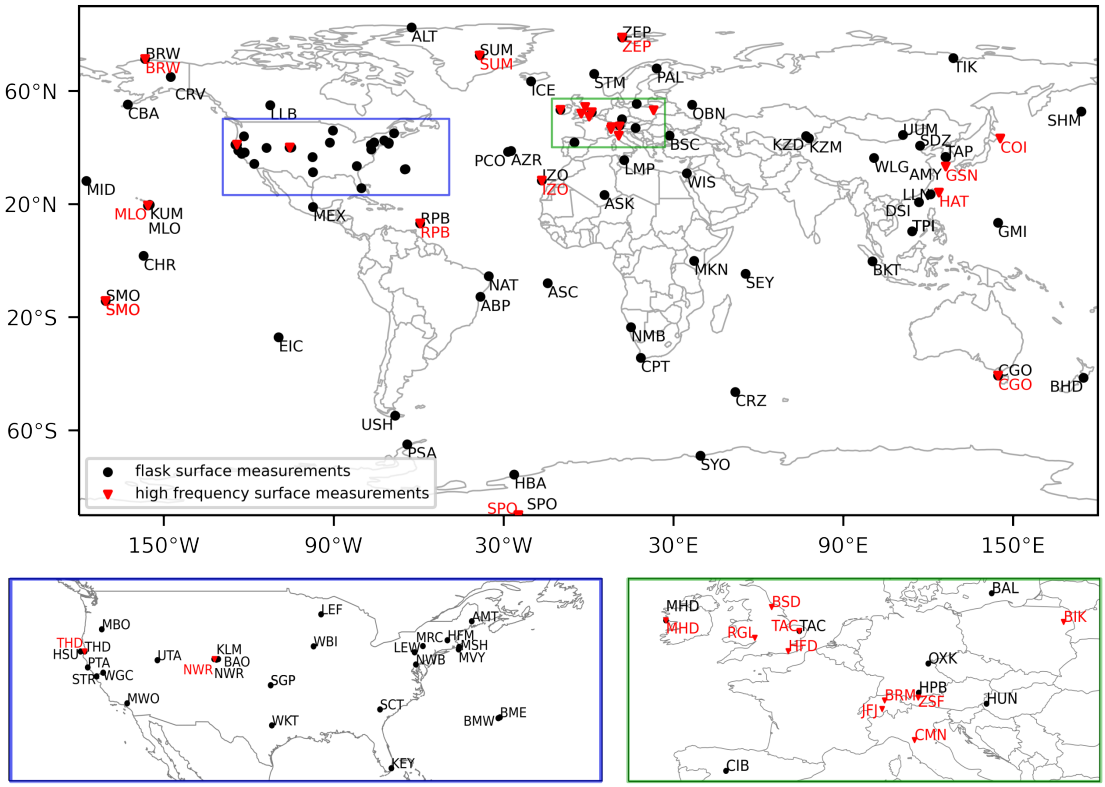

Figure 1. Locations of stations with continuous surface measurements (red triangles) and surface flask measurements (black dots) used in the inversion.

$$\mathbf{y} = \mathbf{H_e e} + \mathbf{H_i y_i} = \mathbf{H x}, \tag{1}$$

where $\mathbf{H}$ is the complete atmospheric transport operator combining $\mathbf{H_e}$ and $\mathbf{H_i}$, and $\mathbf{x}$ is the state vector combining $\mathbf{e}$ and $\mathbf{y_i}$.

We run FLEXPART with hourly ECMWF ERA5 wind fields (Hersbach et al., 2018) with 0.5°×0.5° resolution, and 137 vertical levels. The global output grid has a resolution of 1°×1° and 18 vertical layers with interface heights at 0.1, 0.5, 1, 2, 3, 4, 5, 7, 9, 11, 13, 15, 17, 20, 25, 30, 40, and 50 km agl. The emission sensitivities were calculated only for the lowest layer from 0 to 100 m agl, where most emissions occur.

https://doi.org/10.5194/egusphere-2024-811
Preprint. Discussion started: 11 April 2024

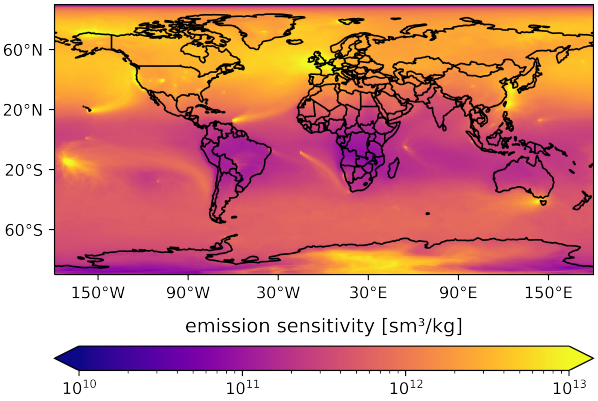

Figure 2. Annually averaged emission sensitivities for the example year 2019 obtained from FLEXPART 50-day backward simulations

2.2.1 Emission sensitivities

Figure 2 shows the annual averaged emission sensitivities for all observations made in the example year 2019. Areas of high sensitivity are well covered by the measurement data set, so that emissions can be well constrained by the inversion. Emission sensitivities in the Northern Hemisphere are much higher than in the Southern Hemisphere, and the high SF_6 emitting countries China and USA are reasonably well covered. The largest values are observed in North-West Europe, which is very well monitored by the dense British observation network. However, large land areas in the Southern Hemisphere, including South America, Southern Africa, and Northern Australia, are poorly sampled due to a lack of continuous measurements. India, which is considered to have high SF_6 emissions, is also poorly covered. In these areas, the emissions cannot be determined well by the inversion.

2.2.2 Initial conditions

Using a LPDM to calculate emission sensitivities for atmospheric inversions, we release virtual particles directly from the measurement location and benefit from almost infinite resolution at the receptor. The disadvantage of using a LPDM is that we have to deal with initial conditions, as virtual particles can be followed backward only for a limited period, due to computational costs. Only emissions that occur within this LPDM simulation period can be directly related to observed mole fraction values and are accessible to the inversion. We, therefore, need to define a baseline that accounts for all the emission contributions prior to the simulation period that contribute to the observed mole fraction. In this study, we use the global-distribution based (GDB) method (Vojta et al., 2022) to determine the baseline. We couple the mole fraction sensitivity at the ending points of the FLEXPART back trajectories to a global field of SF_6 mole fractions (for more details see Thompson and Stohl, 2014). In essence, this propagates the time-resolved 3-d mole fractions in space and time along the 50-day trajectories to the receptor

https://doi.org/10.5194/egusphere-2024-811
Preprint. Discussion started: 11 April 2024

location and time. As pointed out by Vojta et al. (2022), the GDB method has many advantages over observation-based filtering methods. GDB baselines are consistent with the LPDM backward simulation length, account for meteorological variability, and allow the inclusion of low-frequency measurements and measurements from moving platforms in the inversion. However, the method requires unbiased global time-resolved 3-d fields of SF_6.

2.3 Global SF_6 fields

In this study, we generate global fields of SF_6 mole fractions for the period between 2005 and 2021, using the LPDM FLEXPART 8-CTM-1.1 (Henne et al., 2018). The model is described by Groot Zwaaftink et al. (2018), who tested its performance for CH_4, while Vojta et al. (2022) applied it to SF_6. We operate FLEXPART-CTM in a domain-filling mode, where 80 million virtual particles are dispersed globally in proportion to air density. The initialization is based on a latitudinal SF_6 profile determined by interpolation of surface measurements and accounts for the "Age of Air" (Stiller et al., 2021) at higher altitudes (for more details see Sec. S5 in the supplementary materials). Released particles are tracked forward in time and carry both an air tracer and the chemical species SF_6. When they reside in the atmospheric boundary layer, the model accounts for SF_6 emissions by increasing the SF_6 masses of the respective particles. The emission uptake of the particles is driven by the "UP" *a priori* emission data set (see Sec. 2.4).

As model errors and inaccurate emission fields lead to errors and biases in the global SF_6 fields, a nudging routine is used to push the simulated mole fractions towards the observations within predefined kernels centered around the measurement locations. We include the entire observation data set in the nudging routine, comprising continuous surface station measurements, flask measurements, and observations from aircraft and ship campaigns. Furthermore, we assign different kernel sizes to individual observations, according to the observed variability in a selected time window for stationary sites, and according to the measurement height for moving platforms. Small kernels are attributed to observations with higher variability and observations close to the surface to preserve the spatial variability of SF_6 mole fractions over land masses. Detailed kernel configurations can be found in Table S6. We run the model with the $0.5° \times 0.5°$ ERA5 data set and produce daily average output with a resolution of $3° \times 2°$. The daily-resolved global SF_6 mole fraction fields between 2005 and 2021 can be freely downloaded from https://doi.org/10.25365/phaidra.489.

2.4 *A priori* emissions

We generate six different annually resolved global SF_6 emission fields for the period 2005 to 2021 that are used as *a priori* emissions in the inversions (Sec. 2.5). One of these fields is also used to drive FLEXPART-CTM (Sec. 2.3). Our six *a priori* emissions are based on three different inventories (see Table 1) and globally gridded based on different proxy information at a resolution of $1° \times 1°$.

https://doi.org/10.5194/egusphere-2024-811
Preprint. Discussion started: 11 April 2024

Table 1. Overview of global SF_6 *a priori* emission fields used in this study

***a priori* emissions**		
Inventory	**variation**	**distribution of total national emissions**
UNFCCC-ELE	UP	emissions distributed according to population density
	UN	emissions distributed according to night light remote sensing
EDGAR	E8	v8 - distribution provided by EDGAR
	E7P	v7 - emissions distributed according to population density
	E7N	v7 - emissions distributed according to night light remote sensing
GAINS	GS	distribution provided by GAINS

UNFCCC-ELE

For every year, we gather total national SF_6 emissions reported to the UNFCCC (UNFCCC, 2021) and add total Chinese emissions estimated by Fang et al. (2014). We then subtract the total emissions of these countries from the total global SF_6 emissions calculated by Simmonds et al. (2020). The residual emissions are then distributed among all other countries proportionally to their national electricity generation. Gaps in the SF_6 emissions or electricity generation data are filled by linear interpolation. Lastly, the attributed total national SF_6 emissions are further distributed within the respective borders of each country according to two different proxy data sets: (1) the gridded population density (CIESIN, 2018) (UP) and (2) night light remote sensing data (Elvidge et al., 2021) (UN), thus resulting in two different UNFCCC-ELE *a priori* emission versions.

EDGAR

We use the gridded annual global SF_6 emission inventory provided by the Emissions Database for Global Atmospheric Research (EDGAR, 2023; Crippa et al., 2023), part of the recently updated data set EDGARv8.0 (E8). In addition, we also utilize the national annual totals of SF_6 emissions provided by EDGARv7.0 (EDGAR, 2022; Crippa et al., 2021), which are not gridded. As for the UNFCCC-ELE emissions, we distribute those national totals according to the gridded population density (CIESIN, 2018) (E7P) or night light remote sensing (Elvidge et al., 2021) (E7N).

GAINS

Furthermore, we use the GAINS gridded global emission inventory. This inventory is based on the study by Purohit and Höglund-Isaksson (2017) and was updated until 2020 as described in Section S6 in the supplementary material. The provided data set was extended to 2021 by linear extrapolation (GS).

Comparison

Emission fields from the three inventories (UNFCCC-ELE, EDGAR, and GAINS) show much stronger differences than the two variations of UNFCCC-ELE and EDGAR generated by using different proxy information for spatial distribution. In Fig. 3,

https://doi.org/10.5194/egusphere-2024-811
Preprint. Discussion started: 11 April 2024

we therefore only compare three *a priori* emissions (UP, E8, and GS) for 2019, as an example. It is noteworthy that these three emission fields show similar global total SF_6 emissions in 2019. Figure 3 shows significantly higher emissions in the Northern than in the Southern Hemisphere for all three fields, with China being the biggest emitter. Other high-emitting areas are Europe, the USA, and India. While emissions in Europe are comparable across all data sets, notable differences can be seen in other regions: (1) UNFCCC-ELE (electricity generation distributed data for non-reporting countries) shows relatively high emissions in India and the Southern Hemisphere compared to EDGAR and GAINS. (2) EDGAR shows higher emissions in the USA than the other two *a priori* fields, and (3) GAINS exhibits higher emissions in China than UNFCCC-ELE and EDGAR.

2.5 Inversion method

We employ the inversion framework FLEXINVERT+ (Thompson and Stohl, 2014) to calculate optimized emissions (*a posteriori* emissions). FLEXINVERT+ uses equation 1, the atmospheric transport operator $\mathbf{H}$, *a priori* emissions $\mathbf{x}_p$, initial conditions $\mathbf{y}_i$, and observed mole fractions $\mathbf{y}$ to minimize the cost function $\mathbf{J}$ (Eq. 2), which represents the negative exponent of the *a posteriori* emissions probability distribution, derived by Bayes' theorem (e.g., Tarantola, 2005). The *a posteriori* emissions defined by the maximum of the distribution are found by minimizing the mismatch between modeled and observed mole fractions weighted by the observation error covariance matrix $\mathbf{R}$, and the difference between emissions $\mathbf{x}$ and their *a priori* values $\mathbf{x}_p$ weighted by the *a priori* emission error covariance matrix $\mathbf{B}$:

$$\mathbf{J}(\mathbf{x}) = \frac{1}{2}(\mathbf{x}-\mathbf{x}_p)^T\mathbf{B}^{-1}(\mathbf{x}-\mathbf{x}_p) + \frac{1}{2}(\mathbf{H}\mathbf{x}-\mathbf{y})^T\mathbf{R}^{-1}(\mathbf{H}\mathbf{x}-\mathbf{y}), \tag{2}$$

We optimize emissions on a 6-monthly basis and average the results for each year to obtain annual emissions between 2005 and 2021. In addition to the emissions, we also optimize the baseline ($\mathbf{H_i y_i}$) in the inversion on a monthly basis. The uncertainty of the baseline is set to 0.15 ppt. The *a priori* emission uncertainty is estimated to be 70% of the *a priori* value in each grid cell with a minimum value of $1 \cdot 10^{-13} \frac{kg}{m^2 h}$. Correlations between emission uncertainties are accounted for using an exponential decay model with a spatial scale length of 250 km and a temporal scale length of 90 days. For the inversion, we use emission grids with different cell sizes (Fig. 4, Fig. S2, Fig. S3), defined by the aggregation of grid cells with low emission contributions based on emission sensitivities and *a priori* emissions (see Thompson and Stohl, 2014, for a detailed description). We also exclude grid cells over the oceans from the inversion. The global inversion grid has a resolution of 1° to 16°, and the total number of grid cells varies between years, ranging from a minimum of 5841 (2005) to a maximum of 11901 (2016). To study the seasonal emission patterns, we also perform monthly inversions, using a coarser global inversion grid of 953 grid cells for all years and a time scale length of 30 days for the correlation between *a priori* emission uncertainties.

For SF_6 we only expect positive fluxes over land. However, the inversion algorithm may create negative *a posteriori* fluxes. To address this issue, we apply an inequality constraint on the *a posteriori* emissions, using the truncated Gaussian approach by Thacker (2007). *A posteriori* emissions $\hat{\mathbf{x}}$ are corrected to positive values by applying inequality constraints as error-free observations:

$$\hat{\mathbf{x}} = \mathbf{x} + \mathbf{A}\mathbf{P}^T(\mathbf{P}\mathbf{A}\mathbf{P}^T)^{-1}(\mathbf{c}-\mathbf{P}\mathbf{x}), \tag{3}$$

https://doi.org/10.5194/egusphere-2024-811
Preprint. Discussion started: 11 April 2024

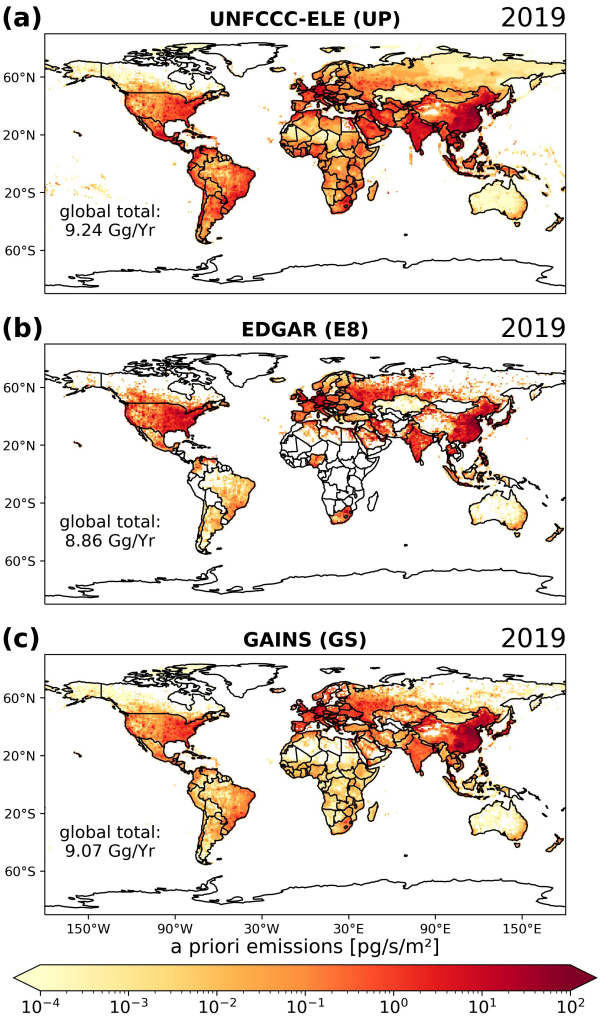

Figure 3. *A priori* emissions from the different sources (a) UNFCCC-ELE (UP), (b) EDGAR (E8), and (c) GAINS (GS) for the year 2019.

where **P** represents a matrix operator selecting the fluxes violating the inequality constraint, and **c** a vector of the inequality constraint. **x** and **A** represent the *a posteriori* emissions and error covariance matrix, respectively.

https://doi.org/10.5194/egusphere-2024-811
Preprint. Discussion started: 11 April 2024

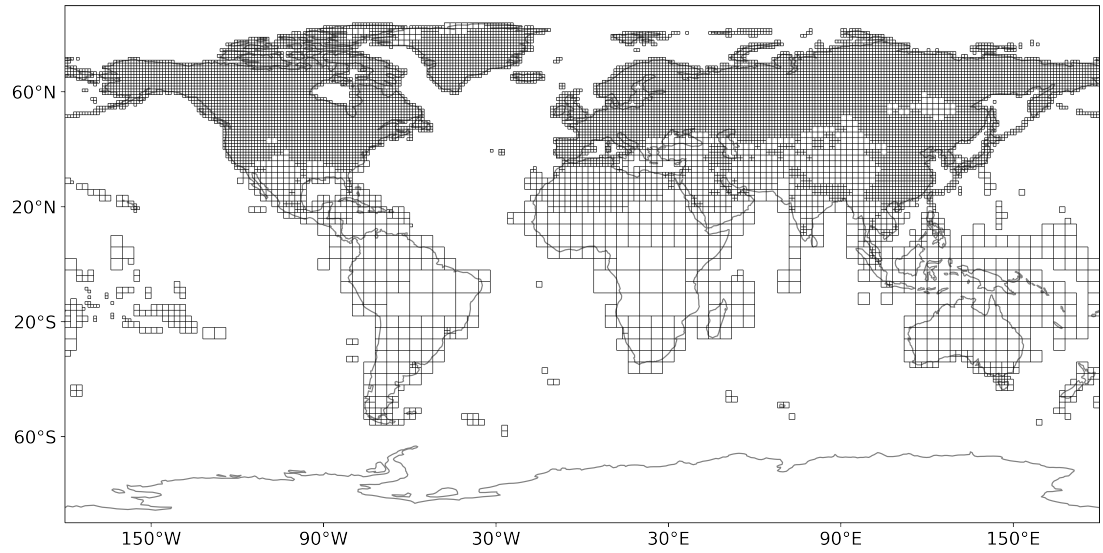

Figure 4. Global inversion grid with variable grid cell sizes for the example year 2019.

2.6 Sensitivity tests and setup

Before deciding on our final inversion setup, we performed several sensitivity tests. We tested different: (1) *a priori* emission uncertainties between 50% and 100% of the respective *a priori* values and minimal absolute uncertainties between $1 \cdot 10^{-14}$ and $1 \cdot 10^{-12} \frac{kg}{m^2 h}$, (2) spatial and temporal correlation scale lengths of the *a priori* uncertainties of 100 to 300 km, and 30 to 180 days, respectively, and (3) baseline uncertainties from 0.05 to 0.25 ppt. We found that inversion results were relatively stable for these different settings and that the choice of the *a priori* emission inventory (UNFCCC-ELE, EDGAR, or GAINS) showed the biggest influence on the inversion results. While the inversion results were similar using different variations of the UNFCCC-ELE (UP and UN) or EDGAR (E8, E7P, and E7N) *a priori* emissions (see Sec. 2.4), we found substantial differences when switching between UNFCCC-ELE, EDGAR and GAINS. Therefore, we ran inversions with all six variations listed in Table 1 individually and averaged the results of UP and UN, as well as E8, E7P, and E7N to compile one inversion result for each *a priori* emission inventory (UNFCCC-ELE, EDGAR, and GAINS). Since it is challenging to identify the most accurate inventory, we also provide an average of these three inversion results.

https://doi.org/10.5194/egusphere-2024-811
Preprint. Discussion started: 11 April 2024

3 Results and discussion

3.1 Observed and modeled mole fractions

To illustrate the inversion optimization process, we compare observed and modeled mole fractions at the Gosan observation station (Fig. 5a), at the Ragged Point station (Fig. 5b), and all other continuous surface measurement sites (Fig. A2, A3, and S4-S23), using the E7P emissions field. The Gosan station is situated on the southwestern tip of the South Korean island Jeju, monitoring pollution events from East Asia. However, during the Asian summer monsoon, typically from June to September, clean air from the Southern Hemisphere, low in SF_6, is episodically passing over the station (e.g. Li et al., 2018b), making it challenging to accurately define the baseline during this period. The background station Ragged Point, located on Barbados' eastern edge, primarily receives clean air masses from the Atlantic. It also exhibits intrusions of southern air masses that are low in SF_6 during the summer, resulting in distinct minima in the mole fraction time series, and a complex baseline. With the GDB method, we can address these challenges of complex baselines. As illustrated in Fig. 5, the calculated baselines capture the low summer observations, representing a significant advantage over statistical baseline methods. This advantage also becomes apparent for other stations with complex baselines such as Hateruma (Japan, Fig. A2) or Izaña (Tenerife, Fig. A3). Additionally, the optimization of the baseline shows relatively little impact at all stations, implying that the GDB method and the utilized global SF_6 mole fraction fields already lead to a well-fitting baseline that cannot be improved substantially by the inversion. This is important, as the optimization can focus on improving the emissions rather than correcting a wrong baseline. Figure 5a also illustrates the emission improvement achieved by the inversion. The optimized *a posteriori* emissions result in mole fractions that are much closer to the observations than the *a priori* modeled values. For Gosan, the correlation (r^2) between (detrended) observed and modeled values improves from 65% to 81% and the mean squared error (MSE) halves from 0.4 ppt^2 to 0.2 ppt^2. Table S7 and Fig. S24 demonstrate the statistical improvements at all continuous surface stations, emphasizing the proper functioning of the inversion. Figure 5b further illustrates the advantage of choosing a rather long 50-day backward simulation period. With this long simulation period, we can see that this remote station is also directly influenced by emissions (i.e., enhancements over the baseline) that can be directly optimized. With shorter simulation times (e.g., 5-10 days), no emission contributions above the baseline could be seen, thus rendering this station useless for emission optimization. For a detailed discussion about the LPDM backward simulation period see Vojta et al. (2022).

3.2 Inversion increments and relative error reduction

Figure 6 shows the inversion increments (*a posteriori* minus *a priori* emissions) and the relative uncertainty reductions ($1 - \frac{a\ posteriori\ uncertainty}{a\ priori\ uncertainty}$) achieved by the inversion for the example year 2019, when using the *a priori* emission fields UP (UNFCCC-ELE), E8 (EDGAR) and GS (GAINS). Across all cases, the emission optimization predominantly occurs in the Northern Hemisphere, characterized by non-zero inversion increments and large error reductions. The limited number of observations in the Southern Hemisphere results in small emission sensitivities there (see Fig. 2), limiting the effects of the inversion primarily to Northern Hemisphere emissions. Only in the case of the UNFCCC-ELE inventory, Fig. 6a shows (negative) inversion increments and notable error reduction in Southern regions like South America and South Africa. This might

https://doi.org/10.5194/egusphere-2024-811
Preprint. Discussion started: 11 April 2024

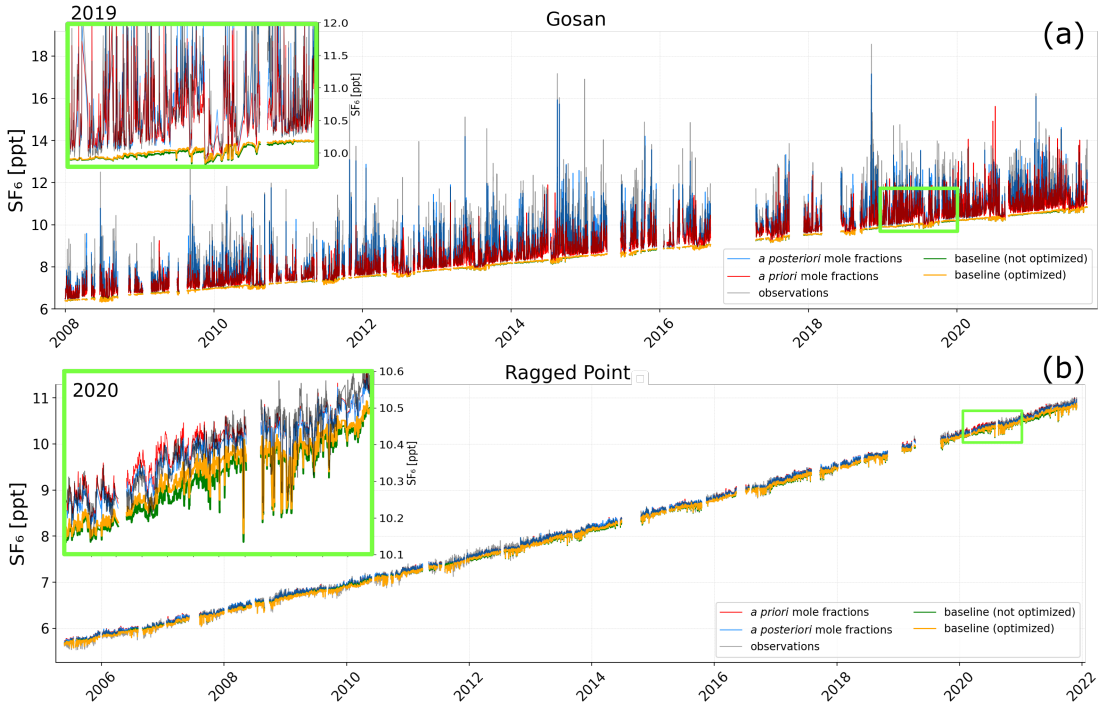

Figure 5. Mole fraction time series at the (a) Gosan and (b) Ragged Point measurement station. Red lines represent the modeled *a priori* mole fractions calculated with the E7P *a priori* emissions and blue lines represent the modeled *a posteriori* mole fractions. The green line illustrates the baseline derived by the GDB method and the orange line shows the optimized baseline. The grey line represents the observed mole fractions. The inset panels zoom into the year (a) 2019 (Gosan) and (b) 2020 (Ragged Point), as illustrated by the light green rectangles.

indicate that the UNFCCC-ELE *a priori* emissions are significantly overestimated in these areas. All three data sets show the biggest error reduction and inversion increments in the USA, Europe, and China, where the *a priori* emissions are high and many observations are available. While the increments look similar for the three *a priori* emissions for Europe and China, they are very different for the USA, where the inversion produces predominantly negative increments when using the EDGAR inventory, while only positive increments are obtained using UNFCCC-ELE and GAINS. These differences suggest that the true 2019 U.S. emissions lie between the high EDGAR and the lower UNFCCC-ELE/GAINS estimates.

https://doi.org/10.5194/egusphere-2024-811
Preprint. Discussion started: 11 April 2024

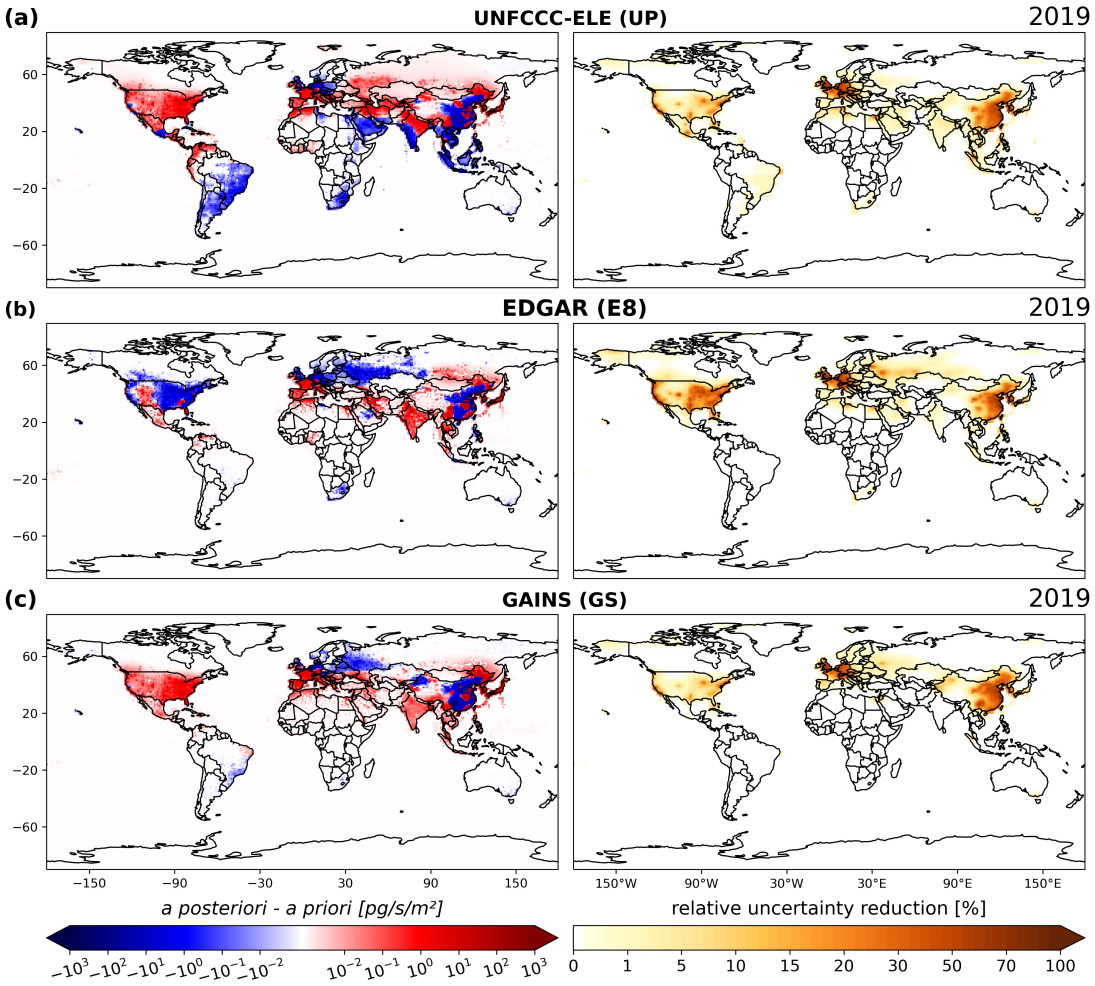

Figure 6. Inversion increments (*a posteriori* minus *a priori* emissions; left panels) and the relative uncertainty reductions (right panels) shown when using the priors (a) UNFCCC-ELE (UP), (b) EDGAR (E8) and (c) GAINS (GS), for the example year of 2019.

3.3 National and regional emissions

Figure 7 illustrates the global SF_6 *a posteriori* emissions for the example year 2019, averaged over all emission fields as described in Sec. 2.6. The highest SF_6 emissions can be seen in the USA, Europe, China, and India, while emissions are

https://doi.org/10.5194/egusphere-2024-811
Preprint. Discussion started: 11 April 2024

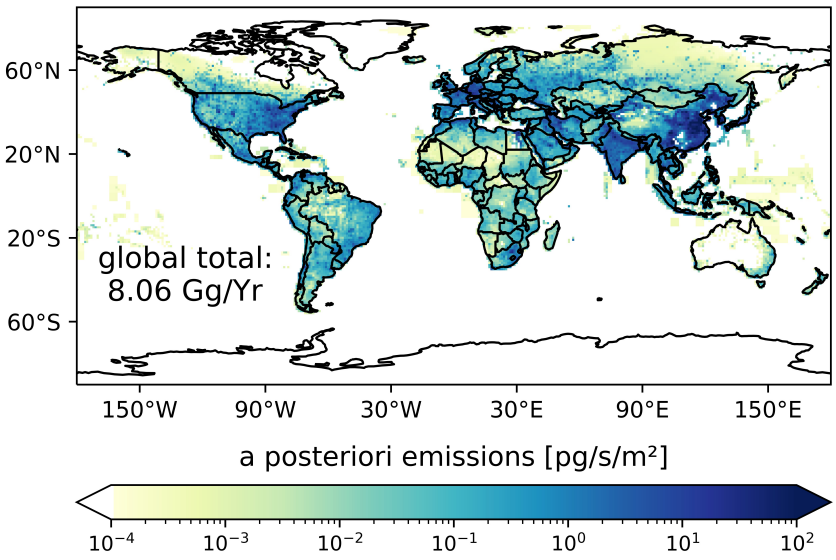

Figure 7. Global *a posteriori* emissions for the example year 2019, averaged over the inversion results using the six different *a priori* emissions.

smaller in South America, Africa, and Australia. SF_6 emissions of these countries and regions are discussed in more detail in the following subsections, showing their national/regional emission time series between 2005 and 2021. National and regional emissions are calculated by aggregating the emissions within the respective grid cells of the corresponding country or region, employing a national identifier grid (CIESIN, 2018).

3.3.1 Emissions from the United States of America

Figure 8 shows the annual *a priori* and *a posteriori* U.S. SF_6 emissions for the different priors in the period between 2005 and 2021. The inversion results show a clearly declining annual emission trend of -0.054 Gg/yr, dropping from 1.25 Gg in 2005 to 0.48 Gg in 2021 (Fig. 8; *a posteriori* average). However, the *a posteriori* emissions are larger (by a factor of 2 on average) than the emissions reported to UNFCCC (Fig. 8; *a priori* UNFCCC-ELE) throughout the entire study period. While the different *a priori* emissions show big differences, *a posteriori* emissions agree within their 1-σ uncertainties. At the beginning of the study period, all three *a posteriori* emissions are substantially higher than the UNFCCC-reported *a priori* emissions, and closer to the EDGAR *a priori* estimates. Between 2005 and 2012 the *a posteriori* emissions show a substantial decrease, after which they approach the UNFCCC-reported values, but still remain higher. It also seems that the GAINS *a priori* emissions are far too low at the beginning of our study period, while the EDGAR *a priori* emissions are far too high at the end of our study

https://doi.org/10.5194/egusphere-2024-811
Preprint. Discussion started: 11 April 2024

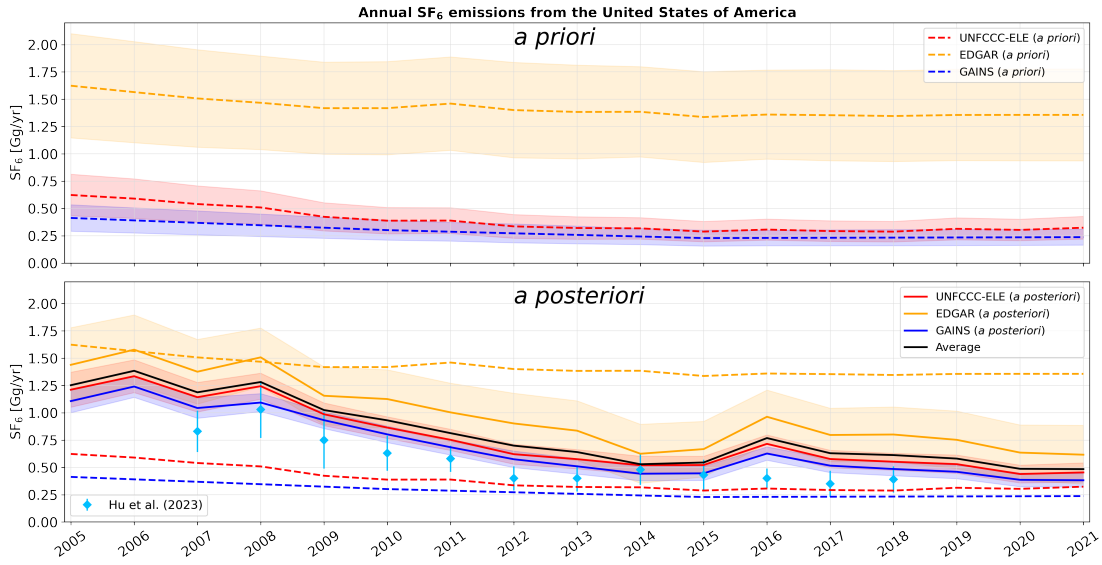

Figure 8. Annual *a priori* (dashed lines) and *a posteriori* (solid lines) SF_6 emissions in the U.S. for the period between 2005 and 2021 when using different *a priori* emissions (UNFCCC-ELE red, EDGAR orange, GAINS blue). The *a priori* emissions (top panel) and *a posteriori* emissions (bottom panel) are shown together with their respective 1-σ uncertainties (colored shadings). The bottom panel also shows the average *a posteriori* emissions (black solid line) and the results of Hu et al. (2023), which are shown with blue diamonds and vertical lines representing their 2-σ uncertainties. For better comparison, the *a priori* emissions (without uncertainties) are also included in the bottom panel.

period. Our results are a bit higher compared to the regional inversion study by Hu et al. (2023), however, show a remarkably similar declining trend in U.S. SF_6 emissions between 2007 and 2018. This good agreement with a regional inversion study focussing on the U.S. with a very different setup is reassuring.

3.3.2 Total emissions from EU countries

Figure 9 illustrates the total annual *a priori* and *a posteriori* SF_6 emissions from all EU countries[1]. Here, the three *a priori* data sets show almost no trend and are very similar to each other throughout the study period, indicating a consistent framework for bottom-up reporting of EU emissions. The annual *a posteriori* emissions show a decreasing trend of -0.006 Gg/yr, dropping from 0.41 Gg in 2005 to 0.25 Gg in 2021 (Fig. 9; *a posteriori* average). While *a posteriori* emissions are relatively stable and exceed the *a priori* emissions until 2017, there is a significant drop in 2018, after which they are closer to the *a priori*

[1]Austria, Belgium, Bulgaria, Croatia, Cyprus, Czech Republic, Denmark, Estonia, Finland, France, Germany, Greece, Hungary, Ireland, Italy, Latvia, Lithuania, Luxembourg, Malta, Netherlands, Poland, Portugal, Romania, Slovakia, Slovenia, Spain, and Sweden

https://doi.org/10.5194/egusphere-2024-811
Preprint. Discussion started: 11 April 2024

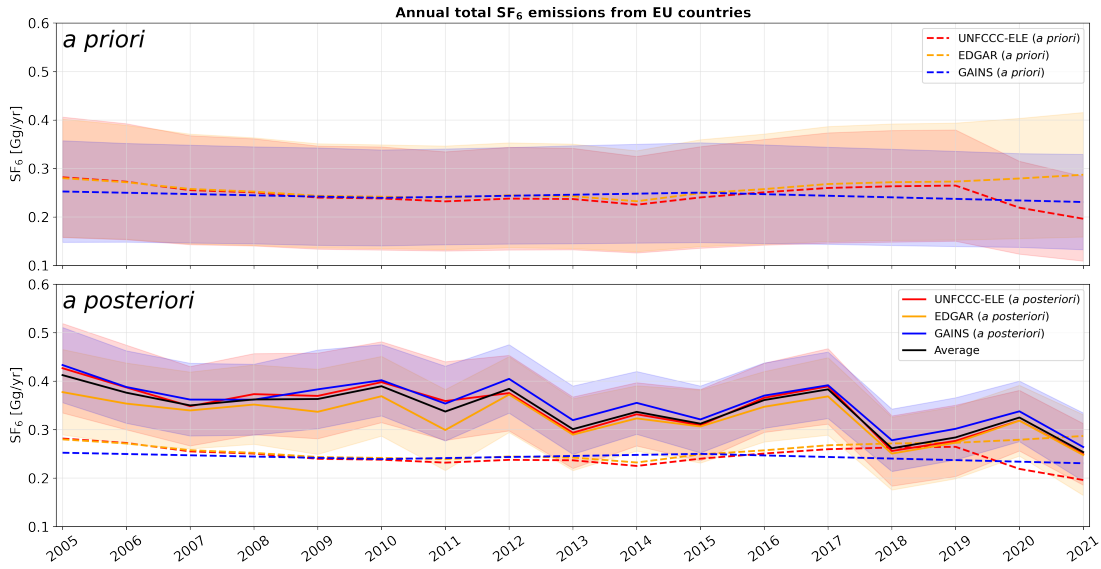

Figure 9. Annual *a priori* (dashed lines) and *a posteriori* (solid lines) SF_6 emissions aggregated for all EU countries, shown for the period between 2005 and 2021 when using different *a priori* emissions (UNFCCC-ELE red, EDGAR orange, GAINS blue). The *a priori* emissions (top panel) and *a posteriori* emissions (bottom panel) are shown together with their respective 1-σ uncertainties (colored shadings). The bottom panel also shows the average *a posteriori* emissions with a black solid line. For better comparison, the *a priori* emissions (without uncertainties) are also included in the bottom panel.

emissions. It seems plausible that this drop in SF_6 emissions in 2018 was a result of the EU's F-gas regulation 517/2014 (European Parliament and Council of the European Union, 2014), which requires new electrical switch gear put into service from 2017 onwards to be equipped with a leak detection system and bans the use of SF_6 for recycling magnesium die-casting alloys from 2018. Our results suggest that in their reports to the UNFCCC, EU countries underestimated their SF_6 emissions prior to 2018, but at the same time underestimated the positive effect of the F-gas regulation 517/2014 in cutting SF_6 emissions.

As one of only three countries, the United Kingdom also includes top-down inversion results in its annual UNFCCC reports (Manning et al., 2022). As part of this top-down approach, Manning et al. (2022) also reported emissions of North-West Europe[2], to which we compare our inversion results (Fig. A4). The *a posteriori* emissions from North-West Europe are generally similar to EU emissions shown in Fig. 9, however, they show an even clearer negative trend of -0.009 Gg/yr. Our results agree well, on average within 16% and better since 2012, with those reported by Manning et al. (2022). Furthermore, Simmonds et al. (2020) presented inversion-derived emissions for Western Europe[3] for four different inversion setups. Our *a posteriori*

[2]Ireland, the United Kingdom of Great Britain, France, Belgium, Netherlands, Luxembourg, and Germany
[3]United Kingdom of Great Britain, Ireland, Benelux, Germany, France, Denmark, Switzerland, Austria, Spain, Italy, and Portugal

https://doi.org/10.5194/egusphere-2024-811
Preprint. Discussion started: 11 April 2024

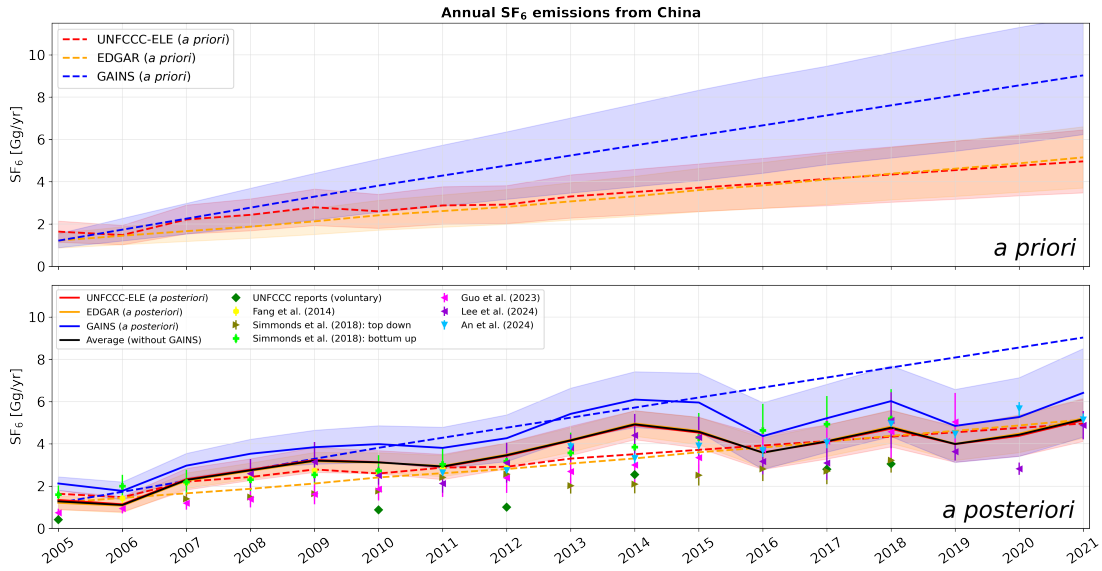

Figure 10. Annual *a priori* (dashed lines) and *a posteriori* (solid lines) SF_6 emissions from China in the period between 2005 and 2021 when using different *a priori* emissions (UNFCCC-ELE red, EDGAR orange, GAINS blue). The *a priori* emissions (top panel) and *a posteriori* emissions (bottom panel) are shown together with their respective 1-σ uncertainties (colored shadings). The bottom panel also shows the average *a posteriori* emissions (excluding GAINS) with a black solid line, together with various reference values. For better comparison, the *a priori* emissions (without uncertainties) are also included in the bottom panel.

emissions agree very well with three of these four inversions (Fig. A5). The fourth inversion shows consistently lower emissions, however, this inversion setup used fewer observation stations than the other three and is likely less accurate. It is likewise noteworthy that the first three inversions of Simmonds et al. (2020) show an emission drop in 2018, which we also find.

3.3.3 Emissions from China

Chinese *a priori* and *a posteriori* SF_6 emissions are illustrated in Fig. 10. The inversion-derived *a posteriori* emissions reveal a distinct positive trend of 0.21 Gg/yr (Fig. 10; *a posteriori* average without GAINS), with a particularly rapid increase between 2006 and 2014 (0.35 Gg/yr), followed by a stabilization thereafter. The UNFCCC-ELE *a priori* Chinese emissions slightly exceed the EDGAR *a priori* emissions between 2007 and 2011, after which they align well. UNFCCC-ELE and EDGAR *a posteriori* emissions show almost identical Chinese emissions that are also close to their *a priori* values. The GAINS *a priori* Chinese emissions differ significantly from the other two inventories. After 2005, the GAINS *a priori* emissions show a very strong upward trend, increasingly diverging from the other two priors until the end of the study period, at which point

https://doi.org/10.5194/egusphere-2024-811
Preprint. Discussion started: 11 April 2024

the GAINS Chinese emissions are almost twice as high as the other priors. In the GAINS inventory, China's 2021 emissions alone would account for almost all of the known total global SF_6 emissions (see Sec. 3.3.5), which seems unrealistic. The GAINS *a posteriori* emissions for China show lower values compared to the *a priori* emissions, however still exceed the UNFCCC-ELE- and EDGAR-derived results, even though there is an overlap in the uncertainty bands. It seems likely that the inversion improves the overestimated Chinese GAINS emissions, yet it may not entirely correct them, given the considerably overestimated *a priori* estimates. Due to these concerns about the Chinese GAINS *a priori* emissions, we provide both a Chinese *a posteriori* emissions average including (see Table A3) and excluding GAINS inversions (black solid line in Fig. 10).

China is not obliged to report its national emissions but it voluntarily reported bottom-up SF_6 estimates in their national communications and biennial updates to the UNFCCC for 2005 (China, 2012), 2010 (China, 2018a), 2012 (China, 2016), 2014 (China, 2018b), 2017 (China, 2023a), and 2018 (China, 2023b). These reported values are much smaller than our *a posteriori* emissions, especially in 2010, 2012, and 2014. We also compare our results to various other studies of Chinese emissions, both using bottom-up and top-down approaches. Our results agree within 15% with the inversion study by Fang et al. (2014) who used a similar inversion setup, based on the continuous measurements in Gosan (South Korea), Hateruma (Japan) and Cape Ochiishi (Japan), and FLEXPART atmospheric transport modeling. Furthermore, our results align closely with a recent inversion study by An et al. (2024) (agreeing within 12%), who had access to data from a relatively dense monitoring network over China. Our results also agree well (within 15%) with the findings of (Lee et al., 2024), whose regional inversion study (in preparation) utilizes observations from Gosan to estimate emissions in South-East Asia. Note that the patterns of our time series are very similar to the ones of Lee et al. (2024), suggesting that our Chinese *a posteriori* emissions are highly influenced by the Gosan observations station. Our derived emissions also agree well within 8% with bottom-up estimates by Guo et al. (2023) after 2015 and within 18% with the bottom-up estimates by Simmonds et al. (2020). Our results are, however, higher than the bottom-up estimates by Guo et al. (2023) between 2008 and 2015 and the inversion-derived emissions by Simmonds et al. (2020). However, Simmonds et al. (2020) based their inversion results on only one station (Gosan), coarser meteorology, and an inversion domain representing only 34% of China's population, which could have resulted in a substantial underestimation of the emissions (An et al., 2023).

3.3.4 Other regions

In this section, we present the *a priori* and *a posteriori* SF_6 emissions from Africa, South America, Australia, and India. It is important to note that there are no emission reports to the UNFCCC for Africa, South America, and India. In these regions, the UNFCCC-ELE *a priori* emissions are derived by distributing the emissions residuals from the global total emissions (Simmonds et al., 2020) when subtracting the cumulative reported emissions from Annex-I countries, according to the national electricity generation as described in Sec. 2.4.

Africa

Figure 11 shows African *a priori* and *a posteriori* SF_6 emissions. One can see that the GAINS inventory is very low and the UNFCCC-ELE inventory is very high in comparison to the EDGAR inventory. Before 2018, the UNFCCC-ELE *a posteriori*

https://doi.org/10.5194/egusphere-2024-811
Preprint. Discussion started: 11 April 2024

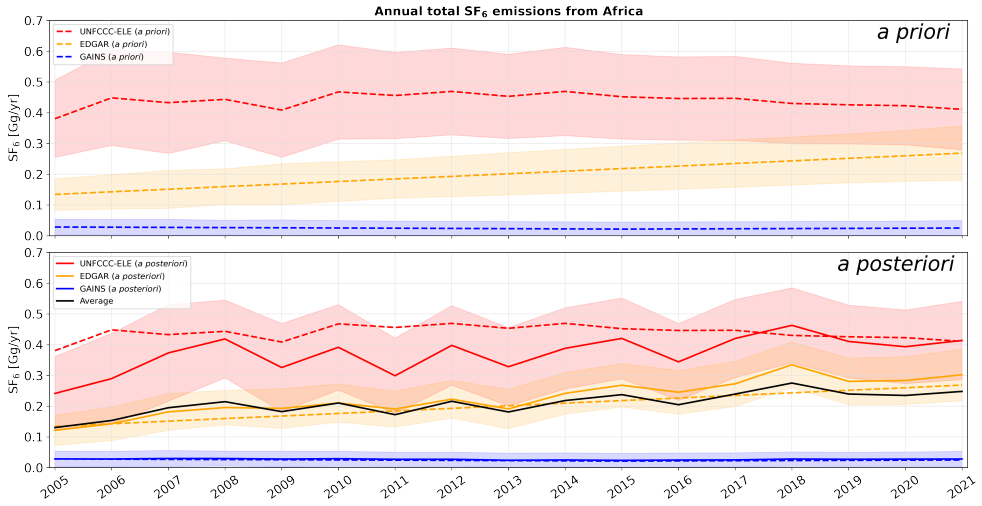

Figure 11. Annual *a priori* (dashed lines) and *a posteriori* (solid lines) SF_6 emissions from Africa, shown for the period between 2005 and 2021 when using different *a priori* emissions (UNFCCC-ELE red, EDGAR orange, GAINS blue). The *a priori* emissions (top panel) and *a posteriori* emissions (bottom panel) are shown together with their respective 1-σ uncertainties (colored shadings). The bottom panel also shows the average *a posteriori* emissions with a black solid line. For better comparison, the *a priori* emissions (without uncertainties) are also included in the bottom panel.

emissions are lower than the *a priori* values and align with them afterwards. EDGAR *a posteriori* emissions are overall higher than the respective *a priori* emissions. It seems likely that the inversion improves the UNFCCC-ELE overestimation and the EDGAR underestimation, however cannot entirely correct them, as large parts of Africa are poorly covered by the observation network (see Fig. 2). The GAINS *a posteriori* emissions are consistently higher than the GAINS *a priori* emissions but the increases are very small. It seems that the GAINS *a priori* emissions are too small and the inversion tries to increase them but is bound by the low uncertainties assumed, resulting only in minor corrections. Thus, even the GAINS *a posteriori* likely underestimate the true emissions. Note that both, UNFCCC-ELE and EDGAR *a posteriori* emissions show a larger positive trend than the *a priori* emissions. This is also true for the GAINS prior, however differences are very small. The averaged *a posteriori* emissions are close to the EDGAR inventory and show a slowly increasing trend of 0.006 Gg/yr, growing from 0.13 Gg in 2005 to 0.25 Gg in 2021.

South America

For South America (see Fig. A6), the UNFCCC-ELE inventory is more than 10 times higher than the EDGAR and GAINS inventory, and GAINS is on average 38% higher than EDGAR. Due to the narrow uncertainty bands and the poor observa-

https://doi.org/10.5194/egusphere-2024-811
Preprint. Discussion started: 11 April 2024

tional coverage of South America, the inversion results stay close to the *a priori* emissions for EDGAR and GAINS. For UNFCCC-ELE *a posteriori* emissions are smaller than the *a priori* values, especially at the beginning of the study period. We therefore suspect a substantial overestimation by the UNFCCC-ELE *a priori* inventory, given that the UNFCCC-ELE *a posteriori* emissions are partly lowered considerably, despite the poor coverage. Note also that UNFCCC-ELE inversion results show a positive trend of 0.007 Gg/yr, in contrast to the *a priori* inventory.

Australia

Figure A7 shows Australian *a priori* and *a posteriori* SF_6 emissions. All *a priori* emission inventories show similar values throughout the whole study period, well below 0.01 Gg/yr. The relatively wide uncertainty bands result from the chosen minimal *a priori* uncertainty, which is assigned to grid cells with low emissions (see Sec. 3), providing the algorithm with more freedom to deviate from the *a priori* emissions. Nevertheless, inversion results stay close to the *a priori* values. This is to be expected given that there are no SF_6 measurements available within the country, except the Cape Grim station in Tasmania, which predominantly captures clean air from the Indian Ocean.

India

India can be identified as the most challenging region for SF_6 inverse modeling, where *a priori* emission inventories show substantial differences but where emissions could be of global significance (UNFCCC-ELE emissions are about 8% of global emissions in 2021) (Fig. A8). For the UNFCCC-ELE inventory, Indian inversion increments are much higher compared to EDGAR or GAINS (see Fig. 6), resulting in large discrepancies across the *a posteriori* emissions of the different inventories (Fig. A8). This can be related to the poor observational coverage (see Fig. 2) in combination with the relatively high UNFCCC-ELE *a priori* uncertainties, which might allow the algorithm to excessively relate the distant high East Asian measurements to Indian emissions. The GAINS inventory shows by far the lowest Indian *a priori* emission, while inversion results stay very close to the prior values, due to the small *a priori* uncertainty bands. However, all inversions show a much stronger trend in *a posteriori* SF_6 emissions than in the *a priori* emissions. A strong upward trend in SF_6 emissions may indeed be expected given that the installed electric power generation capacity in India has almost quadrupled between 2002 and 2022 (Government of India, 2023)

3.3.5 The global perspective

Our study aimed to incorporate all globally accessible SF_6 observations in the inversion, in combination with long backward trajectories of 50 days to make the best use of the observation network (Vojta et al., 2022). These are optimal conditions for constraining both regional and global SF_6 emissions. To judge the quality of our *a posteriori* global emission, we compare our results with the global emissions calculated by Simmonds et al. (2020) for the years 2005 to 2018 using the AGAGE 12-box model (e.g., Rigby et al., 2013), which we linearly extrapolated until 2021. Such box models are considered to be capable of constraining the global total SF_6 emissions within a few percent, because the average atmospheric growth rate can be measured

https://doi.org/10.5194/egusphere-2024-811
Preprint. Discussion started: 11 April 2024

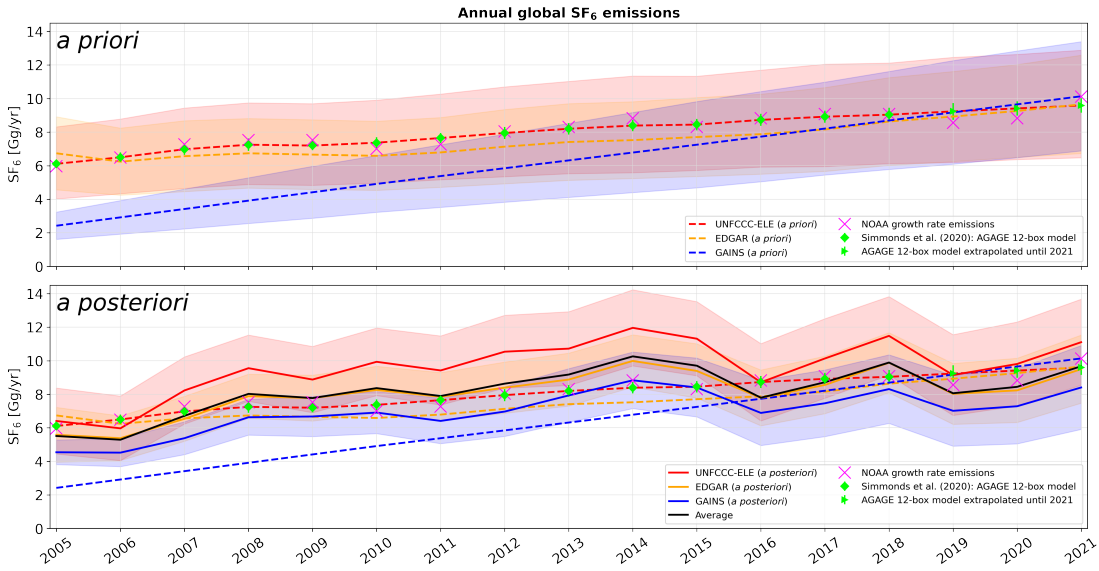

Figure 12. Annual total global *a priori* (dashed lines) and *a posteriori* (solid lines) SF_6 emissions in the period between 2005 and 2021. The *a priori* emissions (top panel) and *a posteriori* emissions (bottom panel) are shown together with their respective 1-σ uncertainties (colored shadings). The bottom panel also shows the average *a posteriori* emissions with a black solid line. Reference values of the AGAGE 12-box model (linearly extrapolated until 2021) and NOAA growth rate emissions are shown with green diamonds/rectangles and purple crosses, respectively. For better comparison, the *a priori* emissions (without uncertainties) are also included in the bottom panel.

accurately and the very long atmospheric lifetime of SF_6 leads to small uncertainties in global total emissions. In addition, we compare our results with global emissions directly calculated from annual increases in globally-averaged atmospheric SF_6 mole fractions provided by NOAA (Lan et al., 2024), which we multiply by the factor $\frac{M_{SF_6}}{M_{air}} \cdot m_{atm}$, where M_{SF_6} and M_{air} represent the molecular weights of SF_6 and air, and m_{atm} is the mass of the atmosphere. We refer to these emissions as "NOAA growth rate emissions".

Figure 12 illustrates the *a priori* and *a posteriori* total global SF_6 emissions, compared to the reference values of the AGAGE 12-box model and the NOAA growth rate emissions. In general, the NOAA growth rate emissions agree well with the box model, however, show more temporal variability. The UNFCCC-ELE *a priori* global emissions coincide per definition with the AGAGE 12-box model (Sec. 2.4), while the UNFCCC-ELE *a posteriori* global emissions are on average 16% higher. The uncertainties stated for the AGAGE 12-box model are only about 3%, with an additional 1% that may be attributed to SF_6 lifetime uncertainties (Simmonds et al., 2020), while our uncertainties are higher. The two estimates are within the combined uncertainties for most individual years but overall our UNFCCC-ELE *a posteriori* global emissions seem to be systematically

https://doi.org/10.5194/egusphere-2024-811
Preprint. Discussion started: 11 April 2024

too high. One possibility for explaining this discrepancy is a potential ocean sink of SF_6 that is not accounted for in the AGAGE 12-box model, leading to a potential underestimation of global emissions in the box model. Ni et al. (2023) recently suggested that such an ocean sink may account for about 7% of the global SF_6 emissions. We tested this hypothesis by allowing for an oceanic sink in our inversion. However, the inversion-derived oceanic *a posteriori* emissions showed either a lot of noise or no fluxes at all (in case of optimizing ocean fluxes in one aggregated oceanic grid cell). Therefore, we were unable to confirm the presence of oceanic SF_6 sinks with our inversion. Yet, another possible explanation for the increase of the global emissions by the inversion is the positivity constraint employed on the emissions over land, which might lead to a positive bias of the *a posteriori* global emissions. However, tests showed that the positivity constraint on the *a posteriori* emissions had very little effect (<1%) on the total global emissions. There is a better explanation for our too-high *a posteriori* emissions. As discussed in Sec. 3.2 the measurement data puts relatively strong constraints on the high emitting regions China, Europe and USA that are responsible for the biggest part of the global SF_6 emissions. National inversion results showed that reported UNFCCC emissions in these regions are predominantly underestimated. Consequently, to match the global total emission, our UNFCCC-ELE inventory attributed too high emissions to countries not reporting their emissions to the UNFCCC (e.g., in South America, Africa or India). Unfortunately, the emissions in these regions are very poorly constrained by the existing observation network (see Fig. 2). As shown in Sec. 3.3.4, the inversion can reduce large biases in these regions but we cannot expect it to remove them completely, and this leads to a positive bias in *a posteriori* global emissions.

The global GAINS *a priori* emissions are lower than all other inventories at the beginning of the study period, and its positive trend is larger and inconsistent with the global atmospheric SF_6 growth postulated by the box model and the NOAA measurements. Due to this rapid increase, the GAINS *a priori* emissions converge with the other emission inventories by the end of the study period. The global GAINS *a posteriori* emissions are much closer to the AGAGE box model results and NOAA growth rate emissions than the *a priori* emissions and align well with their trends. However, *a posteriori* emissions are 15% lower on average, indicating that aggregated emissions are underestimated in poorly monitored areas. This claim can be supported by comparing the global GAINS and Chinese GAINS *a priori* emissions (Fig. 10). At the beginning of the study period GAINS seems to produce realistic Chinese emissions, while at the same time, global emissions are significantly underestimated. After rapid growth, global emissions are close to the reference box model value, while Chinese emissions are significantly overestimated at the end of the study period. In both cases, this suggests an underestimation of the emission residuals between the global and the Chinese emissions. Consequently, GAINS also provides the lowest *a posteriori* emission estimates in almost all shown regions except China, resulting in an underestimation of the global emissions.

In the case of EDGAR, both, the *a priori* and *a posteriori* emissions agree with the reference values of the AGAGE 12-box model and NOAA growth rate emissions within 8-9%. While the *a priori* emissions are on average biased low by 6%, the *a posteriori* emissions show on average almost no bias (0.1%) compared to the reference values. We, therefore, conclude that EDGAR provides a good estimate for the accumulated SF_6 emissions also from poorly monitored areas, well suited for global inversions.

The average of the total global emissions of the different discussed cases provides a very good estimate for the global SF_6 emissions, showing an average bias of +1,4% compared to both, the AGAGE box model and the NOAA growth rate emissions,

https://doi.org/10.5194/egusphere-2024-811
Preprint. Discussion started: 11 April 2024

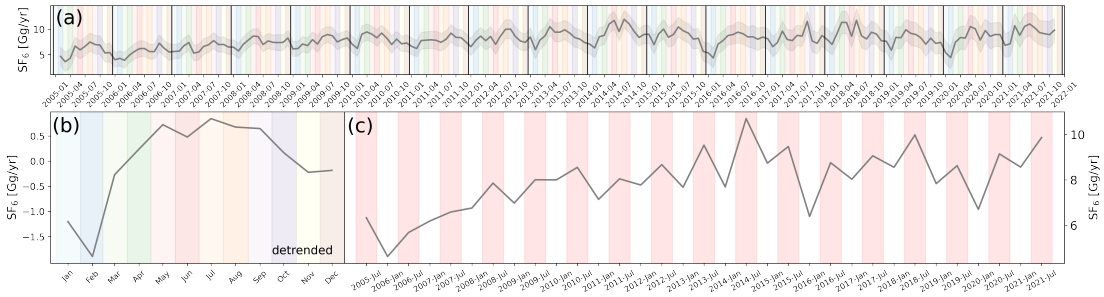

Figure 13. Inversion results from monthly SF_6 inversions for the Northern Hemisphere: (a) monthly *a posteriori* emission in the period 2005-2021, (b) detrended *a posteriori* emissions averaged for each month across all years, and (c) semi-annual *a posteriori* emissions. Distinct months are highlighted with different colors. In panel c, the specified summer (April - September) and winter periods (October - March) are shown in red and white respectively.

with an agreement within 10%. Its trend shows an increase until 2014 followed by a stabilization thereafter (similar to the Chinese emission trend). This is a pattern that can be also observed for the annual increases in the globally-averaged NOAA atmospheric SF_6 mole fractions, and derived emissions. Notice that the average global trend of 0.20 Gg/yr is slightly smaller than for Chinese emissions (0.21 Gg/yr), supporting the finding of An et al. (2024) that Chinese emissions alone have offset the overall decreasing emissions from all other countries.

Despite some potential problems with our inversion setup that can lead to biased *a posteriori* global emissions (as could be clearly seen and explained with the UNFCCC-ELE and GAINS *a priori* emissions), overall our *a posteriori* global emissions seem to be quite accurate, with average biases to the box model and NOAA growth rate emissions of +16%, 0.1%, and -15% for UNFCCC-ELE, EDGAR, and GAINS respectively. Even strongly biased global *a priori* emissions, as for GAINS until 2015, could be brought relatively close to the known values. This is beneficial, since our regional estimates combined are then consistent with the global emissions, which has rarely been achieved before. We attribute this capability of simultaneously constraining both regional as well as global emissions mostly to our long backward calculation period of 50 days (Vojta et al., 2022) and our extensive observation data set. However, the uncertainties of the inversion-derived emissions remain large in India and the Southern Hemisphere. While the aggregated emission in these regions is also quite well known as the residual between global emissions and emissions in well-monitored areas, the distribution of the emissions between and within these regions is less well known. Nevertheless, in most cases, the regional results at least indicate a clear direction in which *a priori* emissions need to be corrected even for these poorly monitored regions.

3.3.6 Seasonality of SF_6 emissions

Our *a priori* emission data sets contain no seasonal information and are assumed to be constant throughout the year. Figure 13 shows the monthly resolved *a posteriori* total SF_6 emissions in the Northern Hemisphere using the E7P *a priori* emission

https://doi.org/10.5194/egusphere-2024-811
Preprint. Discussion started: 11 April 2024

inventory both for the whole time series (Fig. 13a) and as monthly averages over the whole time period, after detrending the time series (Fig. 13b) . While different years have unique seasonal patterns, a notable emission minimum can be observed at the beginning of every year (January/February) and emissions tend to be highest in the summer. This is most clearly seen in the averaged seasonal cycle (Fig. 13b), which shows a minimum in February and a broad maximum from May to September. To better demonstrate the consistency of this seasonal cycle throughout the entire period of our study, Fig. 13c shows semi-annual SF_6 emissions in the Northern Hemisphere, derived by averaging seasonal emissions for winter (October - March) and summer (April - September). In line with panels a) and b), Fig. 13c shows higher emissions in summer than in winter, and this pattern is found in almost every individual year.

However, the seasonal SF_6 emission patterns vary by region (shown for China, USA, and EU in Fig. A9). While there is no clear seasonal cycle in the EU emissions, the Chinese seasonality is similar to the one in the Northern Hemisphere (Fig. 13b). For the USA, we find an even stronger seasonal variation with a May/June peak of SF_6 emissions. This result is in contradiction to Hu et al. (2023), who suggested U.S. SF_6 emissions to peak in winter. Hu et al. (2023) argued that many U.S. companies maintain electrical equipment in the winter rather than in the summer and that cold temperatures can cause sealing materials in electrical equipment to become brittle, resulting in more leaks. We suspect that the contradictions between our two studies are mainly due to the different baseline treatments. As discussed in Sec 3.1, our baseline lowers in the summer for several stations, a feature which we argued is realistic and reflects the transport of different, cleaner air masses over the respective stations. Neglecting such a lowered baseline would lead to underestimated summer emissions. In addition, our inversion results for the USA are mainly driven by the high-frequency measurements from Trinidad Head (THD) and Niwot Ridge (NWR), which have not been used by Hu et al. (2023). A possible explanation for the summer emission maximum might be the seasonal variability of electricity generation, which peaks in summer for most of the Northern Hemisphere. In addition, the increasing SF_6 pressure at high summer temperatures and heat stress of the electrical equipment could lead to more leakage. However, further research on the seasonal cycle of SF_6 emissions is needed to provide a more conclusive answer as to the cause(s).

4 Conclusions

Our inversion study provides observation-based, regionally resolved global SF_6 emission estimates for the period 2005 - 2021, using initial conditions based on an atmospheric SF_6 re-analysis. We further consider different *a priori* emission inventories and use a newly compiled, extensive observation data set along with 50-day LPDM backward simulations to provide accurate estimates of the global, spatially distributed SF_6 emissions. Our main findings are the following:

- The GDB approach is a robust method for estimating initial conditions, especially at challenging measurement stations. We demonstrate that it successfully accounts for meteorological variability (e.g., the Asian summer monsoon) in the baseline, reducing the need for baseline optimization by the inversion. Thus, the information content of the observations can be optimally used for improving the *a priori* emissions.

https://doi.org/10.5194/egusphere-2024-811
Preprint. Discussion started: 11 April 2024

- Our inversion produces regional *a posteriori* emissions that, taken together, are consistent within 10% with the well-known global emissions based on observed atmospheric growth rates. This is a beneficial feature of our inversion setup combining accurate baselines and long (50 days) backward calculation periods.

- The global inversion shows the largest emission improvements in the high emitting regions China, USA, and Europe, where the observation networks used have good coverage. Our annual inversion results are in excellent agreement with several existing regional inversion studies focusing on these three regions.

- Annual U.S. SF_6 emissions strongly decreased from 1.25 Gg in 2005 to 0.48 Gg in 2021, showing a trend of -0.054 Gg/yr. However, these inversion-derived emissions are on average twice as high as the emissions reported to the UNFCCC. Thus, we find that the U.S. are systematically underreporting their SF_6 emissions.

- Annual total SF_6 emissions from EU countries show a decreasing trend of -0.006 Gg/yr, from 0.41 Gg in 2005 to 0.25 Gg in 2021. However, also Europe systematically underreports their SF_6 emissions to UNFCCC.

- The European emissions show a substantial drop in 2018, resulting most likely from the EU's F-gas regulation 517/2014 (European Parliament and Council of the European Union, 2014), which requires new electrical switch gear put into service from 2017 onwards to be equipped with a leak detection system and bans the use of SF_6 for recycling magnesium die-casting alloys from 2018. This is a good example how stringent mitigation measures can successfully reduce SF_6 emissions almost immediately.

- Chinese SF_6 emissions show an increasing trend of 0.21 Gg/yr, growing from 1.28 Gg in 2005 to 5.16 Gg in 2021, with a particularly steep trend until 2014 and a flattening afterwards. The derived trend is slightly steeper than the global total SF_6 emission trend (0.20 Gg/yr), supporting the suggestion that Chinese emissions alone have more than offset the overall decreasing emissions from other countries (An et al., 2024). China's official voluntary reports substantially underestimate their SF_6 emissions (by more than 50%).

- SF_6 emissions in the Southern Hemisphere and some other parts of the world (e.g., India) are hard to constrain due to insufficient coverage by observations. While the inversion most likely reduces large biases of *a priori* estimated emissions in Africa and South America, substantial uncertainties about these emissions remain. However, the EDGAR bottom-up inventory seems to provide a reliable estimate of the aggregated emissions in poorly monitored regions. Nevertheless, more observations in these regions are needed to constrain their regional distribution.

- Despite the above difficulties, our inversions suggest that India's SF_6 emissions have increased substantially, probably doubling since the year 2005.

- Our monthly inversion results show overall higher SF_6 emissions in the summer (April - September) than in winter (October - March) in the Northern Hemisphere, with a distinct minimum at the beginning of the year. While America's SF_6 emissions show a clear peak in May and June and China's emission pattern is similar to the Northern Hemisphere,

https://doi.org/10.5194/egusphere-2024-811
Preprint. Discussion started: 11 April 2024

no clear seasonal pattern is identified for Europe. As our findings for the U.S. are in contradiction to Hu et al. (2023), we suggest that more research on the seasonality of SF_6 emissions is needed.

- On the basis of the inversion results, we can neither confirm nor refute the hypothesis that the ocean sink of SF_6 is a substantial part (up to 7% according to Ni et al. (2023)) of the anthropogenic emission fluxes.
- Since we find that national reports for the U.S., Europe, and China all underreport their SF_6 emissions, while other countries with potentially high emissions (e.g., India) do not report their emissions at all, we suggest that bottom-up methods to determine the emissions need to be refined. This should include a better quantification of the processes causing the emissions that could explain the emission seasonality found here.
- Finally, countries worldwide need to reduce their emissions substantially to avoid further strong increases in the atmospheric burden of the long-lived greenhouse gas SF_6. The stringent regulations recently introduced in Europe are a good example also for other countries - yet are still insufficient to stabilize the atmospheric SF_6 burden.

https://doi.org/10.5194/egusphere-2024-811
Preprint. Discussion started: 11 April 2024

Code and data availability. Daily-resolved global SF_6 mole fraction fields between 2005 and 2021 from the global re-analysis are provided at https://doi.org/10.25365/phaidra.489. The used source code of FLEXPART 10.4 (described in detail by Pisso et al., 2019) can be found at https://doi.org/10.5281/zenodo.3542278. The used FLEXINVERT+ code (described in detail by Thompson and Stohl, 2014) together with setting files are provided at https://doi.org/10.25365/phaidra.488. The source code of FLEXPART 8-CTM-1.1 together with a user's guide can be freely downloaded at https://doi.org/10.5281/zenodo.1249190 (Henne et al., 2018). Atmospheric mole fraction measurements of SF_6 used in this study are freely available from the following sources: AGAGE data: https://agage2.eas.gatech.edu/data_archive/agage/gc-ms-medusa/complete/ (Prinn et al., 2018); Heathfield Tall Tower data: https://catalogue.ceda.ac.uk/uuid/df502fe4715c4177ab5e4e367a99316b (Arnold et al., 2019); Bilsdale Tall Tower data: https://catalogue.ceda.ac.uk/uuid/d2090552c8fe4c16a2fd7d616adc2d9f (O'Doherty et al., 2019); Zeppelin mountain data: https://ebas-data.nilu.no/Pages/DataSetList.aspx?key=4548F59E3CBD48E0A505E8968BD268EB (2005-2010 EBAS, 2024); NOAA/GML Chromatograph for Atmospheric Trace Species (CATS) program: https://gml.noaa.gov/dv/data/index.php?parameter_name=Sulfur%2BHexafluoride&type=Insitu&frequency=Hourly%2Baverages (all stations, hourly data Dutton and Hall, 2023); Monte Cimone, Cape Ochiishi, Izaña, Ragged Point, Zugspitze-Schneefernerhaus: https://gaw.kishou.go.jp/search (di Sarra et al., 2022); Atmospheric SF_6 Dry Air Mole Fractions from the NOAA GML Carbon Cycle Cooperative Global Air Sampling Network: https://gml.noaa.gov/aftp/data/greenhouse_gases/sf6/flask/surface/ (Lan et al., 2023; Dlugokencky et al., 2020); NOAA Global Greenhouse Gas Reference Network provided flask-air PFP sample measurements of SF_6 at Tall Towers and other Continental Sites https://gml.noaa.gov/aftp/data/greenhouse_gases/sf6/pfp/surface/ (Andrews et al., 2022); Atmospheric Sulfur Hexafluoride Dry Air Mole Fractions from the NOAA GML Carbon Cycle Aircraft Vertical Profile Network https://gml.noaa.gov/aftp/data/greenhouse_gases/sf6/pfp/aircraft/: (McKain et al., 2022); NOAA ObsPACK SF_6 data: https://gml.noaa.gov/ccgg/obspack/data.php?id=obspack_sf6_1_v2.1_2018-07-10 (NOAA Carbon Cycle Group ObsPack Team, 2018); IAGOS-CARIBIC Aircraft measurements: https://zenodo.org/records/10495039 (Schuck and Obersteiner, 2024); NOAA/ESRL/GMD/HATS Trace Gas Measurements from Airborne Platforms: https://gml.noaa.gov/aftp/data/hats/airborne/ (Elkins et al., 2020). For the observations at BIK (Popa et al., 2010), BRM (Rust et al., 2022), GSN (Kim et al., 2012), and HAT (Saikawa et al., 2012) we refer to E. Popa <epopa2@yahoo.com>, S. Reimann <stefan.reimann@empa.ch>, S. Park <sparky@knu.ac.kr>, and T. Saito <saito.takuya@nies.go.jp>, respectivley.

Author contributions. MV, AP, and AS designed the study. MV performed the FLEXPART, FLEXPART CTM, and FLEXINVERT+ simulations. RT helped with the FLEXINVERT+ setup and simulation issues. MV made the figures with contributions from SA. JM, SP and GL provided atmospheric observation data. PP and FL provided GAINS emissions estimates. MV wrote the text with input from AP, SA, SP, GL, PP, FL, XL, JM, RT, and AS.

Competing interests. The authors declare that they have no conflict of interest.

Acknowledgements. We thank the whole AGAGE team for providing measurement data, including C.M.Harth, J. Mühle, P.K. Salameh, and R.F. Weiss (Scripps Institution of Oceanography, UCSD); P.B. Krummel, P.J. Fraser, L.P. Steele (CSIRO Environment); R.H.(J.) Wang (Georgia Institute of Technology); S. O'Doherty, D. Young, K.M. Stanley (University of Bristol); M.K. Vollmer, S. Reimann (EMPA: Swiss

https://doi.org/10.5194/egusphere-2024-811
Preprint. Discussion started: 11 April 2024

Federal Laboratories for Materials Science and Technology); C.R. Lunder, O. Hermanson (NILU: Norwegian Institute for Air Research) and particularly all station managers and station operators. AGAGE operations at Mace Head, Trinidad Head, Cape Matatula, Ragged Point, and Cape Grim are supported by NASA (USA) grants to MIT (NAG5-12669, NNX07AE89G, NNX11AF17G, NNX16AC98G) and SIO (NNX07AE87G, NNX07AF09G, NNX11AF15G, NNX11AF16G, NNX16AC96G, NNX16AC97G), and also by: Department for Business, Energy & Industrial Strategy (BEIS, UK), Contract 5488/11/2021 to the University of Bristol for Mace Head and NOAA (USA), contract 1305M319CNRMJ0028 to the University of Bristol for Ragged Point; CSIRO, BoM, DCCEEW, RRA (Australia); NILU (Norway); KNU (Korea); CMA (China); NIES (Japan); and Urbino University (Italy). For Jungfraujoch funding is acknowledged for the project HALCLIM/CLIMGAS-CH by the Swiss Federal Office for the Environment (FOEN) and for ICOS (Integrated Carbon Observation System) by the Swiss National Science Foundation. In addition, measurements are supported by the International Foundation High Altitude Research Stations Jungfraujoch and Gornergrat (HFSJG). The Commonwealth Scientific and Industrial Research Organisation (CSIRO, Australia) and Bureau of Meteorology (Australia) are thanked for their ongoing long-term support and funding of the Cape Grim station and the Cape Grim science program. Operations of the Gosan station on Jeju Island, South Korea were supported by the National Research Foundation of Korea grant funded by the Korean government MSIT no. RS-2023-00229318. We also thank the NOAA Global Monitoring Laboratory for providing access to their data, including G. Dutton, J.W. Elkins, F. Moore, E. Hintsa, D. Hurst, B. Hall, K. McKain, S. Montzka, B. Miller, C. Sweeney, E. Dlugokencky, A. Andrews, D. Nance, C. M. Harth, and key partners: L. Huang (EC), K. Davis (PSU), Observations collected in the Southern Great Plains (SGP) by S. Biraud (Lawrence Berkeley National Laboratory, USA) were supported by the Office of Biological and Environmental Research of the US Department of Energy under contract DE-AC02-05CH11231 as part of the Atmospheric Radiation Measurement Program (ARM) and Environmental System Science (ESS) Program.

We further acknowledge the following people and institutions for sharing their observation data: T. Saito (National Institute for Environmental Studies, Japan); E. Cuevas (State Meteorological Agency, Spain); D. Say, (University of Bristol), J. Arduini (University of Urbino), C. Couret (German Environment Agency), Elena Popa (Utrecht University), S. Sugawara (Miyagi University of Education, Japan), A. Rauthe, J. Williams (Max Planck Institute for Chemistry), T. Schuck (Goethe University Frankfurt), F. Obersteiner (Karlsruhe Institute of Technology), C. Couret (German Federal Environmental Agency), L. Gatti (Instituto Nacional de Pesquisas Espaciais).

The computational results presented have been achieved in part using the Vienna Scientific Cluster (VSC), Project 71878: Demonstration of a Lagrangian re-analysis, to which we are grateful. Further acknowledgment is made for the use of ECMWF's computing and archive facilities provided through a special project (spatvojt) in this research. The study was supported by EYE-CLIMA, a European Union's Horizon Europe research and innovation programme under grant agreement No. 101081395. We thank L. Hu and C. Groot Zwaaftink for the discussions. We further thank M. Dütsch, L. Bakels, S. Bucci, K. Baier, D. Tatsii, An. Raju, R. Subramanian, S. Wittig, O. Nabavi, I. Evangelou, M. Blaschek, A. Skorokhod, P. Seibert (University of Vienna) for their support.

https://doi.org/10.5194/egusphere-2024-811
Preprint. Discussion started: 11 April 2024

Table A1. Inversion results for the annual SF_6 emissions from the United States of America in the period 2005-2021. Annual emissions are shown together with their 1-σ uncertainties, for different *a priori* emissions inventories. We also provide an average of the inversion results, while respective uncertainties represent the minimum and maximum uncertainty limits across the results.

annual total SF_6emissions from the United States of America				
year	**UNFCCC-ELE** [Gg/yr]	**EDGAR** [Gg/yr]	**GAINS** [Gg/yr]	**average** [Gg/yr]
2005	1.21 ± 0.16	1.44 ± 0.34	1.11 ± 0.11	1.25 [1.00, 1.78]
2006	1.34 ± 0.15	1.58 ± 0.32	1.24 ± 0.10	1.38 [1.14, 1.90]
2007	1.14 ± 0.13	1.38 ± 0.30	1.04 ± 0.09	1.19 [0.95, 1.67]
2008	1.24 ± 0.12	1.51 ± 0.27	1.09 ± 0.08	1.28 [1.01, 1.78]
2009	0.99 ± 0.10	1.16 ± 0.26	0.93 ± 0.08	1.03 [0.86, 1.42]
2010	0.86 ± 0.10	1.13 ± 0.27	0.80 ± 0.07	0.93 [0.73, 1.39]
2011	0.75 ± 0.10	1.00 ± 0.27	0.68 ± 0.07	0.81 [0.61, 1.27]
2012	0.62 ± 0.09	0.90 ± 0.28	0.57 ± 0.08	0.70 [0.50, 1.18]
2013	0.58 ± 0.09	0.84 ± 0.27	0.51 ± 0.07	0.64 [0.44, 1.11]
2014	0.52 ± 0.08	0.63 ± 0.27	0.44 ± 0.06	0.53 [0.36, 0.90]
2015	0.52 ± 0.08	0.67 ± 0.25	0.45 ± 0.06	0.55 [0.38, 0.92]
2016	0.72 ± 0.08	0.96 ± 0.24	0.63 ± 0.06	0.77 [0.57, 1.21]
2017	0.58 ± 0.08	0.80 ± 0.24	0.52 ± 0.06	0.63 [0.45, 1.04]
2018	0.55 ± 0.08	0.80 ± 0.25	0.49 ± 0.06	0.61 [0.42, 1.05]
2019	0.53 ± 0.08	0.75 ± 0.26	0.46 ± 0.06	0.58 [0.40, 1.02]
2020	0.44 ± 0.08	0.64 ± 0.25	0.39 ± 0.06	0.49 [0.32, 0.89]
2021	0.45 ± 0.09	0.62 ± 0.27	0.38 ± 0.06	0.48 [0.32, 0.89]

https://doi.org/10.5194/egusphere-2024-811
Preprint. Discussion started: 11 April 2024

Table A2. Inversion results for the annual total SF_6 emissions from EU countries in the period 2005-2021. Annual emissions are shown together with their 1-σ uncertainties, for different *a priori* emissions inventories. We also provide an average of the inversion results, while respective uncertainties represent the minimum and maximum uncertainty limits across the results.

annual total SF_6 emissions from EU countries				
year	**UNFCCC-ELE** [Gg/yr]	**EDGAR** [Gg/yr]	**GAINS** [Gg/yr]	**average** [Gg/yr]
2005	0.43 ± 0.09	0.38 ± 0.09	0.43 ± 0.08	0.41 [0.29, 0.52]
2006	0.39 ± 0.09	0.35 ± 0.08	0.39 ± 0.07	0.38 [0.27, 0.47]
2007	0.35 ± 0.08	0.34 ± 0.08	0.36 ± 0.07	0.35 [0.26, 0.44]
2008	0.37 ± 0.08	0.35 ± 0.08	0.36 ± 0.07	0.36 [0.27, 0.46]
2009	0.37 ± 0.09	0.34 ± 0.09	0.38 ± 0.08	0.36 [0.25, 0.46]
2010	0.40 ± 0.08	0.37 ± 0.08	0.40 ± 0.07	0.39 [0.29, 0.48]
2011	0.36 ± 0.08	0.30 ± 0.08	0.35 ± 0.08	0.34 [0.22, 0.44]
2012	0.38 ± 0.08	0.37 ± 0.08	0.40 ± 0.07	0.38 [0.29, 0.48]
2013	0.29 ± 0.07	0.29 ± 0.07	0.32 ± 0.07	0.30 [0.22, 0.39]
2014	0.33 ± 0.07	0.32 ± 0.07	0.36 ± 0.06	0.34 [0.26, 0.42]
2015	0.31 ± 0.07	0.31 ± 0.08	0.32 ± 0.07	0.31 [0.23, 0.39]
2016	0.37 ± 0.07	0.35 ± 0.07	0.37 ± 0.07	0.36 [0.27, 0.44]
2017	0.39 ± 0.08	0.37 ± 0.08	0.39 ± 0.07	0.38 [0.29, 0.47]
2018	0.26 ± 0.07	0.25 ± 0.08	0.28 ± 0.06	0.26 [0.18, 0.34]
2019	0.28 ± 0.07	0.27 ± 0.07	0.30 ± 0.06	0.28 [0.20, 0.37]
2020	0.32 ± 0.06	0.32 ± 0.07	0.34 ± 0.06	0.33 [0.25, 0.40]
2021	0.25 ± 0.06	0.25 ± 0.08	0.26 ± 0.07	0.25 [0.16, 0.33]

https://doi.org/10.5194/egusphere-2024-811
Preprint. Discussion started: 11 April 2024

Table A3. Inversion results for the annual Chinese SF_6 emissions in the period 2005-2021. Annual emissions are shown together with their 1-σ uncertainties, for different *a priori* emissions inventories. We also provide an average of the inversion results, and an average excluding the GAINS-derived inversion, while uncertainties represent the minimum and maximum uncertainty limits across the respective inversions results.

annual total SF_6emissions from China					
year	**UNFCCC-ELE** [Gg/yr]	**EDGAR** [Gg/yr]	**GAINS** [Gg/yr]	**average** [Gg/yr]	**average without GAINS** [Gg/yr]
2005	1.35 ± 0.45	1.21 ± 0.32	2.13 ± 0.31	1.56 [0.89, 2.44]	1.28 [0.89, 1.80]
2006	1.14 ± 0.36	1.08 ± 0.33	1.78 ± 0.42	1.33 [0.75, 2.20]	1.11 [0.75, 1.50]
2007	2.33 ± 0.51	2.26 ± 0.37	2.97 ± 0.58	2.52 [1.82, 3.55]	2.29 [1.82, 2.84]
2008	2.78 ± 0.51	2.72 ± 0.37	3.53 ± 0.68	3.01 [2.27, 4.22]	2.75 [2.27, 3.29]
2009	3.24 ± 0.59	3.17 ± 0.42	3.84 ± 0.80	3.42 [2.66, 4.64]	3.21 [2.66, 3.83]
2010	3.13 ± 0.55	3.12 ± 0.46	3.99 ± 0.87	3.41 [2.59, 4.86]	3.13 [2.59, 3.68]
2011	2.91 ± 0.60	2.95 ± 0.50	3.81 ± 0.97	3.22 [2.32, 4.78]	2.93 [2.32, 3.51]
2012	3.44 ± 0.62	3.50 ± 0.54	4.27 ± 1.10	3.73 [2.82, 5.37]	3.47 [2.82, 4.05]
2013	4.14 ± 0.69	4.19 ± 0.58	5.42 ± 1.21	4.59 [3.45, 6.64]	4.17 [3.45, 4.84]
2014	4.89 ± 0.69	4.96 ± 0.60	6.09 ± 1.32	5.31 [4.20, 7.41]	4.92 [4.20, 5.57]
2015	4.53 ± 0.73	4.61 ± 0.65	5.96 ± 1.38	5.03 [3.80, 7.34]	4.57 [3.80, 5.26]
2016	3.60 ± 0.80	3.57 ± 0.71	4.37 ± 1.58	3.85 [2.79, 5.95]	3.58 [2.79, 4.40]
2017	4.10 ± 0.81	4.15 ± 0.74	5.21 ± 1.60	4.49 [3.29, 6.82]	4.12 [3.29, 4.90]
2018	4.72 ± 0.86	4.82 ± 0.79	6.02 ± 1.67	5.18 [3.86, 7.70]	4.77 [3.86, 5.60]
2019	3.99 ± 0.85	4.00 ± 0.79	4.85 ± 1.72	4.28 [3.13, 6.57]	3.99 [3.13, 4.84]
2020	4.38 ± 0.96	4.48 ± 0.89	5.27 ± 1.86	4.71 [3.41, 7.13]	4.43 [3.42, 5.38]
2021	5.12 ± 1.00	5.21 ± 0.94	6.41 ± 2.09	5.58 [4.12, 8.50]	5.16 [4.12, 6.15]

https://doi.org/10.5194/egusphere-2024-811
Preprint. Discussion started: 11 April 2024

Table A4. Inversion results for the annual global total SF_6 emissions in the period 2005-2021. Annual emissions are shown together with their 1-σ uncertainties, for different *a priori* emissions inventories. We also provide an average of the inversion results, while respective uncertainties represent the minimum and maximum uncertainty limits across the results.

Annual global total SF_6 emissions				
year	**UNFCCC-ELE** [Gg/yr]	**EDGAR** [Gg/yr]	**GAINS** [Gg/yr]	**average** [Gg/yr]
2005	6.41 ± 1.96	5.59 ± 1.63	4.54 ± 0.73	5.51 [3.81, 8.37]
2006	5.97 ± 1.92	5.38 ± 1.33	4.52 ± 0.83	5.29 [3.69, 7.89]
2007	8.23 ± 2.00	6.54 ± 1.34	5.38 ± 0.98	6.72 [4.40, 10.23]
2008	9.56 ± 1.97	7.89 ± 1.31	6.63 ± 1.06	8.02 [5.57, 11.53]
2009	8.88 ± 1.97	7.77 ± 1.37	6.68 ± 1.19	7.78 [5.48, 10.85]
2010	9.94 ± 2.01	8.26 ± 1.41	6.91 ± 1.25	8.37 [5.66, 11.95]
2011	9.42 ± 2.06	7.85 ± 1.44	6.41 ± 1.35	7.90 [5.06, 11.48]
2012	10.54 ± 2.17	8.39 ± 1.53	6.97 ± 1.48	8.63 [5.49, 12.71]
2013	10.72 ± 2.20	8.88 ± 1.58	7.93 ± 1.60	9.18 [6.34, 12.92]
2014	11.96 ± 2.27	9.99 ± 1.56	8.83 ± 1.68	10.26 [7.15, 14.23]
2015	11.31 ± 2.21	9.39 ± 1.62	8.41 ± 1.75	9.70 [6.65, 13.52]
2016	8.72 ± 2.30	7.79 ± 1.66	6.89 ± 1.94	7.80 [4.95, 11.02]
2017	10.14 ± 2.37	8.56 ± 1.71	7.46 ± 1.98	8.72 [5.48, 12.50]
2018	11.48 ± 2.34	9.88 ± 1.79	8.31 ± 2.04	9.89 [6.27, 13.82]
2019	9.15 ± 2.41	8.02 ± 1.81	7.02 ± 2.11	8.06 [4.91, 11.55]
2020	9.81 ± 2.50	8.23 ± 1.91	7.29 ± 2.24	8.44 [5.05, 12.31]
2021	11.11 ± 2.56	9.50 ± 2.03	8.41 ± 2.50	9.67 [5.91, 13.67]

100

https://doi.org/10.5194/egusphere-2024-811
Preprint. Discussion started: 11 April 2024

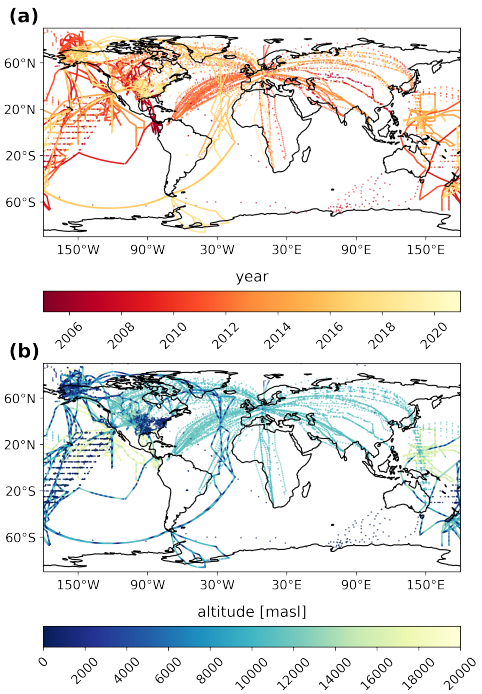

Figure A1. Observations from aircraft and ship campaigns from 2005 - 2021. The color bars indicate (a) the measurement date and (b) the altitude of the respective observations.

https://doi.org/10.5194/egusphere-2024-811
Preprint. Discussion started: 11 April 2024

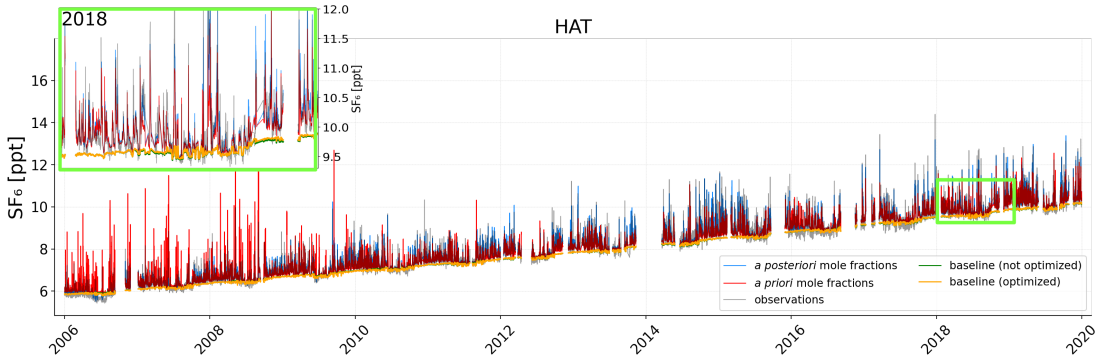

Figure A2. Mole fraction time series at the Hateruma (Japan) measurement station. Red lines represent the modeled *a priori* mole fractions calculated with the UP *a priori* emissions and blue lines represent the modeled *a posteriori* mole fractions. The green line illustrates the baseline derived by the GDB method and the orange line shows the optimized baseline. The grey line represents the observed mole fractions. The inset panel zooms into the year 2018, as illustrated by the lightgreen rectangle.

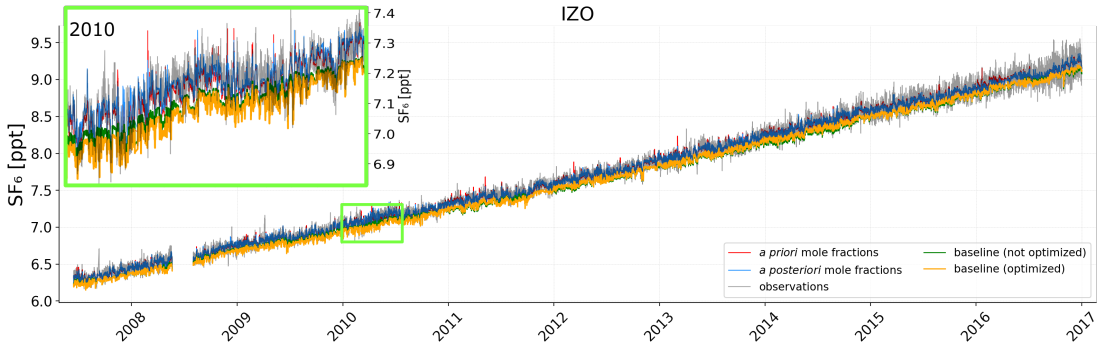

Figure A3. Mole fraction time series at the Izaña (Tenerife) measurement station. Red lines represent the modeled *a priori* mole fractions calculated with the UP *a priori* emissions and blue lines represent the modeled *a posteriori* mole fractions. The green line illustrates the baseline derived by the GDB method and the orange line shows the optimized baseline. The grey line represents the observed mole fractions. The inset panel zooms into the year 2010, as illustrated by the lightgreen rectangle.

https://doi.org/10.5194/egusphere-2024-811
Preprint. Discussion started: 11 April 2024

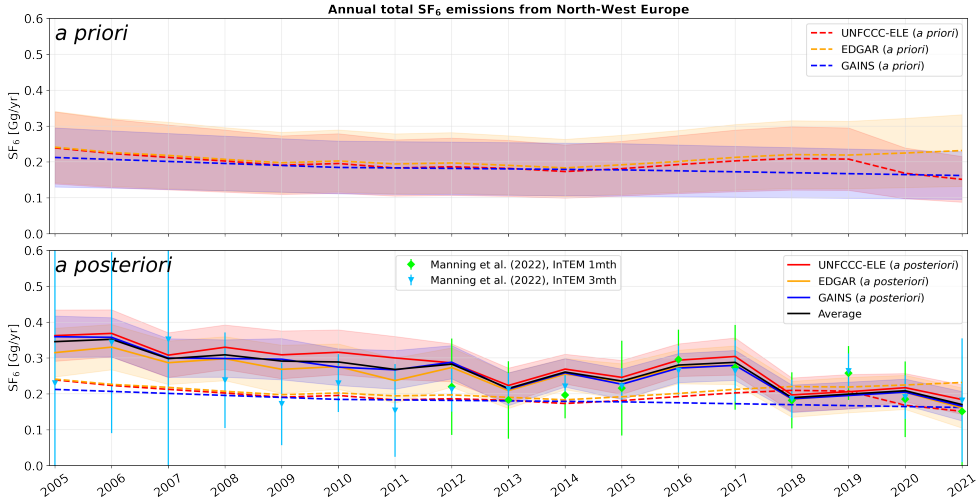

Figure A4. Annual *a priori* (dashed lines) and *a posteriori* (solid lines) SF_6 emissions from North-West Europe, shown for the period between 2005 and 2021 when using different *a priori* emissions (UNFCCC-ELE red, EDGAR orange, GAINS blue). The *a priori* emissions (top panel) and *a posteriori* emissions (bottom panel) are shown together with their respective 1-σ uncertainties (colored shadings). The bottom panel also shows the average *a posteriori* emissions with a black solid line. The blue rectangles and the green diamonds represent the results from Manning et al. (2022) using the InTEM (Inversion Technique for Emissions Modelling) model with inversion time frames set to 3- and 1-months, respectively. For better comparison, the *a priori* emissions (without uncertainties) are also included in the bottom panel.

https://doi.org/10.5194/egusphere-2024-811
Preprint. Discussion started: 11 April 2024

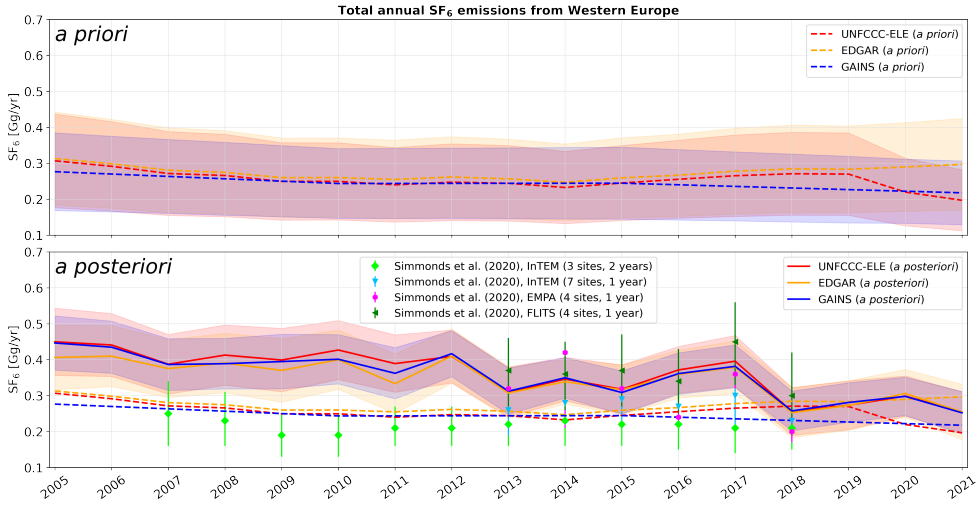

Figure A5. Annual *a priori* (dashed lines) and *a posteriori* (solid lines) SF_6 emissions from Western Europe, shown for the period between 2005 and 2021 when using different *a priori* emissions (UNFCCC-ELE red, EDGAR orange, GAINS blue). The *a priori* emissions (top panel) and *a posteriori* emissions (bottom panel) are shown together with their respective 1-σ uncertainties (colored shadings). The bottom panel also shows the average *a posteriori* emissions (black solid line), together with the results from Simmonds et al. (2020), using four different inversion setups.

https://doi.org/10.5194/egusphere-2024-811
Preprint. Discussion started: 11 April 2024

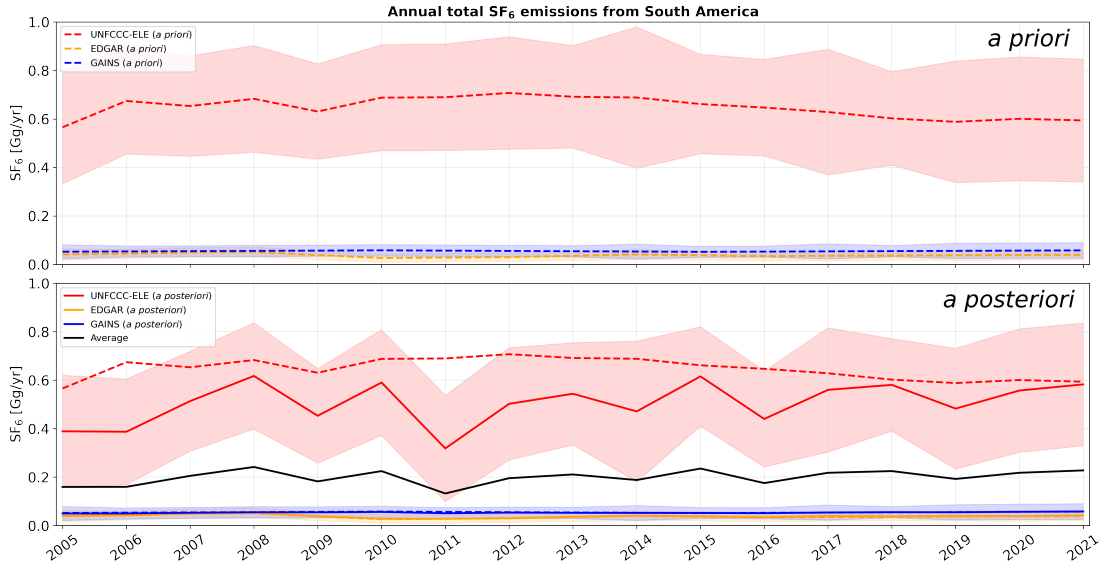

Figure A6. Annual *a priori* (dashed lines) and *a posteriori* (solid lines) SF_6 emissions from South America, shown for the period between 2005 and 2021 when using different *a priori* emissions (UNFCCC-ELE red, EDGAR orange, GAINS blue). The *a priori* emissions (top panel) and *a posteriori* emissions (bottom panel) are shown together with their respective 1-σ uncertainties (colored shadings). The bottom panel also shows the average *a posteriori* emissions with a black solid line. For better comparison, the *a priori* emissions (without uncertainties) are also included in the bottom panel.

https://doi.org/10.5194/egusphere-2024-811
Preprint. Discussion started: 11 April 2024

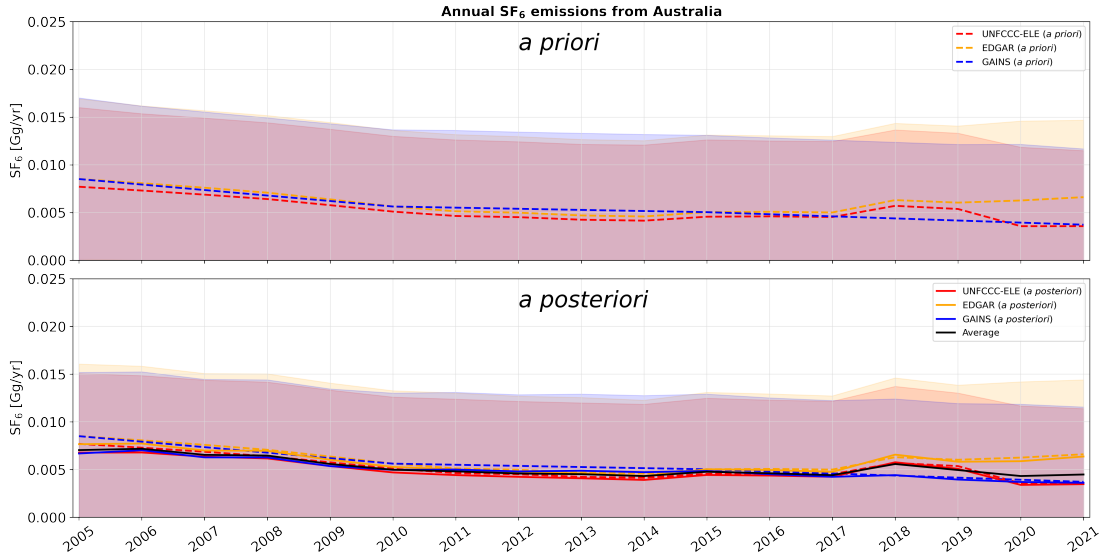

Figure A7. Annual *a priori* (dashed lines) and *a posteriori* (solid lines) SF_6 emissions from Australia, shown for the period between 2005 and 2021 when using different *a priori* emissions (UNFCCC-ELE red, EDGAR orange, GAINS blue).The *a priori* emissions (top panel) and *a posteriori* emissions (bottom panel) are shown together with their respective 1-σ uncertainties (colored shadings). The bottom panel also shows the average *a posteriori* emissions with a black solid line. For better comparison, the *a priori* emissions (without uncertainties) are also included in the bottom panel.

https://doi.org/10.5194/egusphere-2024-811
Preprint. Discussion started: 11 April 2024

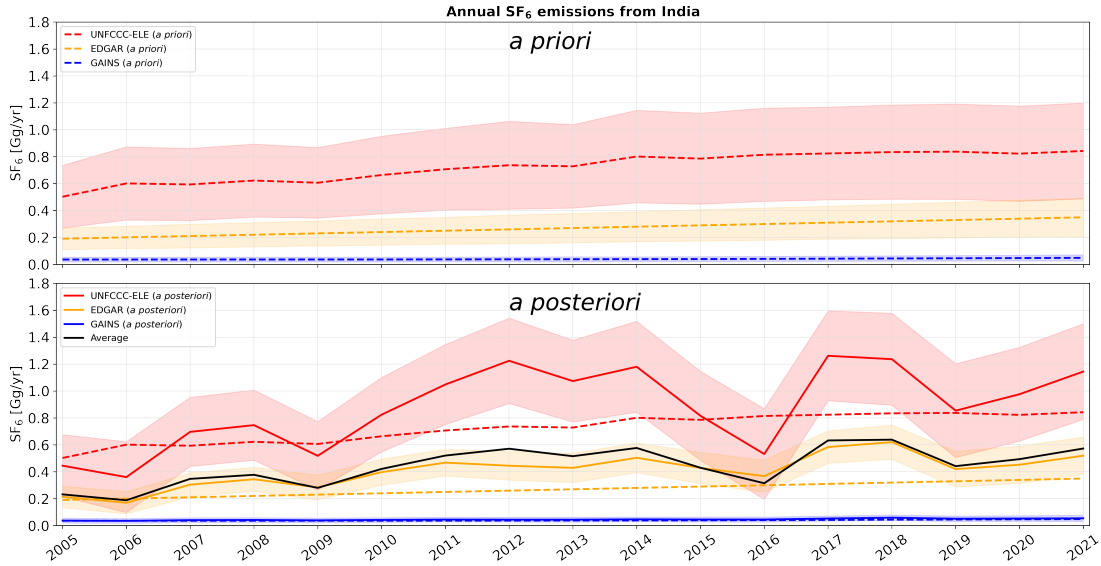

Figure A8. Annual *a priori* (dashed lines) and *a posteriori* (solid lines) SF_6 emissions from India, shown for the period between 2005 and 2021 when using different *a priori* emissions (UNFCCC-ELE red, EDGAR orange, GAINS blue). The *a priori* emissions (top panel) and *a posteriori* emissions (bottom panel) are shown together with their respective 1-σ uncertainties (colored shadings). The bottom panel also shows the average *a posteriori* emissions with a black solid line. For better comparison, the *a priori* emissions (without uncertainties) are also included in the bottom panel.

https://doi.org/10.5194/egusphere-2024-811
Preprint. Discussion started: 11 April 2024

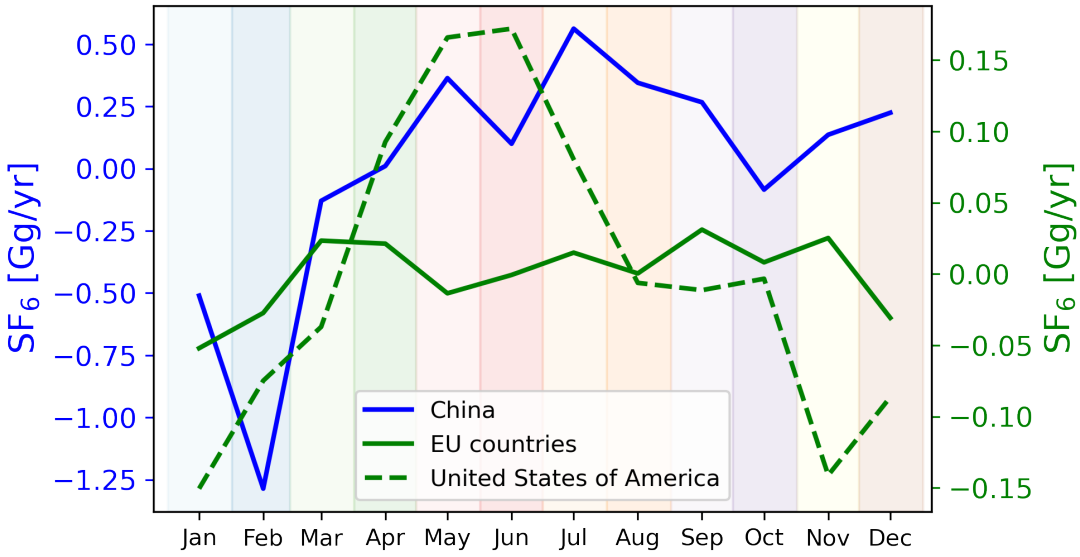

Figure A9. Seasonal variation of SF_6 emissions in China, the United States of America, and EU countries. The figure shows detrended monthly inversion results averaged for each month across all years in the period 2005-2021

https://doi.org/10.5194/egusphere-2024-811
Preprint. Discussion started: 11 April 2024

References

An, M., Prinn, R., Western, L., Yao, B., Hu, J., and Rigby, M.: Emissions of SF6 in China inferred from atmospheric observations, Tech. rep., Copernicus Meetings, https://doi.org/10.5194/egusphere-egu23-7010, 2023.

An, M., Prinn, R., Western, L., Zhao, X., Yao, B., Hu, J., Ganesan, A. L., Mühle, J., Weiss, R. F., Krummel, P. B., O'Doherty, S., Young, D., and Rigby, M.: Sustained growth of sulfur hexafluoride emissions in China inferred from atmospheric observations. Nat Commun 15, 1997, https://doi.org/10.1038/s41467-024-46084-3, 2024.

Andersen, O., Gilpin, G., and Andrae, A. S.: Cradle-to-gate life cycle assessment of the dry etching step in the manufacturing of photovoltaic cells, AIMS Energy, 2, 410–423, https://doi.org/10.3934/energy.2014.4.410, 2014.

Andrews, A., Crotwell, A., Crotwell, M., Handley, P., Higgs, J., Kofler, J., Lan, X., Legard, T., Madronich, M., McKain, K., Miller, J., Moglia, E., Mund, J., Neff, D., Newberger, T., Petron, G., Turnbull, J., Vimont, I., Wolter, S., and NOAA Global Monitoring Laboratory: NOAA Global Greenhouse Gas Reference Network Flask-Air PFP Sample Measurements of SF6 at Tall Tower and other Continental Sites, 2005-Present [Data set]., Version: 2022-11-01., NOAA GML., https://doi.org/10.15138/5R14-K382, 2022.

Arnold, T., Rennick, C., O'Doherty, S., Say, D., Young, D., Stavert, A., and Wenger, A.: Deriving Emissions related to Climate Change Network: CO2, CH4, N2O, SF6 and CO measurements from Heathfield Tall Tower, East Sussex. Centre for Environmental Data Analysis, https://catalogue.ceda.ac.uk/uuid/df502fe4715c4177ab5e4e367a99316b, last accessed: 2024-02-1, 2019.

Brinton, D. A. and Wilkinson, C. P.: Retinal Detachment: Priniciples and Practice, vol. 1, Oxford University Press, 2009.

Brunner, D., Arnold, T., Henne, S., Manning, A., Thompson, R. L., Maione, M., O'Doherty, S., and Reimann, S.: Comparison of four inverse modelling systems applied to the estimation of HFC-125, HFC-134a, and SF_6 emissions over Europe, Atmospheric Chemistry and Physics, 17, 10 651–10 674, https://doi.org/10.5194/acp-17-10651-2017, 2017.

CEDA: World Data Centre for Greenhouse Gases, https://archive.ceda.ac.uk//, last accessed: 2023-09-10, 2023.

China: The People's Republic of China second national communication on climate change, https://unfccc.int/resource/docs/natc/chnnc2e.pdf, last accessed: 2024-01-27, 2012.

China: The People's Republic of China first biennial update report on climate change, https://unfccc.int/sites/default/files/resource/3_China_FSV_Presentation.pdf, last accessed: 2024-01-27, 2016.

China: The People's Republic of China third national communication on climate change, https://english.mee.gov.cn/Resources/Reports/reports/201907/P020190702566752327206.pdf, last accessed: 2024-01-27, 2018a.

China: The People's Republic of China second biennial update report on climate change, https://unfccc.int/sites/default/files/resource/China%202BUR_English.pdf, last accessed: 2024-01-27, 2018b.

China: The People's Republic of China fourth national communication on climate change, https://unfccc.int/sites/default/files/resource/China_NC4_English.pdf, last accessed: 2024-01-27, 2023a.

China: The People's Republic of China third biennial update report on climate change, https://unfccc.int/sites/default/files/resource/China_BUR3_English.pdf, last accessed: 2024-01-27, 2023b.

CIESIN: Center for International Earth Science Information Network, Columbia University, Gridded Population of the World, Version 4 (GPWv4): Population Density, Revision 11. Palisades, NY: NASA Socioeconomic Data and Applications Center (SEDAC), https://doi.org/10.7927/H49C6VHW, last accessed: 2023-04-27, 2018.

https://doi.org/10.5194/egusphere-2024-811
Preprint. Discussion started: 11 April 2024

Crippa, M., Guizzardi, D., Solazzo, E., Muntean, M., Schaaf, E., Monforti-Ferrario, F., Banja, M., Olivier, J., Grassi, G., Rossi, S., and Vignati, E.: GHG emissions of all world countries - 2021 Report, EUR 30831 EN, Publications Office of the European Union, Luxembourg, ISBN 978-92-76-41547-3, https://doi.org/10.2760/173513, 2021.

Crippa, M., D., G., Pagani, F., Banja, M., Muntean, M., E., S., Becker, W., Monforti-Ferrario, F., Quadrelli, R., Risquez Martin, A., Taghavi-Moharamli, P., Köykkä, J., Grassi, G., Rossi, S., Brandao De Melo, J., Oom, D., Branco, A., San-Miguel, J., and Vignati, E.: GHG emissions of all world countries, Publications Office of the European Union, Luxembourg, 2023, https://doi.org/10.2760/953322, 2023.

Cui, Z., Li, Y., Xiao, S., Tian, S., Tang, J., Hao, Y., and Zhang, X.: Recent progresses, challenges and proposals on SF6 emission reduction approaches, Science of The Total Environment, p. 167347, https://doi.org/10.1016/j.scitotenv.2023.167347, 2024.

di Sarra, A., Hall, B. D., Dylag, C., Couret, C., Lunder, C., Sweeney, C., Sferlazzo, D., Say, D., Mondeel, D. J., Young, D., Dlugokencky, E., Cuevas, E., Meinhardt, F., Technos, G. E., Dutton, G. S., Lee, H., Nance, J. D., Arduini, J., Pitt, J., Tsuboi, K., Stanley, K., Gatti, L. V., Steinbacher, M., Vollmer, M., Krummel, P., Rivas, P., Weiss, R. F., Wang, R., Chiavarini, S., Piacentino, S., O'Doherty, S., Reimann, S., A. Montzka, S., Saito, T., and Lan, X.: All SF6 data contributed to WDCGG by GAW stations and mobiles by 2022-09-05, https://doi.org/10.50849/WDCGG_SF6_ALL_2022, 2022.

Dlugokencky, E., Crotwell, A., Mund, J., Crotwell, M., and Thoning, K.: Atmospheric Sulfur Hexafluoride Dry Air Mole Fractions from the NOAA GML Carbon Cycle Cooperative Global Air Sampling Network, 1997-2019, Version: 2020-07, https://doi.org/10.15138/p646-pa37, 2020.

Dutton, G. and Hall, B.: Global Atmospheric Sulfur hexaflouride Dry Air Mole Fractions from the NOAA GML Halocarbons in situ Network, 1998-2023, Version: 2023-04-13, https://doi.org/10.7289/V5X0659V, 2023.

EBAS: Measured sulfur hexafluoride mole fractions at the Zeppelin mountain (Ny-Ålesund) station [data-set] (2005 - 2010), https://ebas-data.nilu.no/Pages/DataSetList.aspx?key=4548F59E3CBD48E0A505E8968BD268EB, last accessed: 2024-02-1, 2024.

EDGAR: (Emissions Database for Global Atmospheric Research) Community GHG Database version 7.0, European Commission, Joint Research Centre (JRC), the International Energy Agency (IEA), Datasets, https://edgar.jrc.ec.europa.eu/dataset_ghg70, last accessed: 2024-01-27, 2022.

EDGAR: (Emissions Database for Global Atmospheric Research) Community GHG Database version 8.0, European Commission, Joint Research Centre (JRC), the International Energy Agency (IEA), Datasets, https://edgar.jrc.ec.europa.eu/dataset_ghg80, last accessed: 2024-01-27, 2023.

Elkins, J. W., Moore, F., Hintsa, E., Hurst, D., Hall, B., Montzka, S., Miller, B., Dutton, G., and Nance, D.: HATS Airborne Projects, www.esrl.noaa.gov/gmd/hats/airborne/, last accessed: 2024-02-1, 2020.

Elvidge, C. D., Zhizhin, M., Ghosh, T., Hsu, F.-C., and Taneja, J.: Annual time series of global VIIRS nighttime lights derived from monthly averages: 2012 to 2019, Remote Sensing, 13, 922, https://doi.org/10.3390/rs13050922, 2021.

EPA: Assessment of the Use of Sulfur Hexafluoride (SF 6) Gas Insulated Switchgears (GIS) within the Offshore Wind . Environmental Protection Agency (EPA), Eastern Research Group, https://www.epa.gov/system/files/documents/2023-12/ocs-sf6.pdf, last accessed: 2024-02-15, 2023.

European Parliament and Council of the European Union: Regulation (EU) No. 517/2014 of the European Parliament and of the Council on fluorinated greenhouse gases and repealing Regulation (EC) No. 842/2006. Official Journal of the European Union, L 150/195., https://faolex.fao.org/docs/pdf/eur133686.pdf, last accessed: 2024-01-31, 2014.

https://doi.org/10.5194/egusphere-2024-811
Preprint. Discussion started: 11 April 2024

Fang, X., Thompson, R. L., Saito, T., Yokouchi, Y., Kim, J., Li, S., Kim, K. R., Park, S., Graziosi, F., and Stohl, A.: Sulfur hexafluoride (SF6) emissions in East Asia determined by inverse modeling, Atmospheric Chemistry and Physics, 14, 4779–4791, https://doi.org/10.5194/acp-14-4779-2014, 2014.

Ganesan, A. L., Rigby, M., Zammit-Mangion, A., Manning, A. J., Prinn, R. G., Fraser, P. J., Harth, C. M., Kim, K.-R., Krummel, P. B., Li, S., Mühle, J., O'Doherty, S. J., Park, S., Salameh, P. K., Steele, L. P., and Weiss, R. F.: Characterization of uncertainties in atmospheric trace gas inversions using hierarchical Bayesian methods, Atmospheric Chemistry and Physics, 14, 3855–3864, https://doi.org/10.5194/acp-14-3855-2014, 2014.

Gouda, O. E., Ali, M. D., and Ali-Hassan, A.-H.: Comparasion between Oil Immersed and SF6 Gas Power Transformers Ratings, TELKOMNIKA (Telecommunication Computing Electronics and Control), 10, 43–54, https://doi.org/10.12928/telkomnika.v10i1.797, 2012.

Government of India: Growth of electricity sector in India from 1947-2023. Government of India, Ministry of Power, Central electricity authority, New Dehli, https://cea.nic.in/wp-content/uploads/pdm/2023/10/Growth_Book_2.pdf, last accessed: 2024-03-15, 2023.

Groot Zwaaftink, C. D., Henne, S., Thompson, R. L., Dlugokencky, E. J., Machida, T., Paris, J.-D., Sasakawa, M., Segers, A., Sweeney, C., and Stohl, A.: Three-dimensional methane distribution simulated with FLEXPART 8-CTM-1.1 constrained with observation data, Geoscientific Model Development, 11, 4469–4487, https://doi.org/10.5194/gmd-11-4469-2018, 2018.

Guo, L., Yang, Y., Fraser, P. J., Velders, G. J., Liu, Z., Cui, D., Quan, J., Cai, Z., Yao, B., Hu, J., et al.: Projected increases in emissions of high global warming potential fluorinated gases in China, Communications Earth & Environment, 4, 205, https://doi.org//10.1038/s43247-023-00859-6, 2023.

Henne, S., Brunner, D., Groot Zwaaftink, C. D., and Stohl, A.: FLEXPART 8-CTM-1.1: Atmospheric Lagrangian Particle Dispersion Model for global tracer transport, https://doi.org/10.5281/zenodo.1249190, last accessed: 2022-04-27, 2018.

Hersbach, H., de Rosnay, P., Bell, B., Schepers, D., Simmons, A., Soci, C., Abdalla, S., Alonso-Balmaseda, M., Balsamo, G., Bechtold, P., Berrisford, P., Bidlot, J.-R., de Boisséson, E., Bonavita, M., Browne, P., Buizza, R., Dahlgren, P., Dee, D., Dragani, R., Diamantakis, M., Flemming, J., Forbes, R., Geer, A., Haiden, T., Hólm, E., Haimberger, L., Hogan, R., Horányi, A., Janiskova, M., Laloyaux, P., Lopez, P., Munoz-Sabater, J., Peubey, C., Radu, R., Richardson, D., Thépaut, J.-N., Vitart, F., Yang, X., Zsótér, E., and Zuo, H.: Operational global reanalysis: progress, future directions and synergies with NWP, https://doi.org/10.21957/tkic6g3wm, series: ERA Report, 2018.

Hu, L., Ottinger, D., Bogle, S., Montzka, S. A., DeCola, P. L., Dlugokencky, E., Andrews, A., Thoning, K., Sweeney, C., Dutton, G., et al.: Declining, seasonal-varying emissions of sulfur hexafluoride from the United States, Atmospheric Chemistry and Physics, 23, 1437–1448, https://doi.org/10.5194/acp-23-1437-2023, 2023.

IEEE: IEEE Guide for Sulphur Hexafluoride (SF6) Gas Handling for High-Voltage (over 1000 Vac) Equipment, https://doi.org/10.1109/IEEESTD.2012.6127885, 2012.

Kim, J., Li, S., Mühle, J., Stohl, A., Kim, S.-K., Park, S., Park, M.-K., Weiss, R. F., and Kim, K.-R.: Overview of the findings from measurements of halogenated compounds at Gosan (Jeju Island, Korea) quantifying emissions in East Asia, Journal of Integrative Environmental Sciences, 9, 71–80, https://doi.org/10.1080/1943815X.2012.696548, 2012.

Koch, E.-C.: Special materials in pyrotechnics: III. Application of lithium and its compounds in energetic systems, Propellants, Explosives, Pyrotechnics: An International Journal Dealing with Scientific and Technological Aspects of Energetic Materials, 29, 67–80, https://doi.org/10.1002/prep.200400032, 2004.

Koch, H.: Basic information on gas insulated transmission lines (GIL), in: 2008 IEEE Power and Energy Society General Meeting-Conversion and Delivery of Electrical Energy in the 21st Century, pp. 1–4, IEEE, https://doi.org/10.1109/PESW.2000.850061, 2008.

https://doi.org/10.5194/egusphere-2024-811
Preprint. Discussion started: 11 April 2024

Kovács, T., Feng, W., Totterdill, A., Plane, J., Dhomse, S., Gómez-Martín, J. C., Stiller, G. P., Haenel, F. J., Smith, C., Forster, P. M., et al.: Determination of the atmospheric lifetime and global warming potential of sulfur hexafluoride using a three-dimensional model, Atmospheric Chemistry and Physics, 17, 883–898, https://doi.org/10.5194/acp-17-883-2017, 2017.

Lan, X., Mund, J., Crotwell, A., Crotwell, M., Moglia, E., Madronich, M., Neff, D., and Thoning, K.: Atmospheric Sulfur Hexafluoride Dry Air Mole Fractions from the NOAA GML Carbon Cycle Cooperative Global Air Sampling Network, 1997-2022, Version: 2023-08-28, https://doi.org/10.15138/p646-pa37, 2023.

Lan, X., Thoning, K., and Dlugokencky, E.: Trends in globally-averaged CH4, N2O, and SF6 determined from NOAA Global Monitoring Laboratory measurements. Version 2024-02, https://doi.org/10.15138/P8XG-AA10, last accessed: 2024-02-19, 2024.

Laube, J. C., Tegtmeier, S., Fernandez, R. P., Harrison, J., Hu, L., Krummel, P., Mahieu, E., Park, S., and Western, L.: Update on Ozone-Depleting Substances (ODSs) and Other Gases of Interest to the Montreal Protocol, 978-9914-733-97-6, https://orbi.uliege.be/bitstream/2268/299913/1/Chapter_1_from%20Scientific-Assessment-of-Ozone-Depletion-2022.pdf, last accessed: 2024-02-15, 2023.

Lee, G., Choi, H., Kim, J., Mühle, J., Vojta, M., O'Doherty, S., Krummel, P. B., Weiss, R. F., Stohl, A., and Park, S.: Atmospheric observation-based SF6 emissions in East Asia: comparison of top-down and bottom-up estimates [manuscript in preparation], 2024.

Lee, H. J., Yoon, T.-J., and Yoon, Y. I.: Synthesis of ultrasound contrast agents: characteristics and size distribution analysis (secondary publication), Ultrasonography, 36, 378, https://doi.org/10.14366/usg.17014, 2017.

Lee, H. M., Chang, M. B., and Wu, K. Y.: Abatement of sulfur hexafluoride emissions from the semiconductor manufacturing process by atmospheric-pressure plasmas, Journal of the Air & Waste Management Association, 54, 960–970, https://doi.org/10.1080/10473289.2004.10470963, 2004.

Levin, I., Naegler, T., Heinz, R., Osusko, D., Cuevas, E., Engel, A., Ilmberger, J., Langenfelds, R. L., Neininger, B., Rohden, C. v., et al.: The global SF 6 source inferred from long-term high precision atmospheric measurements and its comparison with emission inventories, Atmospheric Chemistry and Physics, 10, 2655–2662, https://doi.org/10.5194/acp-10-2655-2010, 2010.

Li, M., Karu, E., Brenninkmeijer, C., Fischer, H., Lelieveld, J., and Williams, J.: Tropospheric OH and stratospheric OH and Cl concentrations determined from CH4, CH3Cl, and SF6 measurements, NPJ Climate and Atmospheric Science, 1, 29, https://doi.org/10.1038/s41612-018-0041-9, 2018a.

Li, S., Park, S., Lee, J.-Y., Ha, K.-J., Park, M.-K., Jo, C., Oh, H., Mühle, J., Kim, K.-R., Montzka, S., et al.: Chemical evidence of inter-hemispheric air mass intrusion into the Northern Hemisphere mid-latitudes, Scientific reports, 8, 4669, https://doi.org/10.1038/s41598-018-22266-0, 2018b.

Lichter, K. E., Bloom, J. R., Sheu, R.-D., Zalavari, L. T., Leung, K., Collins, A., Witztum, A., and Chuter, R.: Tracking and Reducing SF6 Usage in Radiation Oncology: A Step Toward Net-Zero Health Care Emissions, Practical Radiation Oncology, 13, e471–e474, https://doi.org/10.1016/j.prro.2023.06.003, 2023.

Maiss, M. and Brenninkmeijer, C. A.: Atmospheric SF6: trends, sources, and prospects, Environmental Science & Technology, 32, 3077–3086, https://doi.org/10.1021/es9802807, 1998.

Manning, A., Redington, A., O'Doherty, S., Say, D., Young, D., Arnold, T., Rennick, C., Rigby, M., Wisher, A., and Simmonds, P.: Long-Term Atmospheric Measurement and Interpretation of Radiatively Active Trace Gases–Detailed Report (September 2019 to August 2020), Tech. rep., Department for Business, Energy & Industrial Strategy, https://assets.publishing.service.gov.uk/media/62d7b9bee90e071e7e59c97e/verification-uk-greenhouse-gas-emissions-using-atmospheric-observations-annual-report-2021.pdf, (last access 10 November 2023), 2022.

https://doi.org/10.5194/egusphere-2024-811
Preprint. Discussion started: 11 April 2024

Martin, D., Petersson, K., and Shallcross, D.: The use of cyclic perfluoroalkanes and SF6 in atmospheric dispersion experiments, Quarterly Journal of the Royal Meteorological Society, 137, 2047–2063, https://doi.org/10.1002/qj.881, 2011.

McKain, K., Sweeney, C., Baier, B., Crotwell, A., Crotwell, M., Handley, P., Higgs, J., Legard, T.and Madronich, M., Miller, J. B., Moglia, E.and Mund, J. N. D., Newberger, T., Wolter, S., and Laboratory, N. G. M.: NOAA Global Greenhouse Gas Reference Network Flask-Air PFP Sample Measurements of CO2, CH4, CO, N2O, H2, SF6 and isotopic ratios collected from aircraft vertical profiles [Data set]. Version: 2022-12-01, https://doi.org/10.15138/39HR-9N34, 2022.

Ni, J., Liu, S.-S., Lang, X.-P., He, Z., and Yang, G.-P.: Sulfur hexafluoride in the marine atmosphere and surface seawater of the Western Pacific and Eastern Indian Ocean, Environmental Pollution, 335, 122 266, https://doi.org/10.1016/j.envpol.2023.122266, 2023.

NOAA Carbon Cycle Group ObsPack Team: Multi-laboratory compilation of atmospheric sulfure hexafluoride data for the period 1983-2017; obspacksf61v2.1.12018−08−17; NOAA Earth System Research Laboratory, Global Monitoring Division, https://doi.org/10.15138/g3ks7p, 2018.

O'Doherty, S., Say, D., Stanley, K., Young, D., Pitt, J., and Wenger, A.: Deriving Emissions related to Climate Change Network: CO2, CH4, N2O, SF6 and CO measurements from Bilsdale Tall Tower, North York Moors National Park. Centre for Environmental Data Analysis, https://catalogue.ceda.ac.uk/uuid/d2090552c8fe4c16a2fd7d616adc2d9f, last accessed: 2024-02-1, 2019.

Patra, P. K., Lal, S., Subbaraya, B., Jackman, C. H., and Rajaratnam, P.: Observed vertical profile of sulphur hexafluoride (SF6) and its atmospheric applications, Journal of Geophysical Research: Atmospheres, 102, 8855–8859, https://doi.org/10.1029/96JD03503, 1997.

Pedersen, P. H.: Ways of reducing consumption and emission of potent greenhouse gases (HFCs, PFCs and SF6), Nordic Council of Ministers, http://norden.diva-portal.org/smash/get/diva2:702766/FULLTEXT01.pdf, last accessed: 2024-03-12, 2000.

Pisso, I., Sollum, E., Grythe, H., Kristiansen, N. I., Cassiani, M., Eckhardt, S., Arnold, D., Morton, D., Thompson, R. L., Groot Zwaaftink, C. D., Evangeliou, N., Sodemann, H., Haimberger, L., Henne, S., Brunner, D., Burkhart, J. F., Fouilloux, A., Brioude, J., Philipp, A., Seibert, P., and Stohl, A.: The Lagrangian particle dispersion model FLEXPART version 10.4, Geoscientific Model Development, 12, 4955–4997, https://doi.org/10.5194/gmd-12-4955-2019, 2019.

Popa, M., Gloor, M., Manning, A., Jordan, A., Schultz, U., Haensel, F., Seifert, T., and Heimann, M.: Measurements of greenhouse gases and related tracers at Bialystok tall tower station in Poland, Atmospheric Measurement Techniques, 3, 407–427, https://doi.org/10.5194/amt-3-407-2010, 2010.

Prinn, R. G., Weiss, R. F., Arduini, J., Arnold, T., DeWitt, H. L., Fraser, P. J., Ganesan, A. L., Gasore, J., Harth, C. M., Hermansen, O., Kim, J., Krummel, P. B., Li, S., Loh, Z. M., Lunder, C. R., Maione, M., Manning, A. J., Miller, B. R., Mitrevski, B., Mühle, J., O'Doherty, S., Park, S., Reimann, S., Rigby, M., Saito, T., Salameh, P. K., Schmidt, R., Simmonds, P. G., Steele, L. P., Vollmer, M. K., Wang, R. H., Yao, B., Yokouchi, Y., Young, D., and Zhou, L.: History of chemically and radiatively important atmospheric gases from the Advanced Global Atmospheric Gases Experiment (AGAGE), Earth System Science Data, 10, 985–1018, https://doi.org/10.5194/essd-10-985-2018, 2018.

Purohit, P. and Höglund-Isaksson, L.: Global emissions of fluorinated greenhouse gases 2005–2050 with abatement potentials and costs, Atmospheric Chemistry and Physics, 17, 2795–2816, https://doi.org/10.5194/acp-17-2795-2017, 2017.

Ravishankara, A. R., Solomon, S., Turnipseed, A. A., and Warren, R. F.: Atmospheric lifetimes of long-lived halogenated species, Science (New York, N.Y.), 259, 194–199, https://doi.org/10.1126/science.259.5092.194, 1993.

Ray, E. A., Moore, F. L., Elkins, J. W., Rosenlof, K. H., Laube, J. C., Röckmann, T., Marsh, D. R., and Andrews, A. E.: Quantification of the SF6 lifetime based on mesospheric loss measured in the stratospheric polar vortex, Journal of Geophysical Research: Atmospheres, 122, 4626–4638, https://doi.org/10.1002/2016JD026198, 2017.

https://doi.org/10.5194/egusphere-2024-811
Preprint. Discussion started: 11 April 2024

Rigby, M., Mühle, J., Miller, B. R., Prinn, R. G., Krummel, P. B., Steele, L. P., Fraser, P. J., Salameh, P. K., Harth, C. M., Weiss, R. F., Greally, B. R., O'Doherty, S., Simmonds, P. G., Vollmer, M. K., Reimann, S., Kim, J., Kim, K.-R., Wang, H. J., Olivier, J. G. J., Dlugokencky, E. J., Dutton, G. S., Hall, B. D., and Elkins, J. W.: History of atmospheric SF_6; from 1973 to 2008, Atmospheric Chemistry and Physics, 10, 10 305–10 320, https://doi.org/10.5194/acp-10-10305-2010, 2010.

Rigby, M., Manning, A., and Prinn, R.: Inversion of long-lived trace gas emissions using combined Eulerian and Lagrangian chemical transport models, Atmospheric Chemistry and Physics, 11, 9887–9898, https://doi.org/10.5194/acp-11-9887-2011, 2011.

Rigby, M., Prinn, R., O'Doherty, S., Montzka, S., McCulloch, A., Harth, C., Mühle, J., Salameh, P., Weiss, R., Young, D., et al.: Re-evaluation of the lifetimes of the major CFCs and CH_3CCl_3 using atmospheric trends, Atmospheric Chemistry and Physics, 13, 2691–2702, https://doi.org/10.5194/acp-13-2691-2013, 2013.

Rust, D., Katharopoulos, I., Vollmer, M. K., Henne, S., O'doherty, S., Say, D., Emmenegger, L., Zenobi, R., and Reimann, S.: Swiss halocarbon emissions for 2019 to 2020 assessed from regional atmospheric observations, Atmospheric Chemistry and Physics, 22, 2447–2466, https://doi.org/10.5194/acp-22-2447-2022, 2022.

Saikawa, E., Rigby, M., Prinn, R. G., Montzka, S. A., Miller, B. R., Kuijpers, L. J. M., Fraser, P. J. B., Vollmer, M. K., Saito, T., Yokouchi, Y., Harth, C. M., Mühle, J., Weiss, R. F., Salameh, P. K., Kim, J., Li, S., Park, S., Kim, K.-R., Young, D., O'Doherty, S., Simmonds, P. G., McCulloch, A., Krummel, P. B., Steele, L. P., Lunder, C., Hermansen, O., Maione, M., Arduini, J., Yao, B., Zhou, L. X., Wang, H. J., Elkins, J. W., and Hall, B.: Global and regional emission estimates for HCFC-22, Atmospheric Chemistry and Physics, 12, 10 033–10 050, https://doi.org/10.5194/acp-12-10033-2012, 2012.

Schuck, T. and Obersteiner, F.: IAGOS-CARIBIC whole air sampler data (v2024.01.12) [Data set]. Zenodo., https://doi.org/10.5281/zenodo.10495039, 2024.

Schwaab, K.: Emissions Reduction Potentials for SF6 in Germany, in: Conference Paper (EPA): SF6 and the environment: Emission reduction strategies., Citeseer, https://citeseerx.ist.psu.edu/document?repid=rep1&type=pdf&doi=d885668be934608b9a54db7ac2dc9ecdcda6b26a, last accessed: 2024-02-15, 2000.

Schwarz, W.: Emissions, activity data, and emission factors of fluorinated greenhouse gases (F-Gases) in Germany 1995-2002, Research Report 201 41 261/01, UBA-FB 000811/e, Umweltbundesamt, Berlin, https://www.osti.gov/etdeweb/biblio/21154958, last accessed: 2024-02-15, 2005.

Simmonds, P. G., Rigby, M., Manning, A. J., Park, S., Stanley, K. M., McCulloch, A., Henne, S., Graziosi, F., Maione, M., Arduini, J., Reimann, S., Vollmer, M. K., Mühle, J., O'Doherty, S., Young, D., Krummel, P. B., Fraser, P. J., Weiss, R. F., Salameh, P. K., Harth, C. M., Park, M.-K., Park, H., Arnold, T., Rennick, C., Steele, L. P., Mitrevski, B., Wang, R. H. J., and Prinn, R. G.: The increasing atmospheric burden of the greenhouse gas sulfur hexafluoride (SF_6), Atmospheric Chemistry and Physics, 20, 7271–7290, https://doi.org/10.5194/acp-20-7271-2020, 2020.

Smith, C., Nicholls, Z., Armour, K., Collins, W., Forster, P., Meinshausen, M., Palmer, M., and Watanabe, M.: The Earth's Energy Budget, Climate Feedbacks, and Climate Sensitivity Supplementary Material. In Climate Change 2021: The Physical Science Basis. Contribution of Working Group I to the Sixth Assessment Report of the Intergovernmental Panel on Climate Change [Masson-Delmotte, V., P. Zhai, A. Pirani, S.L. Connors, C. Péan, S. Berger, N. Caud, Y. Chen, L. Goldfarb, M.I. Gomis, M. Huang, K. Leitzell, E. Lonnoy, J.B.R. Matthews, T.K. Maycock, T. Waterfield, O. Yelekçi, R. Yu, and B. Zhou (eds.)]. Available from https://www.ipcc.ch, 2021.

Stiller, G., Harrison, J. J., Haenel, F., Glatthor, N., and Kellmann, S.: MIPAS monthly zonal mean Age of Air data, based on MIPAS SF6 retrievals, processed at KIT-IMK, Karlsruhe, https://doi.org/10.5445/IR/1000139453, 2021.

https://doi.org/10.5194/egusphere-2024-811
Preprint. Discussion started: 11 April 2024

Tarantola, A.: Inverse Problem Theory and Methods for Model Parameter Estimation, pp. 1–67, Society for Industrial and Applied Mathematics, https://doi.org/10.1137/1.9780898717921, 2005.

Thacker, W. C.: Data assimilation with inequality constraints, Ocean Modelling, 16, 264–276, https://doi.org/10.1016/j.ocemod.2006.11.001, 2007.

Thompson, R. L. and Stohl, A.: FLEXINVERT: an atmospheric Bayesian inversion framework for determining surface fluxes of trace species using an optimized grid, Geoscientific Model Development, 7, 2223–2242, https://doi.org/10.5194/gmd-7-2223-2014, 2014.

Tørseth, K., Aas, W., Breivik, K., Fjæraa, A. M., Fiebig, M., Hjellbrekke, A.-G., Lund Myhre, C., Solberg, S., and Yttri, K. E.: Introduction to the European Monitoring and Evaluation Programme (EMEP) and observed atmospheric composition change during 1972–2009, Atmospheric Chemistry and Physics, 12, 5447–5481, https://doi.org/10.5194/acp-12-5447-2012, 2012.

UNFCCC: United Nations Framework Convention on Climate Change, https://di.unfccc.int/time_series, last accessed: 2023-03-10, 2021.

Vojta, M., Plach, A., Thompson, R. L., and Stohl, A.: A comprehensive evaluation of the use of Lagrangian particle dispersion models for inverse modeling of greenhouse gas emissions, Geoscientific Model Development, 15, 8295–8323, https://doi.org/10.5194/gmd-15-8295-2022, 2022.

Zhou, S., Teng, F., and Tong, Q.: Mitigating sulfur hexafluoride (SF6) emission from electrical equipment in China, Sustainability, 10, 2402, https://doi.org/10.3390/su10072402, 2018.

Chapter 5

Conclusions

SF_6 has the highest GWP of any known GHGs listed under the UNFCCC. Due to its exceptionally long atmospheric lifetime, emissions accumulate in the atmosphere and will contribute to climate warming for centuries. While SF_6 is included in the Kyoto Protocol, and efforts have been made to regulate its emissions in different parts of the world, the gas is still widely used in various industries (especially in the power industry) and global emissions have been increasing since the beginning of the 20^{th} century. To monitor progress toward emission reduction targets, national GHG inventories are compiled, by using bottom-up methods. Within these methods, a large number of statistical activity data (e.g. industrial production and consumption) is used together with source-specific emission factors to statistically determine an aggregated national emission estimate. However, the reliability of these inventories has been questioned, as bottom-up methods are suspected to suffer from substantial uncertainties, emphasizing the need for verification. Atmospheric inverse modeling provides a verification tool, which allows estimating emissions based on atmospheric measurements using an atmospheric transport model. When inversions are based on LPDMs, the definition of the baseline is a major source of uncertainty, and the influence of the LPDM backward simulation period is not well understood. The main research objectives of this thesis are

1) the evaluation of the use of LPDMs for inverse modeling of GHGs

2) the determination of the global SF_6 emission distribution for the period 2005-2021

They are addressed in the research articles Vojta et al. (2022) and Vojta et al. (2024) presented in chapter 3 and chapter 4 respectively. The following sections summarize and discuss the main findings, particularly in relation to preceding research, while implications are set in a broader context.

5.1 The evaluation of the use of LPDMs for inverse modeling of GHGs

The choice of the baseline method

- **Statistical baseline methods can cause large systematic errors**
  In chapter 3 (Vojta et al. 2022), I demonstrated that purely statistical baseline methods

(e.g. the REBS method), that solely rely on observations at individual measurement stations, can lead to unreliable inversion results, that are substantially influenced by the choice of the LPDM backward simulation period. The main problem is, that by definition, purely statistical methods are not able to take the LPDM simulation length into account. However, by increasing the simulation period, additional emission contributions are directly related to the respective observations by the LPDM and are included in the optimization, while they should be excluded from the baseline. A baseline method, that cannot account for that, will systematically produce too high *a priori* mixing ratios that will be corrected downwards by the inversion, resulting in an underestimation of the *a posteriori* emissions. This is particularly evident at polluted sites (e.g. Gosan), where air masses rarely remain unaffected by emissions during the backward simulation period. In chapter 3, I demonstrated that by increasing the backward simulation periods from 1 to 50 days, global total 2012 SF_6 emissions produced by using the REBS method, decreased by more than a factor of 3. To tackle this problems, studies employing the REBS method (e.g. Annadate et al. 2023; Henne et al. 2016; Schoenenberger et al. 2018) usually optimize the baseline as part of the inversion, which can reduce the overestimation, however this might not be sufficient to avoid biases completely. For the example of global SF_6 emissions, large biases in the *a posteriori* emissions remain, despite optimizing the baseline. Another drawback of statistical baseline methods is, that they have to assume smooth baselines, as pointed out by Rigby et al. (2011). Thus, they cannot account for sudden changes in the baseline due to meteorological events (e.g. East-Asian summer monsoon), as illustrated in chapter 3 . Further, statistical baseline methods do not allow to include low frequency measurements (e.g. flask measurements) or observations from moving platforms in the inversion.

- **Including model information can improve statistical baseline methods**
  In chapter 3, I used the example of a baseline method introduced by Stohl et al. (2009), to demonstrate that the performance of statistical baseline methods can be improved by including model information. To avoid the discussed overestimation of a purely statistical baseline, Stohl's method corrects for emissions occurring during the LPDM backward simulation period, leading to much smaller sensitivity to the LPDM simulation period, compared to the REBS method. However, the method likely underestimates the baseline in general, and thus overestimates *a posteriori* emissions, given the low baseline values at background measurement stations, the solely positive global inversion increments, and relatively high global total SF_6 *a posteriori* emissions for 2012. This suspicion is reinforced when examining other studies utilizing Stohl's method (e.g. Fang et al. 2014; Stohl et al. 2010, 2009). All of them show, that the optimization of the baseline leads to substantial higher *a posteriori* baselines at almost all measurement stations, than *a priori* modeled. In case of the global SF_6 inversion 2012 presented in chapter 3, I showed that the optimization of the baseline resulted in substantially lower global total SF_6 emissions, close to the reference value from Simmonds et al. (2020).

- **The advantages of a GDB approach**
  In chapter 3 (Vojta et al. 2022) and chapter 4 (Vojta et al. 2024), I demonstrated many benefits of a GDB approach, in which the LPDM back-trajectories are coupled to a global model. In chapter 3, I illustrated that the GDB approach is fully consistent with the length of the LPDM backward simulation period, with global 2012 SF_6 inversion results showing almost no change for different simulation periods. Thus, the GDB method ensures more robust inversion results, that are not sensitive to the subjective choice of the LPDM simulation period. In chapter 3 and chapter 4, I further demonstrated that the GDB method successfully accounts for meteorological variability of complex baselines at challenging measurement stations, such as Gosan or Ragged Point (Barbados). Low SF_6 summer measurements, representing intrusions of southern SF_6-poor air masses, were captured well by the GDB baseline, ensuring more reliable inversion results during these intrusions. This is a great advantage over statistical baselines, which assume a smooth baseline and can therefore not account for this meteorological variability, which will likely result in an underestimation of emissions during intrusions of southern air masses. As inversion results are highly sensitive to the estimated baseline, inversions based on statistical baseline methods rely strongly on the baseline optimization. In chapter 4, I showed that the optimization of the baseline had a relatively small impact, suggesting that the GDB method already yields an appropriate baseline, which is not substantially enhanced through the inversion. Hence, the information content of the measurements can be effectively utilized to improve the emission estimate. Another benefit of using the GDB approach is that it enables the inclusion of low-frequency observations and measurements from moving platforms in the inversion, as mentioned above.

Based on the problems of statistical methods and the benefits from a GDB approach demonstrated in chapter 3 and in chapter 4, I recommend to employ GDB methods instead of statistical baseline methods, whenever possible. While statistical methods are easy to implement and might work well at observation stations with a non-complex baseline (where "clean" and "polluted" observations can be easily distinguished, e.g. Mace Head) it will still be necessary to include model information (e.g. Manning et al. 2021; Stohl et al. 2009), and to optimize the baseline to overcome intrinsic problems. Furthermore, these methods encounter large problems at measurement sites characterized by complex baselines and at polluted continental areas where air masses seldom remain unaffected by emissions, that will likely not be sufficiently compensated by a baseline optimization. Great care should be taken to ensure that the discussed problems do not arise. Given the demonstrated benefits, the GDB approach proves as the most appropriate method to estimate the baseline for inversion purposes. Its performances will however depend on the quality of the global mole fraction fields which are coupled with the LPDM, and it is important that the employed 3-d fields are not substantially biased. The optimization of the baseline, will therefore still be useful to compensate for potential biases of these fields, as done in Vojta et al. (2024). While the coupling at the end of the LPDM simulation period provides a robust method for global and regional inversions, the coupling at the spatial boundaries of the regional inversion domain (e.g. Ganesan et al. 2017; Lunt et al. 2016; Ramsden et al. 2022; Say

et al. 2019) appears to be a suitable alternative for regional inversions.

The value of low-frequency measurements

Weiss et al. (2021) suggested the use of low-frequency flask measurements to improve the constraint on emissions, especially in poorly covered areas. In chapter 3, I followed this suggestion and incorporated low frequency flask measurements additionally to online measurements in the global SF_6 inversions. This improved the observational constraint of SF_6 emissions close to the flask measurement sites, where additional error reduction up to 73% could be reached, underlining the potential value of these measurements. However, as the additional observation constraint was only substantial in the vicinity of the measurements, the location of these measurements is of great importance. The current locations of many flask sampling sites are chosen to measure background mole fractions and therefore do not suit the purposes of inverse modeling well. Establishing more flask sampling sites downstream of potential emission sources in currently poorly covered regions would help to constrain the emissions in those regions, and enhance the knowledge about emissions globally.

The LPDM backward simulation period

Given that computational costs set a limit to the LPDM simulation, it has to be decided how long particles are traced backward in time before they are terminated. In chapter 3, I proposed to employ relatively long LPDM backward simulation periods, beyond 5–10 days, whenever possible. This suggestion was based on various findings, when varying the simulation period in the range of 1 to 50 days for the global SF_6 inversion. Firstly, it was observed that extending the trajectory length from 10 to 50 days leads to statistical improvements in the comparison between observed and *a priori* modeled mole fractions, represented by a growing correlation and decreasing bias and MSE. Thus, the overall LPDM performance increases for longer simulation periods, as additional emissions are directly related to respective observations by the model. In contrast to short simulation periods, 50-day periods allow even observations of remote stations to be directly related to emissions within the simulation period, thereby become accessible to the inversion. Thus, longer simulations might also allow an additional emissions constraint from remote background stations, although statistical improvements at those stations are typically small, as shown in chapter 4. In chapter 3, I further demonstrated, that with longer backward simulation periods, inversion results became less sensitive to biases in the baseline and the *a priori* emissions. It was shown that strongly biased global *a priori* emissions could only poorly be corrected with backward simulation periods of 1 to 10 days, whereas more accurate results were obtained with 50-day simulations. In chapter 4, I also demonstrated, that strongly biased global SF_6 *a priori* emission fields could be brought relatively close to known reference values by the inversion, using a LPDM simulation period of 50 days. In addition, the 50-day LPDM based global inversion could most likely reduce large *a priori* emission biases even in poorly monitored regions, indicating a direction in which emission inventories should be corrected. This suggests that longer backward simulation periods might help to

get additional information on emissions in poorly sampled areas. This is not to say that the huge gaps in the monitoring systems can be offset by simply extending the LPDM simulation period. As shown in chapter 4, the use of long simulation periods does not change the fact that the emission distribution in poorly monitored regions cannot be constrained without further observations, supporting the claim for a detection network expansion (e.g. Leip et al. 2017; Weiss et al. 2021). However, as demonstrated in chapter 3 and chapter 4, there is additional information to be gained from longer LPDM simulations, which is why I propose to employ them in order to make the best use of the existing monitoring network.

5.2 Global SF_6 emission distribution for the period 2005-2021

U.S. SF_6 emissions between 2005-2021

In chapter 4, I demonstrate that U.S. SF_6 emissions have been drastically decreasing between 2005 and 2021. A regional inversion study by Hu et al. (2023), showed a very similar declining U.S. emissions trend, however for a shorter period spanning from 2007 to 2018. While the two studies use a very different inversion set-up and do not precisely match in terms of magnitude, they collectively provide clear evidence about the substantial decline in U.S. SF_6 emissions. This inversion-derived finding, is of particular importance, given that existing emission inventories (i.e. reports to the IPCCC, EDGAR, GAINS) show substantial discrepancies, while none of them is able to account for this observed substantial decrease in SF_6 emissions. It implies that U.S. regulations enforced through EPA and through individual states, such as California, Massachusetts, and Maine, have great impact on the U.S. SF_6 emissions, which is likely underestimated by current inventories. Another shared finding of Vojta et al. (2024) and Hu et al. (2023) is that the U.S. has been under-reporting its SF_6 emissions, especially until the early 2010s, before it became mandatory for high emitting industries to declare their SF_6 emissions. Nevertheless, given the demonstrated decrease, the U.S. and its regulatory measures could serve as a role model for effectively reducing SF_6 emissions.

European SF_6 emissions between 2005-2021

As demonstrated in chapter 4, SF_6 emissions have also declined in the European Union. The decreasing trend is however much smaller than in the U.S. and a significant portion of the emissions reduction is due to a large emissions drop after 2017. The inversion results of this study align very well (both in magnitude and pattern) with the findings of Simmonds et al. (2020) and Manning et al. (2022) who performed regional inversions for West and Northwest Europe respectively. Especially noteworthy is the excellent agreement about the emissions of Northwest Europe after 2012, where the observational coverage is very good. This demonstrates the huge potential of inverse modeling determining reliable emission estimates under the condition of a dense monitoring system, emphasising the need to extend the existing network (e.g. Leip et al. 2017; Weiss et al. 2021). The findings of Manning et al. (2022) were included in the United Kingdom's annual UNFCCC reports which is

a good example of how top-down methods can enhance the quality of the self-reporting system, as suggested by Rypdal et al. (2005). The prominent emission drop after 2017 is most likely the consequence of the EU's 2014 F-gas regulation, which prohibits SF_6 to be used in recycling of magnesium die-casting alloys from 2018 onwards, and mandates that newly installed electrical switchgear since 2017 must include a leak detection system. This demonstrates the huge potential of regulations to effectively cut emissions, even soon after their enforcement.

Chinese SF_6 emissions between 2005-2021

China is the largest emitter of SF_6, accounting for roughly half of the global total emissions. Consequently, various studies - both, bottom-up and top-down - have been investigating the Chinese emission trend in recent years (e.g. An et al. 2024; Fang et al. 2014; Guo et al. 2023; Lee et al. forthcoming; Simmonds et al. 2020). All of these studies found a substantial increase in Chinese emissions in the 21^{th} century, however the determined magnitudes cover a wide range. In chapter 4, I confirmed the upward Chinese emission trend and provided emission estimates updated to the year 2021 showing remarkable agreement with the latest regional inversion study by An et al. (2024). This agreement is noteworthy, as An et al. (2024) did not only employ a different inversion system (based on MCMC methods), but also used a different observation network from inside China. The similarity of results, despite the different inversion set-up, is reassuring and underscores the reliability of these estimates. Another important finding in chapter 4 is that the growth of Chinese SF_6 emissions has slightly slowed down since the mid-2010s, suggesting that Chinese regulations implemented in 2012 and 2015 had a positive effect. However, achieving substantial reductions will require more stringent measures, such as those implemented in the EU or in the U.S. which could have substantial impact on the global total SF_6 emissions.

Other regions

SF_6 emissions from other regions, such as Africa, South America, Australia or India are challenging to constrain with inverse modeling techniques, due to the poor observational coverage of these regions. This was already found by Rigby et al. (2010), who used an Eulerian model to constrain SF_6 emissions on a continental scale for the period 2004-2008. With the inversion set-up used in chapter 4, based on 50 days LPDM trajectories, I also found that the achieved error reduction in these regions was low and that inversion results were very sensitive to the employed *a priori* emissions. However, the results suggested that potential large biases in the *a priori* fields could be reduced by the inversion, indicating a direction in which emission inventories should be corrected. Given that inversion results employing EDGAR *a priori* emission fields gave an excellent total global SF_6 estimate, I also concluded in chapter 4, that EDGAR provides a good estimate for the aggregated emissions in poorly covered regions. Nevertheless, substantial uncertainties about these emissions remain and there is the need to enhance their observational coverage to constrain their regional distribution.

Global total emissions

In chapter 4, I further compared the aggregated *a posteriori* emissions of the global SF_6 inversion results to the global total emissions values computed with a global box model (Simmonds et al. 2020) and values directly calculated from atmospheric growth rates. Generally, the inversion results are in relatively good agreement with these reference values, however they are sensitive to the employed *a priori* emission fields, most likely due to the discussed difficulties constraining emissions in poorly covered regions. The consistency with the global total emissions is favorable, as it implies that the spatially resolved *a posteriori* emissions also amount to a reasonable aggregated result that can be compared with relatively well known reference values. On the other hand, discrepancies between the aggregated *a posteriori* emissions and the total global reference values might also hold information on biases in the employed *a priori* fields (as discussed in chapter 4) or indicate other potential problems. In simple terms, it is another piece of information that can be used to constrain emissions.

Monthly SF_6 emissions

Monthly inversion results (chapter 4) showed overall higher SF_6 emissions in summer than in winter in the Northern Hemisphere, which might result from increased SF_6 pressure and heat stress of electrical equipment during hot summer temperatures. While no clear seasonal pattern could be found for Europe, China's monthly emission patterns mirrored that of the Northern Hemisphere, and U.S. emissions showed a peak from May to June. This finding, however, is in contradiction to Hu et al. (2023), who found U.S. SF_6 emissions to peak in winter. They argued that cold temperatures could cause electrical equipment sealing materials to become brittle and that many U.S. companies maintain the equipment in winter. To my knowledge, no other study has investigated the seasonal cycle of SF_6 emissions, which is why I suggest further research on this topic to provide a more conclusive answer.

5.3 Outlook

5.3.1 Log-normal distribution of a priori emissions

In chapter 3, I investigated uncertainties related to LPDM-based atmospheric inversions. As outlined in Sec 1.4, many other uncertainties can affect the inversion. A major challenge is the estimation of the error distributions. The analytical solution to the inverse problem requires state and observation errors to be Gaussian distributed (see Sec. 2.2.3). The assumption of Gaussian *a priori* emission errors poses two problems. Firstly, the emissions of many species (including SF_6) follow a log-normal distribution rather than a Gaussian one. It is therefore likely, that their errors are also log-normally distributed, making the Gaussian assumption invalid. Secondly, while surface fluxes for many species are exclusively positive, the Gaussian error assumption allows for negative values in the *a posteriori* emissions. One possible solution to this problem is to use a MCMC method and apply a large ensemble

of log-normally distributed state vector values (see Sec. 2.2.5). Alternatively, variational methods could be used to develop a cost function that accounts for non-Gaussian error distributions (see Sec. 2.2.4). Recently, the option of log-normal error distributions in the state space was implemented in FLEXINVERT+, using variational methods. I evaluated its performance for the example of optimizing SF_6 emissions. The key point of defining an appropriate cost function, that accounts for log-normal errors in the state space, is the choice of the central tendency of the log-normal distribution. Unlike for Gaussian distributions, the mean, median, and mode are not the same for log-normal distributions. Which of them should be used as a statistical estimator? While Fletcher and Zupanski (2006) argued, that the mode generally represents the best choice, my tests showed that the median was the only estimator providing reliable results in the case of SF_6 inversions. This can be explained by the findings of Fletcher et al. (2019), suggesting that there are different mathematical regions where each one of these three estimators are optimal for the minimization. A study that further explores this topic is in progress.

5.3.2 European sulfur hexafluoride emissions

In chapter 4, I used a global inversion approach to determine the global distribution of SF_6 emissions. While recent studies have employed regional inversions to constrain emissions in China (An et al. 2024), and the U.S. (Hu et al. 2023) in high resolution, there is no updated high-resolution regional study about SF_6 emissions in Europe. I am currently working on closing this gap. For this new study I use exactly the same inversion set-up as in chapter 4, but base the inversions on $0.25^\circ \times 0.25^\circ$ resolved FLEXPART sensitivities, driven by hourly ECMWF ERA5 wind fields with the same resolution and a variable inversion grid with a resolution ranging from 0.25° to 1°. First results show, that Germany is by far the biggest SF_6 emitter in Europe (see Fig. 5.1 for the example year of 2021), confirming the findings of previous studies (e.g. Brunner et al. 2017; Ganesan et al. 2014; Simmonds et al. 2020). An interesting fact is that the inversion allocates large emissions to an area close to Frankfurt, where there are not only a lot of power plants, but also the Siemens AG Switch gear Plant Frankfurt - the biggest switch gear plant in Germany. My results also indicate a slow decline in German SF_6 emissions between 2005 and 2021, showing a similar drop as found for the total EU emissions after 2017. Another finding is, that SF_6 emissions have been strongly decreasing in the UK (see Fig. 5.2). Similar to Northwest-European emissions (chapter 4), I find an exceptional agreement with Manning et al. (2022) (especially after 2012) whose UK emission estimates were reported to the UNFCCC. Again, this demonstrates the huge potential of atmospheric inversions under the conditions of a good observational coverage. Further, the substantial decrease in SF_6 emissions in the UK might suggest that reporting top-down results may positively influence emission reduction efforts. Notably, after 2017, my results show even lower SF_6 emissions in the UK, than those reported to the UNFCCC.

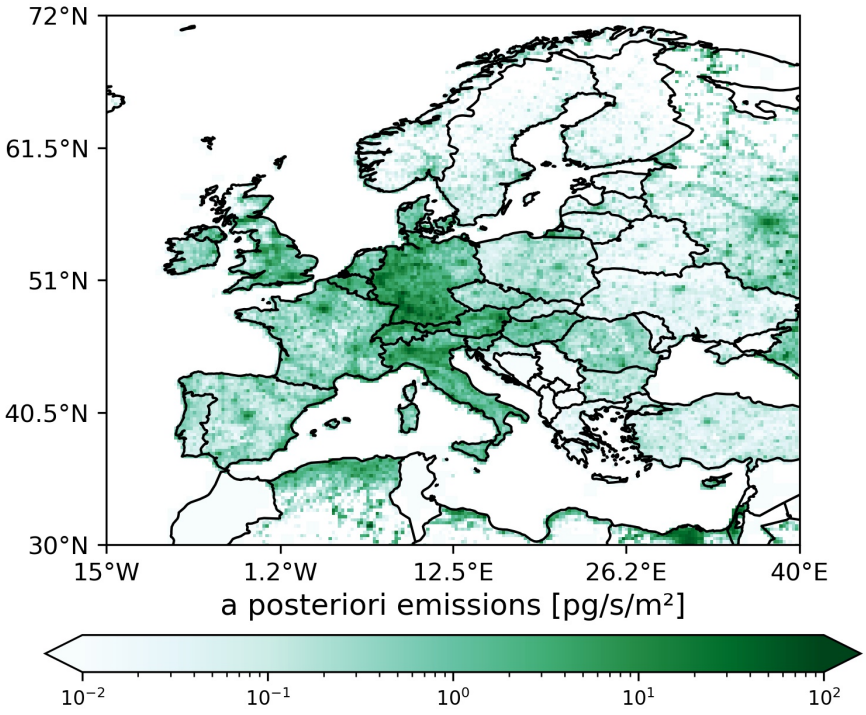

Figure 5.1: European SF_6 emissions derived from inverse modeling for the year 2021.

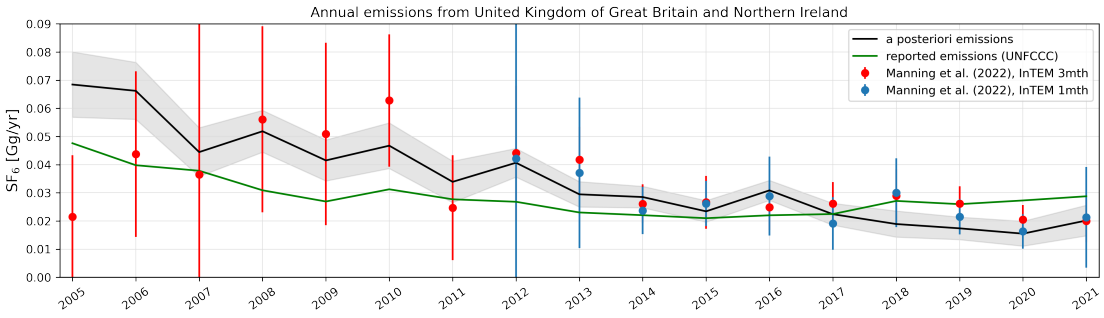

Figure 5.2: Annual SF_6 emissions in the UK between 2005 and 2021. Inversion-derived *a posterior* emissions are shown with a black solid line, together with their respective 1-σ uncertainties (grey shadings). The red and blue dots represent the results from Manning et al. (2022) using the InTEM (Inversion Technique for Emissions Modelling) model with inversion time frames set to 3- and 1-months, respectively. Reported emissions to the UNFCCC are represented by a green solid line.

Chapter A

Appendix

Supplementary Figures - A comprehensive evaluation of the use of Lagrangian particle dispersion models for inverse modeling of greenhouse gas emissions

Martin Vojta, Andreas Plach, Rona L. Thompson, Andreas Stohl

Supplementary Figures S1-S36 illustrate the three investigated baseline methods (REBS method, Stohl's method, and GDB method) at all considered *in situ* measurement sites. The GDB method is illustrated for all tested backward simulation periods, including a case without any backward simulation (0 days). In this extreme case the baseline is obtained directly from the value of the global mixing ratio field simulated with FLEXPART CTM in the spatio-temporal grid cell of the respective observation. REBS and Stohl's method are illustrated for backward simulation periods of 1, 10, and 50 days. Baseline mixing ratios are plotted together with respective observations and *a priori* mixing ratios (sum of the baseline and direct emission contributions).

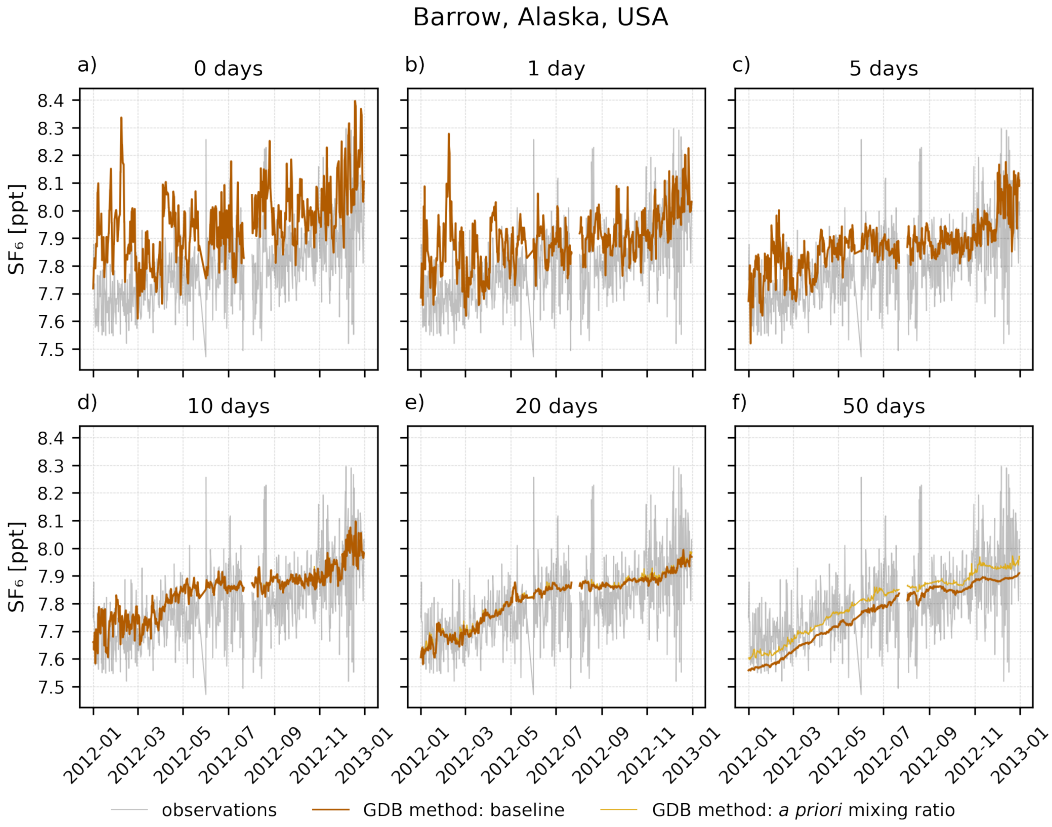

Figure S1: Baseline and *a priori* SF_6 mixing ratios calculated with the GDB method at the Barrow observation station for backward simulation times of 0 days (panel a), 1 day (b), 5 days (c), 10 days (d), 20 days (e) and 50 days (f).

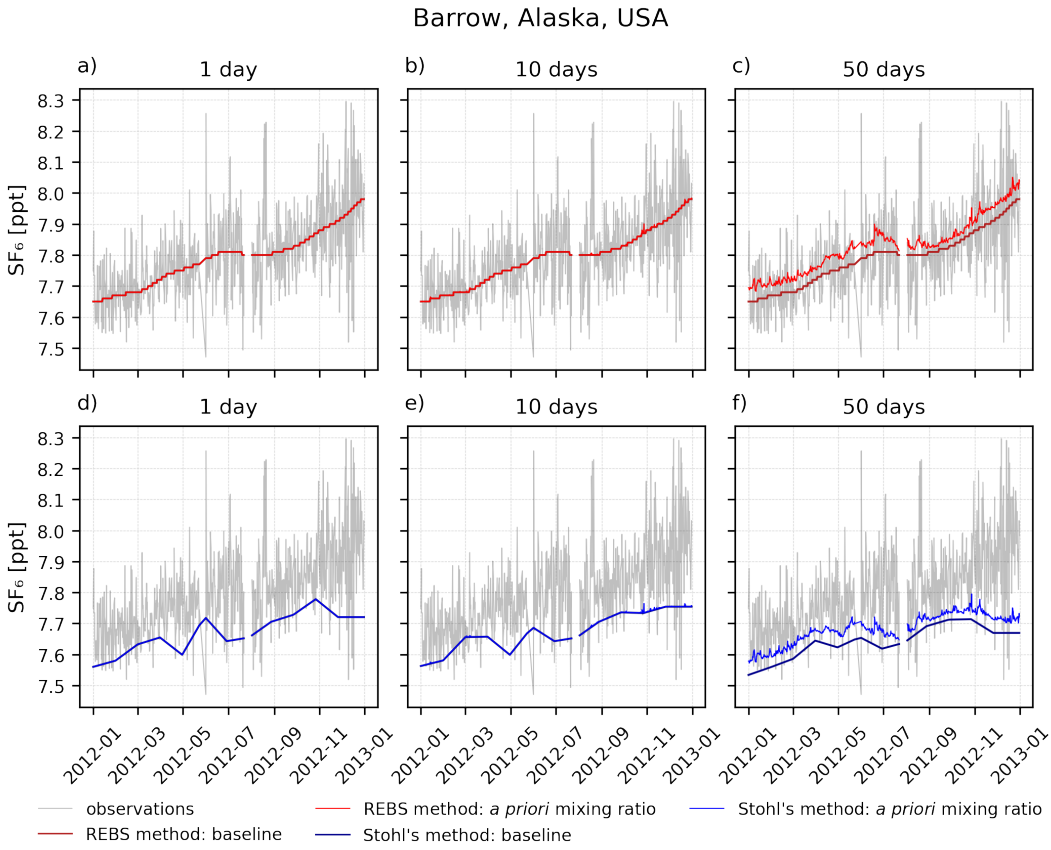

Figure S2: Baseline and *a priori* SF_6 mixing ratios calculated with the REBS (upper panels) and Stohl's method (lower panels) at the Barrow observation station, compared to SF_6 observations. Model results are shown for backward simulations of 1 day (panels a and d), 10 days (panels b and e) and 50 days (panels c and f).

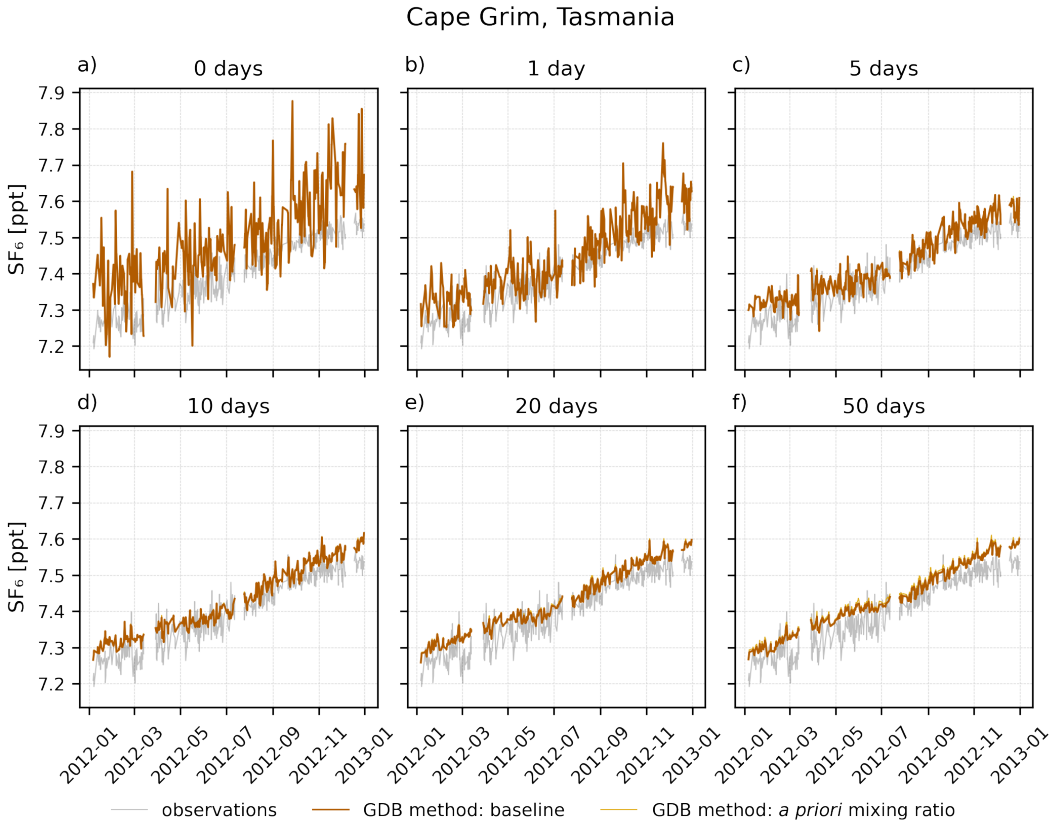

Figure S3: Baseline and *a priori* SF_6 mixing ratios calculated with the GDB method at the Cape Grim observation station for backward simulation times of 0 days (panel a), 1 day (b), 5 days (c), 10 days (d), 20 days (e) and 50 days (f).

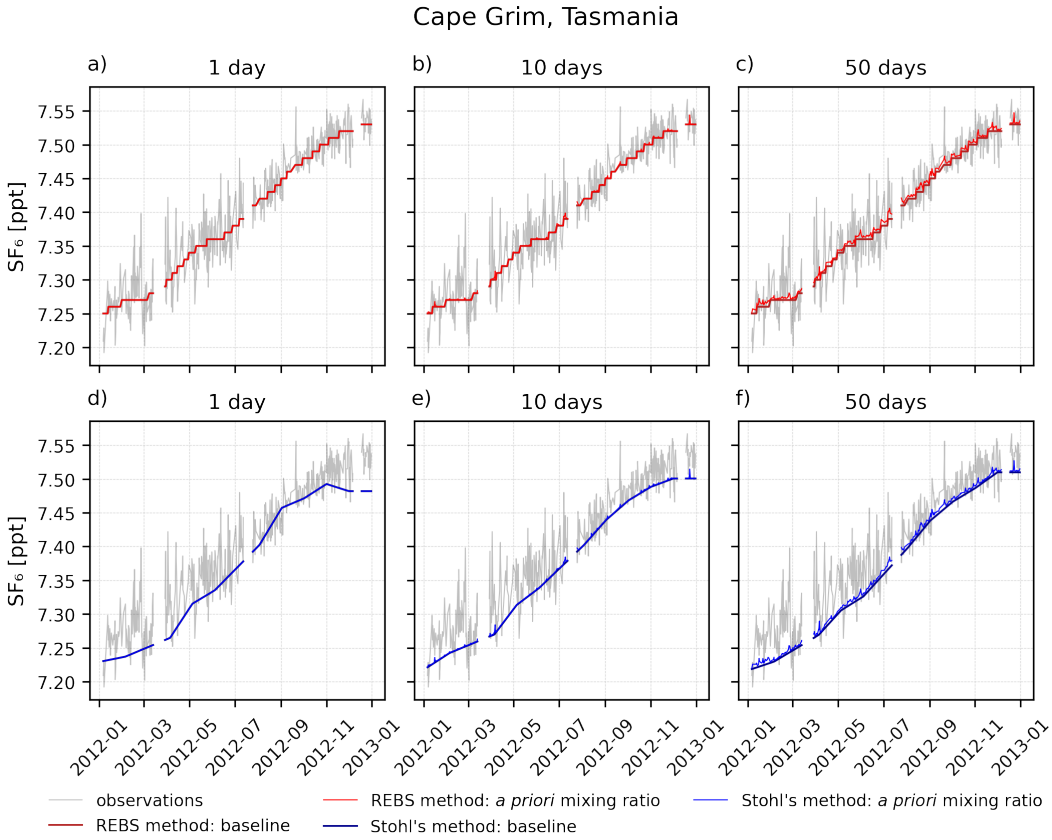

Figure S4: Baseline and *a priori* SF_6 mixing ratios calculated with the REBS (upper panels) and Stohl's method (lower panels) at the Cape Grim observation station, compared to SF_6 observations. Model results are shown for backward simulations of 1 day (panels a and d), 10 days (panels b and e) and 50 days (panels c and f).

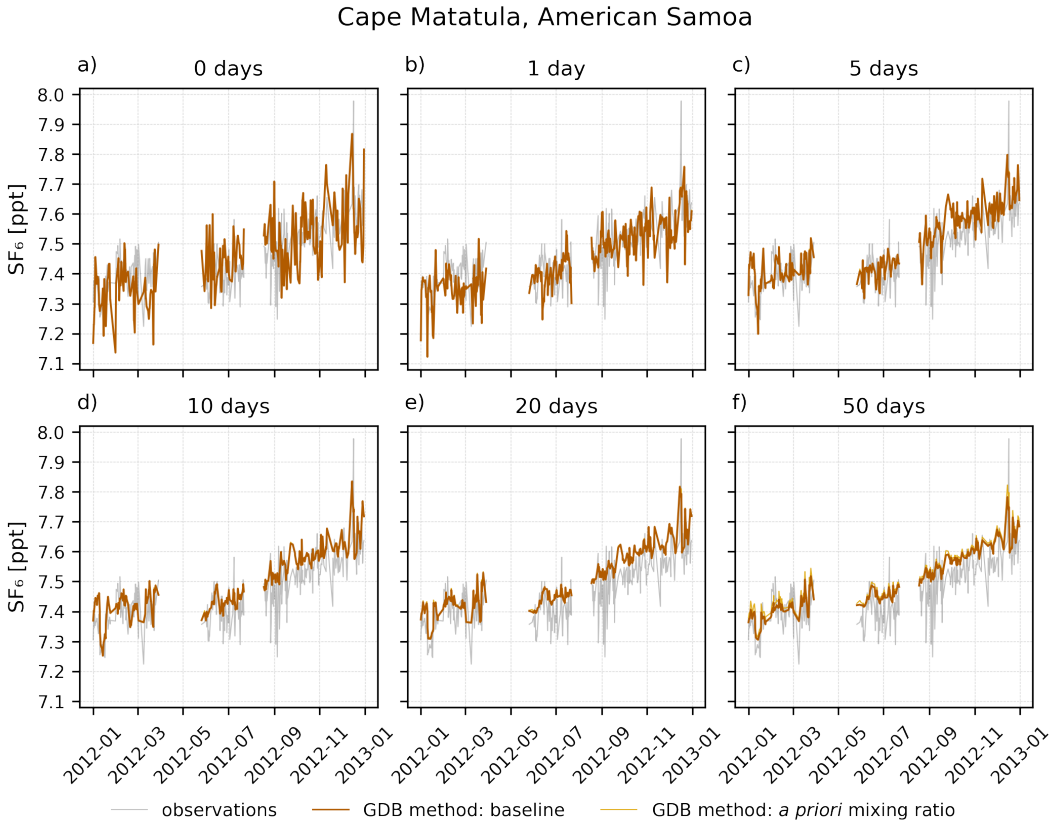

Figure S5: Baseline and *a priori* SF_6 mixing ratios calculated with the GDB method at the Cape Matatula observation station for backward simulation times of 0 days (panel a), 1 day (b), 5 days (c), 10 days (d), 20 days (e) and 50 days (f).

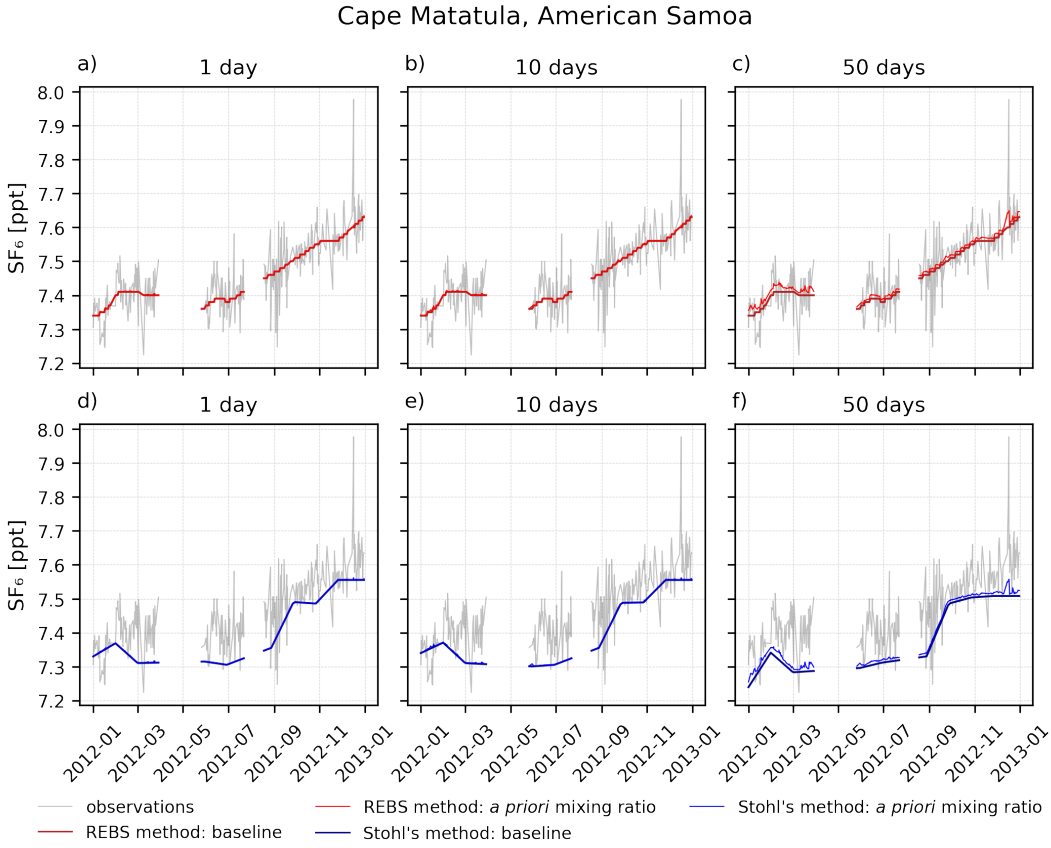

Figure S6: Baseline and *a priori* SF_6 mixing ratios calculated with the REBS (upper panels) and Stohl's method (lower panels) at the Cape Matatula observation station, compared to SF_6 observations. Model results are shown for backward simulations of 1 day (panels a and d), 10 days (panels b and e) and 50 days (panels c and f).

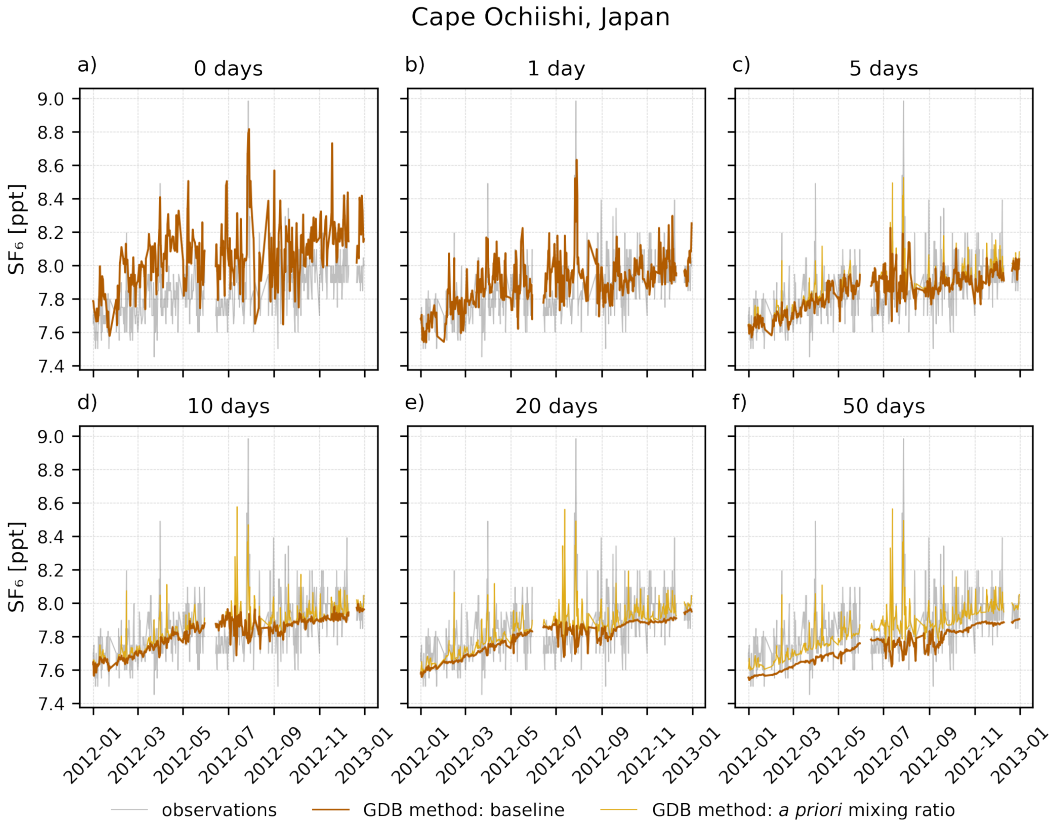

Figure S7: Baseline and *a priori* SF_6 mixing ratios calculated with the GDB method at the Cape Ochiishi observation station for backward simulation times of 0 days (panel a), 1 day (b), 5 days (c), 10 days (d), 20 days (e) and 50 days (f).

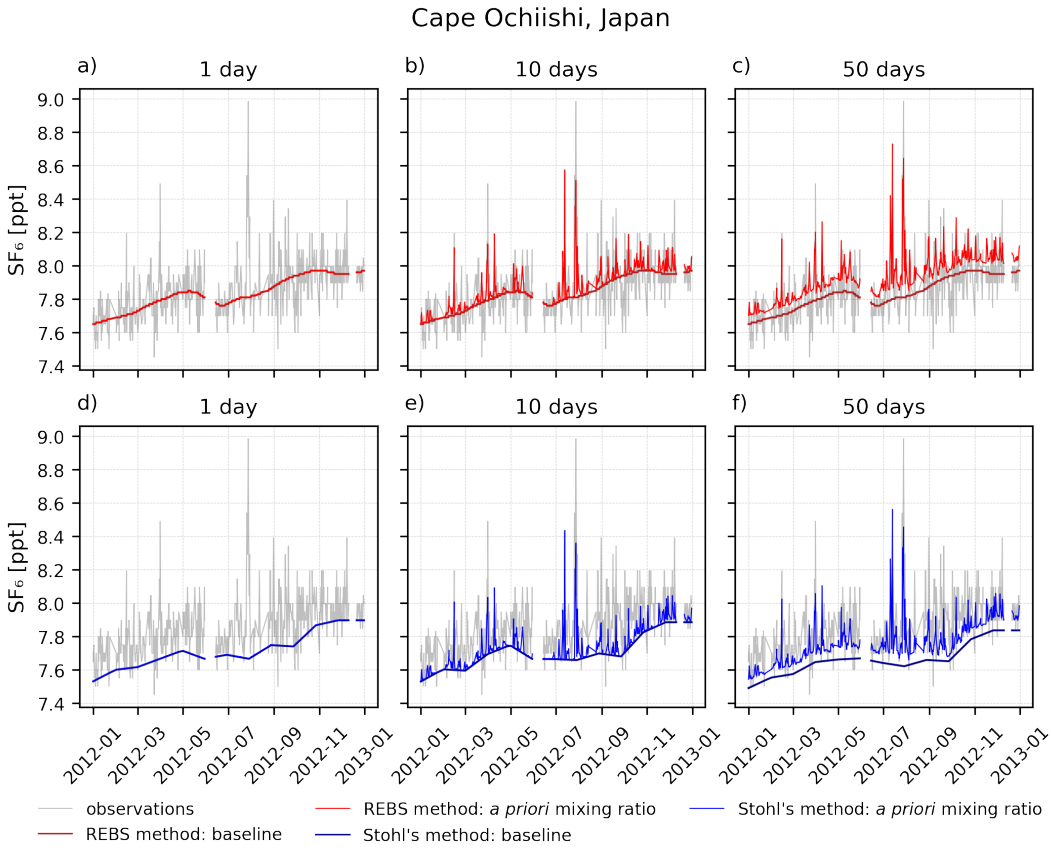

Figure S8: Baseline and *a priori* SF_6 mixing ratios calculated with the REBS (upper panels) and Stohl's method (lower panels) at the Cape Ochiishi observation station, compared to SF_6 observations. Model results are shown for backward simulations of 1 day (panels a and d), 10 days (panels b and e) and 50 days (panels c and f).

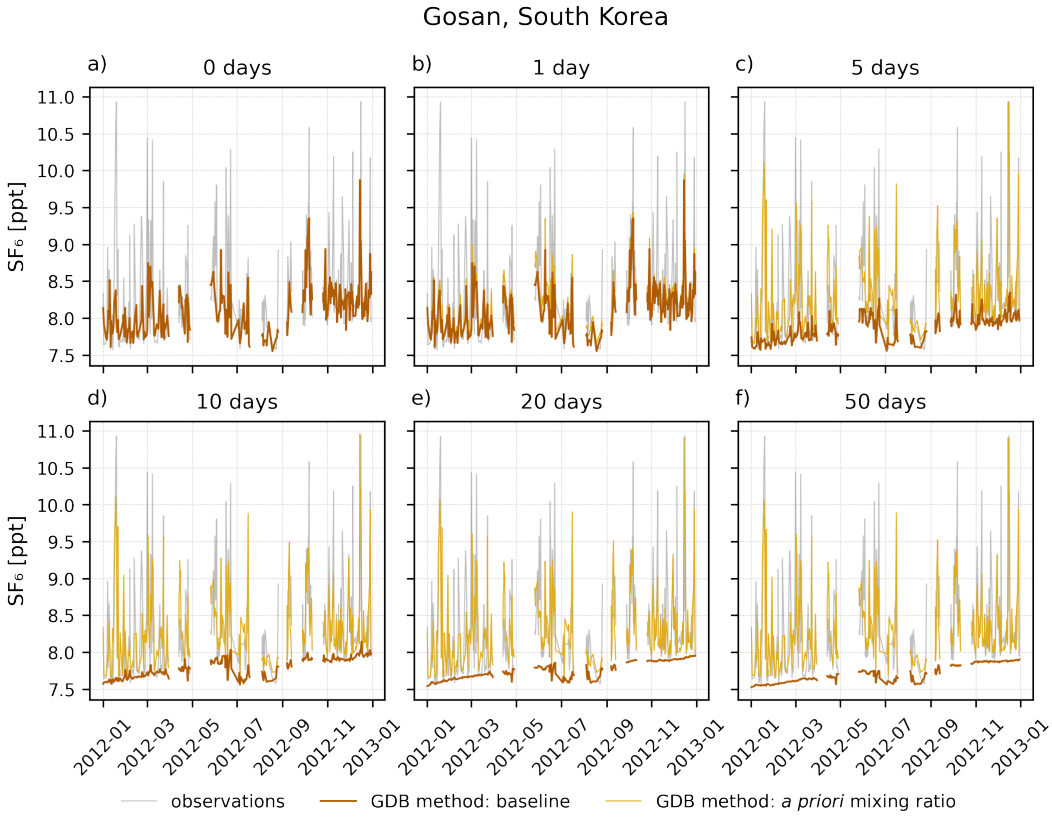

Figure S9: Baseline and *a priori* SF_6 mixing ratios calculated with the GDB method at the Gosan observation station for backward simulation times of 0 days (panel a), 1 day (b), 5 days (c), 10 days (d), 20 days (e) and 50 days (f).

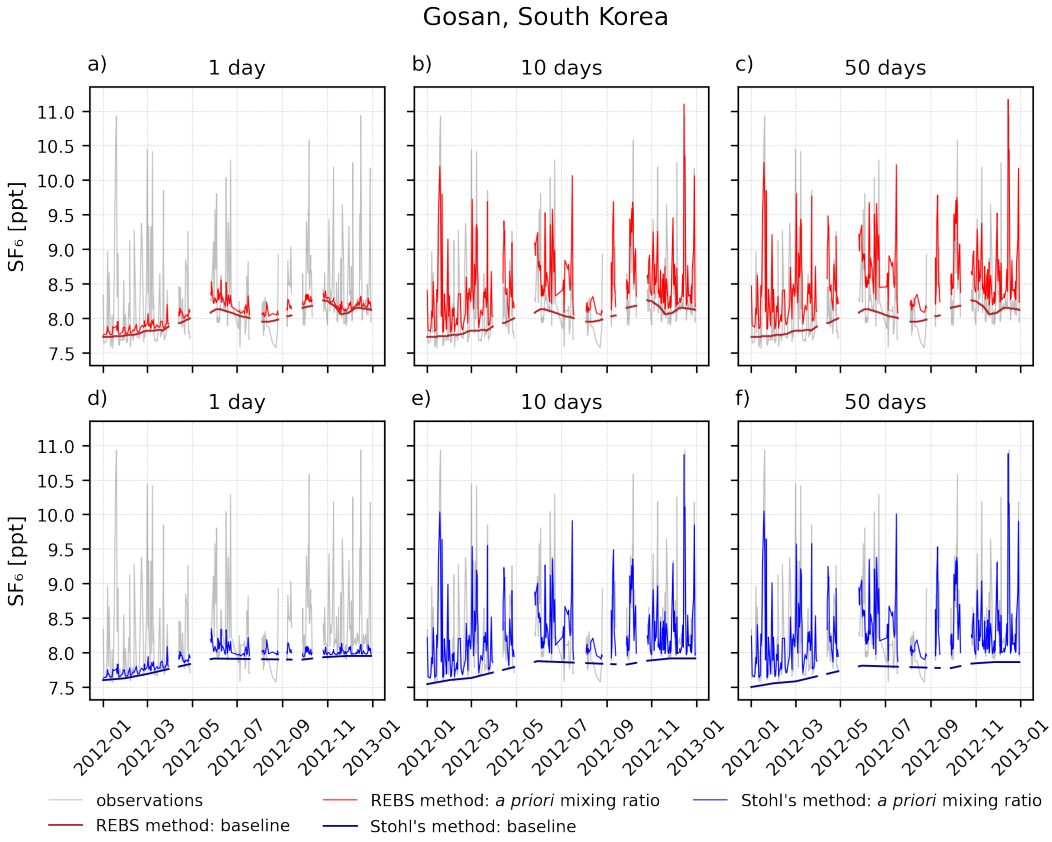

Figure S10: Baseline and *a priori* SF_6 mixing ratios calculated with the REBS (upper panels) and Stohl's method (lower panels) at the Gosan observation station, compared to SF_6 observations. Model results are shown for backward simulations of 1 day (panels a and d), 10 days (panels b and e) and 50 days (panels c and f).

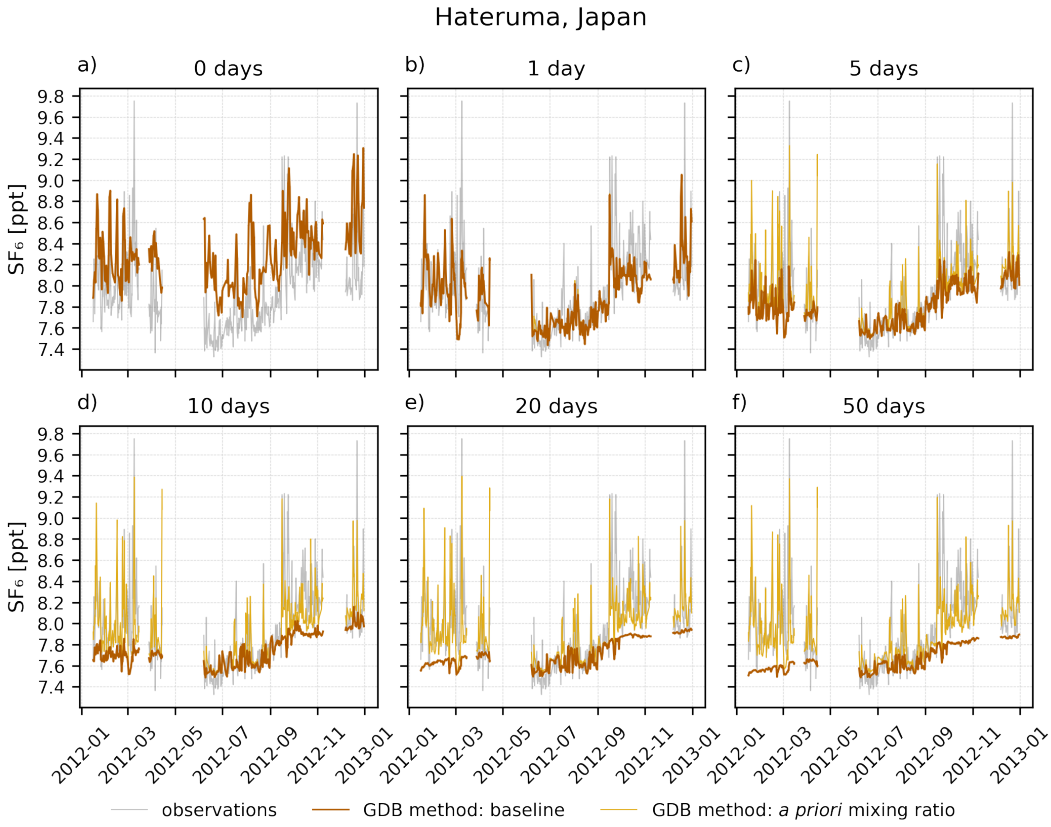

Figure S11: Baseline and *a priori* SF_6 mixing ratios calculated with the GDB method at the Hateruma observation station for backward simulation times of 0 days (panel a), 1 day (b), 5 days (c), 10 days (d), 20 days (e) and 50 days (f).

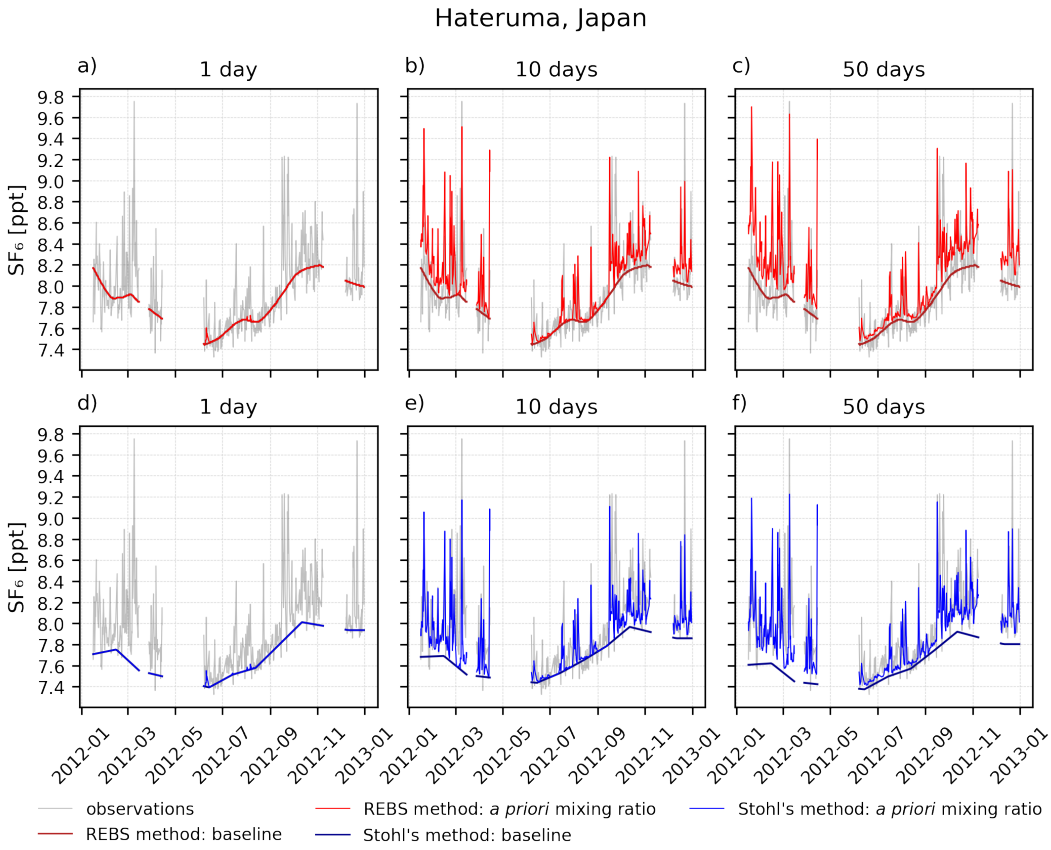

Figure S12: Baseline and *a priori* SF_6 mixing ratios calculated with the REBS (upper panels) and Stohl's method (lower panels) at the Hateruma observation station, compared to SF_6 observations. Model results are shown for backward simulations of 1 day (panels a and d), 10 days (panels b and e) and 50 days (panels c and f).

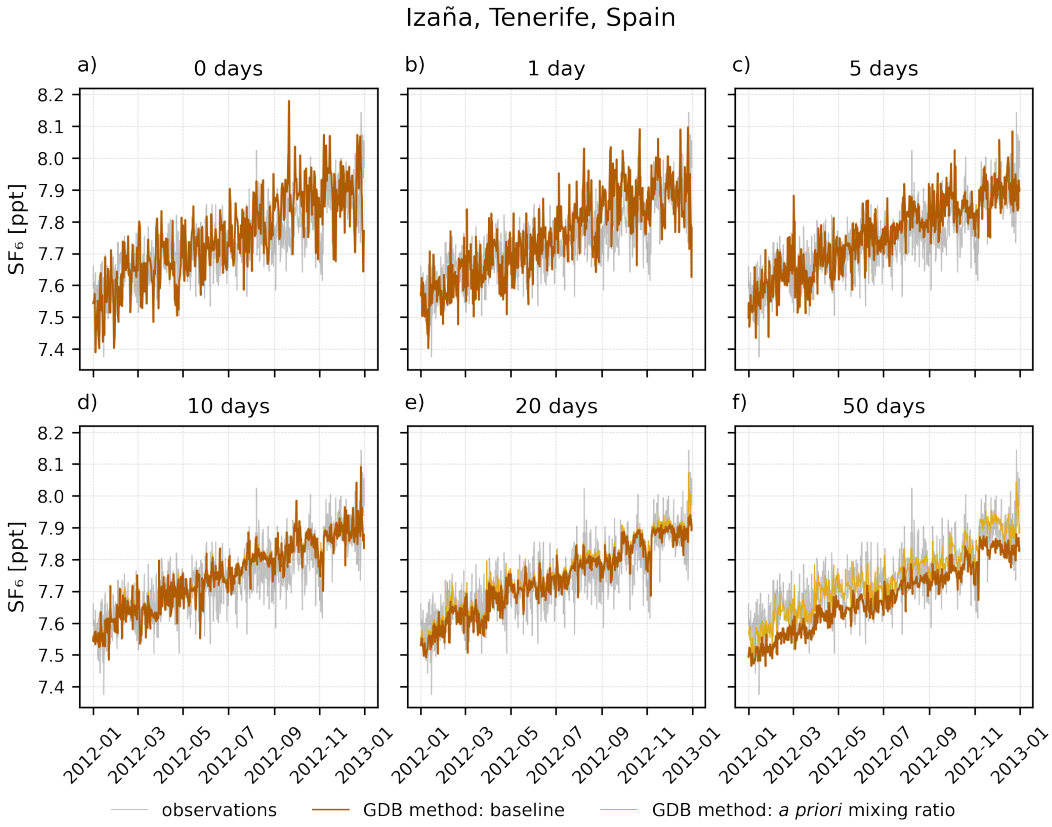

Figure S13: Baseline and *a priori* SF_6 mixing ratios calculated with the GDB method at the Izaña observation station for backward simulation times of 0 days (panel a), 1 day (b), 5 days (c), 10 days (d), 20 days (e) and 50 days (f).

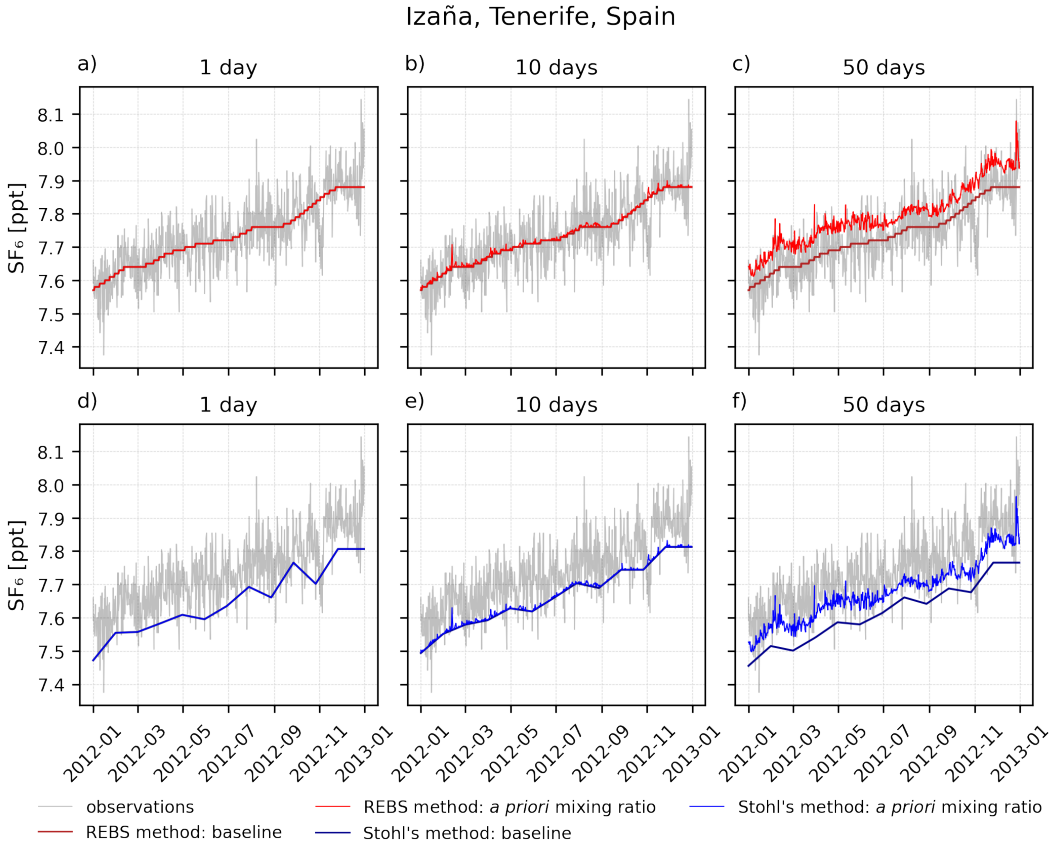

Figure S14: Baseline and *a priori* SF_6 mixing ratios calculated with the REBS (upper panels) and Stohl's method (lower panels) at the Izaña observation station, compared to SF_6 observations. Model results are shown for backward simulations of 1 day (panels a and d), 10 days (panels b and e) and 50 days (panels c and f).

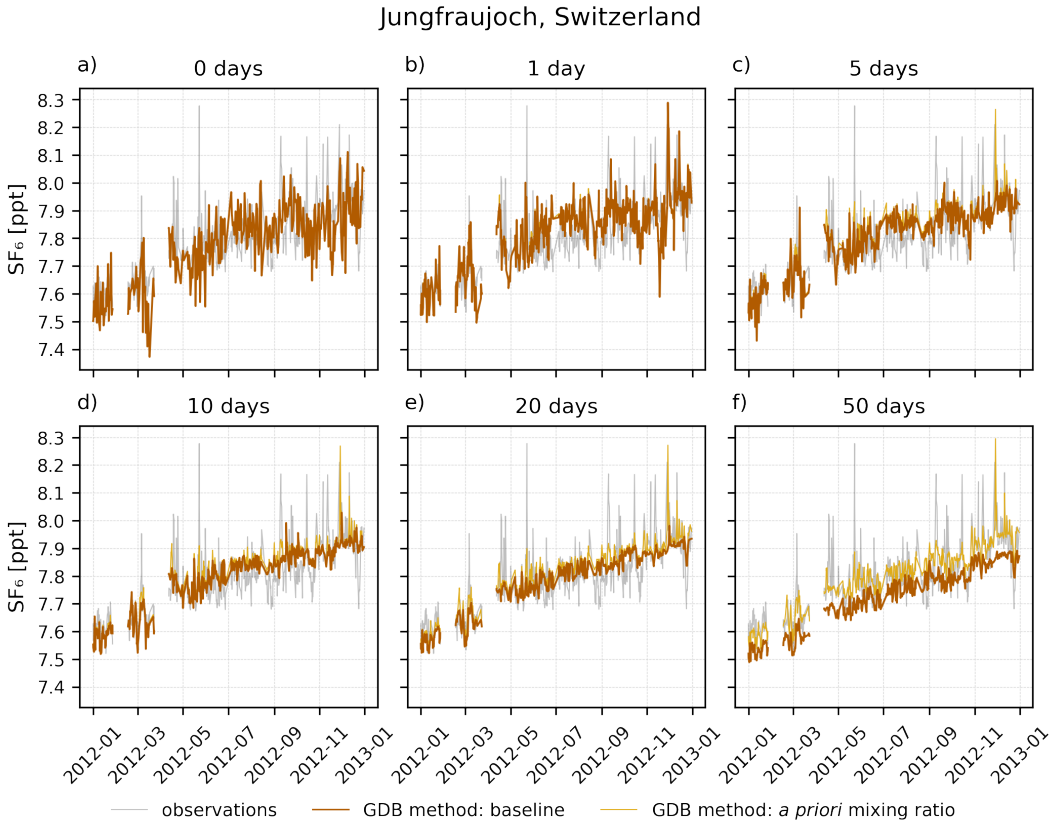

Figure S15: Baseline and *a priori* SF_6 mixing ratios calculated with the GDB method at the Jungfraujoch observation station for backward simulation times of 0 days (panel a), 1 day (b), 5 days (c), 10 days (d), 20 days (e) and 50 days (f).

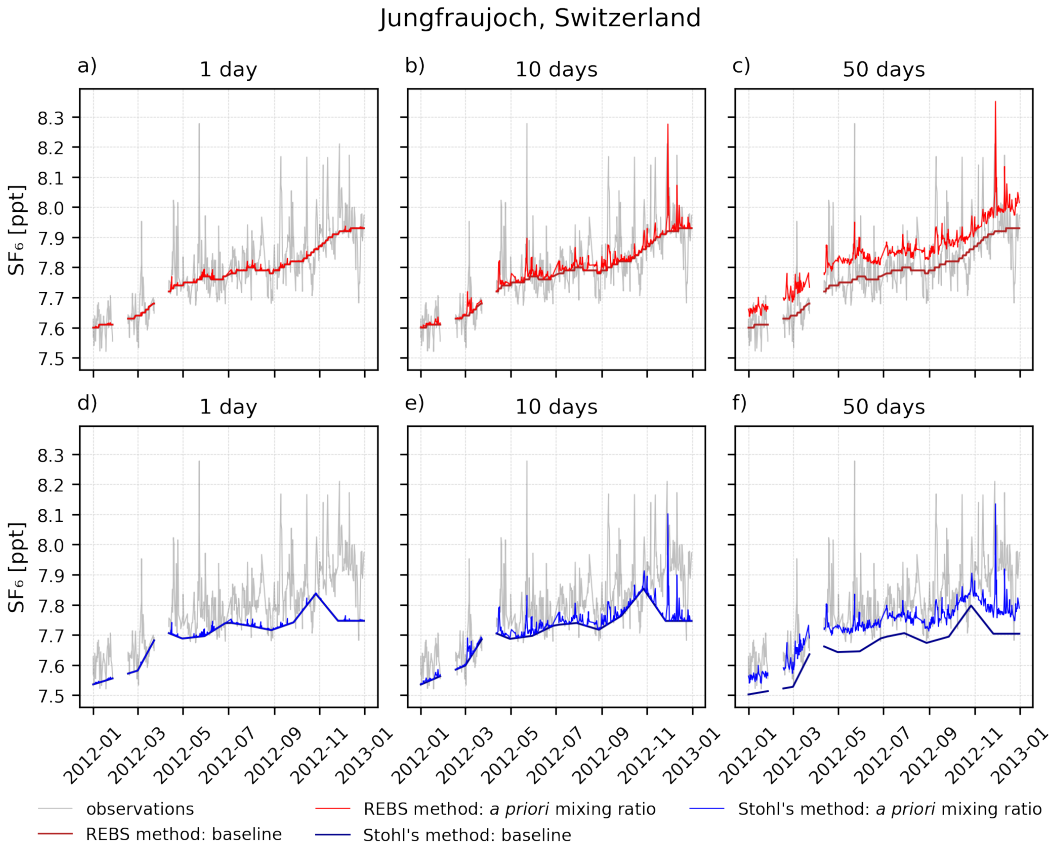

Figure S16: Baseline and *a priori* SF_6 mixing ratios calculated with the REBS (upper panels) and Stohl's method (lower panels) at the Jungfraujoch observation station, compared to SF_6 observations. Model results are shown for backward simulations of 1 day (panels a and d), 10 days (panels b and e) and 50 days (panels c and f).

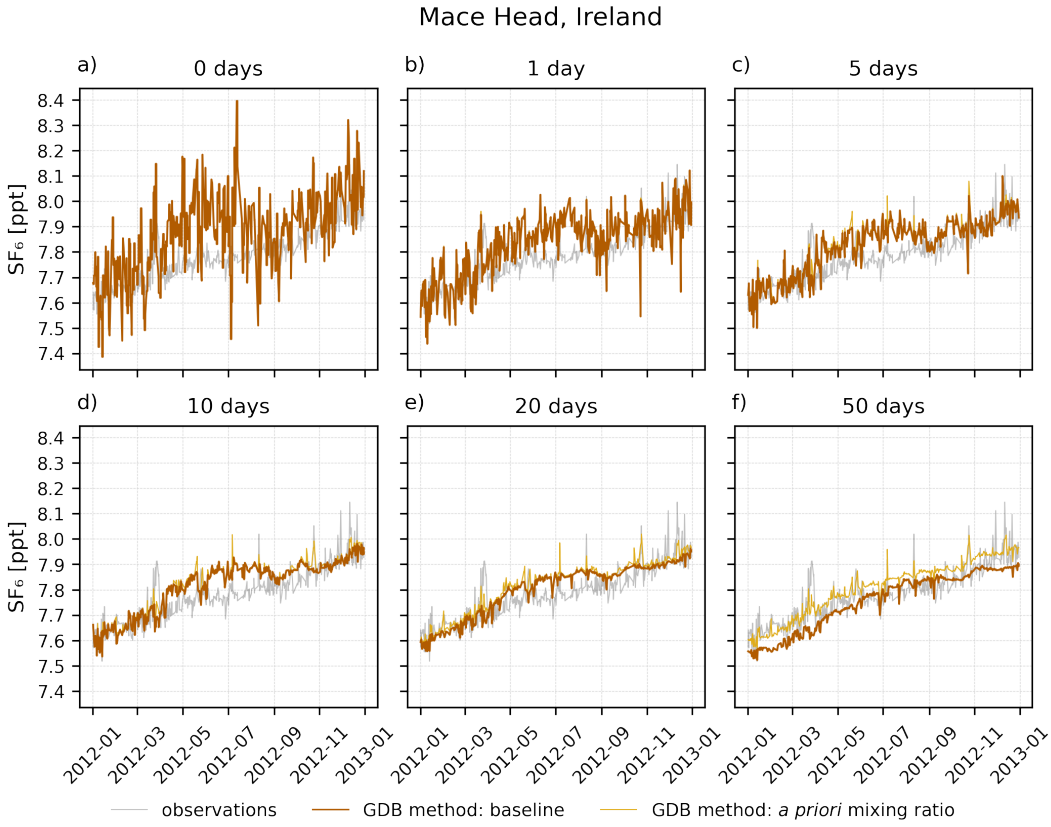

Figure S17: Baseline and *a priori* SF_6 mixing ratios calculated with the GDB method at the Mace Head observation station for backward simulation times of 0 days (panel a), 1 day (b), 5 days (c), 10 days (d), 20 days (e) and 50 days (f).

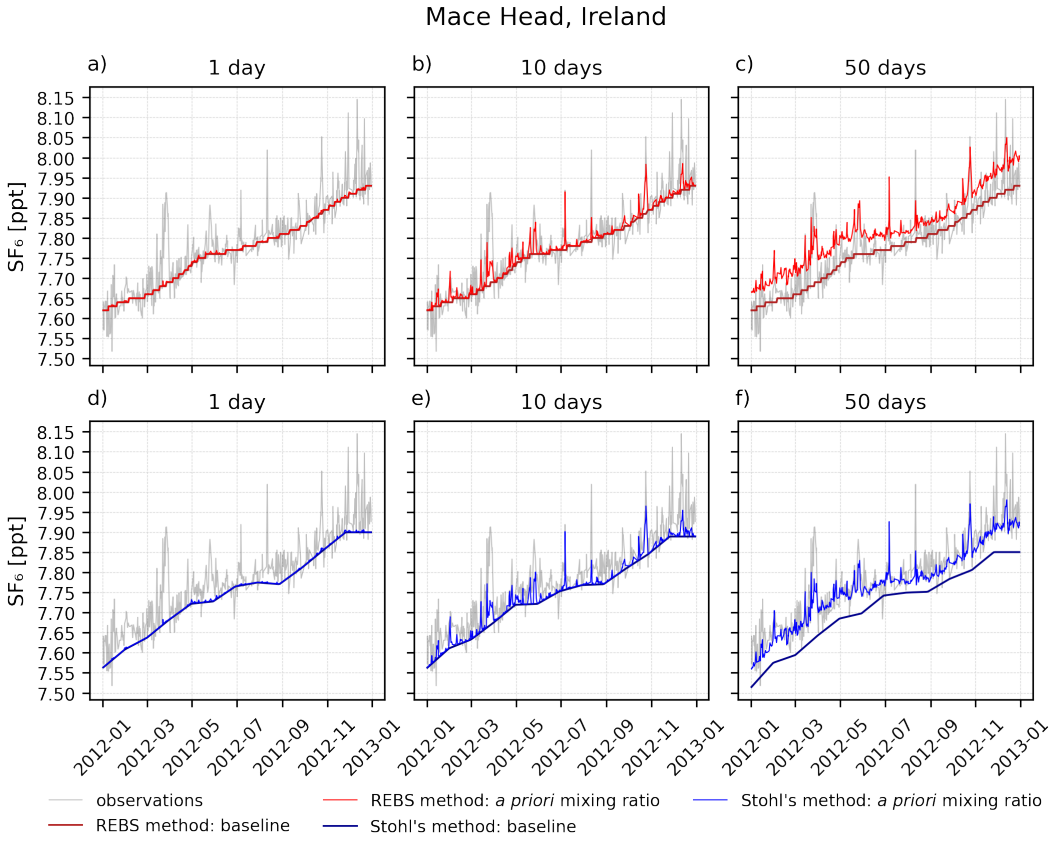

Figure S18: Baseline and *a priori* SF_6 mixing ratios calculated with the REBS (upper panels) and Stohl's method (lower panels) at the Mace Head observation station, compared to SF_6 observations. Model results are shown for backward simulations of 1 day (panels a and d), 10 days (panels b and e) and 50 days (panels c and f).

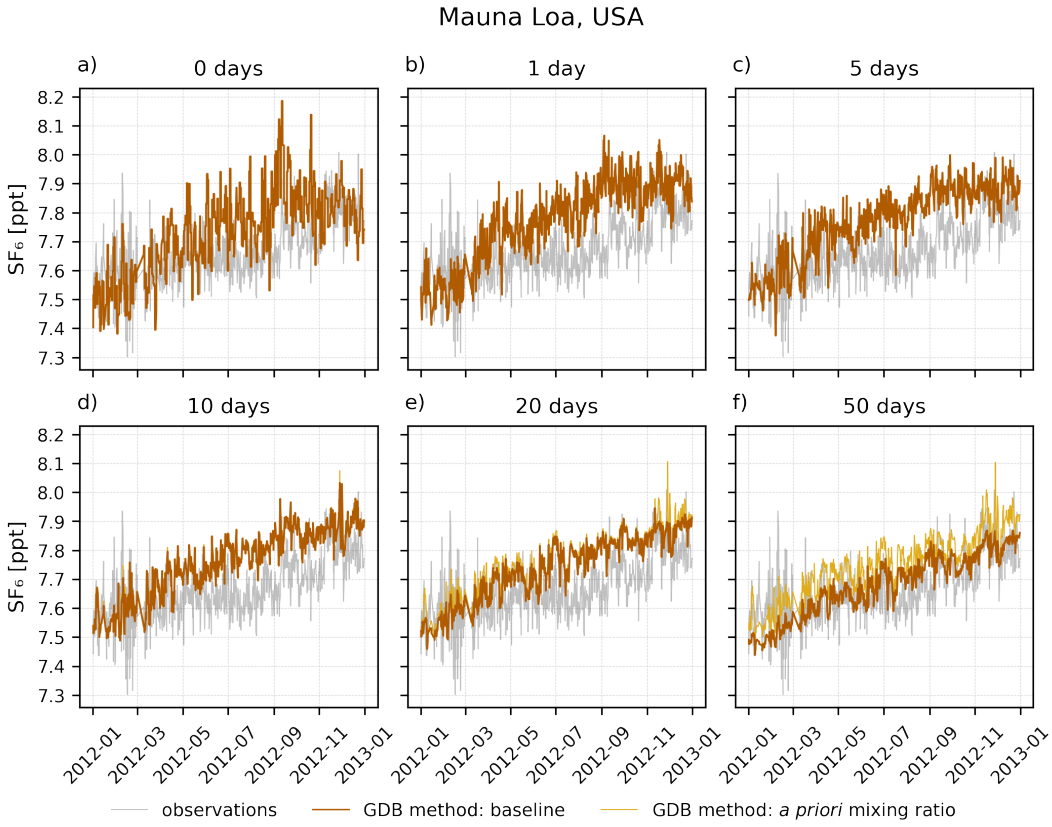

Figure S19: Baseline and *a priori* SF_6 mixing ratios calculated with the GDB method at the Mauna Loa observation station for backward simulation times of 0 days (panel a), 1 day (b), 5 days (c), 10 days (d), 20 days (e) and 50 days (f).

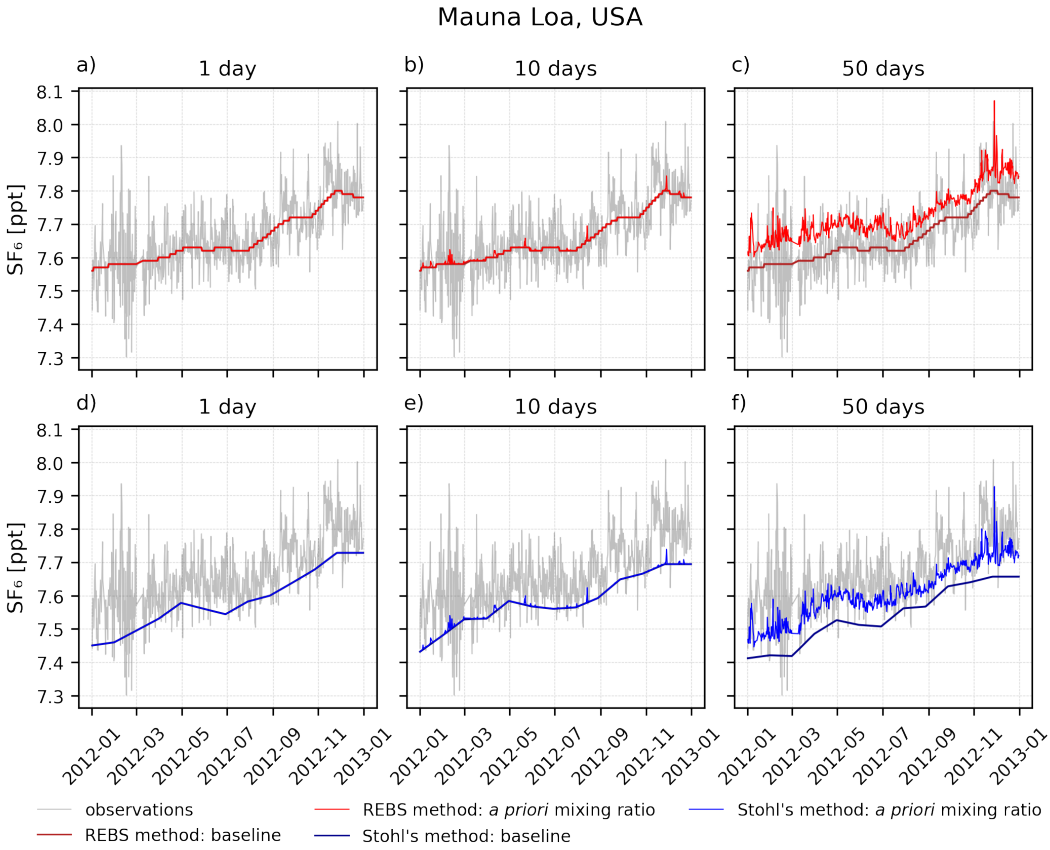

Figure S20: Baseline and *a priori* SF_6 mixing ratios calculated with the REBS (upper panels) and Stohl's method (lower panels) at the Mauna Loa observation station, compared to SF_6 observations. Model results are shown for backward simulations of 1 day (panels a and d), 10 days (panels b and e) and 50 days (panels c and f).

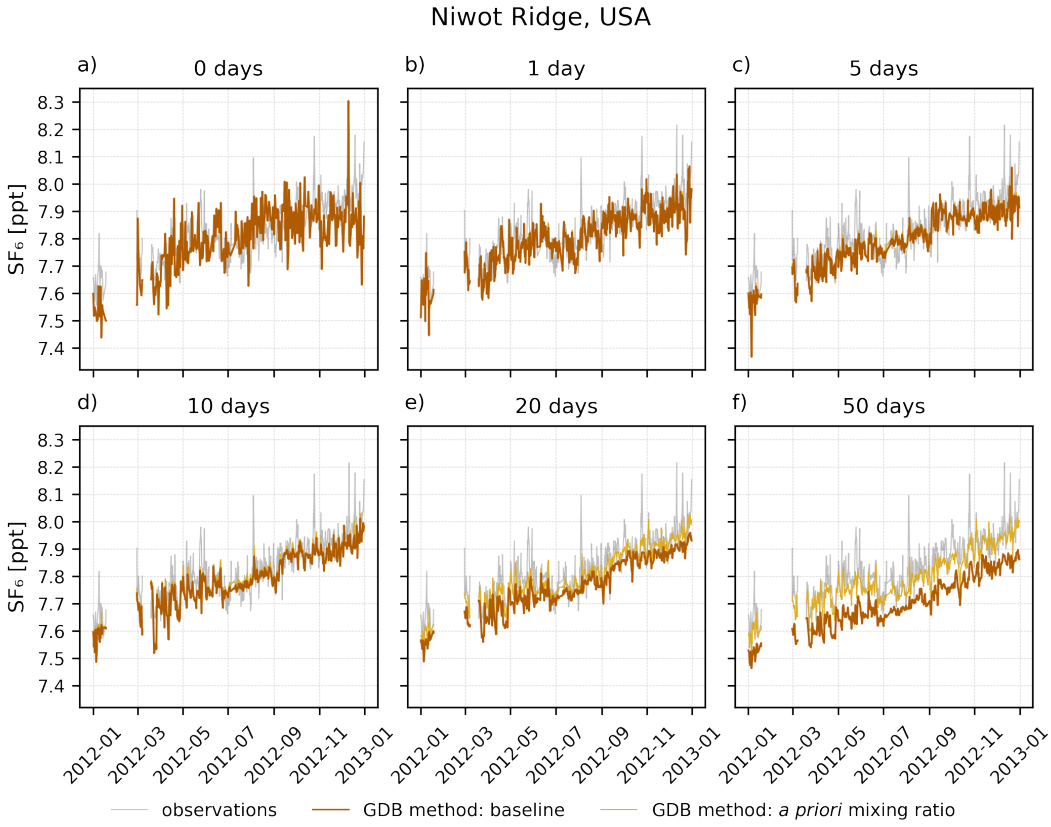

Figure S21: Baseline and *a priori* SF_6 mixing ratios calculated with the GDB method at the Niwot Ridge observation station for backward simulation times of 0 days (panel a), 1 day (b), 5 days (c), 10 days (d), 20 days (e) and 50 days (f).

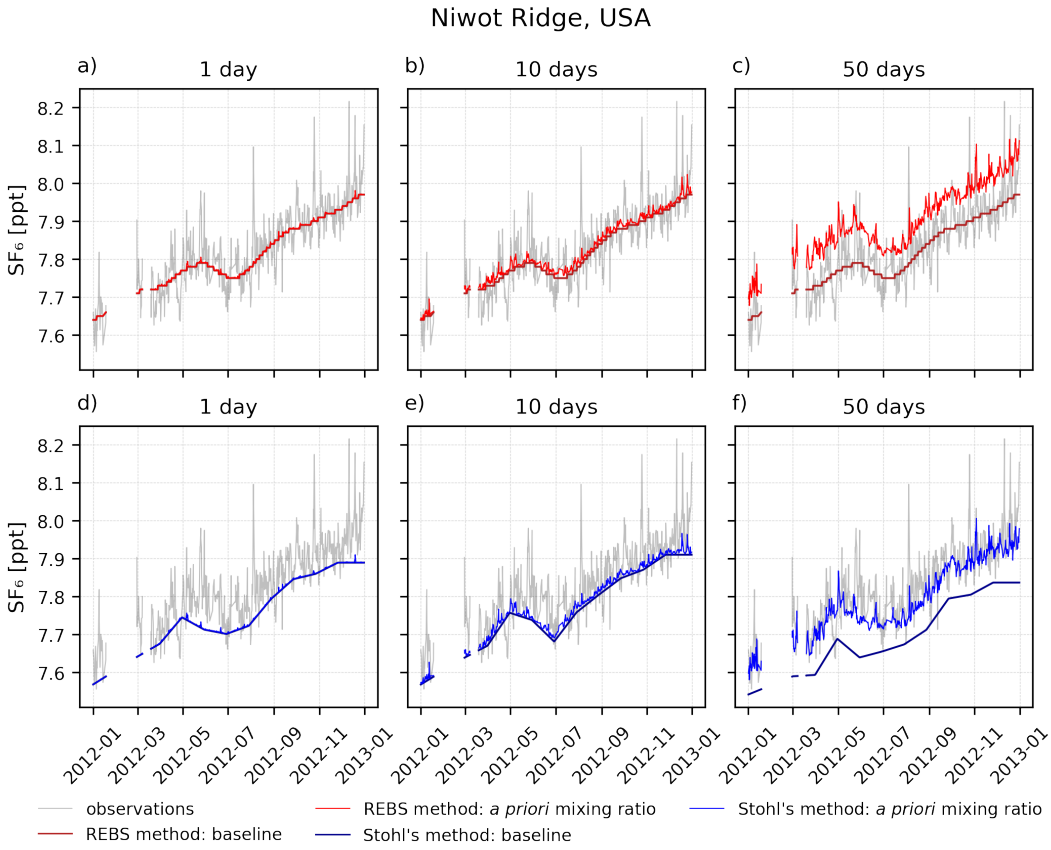

Figure S22: Baseline and *a priori* SF_6 mixing ratios calculated with the REBS (upper panels) and Stohl's method (lower panels) at the Niwot Ridge observation station, compared to SF_6 observations. Model results are shown for backward simulations of 1 day (panels a and d), 10 days (panels b and e) and 50 days (panels c and f).

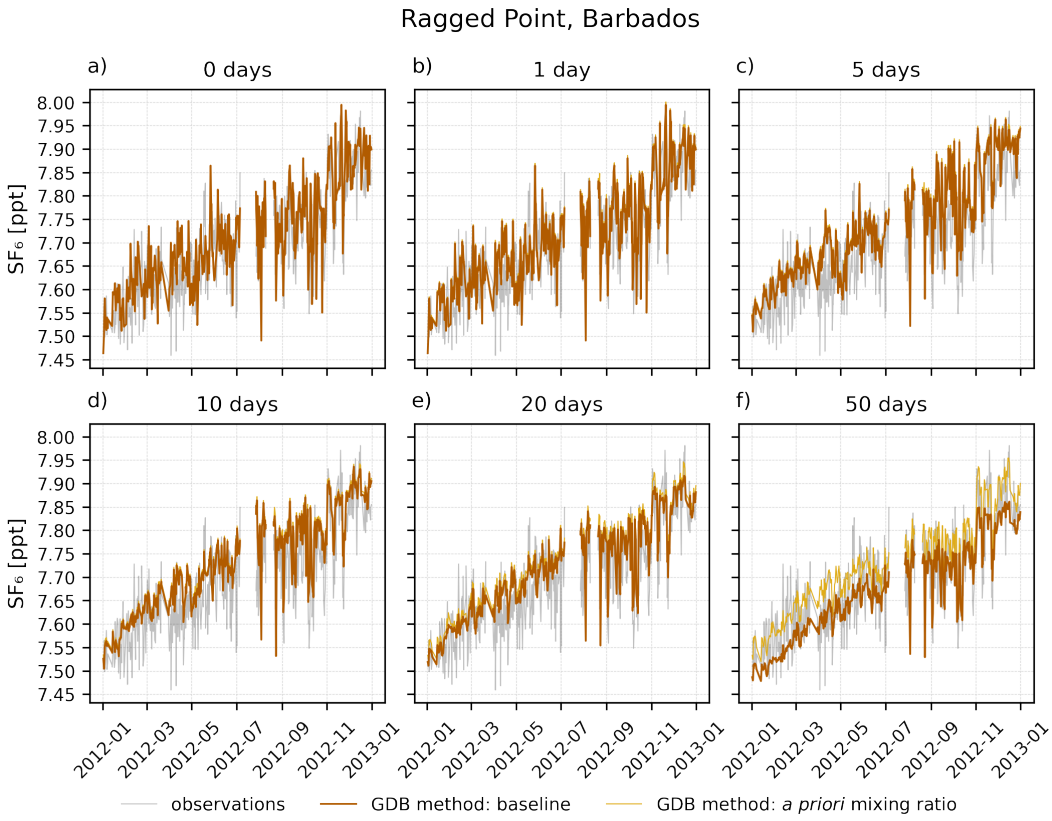

Figure S23: Baseline and *a priori* SF_6 mixing ratios calculated with the GDB method at the Ragged Point observation station for backward simulation times of 0 days (panel a), 1 day (b), 5 days (c), 10 days (d), 20 days (e) and 50 days (f).

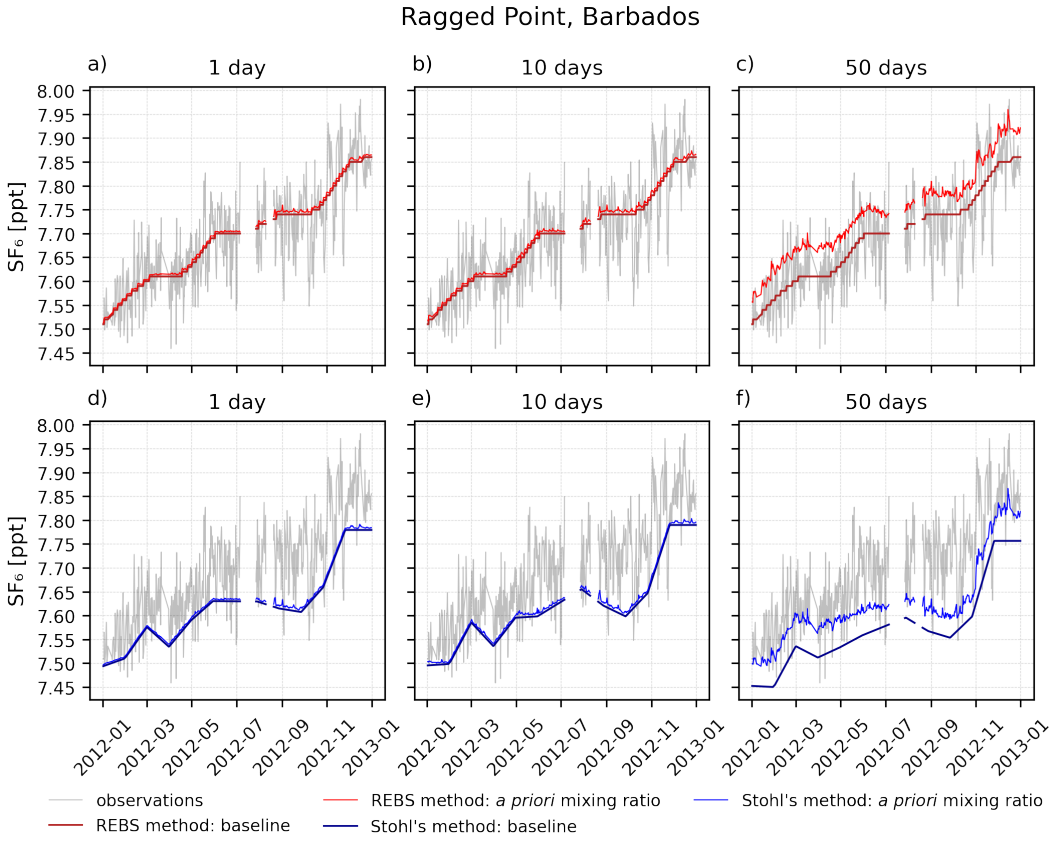

Figure S24: Baseline and *a priori* SF_6 mixing ratios calculated with the REBS (upper panels) and Stohl's method (lower panels) at the Ragged Point observation station, compared to SF_6 observations. Model results are shown for backward simulations of 1 day (panels a and d), 10 days (panels b and e) and 50 days (panels c and f).

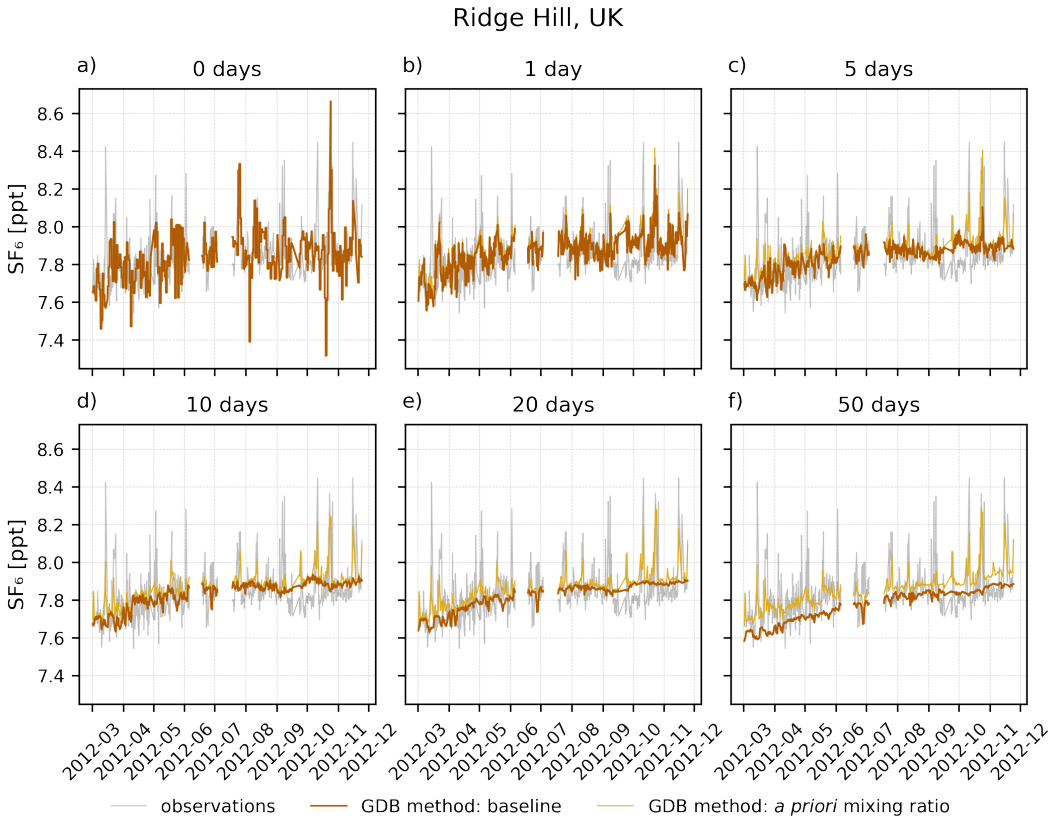

Figure S25: Baseline and *a priori* SF_6 mixing ratios calculated with the GDB method at the Ridge Hill observation station for backward simulation times of 0 days (panel a), 1 day (b), 5 days (c), 10 days (d), 20 days (e) and 50 days (f).

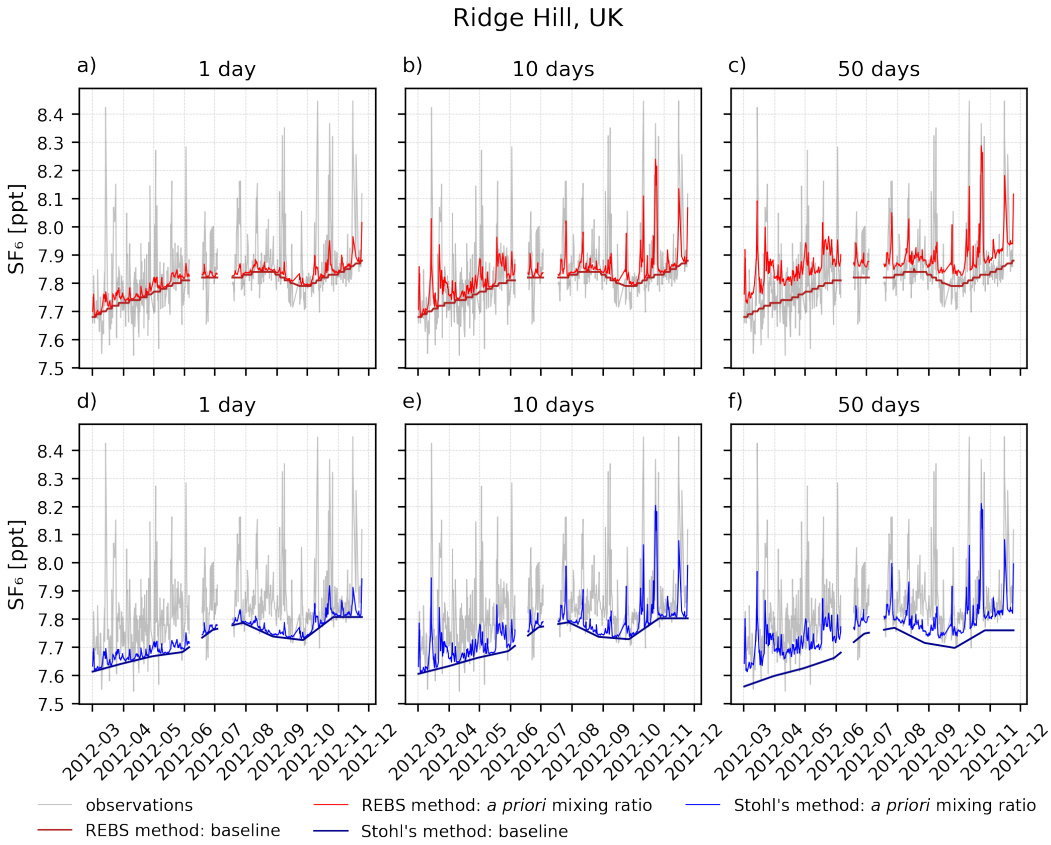

Figure S26: Baseline and *a priori* SF_6 mixing ratios calculated with the REBS (upper panels) and Stohl's method (lower panels) at the Ridge Hill observation station, compared to SF_6 observations. Model results are shown for backward simulations of 1 day (panels a and d), 10 days (panels b and e) and 50 days (panels c and f).

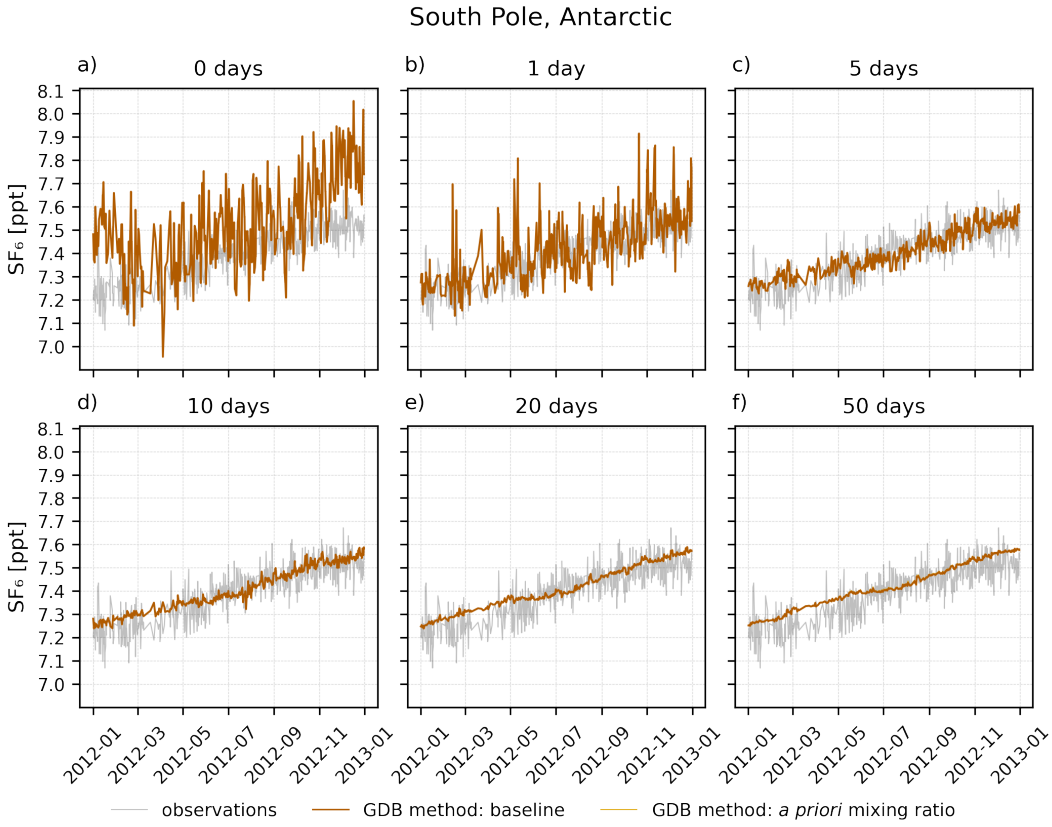

Figure S27: Baseline and *a priori* SF_6 mixing ratios calculated with the GDB method at the South Pole observation station for backward simulation times of 0 days (panel a), 1 day (b), 5 days (c), 10 days (d), 20 days (e) and 50 days (f).

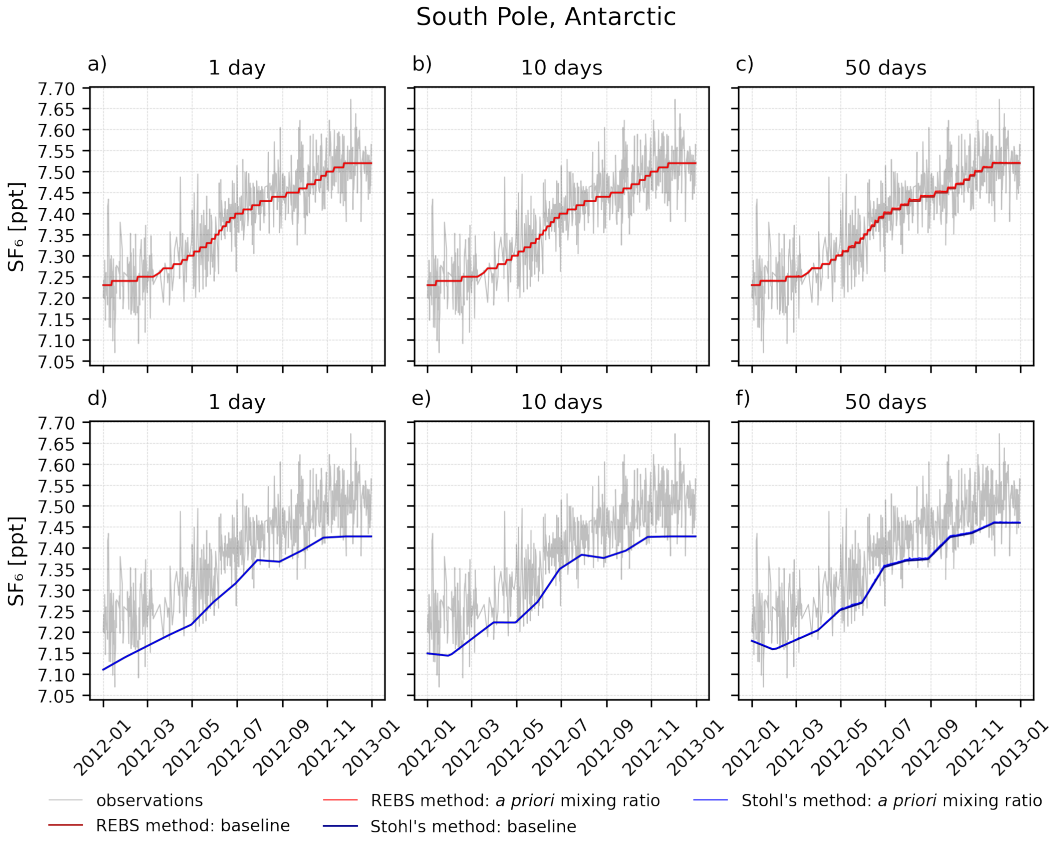

Figure S28: Baseline and *a priori* SF_6 mixing ratios calculated with the REBS (upper panels) and Stohl's method (lower panels) at the South Pole observation station, compared to SF_6 observations. Model results are shown for backward simulations of 1 day (panels a and d), 10 days (panels b and e) and 50 days (panels c and f).

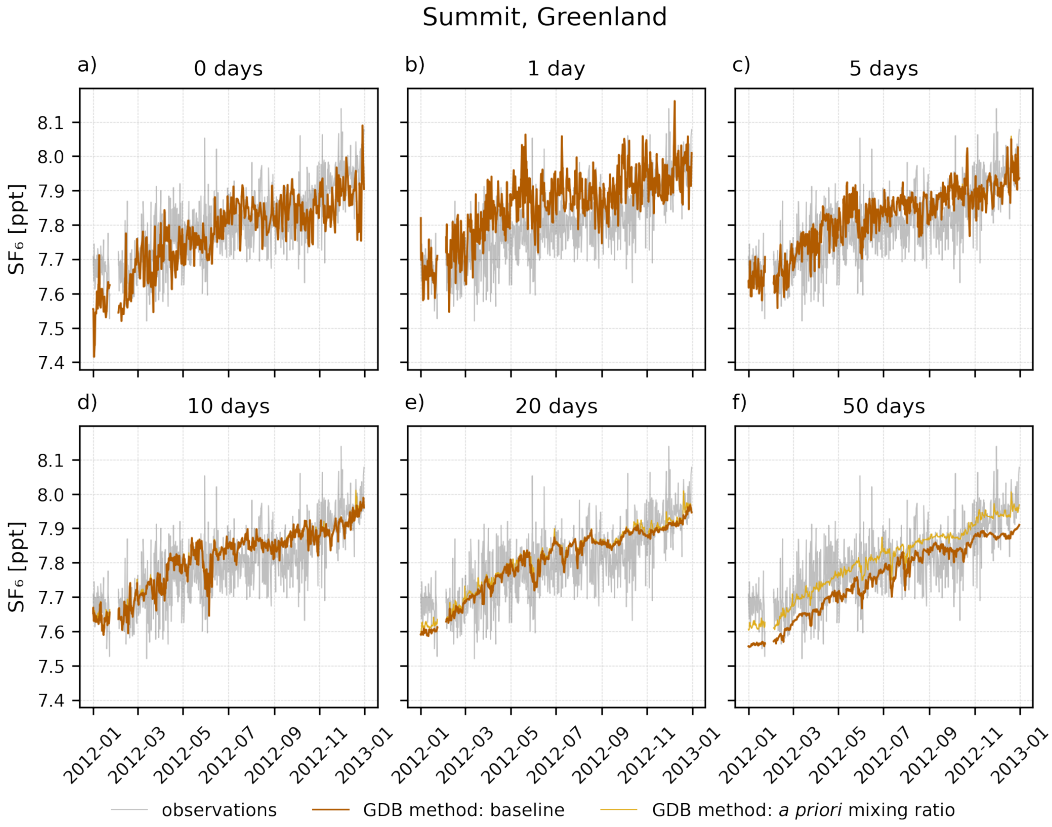

Figure S29: Baseline and *a priori* SF_6 mixing ratios calculated with the GDB method at the Summit observation station for backward simulation times of 0 days (panel a), 1 day (b), 5 days (c), 10 days (d), 20 days (e) and 50 days (f).

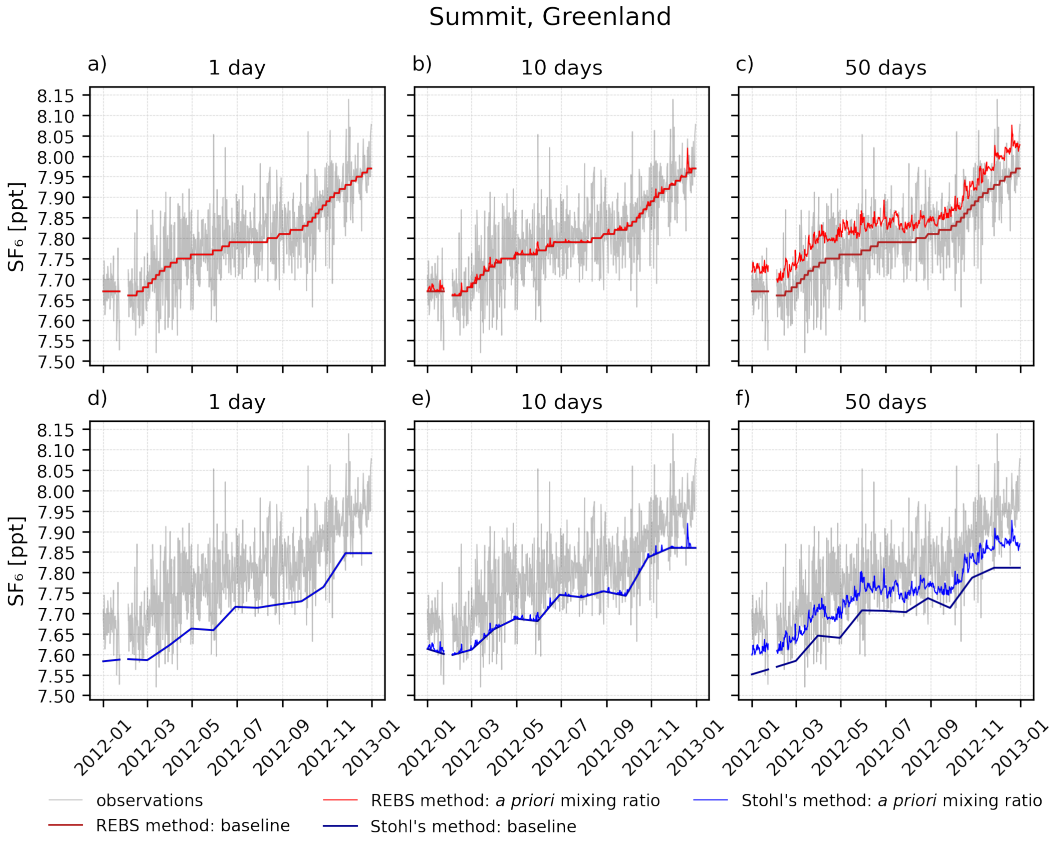

Figure S30: Baseline and *a priori* SF_6 mixing ratios calculated with the REBS (upper panels) and Stohl's method (lower panels) at the Summit observation station, compared to SF_6 observations. Model results are shown for backward simulations of 1 day (panels a and d), 10 days (panels b and e) and 50 days (panels c and f).

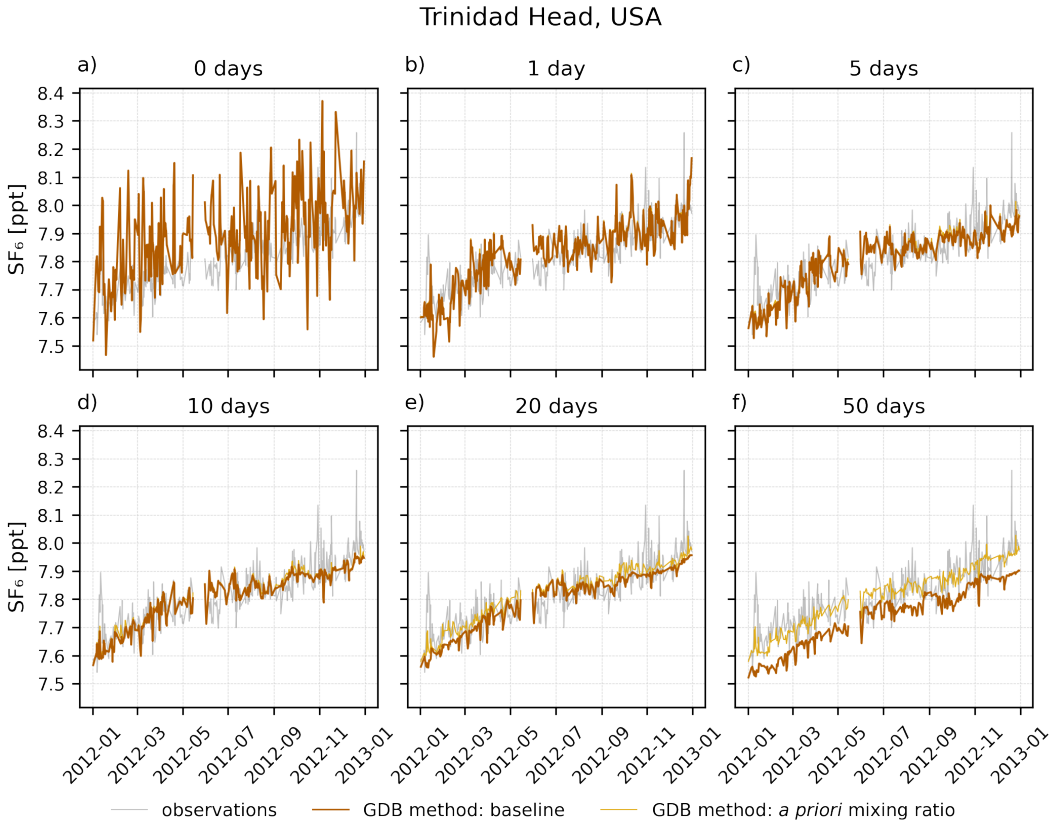

Figure S31: Baseline and *a priori* SF_6 mixing ratios calculated with the GDB method at the Trinidad Head observation station for backward simulation times of 0 days (panel a), 1 day (b), 5 days (c), 10 days (d), 20 days (e) and 50 days (f).

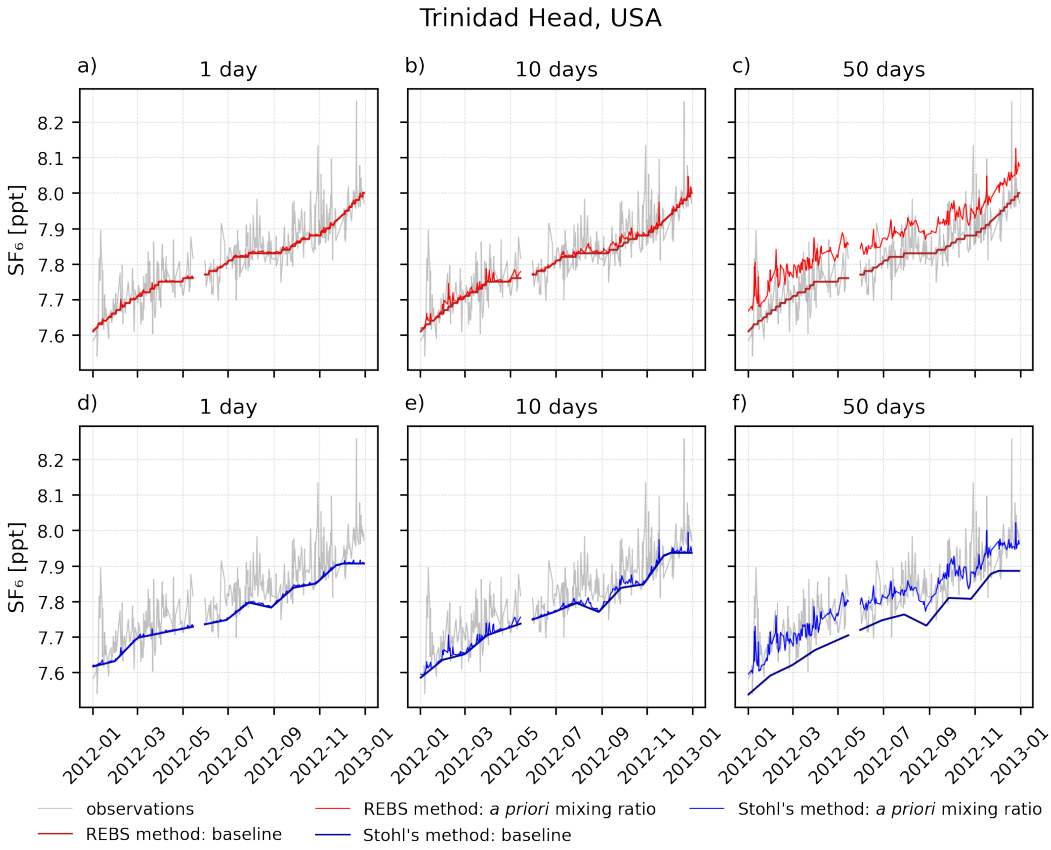

Figure S32: Baseline and *a priori* SF_6 mixing ratios calculated with the REBS (upper panels) and Stohl's method (lower panels) at the Trinidad Head observation station, compared to SF_6 observations. Model results are shown for backward simulations of 1 day (panels a and d), 10 days (panels b and e) and 50 days (panels c and f).

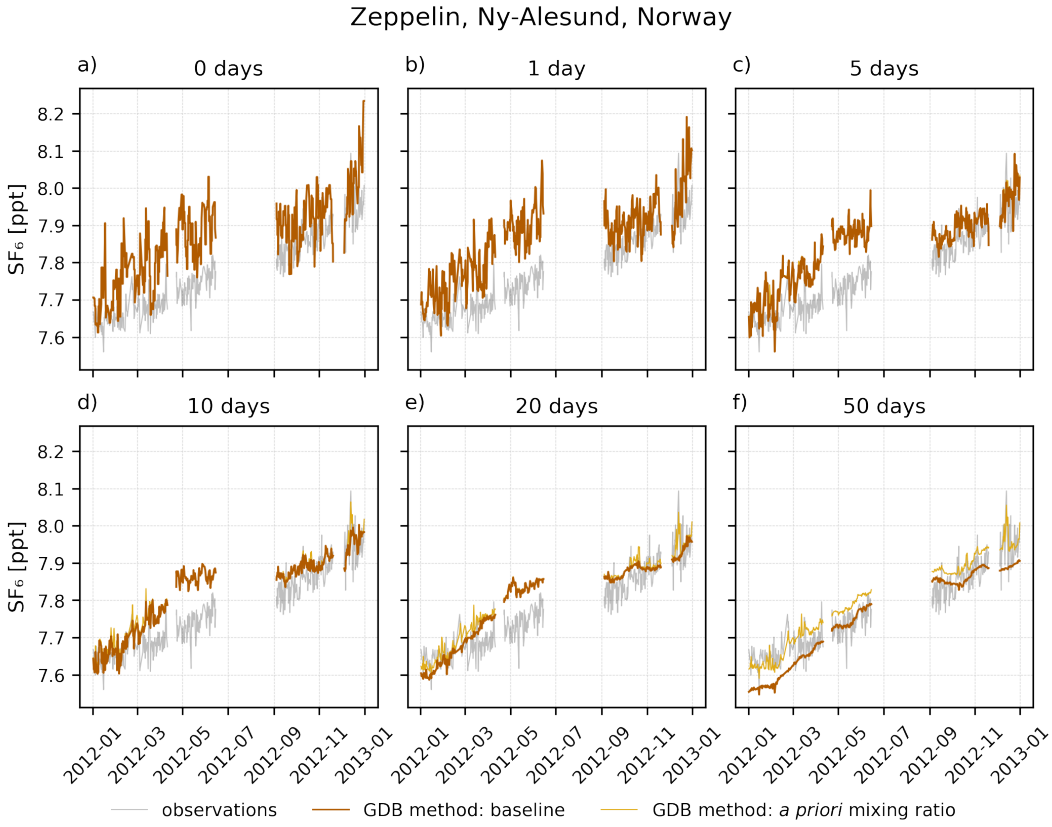

Figure S33: Baseline and *a priori* SF_6 mixing ratios calculated with the GDB method at the Zeppelin observation station for backward simulation times of 0 days (panel a), 1 day (b), 5 days (c), 10 days (d), 20 days (e) and 50 days (f).

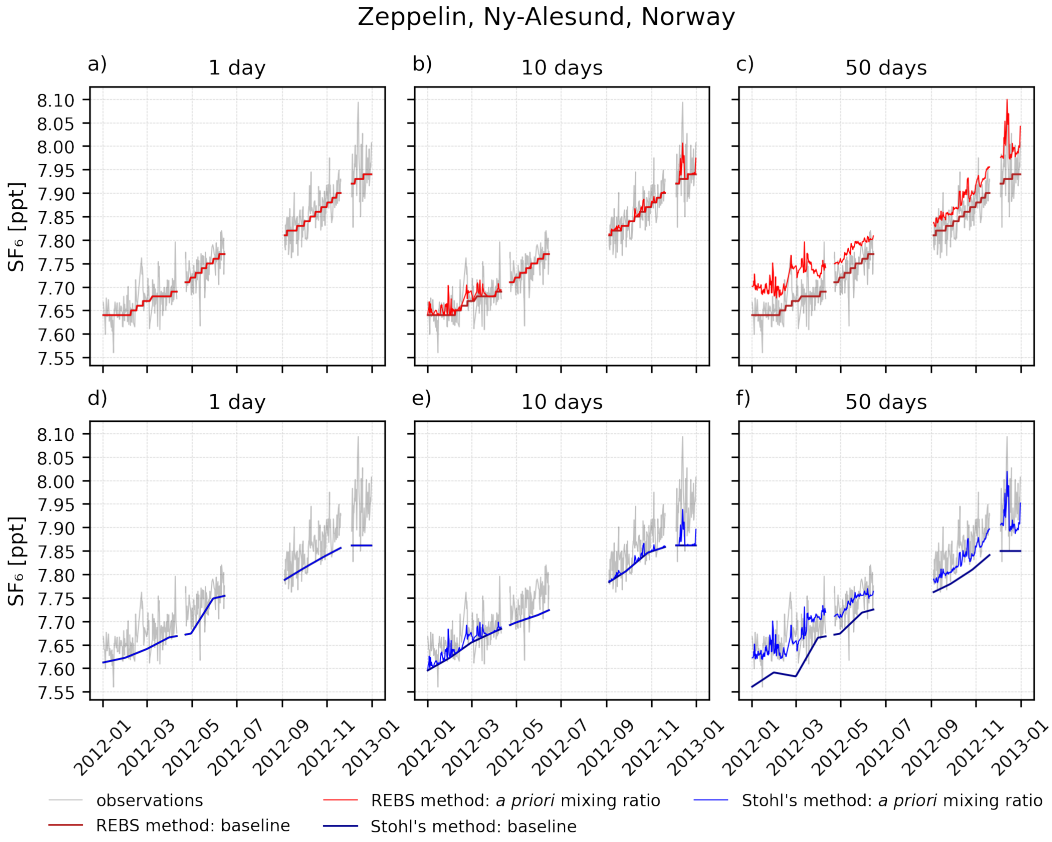

Figure S34: Baseline and *a priori* SF_6 mixing ratios calculated with the REBS (upper panels) and Stohl's method (lower panels) at the Zeppelin observation station, compared to SF_6 observations. Model results are shown for backward simulations of 1 day (panels a and d), 10 days (panels b and e) and 50 days (panels c and f).

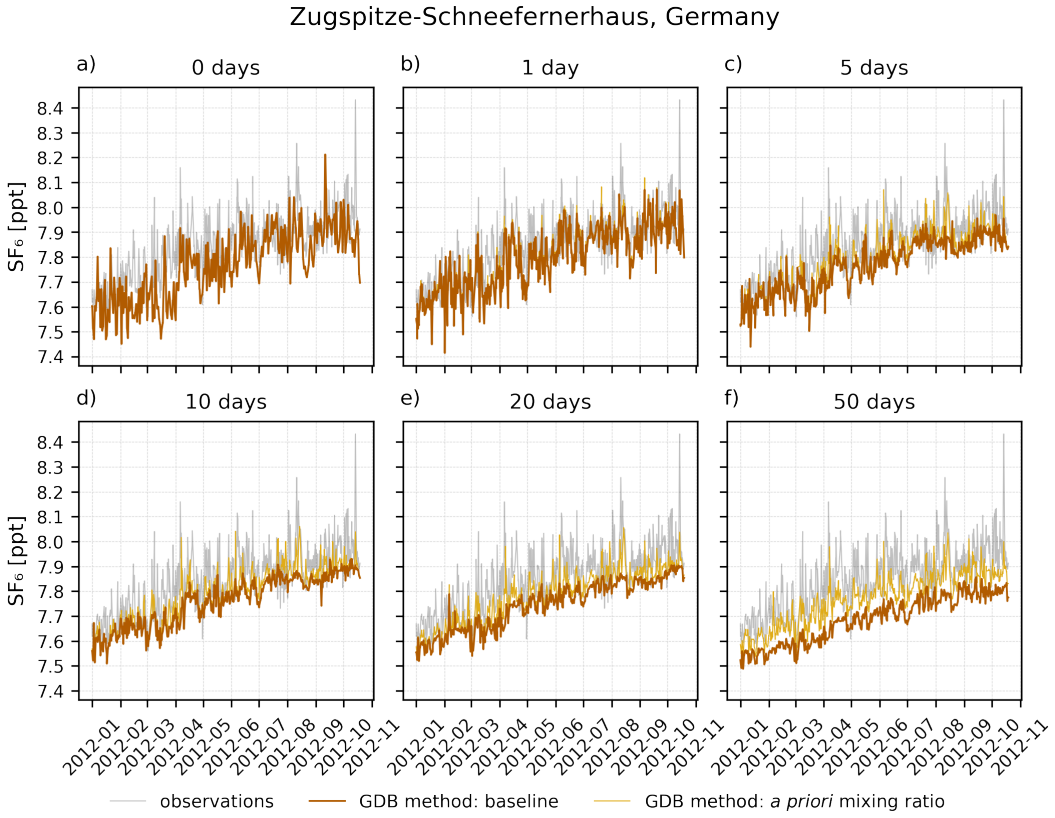

Figure S35: Baseline and *a priori* SF_6 mixing ratios calculated with the GDB method at the Zugspitze-Schneefernerhaus observation station for backward simulation times of 0 days (panel a), 1 day (b), 5 days (c), 10 days (d), 20 days (e) and 50 days (f).

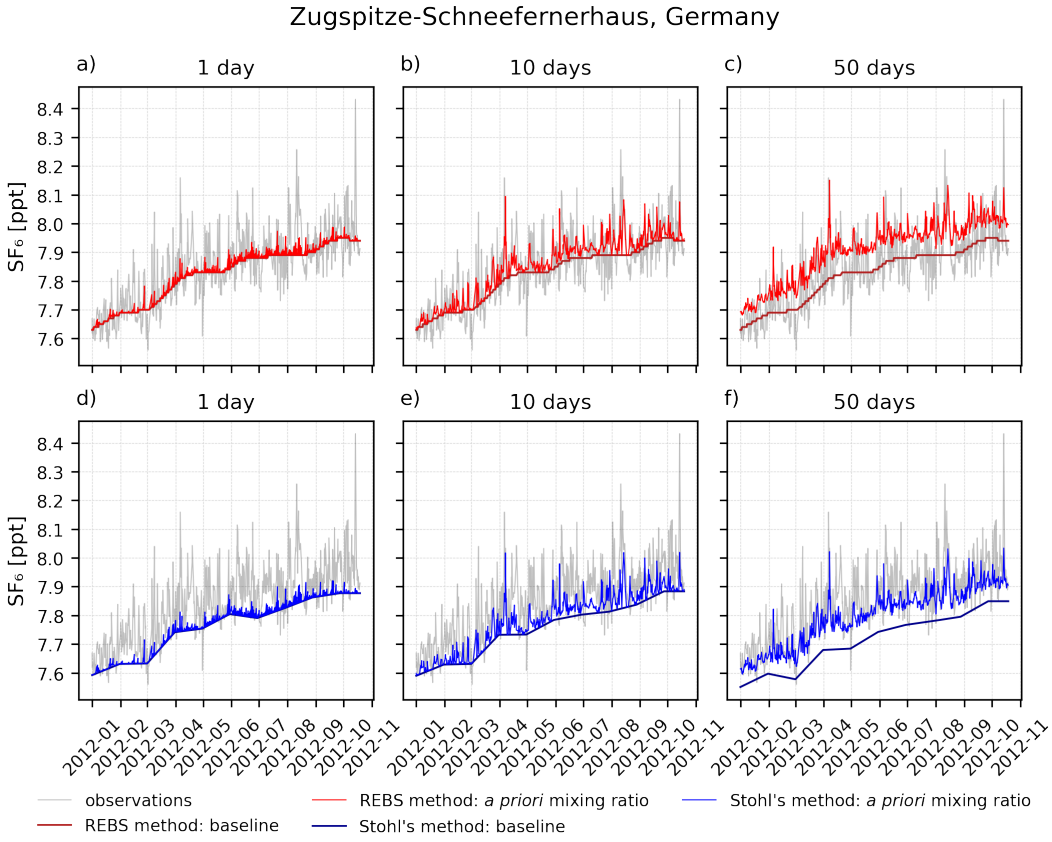

Figure S36: Baseline and *a priori* SF_6 mixing ratios calculated with the REBS (upper panels) and Stohl's method (lower panels) at the Zugspitze-Schneefernerhaus observation station, compared to SF_6 observations. Model results are shown for backward simulations of 1 day (panels a and d), 10 days (panels b and e) and 50 days (panels c and f).

Supplementary Material - A global re-analysis of regionally resolved emissions and atmospheric mole fractions of SF_6 for the period 2005-2021

Martin Vojta[1], Andreas Plach[1], Saurabh Annadate[2,3], Sunyong Park[4], Gawon Lee[4], Pallav Purohit[6], Florian Lindl[6], Xin Lan[8], Jens Mühle[7], Rona L. Thompson[5], and Andreas Stohl[1]

[1]Department of Meteorology and Geophysics, University of Vienna, Vienna, Austria
[2]Department of Pure and Applied Sciences, University of Urbino "Carlo Bo", Urbino, Italy
[3]University School for Advanced Studies IUSS, 27100 Pavia, Italy
[4]Kyungpook National University, Department of Oceanography, School of Earth System Sciences, Daegu, South Korea
[5]NILU, Kjeller, Norway
[6]International Institute for Applied Systems Analysis (IIASA), Laxenburg, Austria
[7]Scripps Institution of Oceanography, University of California, San Diego, CA, 92037, USA
[8]NOAA Global Monitoring Laboratory, Boulder, CO, USA

S1 Supplementary Figures

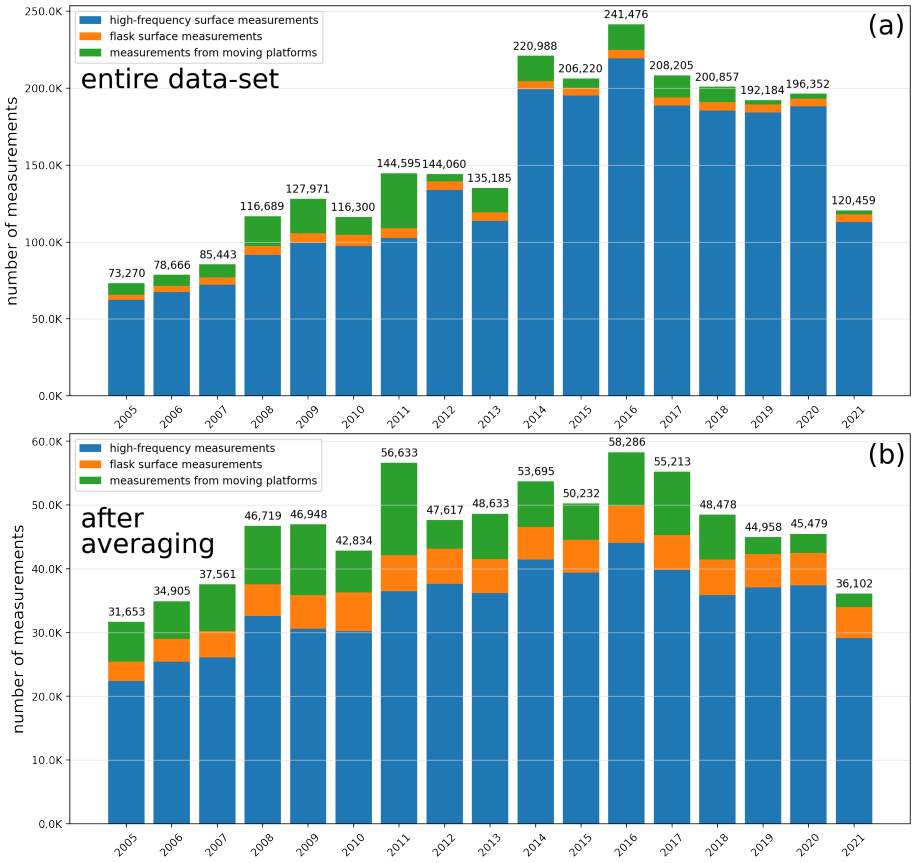

Figure S1. The total number of annual available observations of (a) the entire measurement dataset and (b) the dataset after averaging. The different colors indicate the different measurement types; blue: continuous, high-frequency surface measurements; orange: flask surface measurements; green: measurements from moving platforms.

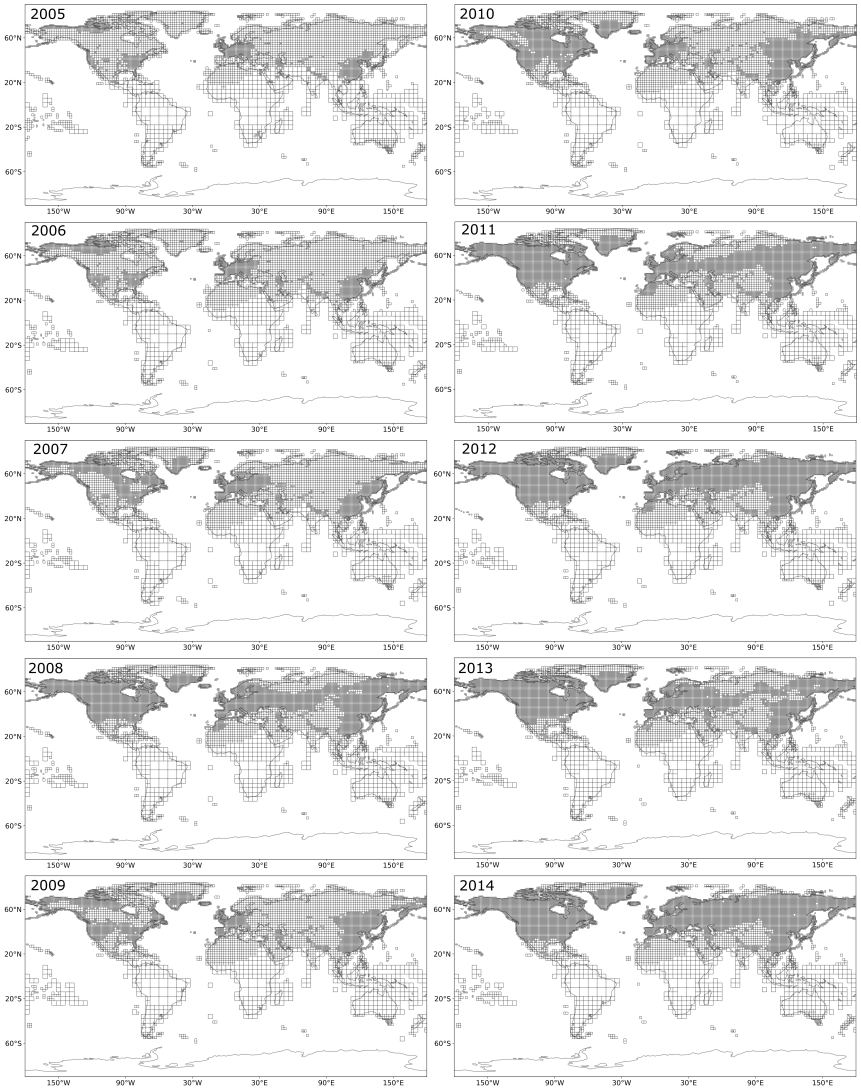

Figure S2. Global inversion grids for the years 2005 - 2014

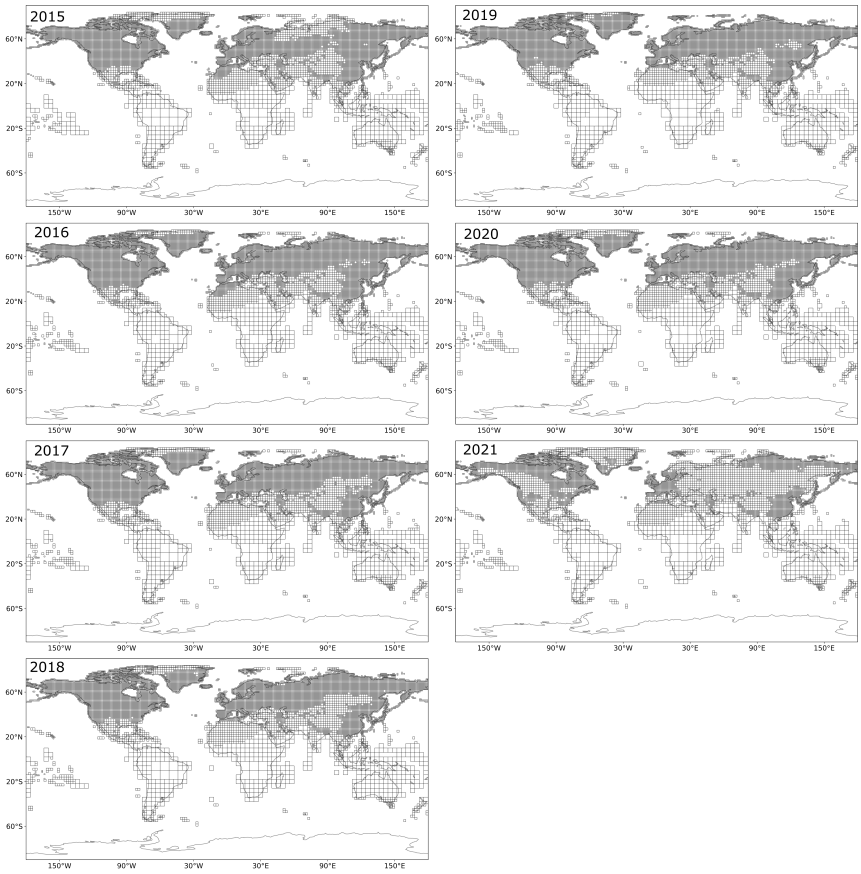

Figure S3. Global inversion grids for the years 2015 - 2021

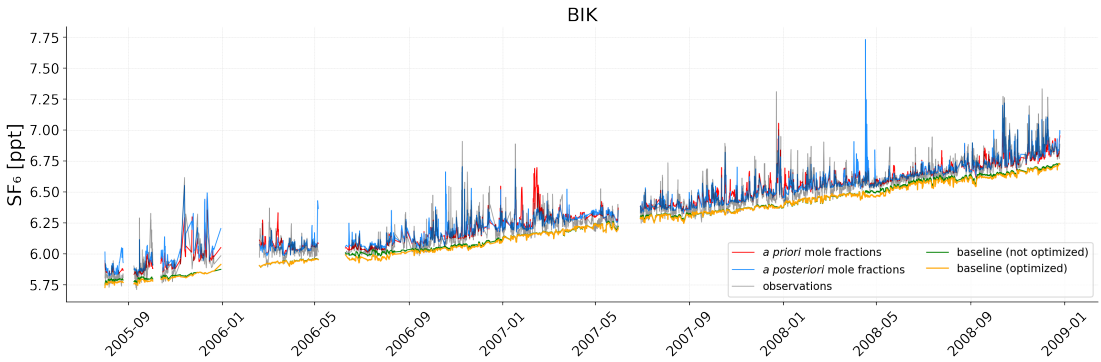

Figure S4. Mole fraction time series at the Bialystok (Poland) measurement station. Red lines illustrate the modeled *a priori* mole fractions calculated with the E7P *a priori* emissions and blue lines represent the modeled *a posteriori* mole fractions. The green line illustrates the baseline derived by the GDB method and the orange line shows the optimized baseline. The grey line represents the observed mole fractions.

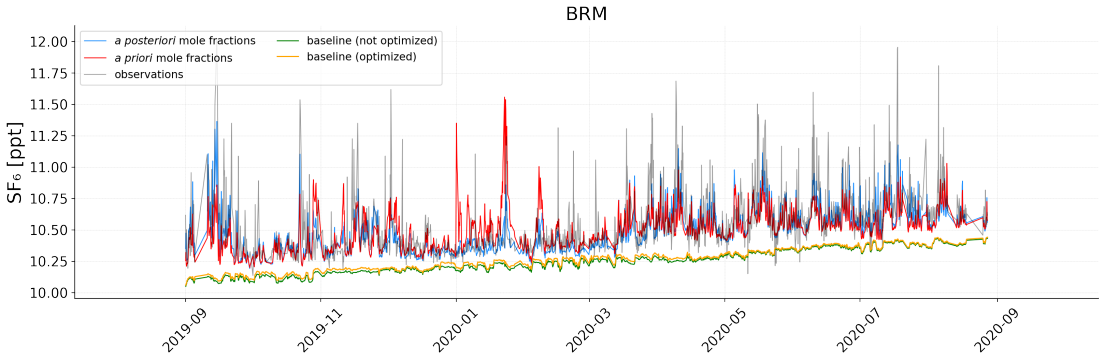

Figure S5. Mole fraction time series at the Beromünster (Switzerland) measurement station. Red lines illustrate the modeled *a priori* mole fractions calculated with the E7P *a priori* emissions and blue lines represent the modeled *a posteriori* mole fractions. The green line illustrates the baseline derived by the GDB method and the orange line shows the optimized baseline. The grey line represents the observed mole fractions.

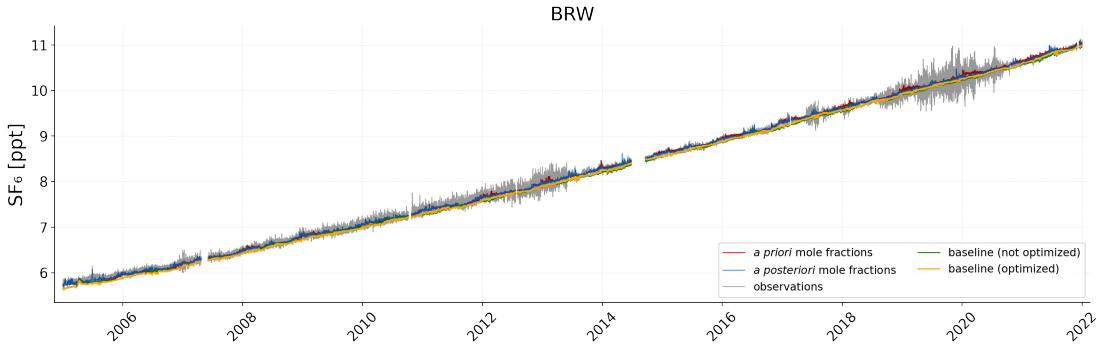

Figure S6. Mole fraction time series at the Barrow (Alaska) measurement station. Red lines illustrate the modeled *a priori* mole fractions calculated with the E7P *a priori* emissions and blue lines represent the modeled *a posteriori* mole fractions. The green line illustrates the baseline derived by the GDB method and the orange line shows the optimized baseline. The grey line represents the observed mole fractions.

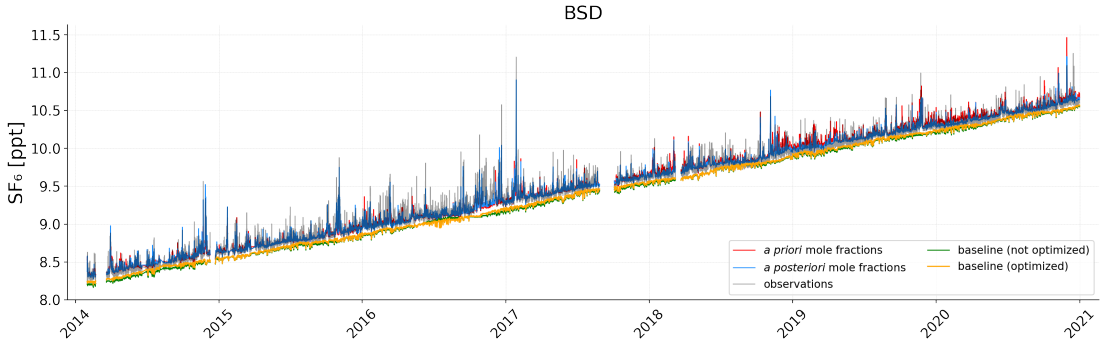

Figure S7. (a) represents the Mole fraction time series at the Bilsdale (UK) measurement station. Red lines illustrate the modeled *a priori* mole fractions calculated with the E7P *a priori* emissions and blue lines represent the modeled *a posteriori* mole fractions. The green line illustrates the baseline derived by the GDB method and the orange line shows the optimized baseline. The grey line represents the observed mole fractions.

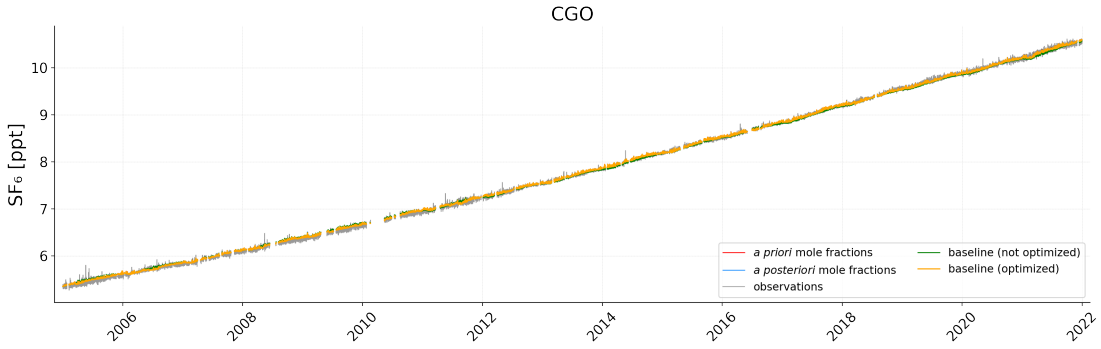

Figure S8. Mole fraction time series at the Cape Grim (Tasmania) measurement station. Red lines illustrate the modeled *a priori* mole fractions calculated with the E7P *a priori* emissions and blue lines represent the modeled *a posteriori* mole fractions. The green line illustrates the baseline derived by the GDB method and the orange line shows the optimized baseline. The grey line represents the observed mole fractions.

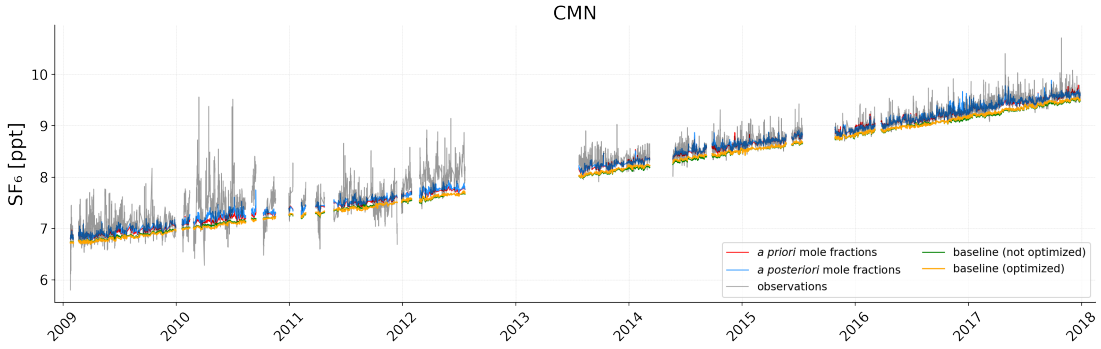

Figure S9. Mole fraction time series at the Monte Cimone (Italy) measurement station. Red lines illustrate the modeled *a priori* mole fractions calculated with the E7P *a priori* emissions and blue lines represent the modeled *a posteriori* mole fractions. The green line illustrates the baseline derived by the GDB method and the orange line shows the optimized baseline. The grey line represents the observed mole fractions.

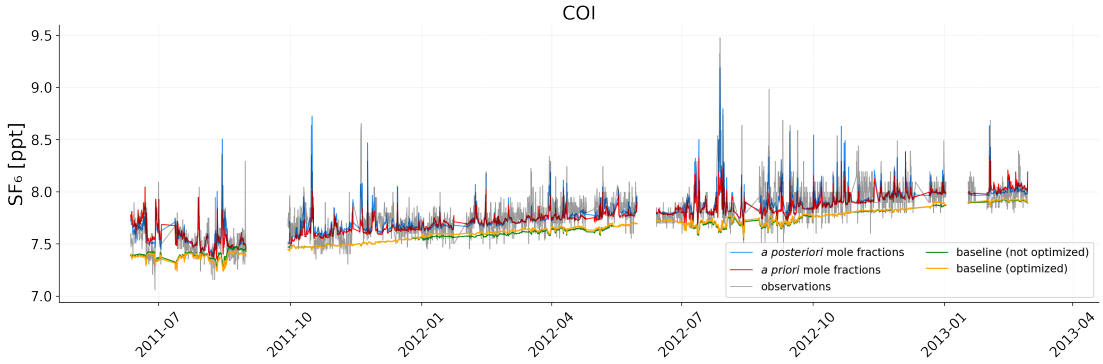

Figure S10. Mole fraction time series at the Cape Ochiishi (Japan) measurement station. Red lines illustrate the modeled *a priori* mole fractions calculated with the E7P *a priori* emissions and blue lines represent the modeled *a posteriori* mole fractions. The green line illustrates the baseline derived by the GDB method and the orange line shows the optimized baseline. The grey line represents the observed mole fractions.

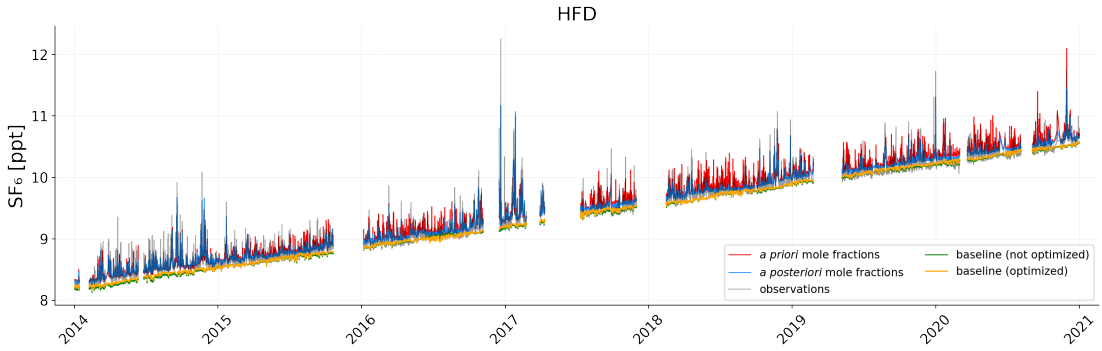

Figure S11. Mole fraction time series at the Heathfield (UK) measurement station. Red lines illustrate the modeled *a priori* mole fractions calculated with the E7P *a priori* emissions and blue lines represent the modeled *a posteriori* mole fractions. The green line illustrates the baseline derived by the GDB method and the orange line shows the optimized baseline. The grey line represents the observed mole fractions.

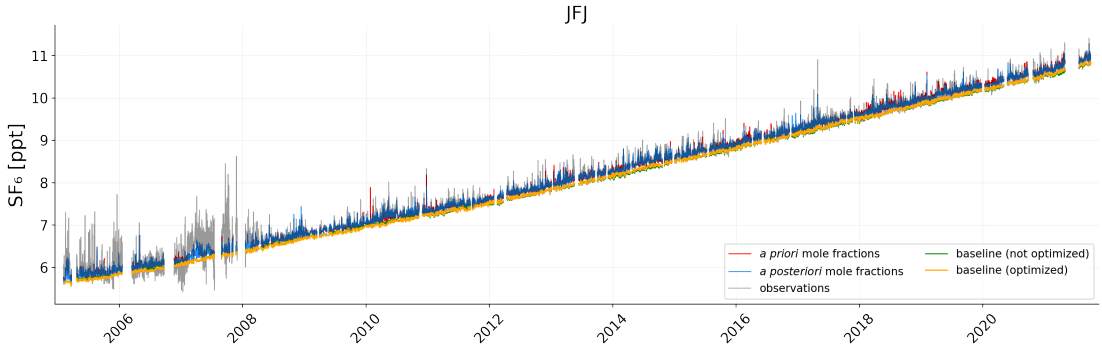

Figure S12. Mole fraction time series at the Jungfraujoch (Switzerland) measurement station. Red lines illustrate the modeled *a priori* mole fractions calculated with the E7P *a priori* emissions and blue lines represent the modeled *a posteriori* mole fractions. The green line illustrates the baseline derived by the GDB method and the orange line shows the optimized baseline. The grey line represents the observed mole fractions.

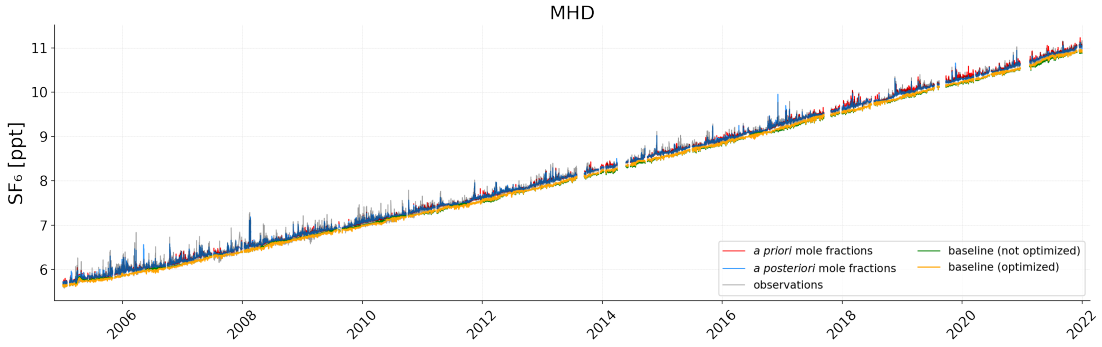

Figure S13. Mole fraction time series at the Mace Head (Ireland) measurement station. Red lines illustrate the modeled *a priori* mole fractions calculated with the E7P *a priori* emissions and blue lines represent the modeled *a posteriori* mole fractions. The green line illustrates the baseline derived by the GDB method and the orange line shows the optimized baseline. The grey line represents the observed mole fractions.

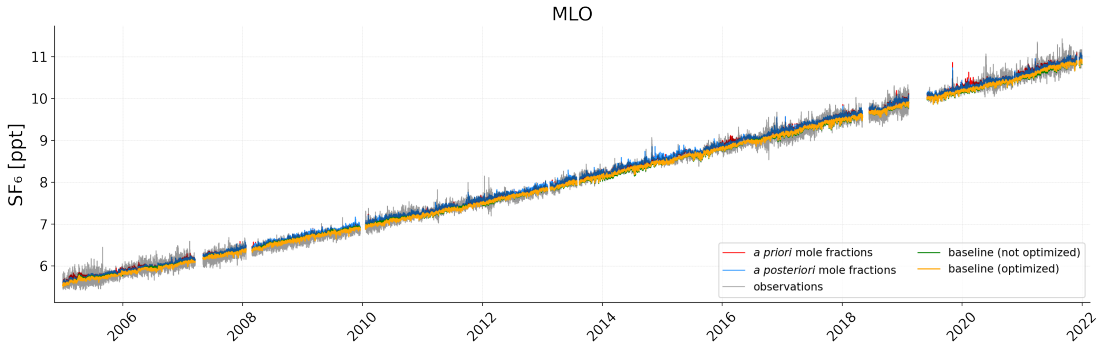

Figure S14. Mole fraction time series at the Mauna Loa (Hawaii) measurement station. Red lines illustrate the modeled *a priori* mole fractions calculated with the E7P *a priori* emissions and blue lines represent the modeled *a posteriori* mole fractions. The green line illustrates the baseline derived by the GDB method and the orange line shows the optimized baseline. The grey line represents the observed mole fractions.

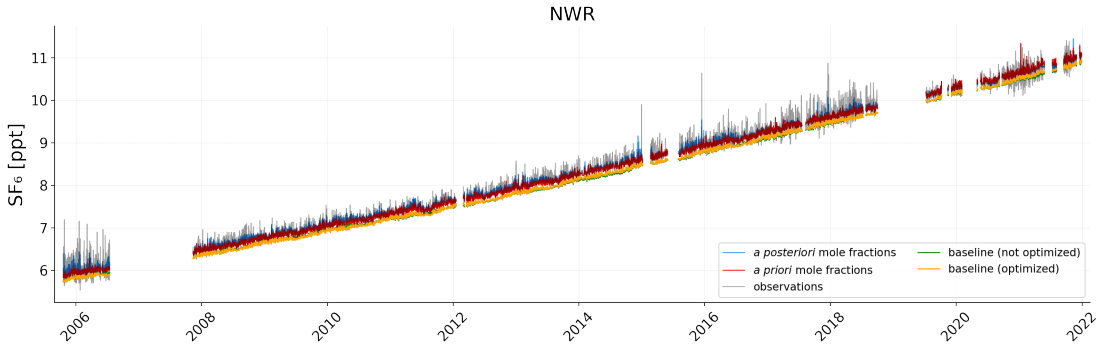

Figure S15. Mole fraction time series at the Niwot Ridge (Colorado) measurement station. Red lines illustrate the modeled *a priori* mole fractions calculated with the E7P *a priori* emissions and blue lines represent the modeled *a posteriori* mole fractions. The green line illustrates the baseline derived by the GDB method and the orange line shows the optimized baseline. The grey line represents the observed mole fractions.

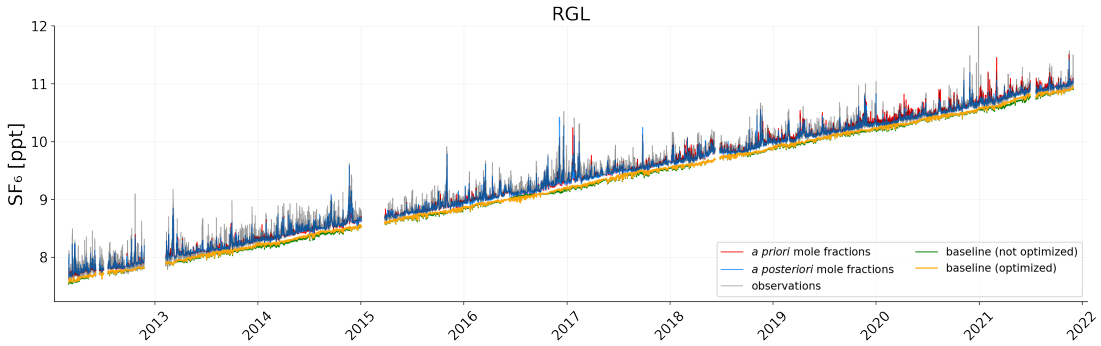

Figure S16. Mole fraction time series at the Ridge Hill (UK) measurement station. Red lines illustrate the modeled *a priori* mole fractions calculated with the E7P *a priori* emissions and blue lines represent the modeled *a posteriori* mole fractions. The green line illustrates the baseline derived by the GDB method and the orange line shows the optimized baseline. The grey line represents the observed mole fractions.

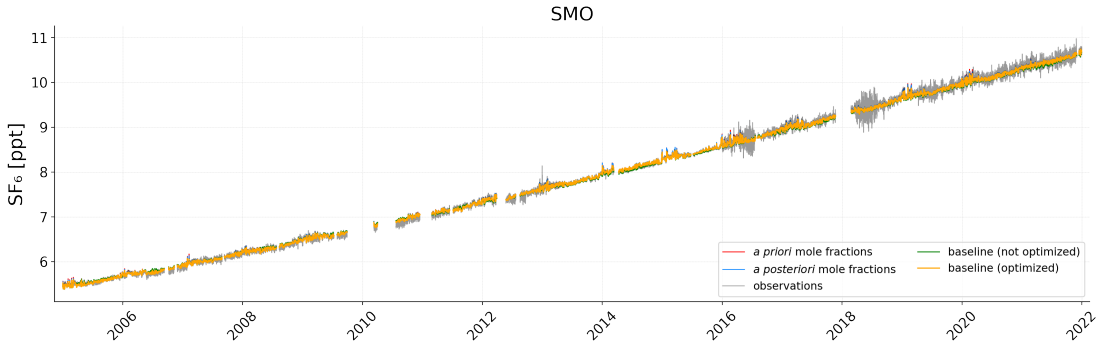

Figure S17. Mole fraction time series at the Cape Matatula (American Samoa) measurement station. Red lines illustrate the modeled *a priori* mole fractions calculated with the E7P *a priori* emissions and blue lines represent the modeled *a posteriori* mole fractions. The green line illustrates the baseline derived by the GDB method and the orange line shows the optimized baseline. The grey line represents the observed mole fractions.

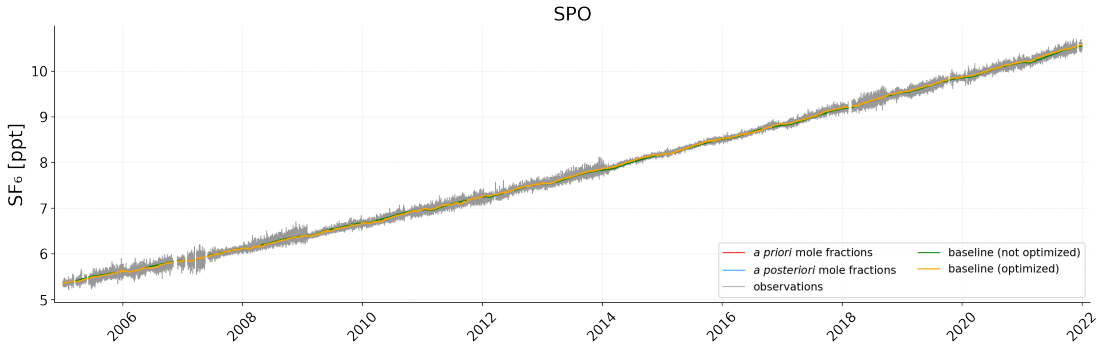

Figure S18. Mole fraction time series at the South Pole, (Antarctica) measurement station. Red lines illustrate the modeled *a priori* mole fractions calculated with the E7P *a priori* emissions and blue lines represent the modeled *a posteriori* mole fractions. The green line illustrates the baseline derived by the GDB method and the orange line shows the optimized baseline. The grey line represents the observed mole fractions.

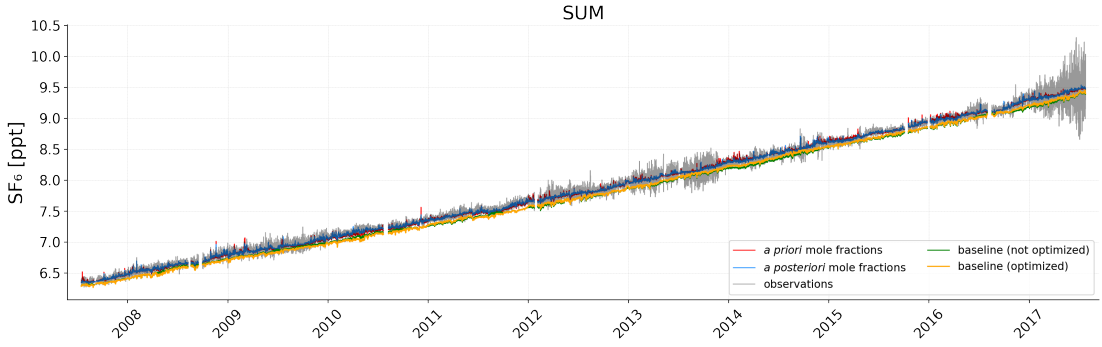

Figure S19. Mole fraction time series at the Summit (Greenland) measurement station. Red lines illustrate the modeled *a priori* mole fractions calculated with the E7P *a priori* emissions and blue lines represent the modeled *a posteriori* mole fractions. The green line illustrates the baseline derived by the GDB method and the orange line shows the optimized baseline. The grey line represents the observed mole fractions.

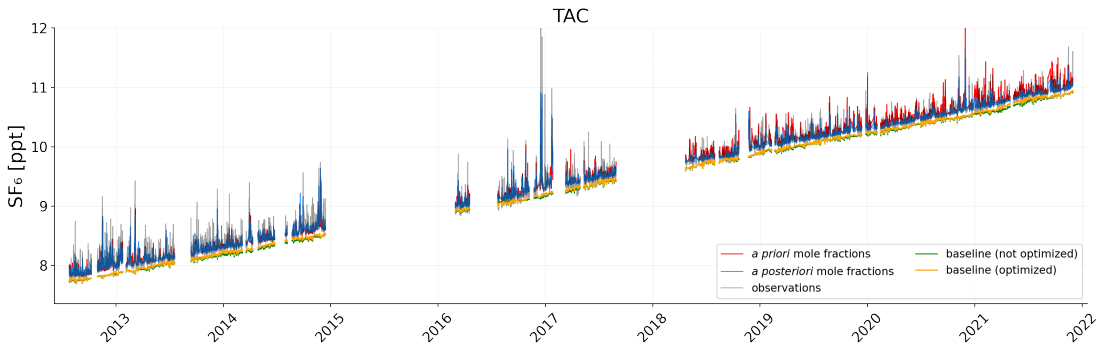

Figure S20. Mole fraction time series at the Tacolneston Tall Tower (UK) measurement station. Red lines illustrate the modeled *a priori* mole fractions calculated with the E7P *a priori* emissions and blue lines represent the modeled *a posteriori* mole fractions. The green line illustrates the baseline derived by the GDB method and the orange line shows the optimized baseline. The grey line represents the observed mole fractions.

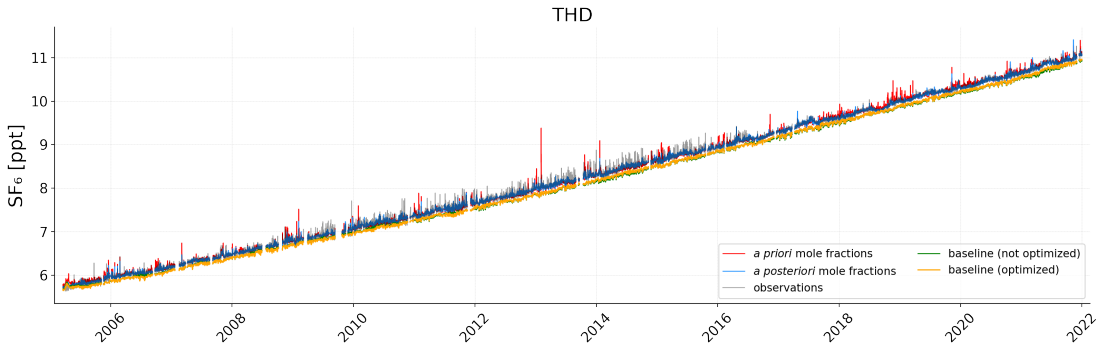

Figure S21. Mole fraction time series at the Trinidad Head (USA) measurement station. Red lines illustrate the modeled *a priori* mole fractions calculated with the E7P *a priori* emissions and blue lines represent the modeled *a posteriori* mole fractions. The green line illustrates the baseline derived by the GDB method and the orange line shows the optimized baseline. The grey line represents the observed mole fractions.

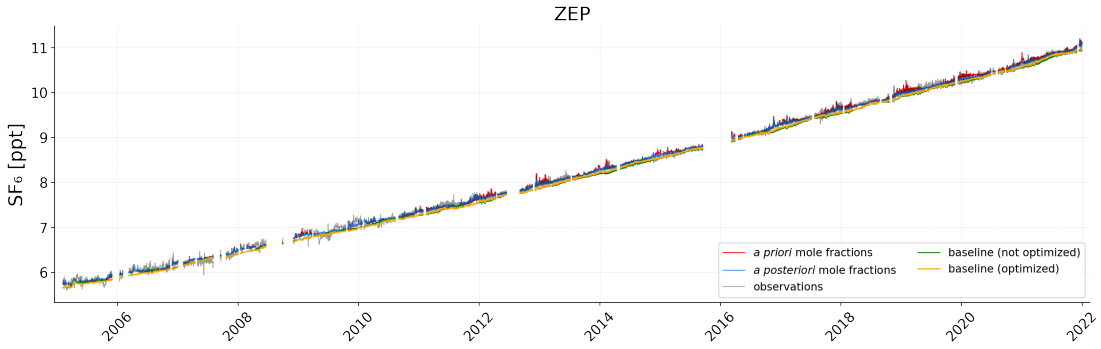

Figure S22. Mole fraction time series at the Zeppelin (Ny-Alesund, Norway) measurement station. Red lines illustrate the modeled *a priori* mole fractions calculated with the E7P *a priori* emissions and blue lines represent the modeled *a posteriori* mole fractions. The green line illustrates the baseline derived by the GDB method and the orange line shows the optimized baseline. The grey line represents the observed mole fractions.

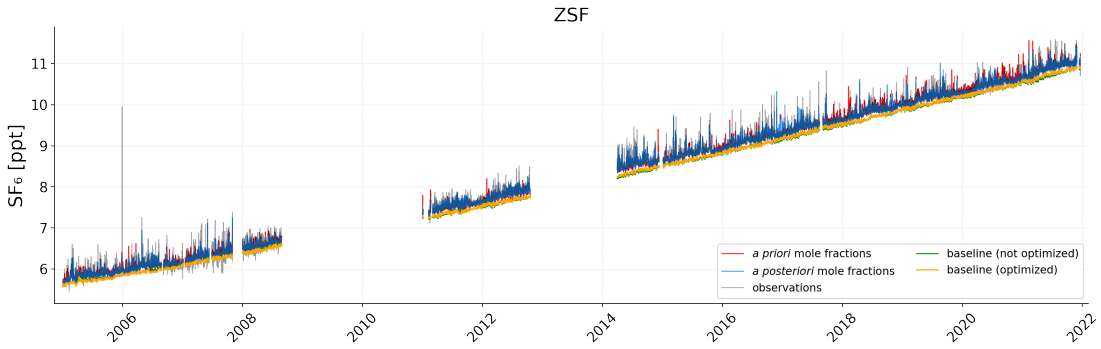

Figure S23. Mole fraction time series at the Zugspitze-Schneefernerhaus, (Germany) measurement station. Red lines illustrate the modeled *a priori* mole fractions calculated with the E7P *a priori* emissions and blue lines represent the modeled *a posteriori* mole fractions. The green line illustrates the baseline derived by the GDB method and the orange line shows the optimized baseline. The grey line represents the observed mole fractions.

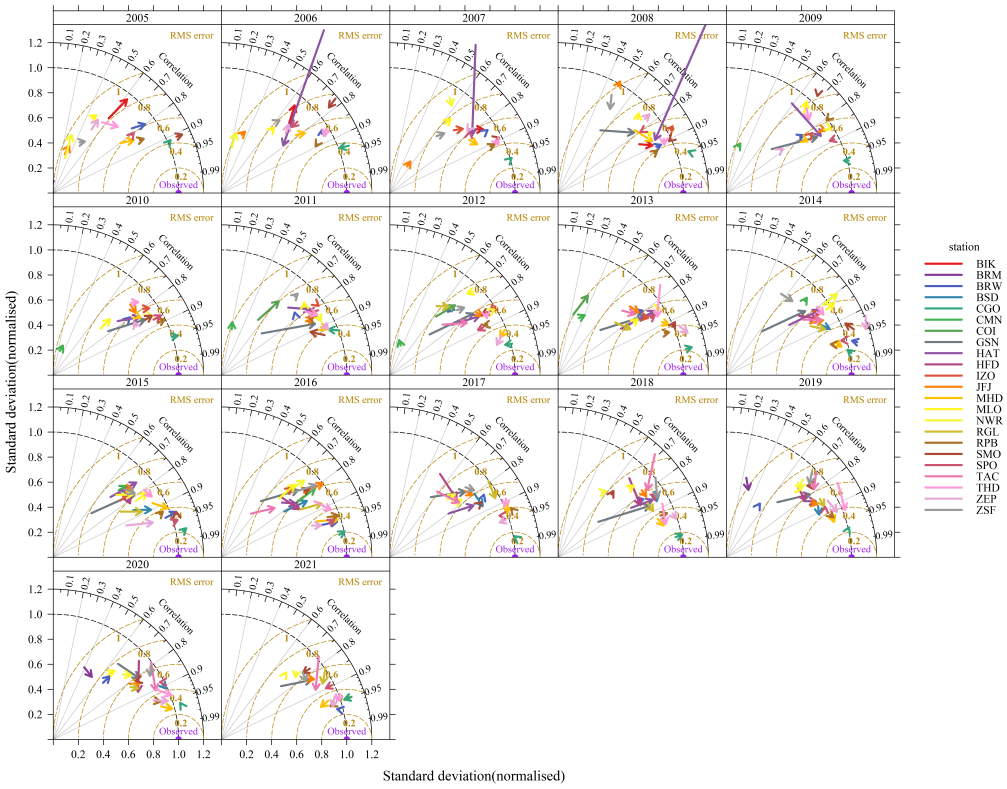

Figure S24. Taylor diagrams for comparing the *a priori* and *a posteriori* simulated mole fractions to the observed mixing ratios at all continuous stations, for the years 2005-2021. The diagram summarizes the match between observed and simulated values, by showing three statistics: (i) the Pearson correlation coefficient, represented by the azimuthal angle, (ii) the (against observations) normalized root mean square error (RMS) which is proportional to the distance from the as "observed" labeled purple dot, and (iii) the normalized standard deviation, represented by the radial distance from the origin. Each colored arrow represents a station, where the tail represents the *a priori* and the head the *a posteriori* simulated mole fractions. The length of each arrow, represents the difference between the *a priori* and *a posteriori* modeled mixing ratios with respect to the observed mixing ratios, indicating the correction made by the inversion. We observe large reductions in root mean square error for HAT and GSN almost across all the years. BRM, HFD, TAC, RGL, and ZSF also show significant improvements in error and correlation. The Taylor diagram can clearly distinguish the background stations from the stations that regularly capture emission events. However, also for background stations, small improvements can be seen.

S2 Supplementary Tables

Table S1. List of surface stations continuously monitoring SF_6.

Site ID	Station	Organisation	Latitude	Longitude	Altitude[a]	Period	total number
BIK	Bialystok, Poland	MPI	53.2°N	23.0°E	180	2005-2008	9412
BRM	Beromünster, Switzerland	EMPA	47.2°N	8.2°E	797	2019-2020	8066
BRW	Barrow, Alaska, USA	NOAA/GML/CATS	71.3°N	156.6°W	18	2005-2021	184428
BSD	Bilsdale, UK	UNIVBRIS	54.4°N	1.1°W	379	2014-2020	464423
CGO	Cape Grim, Tasmania	CSIRO/AGAGE	40.7°S	144.7°E	164	2005-2021	70652
CMN*	Monte Cimone, Italy	UNIURB/AGAGE	44.2°N	10.7°E	2172	2009-2017	126546
COI	Cape Ochiishi, Japan	NIES	43.2°N	145.5°E	100	2011-2013	33412
GSN	South Korea	KNU/AGAGE	33.3°N	126.2°E	89	2008-2021	33785
HAT	Hateruma, Japan	NIES	24.1°N	123.8°E	47	2005-2019	104922
HFD	Heathfield, UK	UNIURB	51.0°N	0.2°E	157	2014-2020	408800
IZO*	Izaña, Tenerife	AEMET	28.3°N	16.5°W	2403	2007-2016	92557
JFJ*	Jungfraujoch, Switzerland	EMPA/AGAGE	46.5°N	8.0°E	3584	2005-2021	87450
MHD	Mace Head, Ireland	UNIVBRIS/AGAGE	53.3°N	9.9°W	26	2005-2021	66944
MLO*	Mauna Loa, Hawaii, USA	NOAA/GML/CATS	19.5°N	155.6°W	3407	2005-2021	179396
NWR*	Niwot Ridge, Colorado, USA	NOAA/GML/CATS	40.0°N	105.5°W	3028	2005-2021	133475
RGL	Ridge Hill, UK	UNIVBRIS	52.0°N	2.5°W	294	2012-2021	501617
RPB	Ragged Point, Barbados	UNIVBRIS/AGAGE	13.2°N	59.4°W	50	2005-2021	55463
SMO	Cape Matatulu, American Samoa, USA	NOAA/GML/CATS/AGAGE	14.3°S	170.6°W	87	2005-2021	121670
SPO	South Pole, Antarctica	NOAA/GML/CATS	90.0°S	24.8°W	2820	2005-2021	174672
SUM	Summit, Greenland	NOAA/GML/CATS	72.6°N	38.5°W	3228	2007-2017	98620
TAC	Tacolneston Tall Tower, UK	UNIVBRIS/AGAGE	52.5°N	1.1°E	183	2012-2021	57590
THD	Trinidad Head, USA	SIO/EAS/AGAGE	41.1°N	124.2°W	127	2005-2021	68466
ZEP	Zeppelin, Ny-Alesund, Norway	NILU/AGAGE	78.9°N	11.9°E	490	2005-2021	42102
ZSF*	Zugspitze-Schneefernerhaus, Germany	UBAG	47.4°N	11.0°E	2670	2005-2021	156336

[a] The altitude specifies the sampling height in meters above sea level. Stations considered as mountain sites are marked with an asterisk.

Table S2. List of flask measurement sampling sites (1)

Site ID	Station	Organisation	Latitude	Longitude	Altitude[a]	Period	total number
ABP	Arembepe, Bahia, Brazil	NOAA/GML/CCGG/INPE	12.8° S	38.2° W	6	2006-2010	114
ALT	Alert, Canada	NOAA/GML/CCGG	82.5° N	62.5° W	190	2005-2021	1162
ALT	Alert, Canada	NOAA/HATS	82.5° N	62.5° W	200	2005-2013	425
AMT	Argyle, Maine, USA	NOAA/GML/CCGG	45.0° N	68.7° W	157	2005-2008	72
AMT	Argyle, Maine, USA	NOAA/HATS	45.0° N	68.7° W	160	2008-2021	1781
AMY	Anmyeon-do, Republic of Korea	NOAA/GML/CCGG	36.5° N	126° E	87.0	2013-2021	340
ASC	Ascension Island, UK	NOAA/GML/CCGG	8.0° S	14.4° W	90	2005-2021	1468
ASK	Assekrem, Algeria, UK	NOAA/GML/CCGG	23.3° N	5.6° E	2715	2005-2020	713
AZR	Serreta (Terceira), Portugal	NOAA/GML/CCGG	38.8° N	27.4° W	24	2005-2021	489
BAL	Baltic Sea, Poland	NOAA/GML/CCGG	55.4° N	17.2° E	28	2005-2011	545
BAO	Boulder Atmospheric Observatory, Colorado, USA	NOAA/GML/GGGRN	40.1° N	105.0° W	1884	2007-2016	2688
BHD	Baring Head, New Zealand	NOAA/GML/CCGG	41.4° S	174.9° E	912	2005-2021	266
BKT	Bukit Kototabang, Indonesia	NOAA/GML/CCGG	0.2° S	100.3° E	875	2005-2021	728
BME	St. Davids Head, Bermuda	NOAA/GML/CCGG	32.4° N	64.6° W	17	2005-2010	77
BMW	Tudor Hill (Bermuda), UK	NOAA/GML/CCGG	32.3° N	64.9° W	55	2005-2021	655
BRW	Barrow, Alaska, USA	NOAA/GML/CCGG	71° N	156.6° W	16/28	2005 - 2021	1656
BRW	Barrow, Alaska, USA	NOAA/HATS	71° N	156.6° W	27	2005 - 2013	400
BSC	Constanta (Black Sea), Romania	NOAA/GML/CCGG	44.2° N	28.7° E	5	2005-2011	330
CBA	Cold Bay (AK), USA	NOAA/GML/CCGG	55.2° N	162.7° W	49	2005-2021	1437
CGO	Cape Grim, Tasmania	NOAA/GML/CCGG	40.7° S	144.7° E	164	2005-2021	623
CGO	Cape Grim, Tasmania	NOAA/HATS	40.7° S	144.7° E	164	2005-2013	344
CHR	Christmas Island, Kiribati	NOAA/GML/CCGG	1.7° N	157.2° W	5	2005-2020	463
CIB	Centro de Investigacion de la Baja Atmosfera (CIBA), Spain	NOAA/GML/CCGG	41.8° N	4.9° W	850	2009-2021	547
CPT	Cape Point, South Africa	NOAA/GML/CCGG	34.4° S	18.5° E	260	2010-2021	398
CRV	Carbon in Arctic Reservoirs Vulnerability Experiment (CARVE), US	NOAA/HATS	65.0° N	147.6° W	643	2012-2017	79
CRV	Carbon in Arctic Reservoirs Vulnerability Experiment (CARVE), US	NOAA/GML/GGGRN	65.0° N	147.6° W	643	2011-2021	1535
CRZ	Crozet Island, France	NOAA/GML/CCGG	46.4° S	51.8° E	202	2005-2021	733
DSI	Dongsha Island, Taiwan	NOAA/GML/CCGG	20.7° N	116.7° E	8	2010-2021	473
EIC	Easter Island, Chile	NOAA/GML/CCGG	27.2° S	109.4° W	64	2005-2019	550
GMI	Guam (Mariana Island), USA	NOAA/GML/CCGG	13.4° N	144.7° E	7	2005-2021	923
HBA	Halley, UK	NOAA/GML/CCGG	75.6° S	26.2° W	35	2005-2021	572
HFM	Harvard Forest (MA), USA	NOAA/GML/GGGRN	42.5° N	72.2° W	370	2016	12
HPB	Hohenpeissenberg, Germany	NOAA/GML/CCGG	47.8° N	11.0° E	941	2006-2021	841
HSU	Humboldt State University, USA	NOAA/GML/CCGG	41.1° N	124.6° W	8	2008-2017	87
HUN	Hegyhatsal, Hungary	NOAA/GML/CCGG	47.0° N	16.6° E	344	2005-2021	741
ICE	Storhofdi, Iceland	NOAA/GML/CCGG	63.4° N	20.3° W	126	2005-2021	846
IZO	Izaña, Tenerife	NOAA/GML/CCGG	28.3° N	16.5° W	2378	2005 - 2021	804
KEY	Key Biscane (FL), USA	NOAA/GML/CCGG	25.7° N	80.2° W	6	2005-2021	692
KLM	Kohler Mesa, USA	NOAA/GML/GGGRN	40.0° N	105.3° W	1730	2006	47
KUM	Cape Kumukahi (HI), USA	NOAA/GML/CCGG	19.5° N	154.8° W	5	2005-2021	1676
KUM	Cape Kumukahi (HI), USA	NOAA/HATS	19.7° N	155.0° W	36	2005-2013	434
KZD	Sary Taukum, Kazakhstan	NOAA/GML/CCGG	44.1° N	76.9° E	600	2005-2009	224
KZM	Plateau Assy, Kazakhstan	NOAA/GML/CCGG	43.2° N	77.9° E	2524	2005-2009	214
LEF	Park Falls (WI), USA	NOAA/GML/CCGG	45.9° N	90.3° W	868	2005-2021	142
LEF	Park Falls (WI), USA	NOAA/GML/GGGRN	45.9° N	90.3° W	868	2006-2021	3414
LEF	Park Falls (WI), USA	NOAA/HATS	45.9° N	90.3° W	482	2005-2013	362
LEW	Lewisburg, Pennsylvania, USA	NOAA/GML/GGGRN	40.9° N	76.9° W	261	2015-2021	717
LLB	Lac La Biche, Alberta, Canada	NOAA/GML/CCGG	55.0° N	112.5° W	568	2008-2013	213
LLN	Lulin, Taiwan, Province of China	NOAA/GML/CCGG	23.5° N	120.9° E	2867	2006-2021	604
LMP	Lampedusa, Italy	NOAA/GML/CCGG	35.5° N	12.6° E	50	2006-2021	659

[a] The altitude specifies the sampling height in meters above sea level.

Table S3. List of flask measurement sampling sites (2).

Site ID	Station	Organisation	Latitude	Longitude	Altitude[a]	Period	total number
MBO	Mt. Bachelor Observatory, USA	NOAA/GML/GGGRN	44.0°N	121.7°W	2742	2011-2021	1914
MEX	Mex High Altitude Global Climate Observation Center, Mexico	NOAA/GML/CCGG	19.0°N	97.3°W	4469	2009-2021	488
MHD	Mace Head, Ireland	NOAA/GML/CCGG	53.3°N	9.9°W	26	2005-2021	777
MHD	Mace Head, Ireland	NOAA/HATS	53.3°N	9.9°W	42	2005-2013	193
MID	Sand Island, Midway, USA	NOAA/GML/CCGG	28.2°N	177.4°W	12	2005-2021	841
MKN	Mt. Kenya, Kenya	NOAA/GML/CCGG	0.1°S	37.3°E	3649	2005-2011	126
MLO	Mauna Loa, Hawaii, USA	NOAA/GML/CCGG	19.5°N	155.6°W	3437	2005-2021	1746
MLO	Mauna Loa, Hawaii, USA	NOAA/HATS	19.5°N	155.6°W	3433	2005-2013	432
MLO	Mauna Loa, Hawaii, USA	NOAA/GML/GGGRN	19.5°N	155.6°W	3433	2021	68
MRC	Marcellus Pennsylvania, USA	NOAA/GML/GGGRN	41.5°N	76.3°W	652	2015-2021	713
MSH	Mashpee, Massachusetts, USA	NOAA/GML/GGGRN	41.7°N	70.5°W	78	2016-2021	503
MVY	Marthas Vineyard, Massachusetts, USA	NOAA/GML/GGGRN	41.3°N	70.6°W	16	2007-2011	210
MWO	Mt. Wilson Observatory, USA	NOAA/GML/GGGRN	34.2°N	118.1°W	1775	2010-2021	4437
NAT	Natal, Brazil	NOAA/GML/CCGG/INPE	5.6°S	35.2°W	49	2010-2020	385
NMB	Gobabeb, Namibia	NOAA/GML/CCGG	23.6°S	15.0°E	461	2006-2021	614
NWB	NW Baltimore, USA	NOAA/GML/GGGRN	39.3°N	76.7°W	190	2018-2021	41
NWR	Niwot Ridge, Colorado	NOAA/GML/CCGG	40.1°N	-105.6°W	3526	2005 - 2021	847
NWR	Niwot Ridge, Colorado	NOAA/HATS	40.1°N	-105.6°W	3523	2005 - 2013	342
NWR	Niwot Ridge, Colorado	NOAA/GML/GGGRN	40.1°N	-105.6°W	3523	2005 - 2021	3712
OBN	Obninsk, Colorado, Russia	NOAA/HATS	55.1°N	36.6°E	484	2005-2009	146
OXK	Ochsenkopf, Germany	NOAA/GML/CCGG	50.0°N	11.8°E	1181	2006-2021	404
PAL	Pallas, Finland	NOAA/GML/CCGG	68.0°N	24.1°E	570	2005-2021	797
PCO	Pico, Azores, Portugal	NOAA/HATS	38.5°N	28.4°W	2230	2010-2011	6
PSA	Palmer Station, USA	NOAA/GML/CCGG	64.9°S	64.0°W	15	2005-2021	835
PSA	Palmer Station, USA	NOAA/HATS	64.9°S	64.0°W	13	2005-2013	183
PTA	Point Arena (CA), USA	NOAA/GML/CCGG	39.0°N	123.7°W	22	2005-2011	291
RPB	Ragged Point, Barbados	NOAA/GML/CCGG	13.2°N	59.4°W	20	2005-2021	841
SCT	Beech Island, South Carolina, USA	NOAA/GML/GGGRN	33.4°N	81.8°W	420	2008-2021	2778
SDZ	Shangdianzi, Peoples Republic of China	NOAA/GML/CCGG	40.6°N	117.1°E	298	2009-2015	154
SEY	Mahe Island, Seychelles	NOAA/GML/CCGG	4.7°S	55.5°E	7	2005-2021	773
SGP	Southern Great Plains, Oklahoma, USA	NOAA/GML/CCGG	36.7°N	97.5°W	374	2005-2021	831
SGP	Southern Great Plains, Oklahoma, USA	NOAA/GML/GGGRN	36.7°N	97.5°W	374	2010-2021	298
SHM	Shemya Island, USA	NOAA/GML/CCGG	52.7°N	174.1°E	28	2005-2021	797
SMO	Cape Matatulu, American Samoa, USA	NOAA/GML/CCGG	14.3°S	170.6°W	60	2005-2021	1561
SMO	Cape Matatulu, American Samoa, USA	NOAA/HATS	14.3°S	170.6°W	77	2005-2013	451
SPO	South Pole, Antarctica	NOAA/GML/CCGG	90.0°S	24.8°W	2820	2005-2021	1228
SPO	South Pole, Antarctica	NOAA/HATS	90.0°S	24.8°W	2837	2005-2021	296
STM	Ocean Station M, Norway	NOAA/GML/CCGG	66.0°N	2.0°E	5	2005-2009	467
STR	Sutro Tower, San Francisco, California, USA	NOAA/GML/GGGRN	37.8°N	122.5°W	426	2007-2021	6790
SUM	Summit, Greenland	NOAA/GML/CCGG	72.6°N	38.5°W	3214	2005-2021	873
SUM	Summit, Greenland	NOAA/HATS	72.6°N	38.5°W	3212	2005-2013	233
SYO	Syowa Station, Antarctic, Japan	NOAA/GML/CCGG	69.0°S	39.6°E	17	2005-2021	403
TAC	Tacolneston Tall Tower, UK	NOAA/GML/CCGG	52.5°N	1.1°E	236	2014-2016	50
TAP	Tae-ahn Peninsula, Republic of Korea	NOAA/GML/CCGG	36.7°N	126.1°E	21	2005-2021	835
THD	Trinidad Head, USA	NOAA/GML/CCGG	41.1°N	124.2°W	112	2005-2017	615
THD	Trinidad Head, USA	NOAA/HATS	41.1°N	124.2°W	120	2005-2013	382
TIK	Tiksi, Russian Federation	NOAA/GML/CCGG	71.6°N	128.9°E	29	2011-2018	340
TPI	Taiping Island	NOAA/GML/CCGG	10.4°N	144.4°E	9	2019 - 2021	121
USH	Ushuaia, Argentina	NOAA/GML/CCGG	54.8°S	68.3°W	32	2005-2021	616
USH	Ushuaia, Argentina	NOAA/HATS	54.8°S	68.3°W	15	2005-2010	46
UTA	Wendover (UT), USA	NOAA/GML/CCGG	39.9°N	113.7°W	1332	2005-2021	910
UUM	Ulaan Uul, Mongolia	NOAA/GML/CCGG	44.5°N	111.1°E	1012	2005-2021	734
WBI	West Branch, Iowa, USA	NOAA/GML/GGGRN	41.7°N	91.4°W	621	2007-2021	3657
WGC	Walnut Grove, California, USA	NOAA/GML/GGGRN	38.3°N	121.5°W	94	2007-2021	2590
WIS	Sede Boker, Israel	NOAA/GML/CCGG	30.6°N	34.9°E	379	2005-2021	815
WKT	Moody, Texas, USA	NOAA/GML/CCGG	31.3°N	97.3°W	372	2005-2010	176
WKT	Moody, Texas, USA	NOAA/GML/GGGRN	31.3°N	97.3°W	372	2006-2021	3101
WLG	Mt. Waliguan, Peoples Republic of China	NOAA/GML/CCGG	36.3°N	100.9°E	3827	2005-2021	660
ZEP	Zeppelin, Ny-Alesund, Norway	NOAA/GML/CCGG	78.9°N	11.9°E	479	2005-2021	848

[a] The altitude specifies the sampling height in meters above sea level.

Table S4. Measurements from moving platforms.

Site ID	Measurements Site	Organisation	Altitude[a] range	Period	total number	platform
AAO	Airborne Aerosol Observatory, Bondville, Illinois, USA	NOAA/GML/CCAVPN	373 - 4859	2006 - 2009	3001	aircraft
ACG	Alaska Coast Guard, USA	NOAA/GML/CCAVPN	48 - 8857	2009 - 2021	1758	aircraft
ACT	Atmospheric Carbon and Transport - America, USA	NOAA/GML/CCAVPN	117 - 9060	2016 - 2019	1477	aircraft
AOC	Atlantic Ocean Cruise	NOAA/ESRL/GMD	10	2005	16	ship
BAO	Boulder Atmospheric Observatory, Colorado, USA	NOAA/GML/CCAVPN	1849 - 4794	2008	12	aircraft
BGI	Bradgate, Iowa, USA	NOAA/GML/CCAVPN	598 - 8074	2005	296	aircraft
BII	Biak, Indonesia	MUE/TU/NIPR	17200 - 28700	2015	7	balloon
BNE	Beaver Crossing, Nebraska, USA	NOAA/GML/CCAVPN	597 - 8157	2005 - 2011	969	aircraft
CAR	Briggsdale, Colorado,USA	NOAA/GML/CCAVPN	1585 - 8469	2005 - 2021	4025	aircraft
CARIBIC	Civil Aircraft for the Regular Investigation of the atmosphere Based on an Instrument Container	KIT/MPIC	947 - 12525	2005 - 2020	7379	aircraft
CMA	Offshore Cape May, New Jersey, USA	NOAA/GML/CCAVPN	247 - 8119	2005 - 2021	3073	aircraft
CON	CONTRAIL (Comprehensive Observation Network for TRace gases by AIrLiner)	NIES/MRI	780 - 13110	2005 - 2017	3192	aircraft
CRS	Miscellaneous Cruises	NOAA/ESRL/GMD	20	2005 - 2011	120	ship
CRV	Carbon in Arctic Reservoirs Vulnerability Experiment (CARVE), USA	NOAA/GML/CCAVPN	2 - 5526	2011 - 2017	2446	aircraft
DND	Dahlen, North Dakota, USA	NOAA/GML/CCAVPN	517 - 8131	2005 - 2016	1941	aircraft
DRP	Drake Passage	NOAA/ESRL/GMD	10	2005 - 2017	375	ship
ECO	East Coast Outflow, USA	NOAA/GML/CCAVPN	146 - 4564	2018, 2020	343	aircraft
ESP	Estevan Point, British Columbia, Canada	NOAA/GML/CCAVPN	18 - 5819	2005 - 2021	4310	aircraft
ETL	East Trout Lake, Saskatchewan, Canada	NOAA/GML/CCAVPN	599 - 7823	2005 - 2020	3041	aircraft
FAM	FAAM Aircraft, United Kingdom	NOAA/ESRL/GMD	129 - 2000	2014 - 2015	12	aircraft
FWI	Fairchild, Wisconsin, USA	NOAA/GML/CCAVPN	589 - 8071	2005	314	aircraft
HAA	Molokai Island, Hawaii, USA	NOAA/GML/CCAVPN	315 - 8096	2005 - 2008	976	aircraft
HFM	Harvard Forest, Massachusetts, USA	NOAA/GML/CCAVPN	582 - 8062	2005 - 2007	717	aircraft
HIL	Homer, Illinois USA	NOAA/GML/CCAVPN	21 - 8117	2005 - 2021	3097	aircraft
INX	INFLUX (Indianapolis Flux Experiment), USA	NOAA/GML/CCAVPN	302 - 3518	2010 - 1016	350	aircraft
LEF	Park Falls, Wisconsin, USA	NOAA/GML/CCAVPN	558 - 4034	2005 - 2017	3268	aircraft
MCI	Mid Continent Intensive, USA	NOAA/GML/CCAVPN	359 - 3702	2007 - 2008	128	aircraft
MRC	Marcellus Pennsylvania, USA	NOAA/GML/CCAVPN	879 - 3123	2015	77	aircraft
NHA	Offshore Portsmouth, New Hampshire (Isles of Shoals) USA	NOAA/GML/CCAVPN	115 - 8136	2005 - 2021	3689	aircraft
NSA	North Slope, Alaska, NSA	NOAA/GML/CCAVPN	10 - 6377	2015 - 2016	378	aircraft
NSK	Northern Saskatchewan, Canada	NOAA/GML/CCAVPN	819 - 6576	2020 - 2021	45	aircraft
OIL	Oglesby, Illinois	NOAA/GML/CCAVPN	529 - 8121	2005	338	aircraft
PAN	Pantanal, Mato Grosso do Sul, Brazil	INPE	152 - 4419	2017 - 2019	438	aircraft
PAO	Pacific-Atlantic Ocean	NOAA/ESRL/GMD	10	2006	90	ship
PFA	Poker Flat, Alaska, USA	NOAA/GML/CCAVPN	131 - 7604	2005 - 2021	3759	aircraft
POC	Pacific Ocean	NOAA/ESRL/GMD	20	2005 - 2017	1834	ship
RTA	Rarotonga, Cook Islands	NOAA/GML/CCAVPN	15 - 6527	2005 - 2021	1943	aircraft
SAN	Santarem, Brazil	INPE	152 - 4268	2007 - 2009	927	aircraft
SCA	Offshore Charleston, South Carolina, USA	NOAA/GML/CCAVPN	218 - 13278	2005 - 2021	3404	aircraft
SGP	Southern Great Plains, Oklahoma, USA	NOAA/GML/CCAVPN	172 - 12926	2006 - 2021	6587	aircraft
SYO	Syowa Station, Antarctica, Japan	TU/AND/MUE	14600 - 28500	2008, 2012, 2013	6	balloon
TGC	Offshore Corpus Christi, Texas, USA	NOAA/GML/CCAVPN	243 - 8207	2005 - 2021	2589	aircraft
THD	Trinidad Head, California, USA	NOAA/GML/CCAVPN	152 - 8131	2005 - 2021	2437	aircraft
ULB	Ulaanbaatar, Mongolia	NOAA/GML/CCAVPN	1511 - 4425	2004 - 2009	503	aircraft
WBI	West Branch, Iowa, USA	NOAA/GML/CCAVPN	543 - 8204	2005 - 2021	2847	aircraft
WGC	Walnut Grove, California, USA	NOAA/GML/CCAVPN	6 - 3177	2008 - 2009	159	aircraft
WPC	Western Pacific, USA	NOAA/ESRL/GMD/NIWA	8 - 10	2005 - 2013	242	ship
NOAA/ESRL/GMD/HATS Trace Gas Measurements from Airborne Platforms, including the NASA campaigns AV-DEMO , AVE-05, CR-AVE, TC4 START-08, HIPPO, GLOPAC, ATTREX, ATOM, POSIDON						

[a] The altitude specifies the sampling height in meters above sea level.

Table S5. Organizations and international observation networks and programs that provided measurement data, and their respective acronyms

Abbrevation	Organization / Program
AEMET	Agencia Estatal de Meteorología (State Meteorological Agency, Spain)
AGAGE	Advanced Global Atmospheric Gases Experiment
CSIRO	Commonwealth Scientific and Industrial Research Organisation (Australia)
EAS	School of Earth and Atmospheric Sciences, Georgia Institute of Technology (USA)
EMPA	Eidgenössische Materialprüfungs- und Forschungsanstalt (Swiss Federal Laboratories for Materials Science and Technology)
INPE	Instituto Nacional de Pesquisas Espaciais (Brazil)
KIT	Karlsruhe Institute of Technology (Germany)
KNU	Kyungpook National University (South Korea)
MPI	Max Planck Institute (Germany)
MPIC	Max Planck Institute for Chemistry (Germany)
MRI	Meteorological Research Institute (Japan)
MUE	Miyagi University of Education (Japan)
NIES	National Institute for Environmental Studies (Japan)
NILU	Norwegian Institute for Air Research
NIPR	National Institute of Polar Research (Japan)
NIWA	National Institute of Water and Atmospheric Research, New Zealand
NOAA	National Oceanic and Atmospheric Administration (USA)
CATS	Chromatograph for Atmospheric Trace Species
CCAVPN	Carbon Cycle Aircraft Vertical Profile Network
CCGG	Carbon Cycle Greenhouse Gases group
ESRL	Earth System Research Laboratory
GGGRN	Global Greenhouse Gas Reference Network
GMD	Global Monitoring Division
GML	Global Monitoring Laboratory
HATS	Halocarbons and other Atmospheric Trace Species
SIO	Scripps Institution of Oceanography (USA)
TU	Tohoku University - Center for Atmospheric and Oceanic Studies
UBAG	Umweltbundesamt (German Federal Environmental Agency)
UNIURB	Università degli Studi di Urbino "Carlo Bo" (University of Urbino, Italy)
UNIVBRIS	University of Bristol (UK)

Table S6. Nudging kernel configuration used to run FLEXPART CTM

Nudging kernel configurations			
kernel dimensions	surface stations	ship measurements	aircraft measurements
latitudinal kernel width h_y [°]	[1-25][a]	10	$1 + 15 \cdot arctan(\frac{altitude}{1000m}^b)$
longitudinal kernel width h_x [°]	same as h_y	same as h_y	same as h_y
kernel height h_z [m]	500 for $h_y > 5°$ 300 for $h_y \leq 5°$	300	$20 \cdot \frac{h_y}{1°}$
temporal kernel length h_t [s]	$86400 \cdot \frac{h_y}{1°}$	$86400 \cdot \frac{h_y}{1°}$	$86400 \cdot \frac{h_y}{1°}$
kernel relaxation time τ [s]	1800	1800	1800

[a] h_y depends on the standard deviation of measurements in a 3-day time interval for continuous measurements ($h_y = 5° \cdot \frac{0.08ppt}{std}$) and a 60-day time interval for flask measurements ($h_y = 5° \cdot \frac{0.15ppt}{std}$)

[b] Altitude indicates the measurement altitude in meters above ground level.

Table S7. Statistical values comparing detrended modeled with detrended observed mole fractions at individual measurement stations, using EP7 as *a priori* emissions. The detrending was done, as for all stations the trend is so strong that very high correlation values of almost 100% would be obtained otherwise.

measurement site	a priori r^2 [%]	a posteriori r^2 [%]	a priori MSE [1000 ppt^2]	a posteriori MSE [1000 ppt^2]
bik	56	60	6.30	6.19
brm	28	37	49.2	45.0
brw	81	81	5.27	4.96
bsd	53	69	6.57	4.18
cgo	91	91	1.05	1.04
cmn	40	44	43.7	37.8
coi	41	53	20.9	18.2
gsn	65	81	405	198
hat	65	83	115	51
hfd	60	79	21.00	9.58
izo	50	51	4.72	4.63
jfj	59	62	20.2	18.3
mhd	92	94	2.72	2.11
mlo	69	69	11.5	10.3
nwr	84	85	10.02	8.42
rgl	56	72	7.51	5.33
rpb	96	96	2.07	2.03
smo	93	93	3.70	3.65
spo	77	77	3.06	3.06
sum	43	45	5.25	5.02
tac	76	85	17.8	11.0
thd	62	68	3.87	2.60
zep	97	98	2.27	1.64
zsf	91	93	13.1	10.6

S3 Measurement data sets

Observations from continuous surface stations

Table S1 lists all the surface stations continuously monitoring SF_6. Measurements at CGO, JFJ, MHD, RPB, SMO, TAC, THD, and ZEP were provided by the international observation network AGAGE (Prinn et al., 2018). Data from BRW, MLO, NWR, SMO, SPO, and SUM were provided by the NOAA/GML Chromatograph for Atmospheric Trace Species (CATS) program (Dutton and Hall, 2023). Data from CMN (Maione et al., 2013), COI (Tohjima et al., 2002), IZO (Gomez-Pelaez and Ramos, 2009), RGL (Stavert et al., 2019), and ZSF (Zellweger et al., 2020) were found in the WDCGG data base https://gaw.kishou.go.jp/search (di Sarra et al., 2022). Observations from HFD (Arnold et al., 2019), BSD (O'Doherty et al., 2019) were found at the CEDA data base (CEDA, 2023), and measurements for ZEP (2005-2010) were found at the EBAS database (Tørseth et al., 2012). For the observations at BIK (Popa et al., 2010), BRM (Rust et al., 2022), GSN (Kim et al., 2012), and HAT (Saikawa et al., 2012) we refer to E. Popa <epopa2@yahoo.com>, S. Reinmann <stefan.reimann@empa.ch>, S. Park <sparky@knu.ac.kr>, and T. Saito <saito.takuya@nies.go.jp>, respectivley

Surface flask measurements

Table S2 and S3 list all the surface flask measurement sampling sides. Measurements at ABP, ALT, AMT, AMY, ASC, ASK, AZR, BAL, BHD, BKT, BME, BMW, BRW, BSC, CBA, CGO, CHR, CIB, CPT, CRZ, DSI, EIC, GMI, HBA, HPB, HSU, HUN, ICE, IZO, KEY, KUM, KZD, KZM, LEF, LLB, LLN, LMP, MEX, MHD, MID, MKN, MLO, NAT, NMB, NWR, OXK, PAL, PSA, PTA, SDZ, SEY, SGP, SHM, SMO, SPO, STM, SUM, SYO, TAP, THD, TIK, TPI, USH, UTA, UUM, WIS, WKT, WLG, ZEP were provided by the Atmospheric SF_6 Dry Air Mole Fractions from the NOAA GML Carbon Cycle Cooperative Global Air Sampling Network (Lan et al., 2023; Dlugokencky et al., 2020). For APB and NAT, INPE collected the samples, and the analysis was done together with NOAA/GML. NOAA Global Greenhouse Gas Reference Network provided flask-air PFP sample measurements of SF_6 at Tall Towers and other Continental Sites (Andrews et al., 2022) at BAO, CRV, HFM, KLM, LEF, LEW, MBO, MLO, MRC, MSH, MVY, MWO, NWB, NWR, SCT, SGP, STR, WBI, WGC, WKT. Measurements at ALT, AMT, CGO, CRV, KUM, LEF, MHD, MLO, NWR, OBN, PCO, PSA, SPO, SUM, THD, USH were provided by NOAA ESRL Halocarbons and other Atmospheric Trace Species (HATS) (Elkins and Dutton, 2008; Hall et al., 2011) and were part of the NOAA ObsPACK SF_6 data set (NOAA Carbon Cycle Group ObsPack Team, 2018).

Measurements from moving platforms

Table S4 lists the measurements from moving platforms. AAO, ACG, ACT, BAO, BGI, BNE, CAR, CMA, CRV, DND, DRP, ECO, ESP, ETL, FWI, HAA, HFM, HIL, INX, LEF, MCI, MRC, NHA, NSA, NSK, OIL, PFA, RTA, SCA, SGP, TGC, THD, ULB, WBI, WGC were provided by the Atmospheric Sulfur Hexafluoride Dry Air Mole Fractions from the NOAA GML Carbon Cycle Aircraft Vertical Profile Network (McKain et al., 2022). Observations at AOC, BII, CON, CRS, DRP, FAM, PAO, POC, SYO, WPC are part of NOAA ObsPACK SF_6 data set (NOAA Carbon Cycle Group ObsPack Team, 2018).

Observations at SAN and PAN were provided by INPE (D'Amelio et al., 2024). IAGOS-CARIBIC Aircraft measurements were provided by Schuck and Obersteiner (2024). NOAA/ESRL/GMD/HATS Trace Gas Measurements from Airborne Platforms (Elkins et al., 2020) provide observations from NASA aircraft measurement campaigns including UAV-DEMO (ALTAIR) (Fahey et al., 2006), AVE-05 (WB57) (Petropavlovskikh et al., 2008), CR-AVE (WB57) (Gensch et al., 2008), TC4 (WB57) (Salawitch et al., 2008), START-08 (GV) (Schauffler et al., 2010), HIPPO (GV) (Wofsy, 2011), GLOPAC (GHAWK) (Newman et al., 2010), ATTREX (GHAWK) (Jensen et al., 2013), ATOM (DC8) (Wofsy et al., 2018), POSIDON (WB57) (Jensen et al., 2020).

S4 Standardization of observations

The measurements from different providers were calibrated with four calibration scales: NIES-2008, WMO-SF_6-X2006, WMO-SF_6-X2014 and SIO-2005. We standardized all observations to the SIO-2005 calibration scale. To convert from WMO-SF_6-X2014 to SIO-2005 scale, we used the factor of 1.002 presented in Guillevic et al. (2018). Note, however, that while according to Krummel et al. (2017), this factor seems appropriate for observations after 2010, it might be too low for earlier data and a factor of 1.008 would have been more appropriate. As the difference is, however, smaller than 1% we expect the impact on our inversion results to be negligible. For future applications, we recommend getting in contact with Paul Krummel <paul.krummel@csiro.au>. To convert the mole fractions from WMO-SF_6-X2006 to WMO-SF_6-X2014, we used the equation $y = ax2 + bx + c$, where y represents the SF_6 mole fractions on the X2014 scale, x represents the mole fractions on the X2006 scale, and the coefficients a, b, and c have values of $2.6821 \cdot 10^{-3}$, $9.7748 \cdot 10^{-1}$, and $3.5831 \cdot 10^{-2}$ (NOAA ESRL, 2014), respectively. The NIES-2008 calibrated data were divided by a factor of 1.013 (Saito, 2021).

S5 The initialization of FLEXPART CTM

SF_6 emissions are higher in the Northern than in the Southern Hemisphere, resulting in a substantial latitudinal gradient of SF_6 mole fractions. To address this in the initialization of the FLEXPART CTM, we provide a latitudinal SF_6 profile determined by interpolation of surface measurements in the first two weeks of the initialization. FLEXPART CTM disperses particles globally in proportion to air density, and according to the provided latitudinal profile. The SF_6 concentration in the stratosphere is influenced by the age of stratospheric air (AoA), defined as the average transport time of an air parcel from its entry into the stratosphere to any point within it (Waugh and Hall, 2002; Loeffel et al., 2022). Regions with high AoA have lower SF_6 concentrations, as they represent the lower tropospheric concentrations in the past, when the corresponding air left the troposphere. To address this, we use the MIPAS 3d AoA fields (Stiller et al., 2021) along with the average global concentrations calculated by Simmonds et al. (2020) to correct the initial concentration fields in the stratosphere. In detail, we calculate a 3d field of correction factors, by building the ratio between the SF_6 concentration at the initialization time and the concentration at the time given by the respective AoA value. Figure S25 shows the initial mole fraction field for 2005.

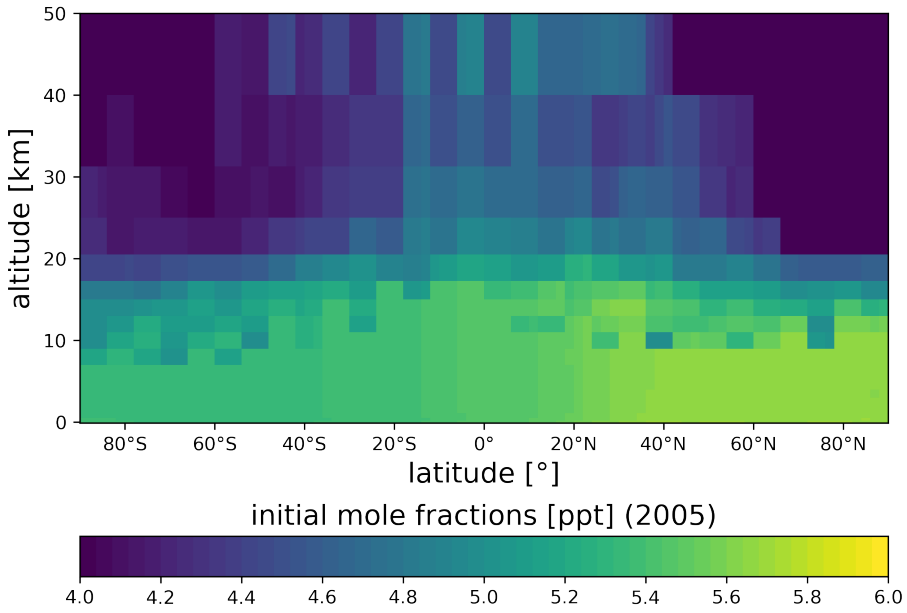

Figure S25. Initial field of SF_6 mole fractions used for the initialization in the year 2005.

S6 SF_6 emission in the GAINS model

SF_6 emissions originate from various sources such as mid- and high-voltage switches, magnesium production and casting, soundproof glazing, and a range of other applications including photovoltaic manufacturing, military applications, biomedical industry, fiber optic production, particle accelerators, and sports equipment. Within the GAINS model, four distinct sources of SF_6 emissions have been identified as follows:

High and mid voltage switches

SF_6 emissions primarily originate from the electrical equipment sector due to leakage, maintenance, and retirement (IPCC/TEAP, 2005). SF_6 functions as an electrical insulator in transmission and distribution equipment in electric systems, primarily within gas-insulated switch gears (GIS) employed in high and mid-voltage electric networks. Emission levels of SF_6 are affected by factors like the age of GIS, with older models exhibiting higher leakage rates than newer ones, and the size of the transmission network, as well as the recycling practices of obsolete equipment (Purohit and Höglund-Isaksson, 2017; Gambhir et al., 2017). In this study, the GAINS model utilizes reported emissions for Annex-I countries from the years 2005, 2010, 2015, and 2020, as documented by UNFCCC (2023). For the historical years, SF_6 emissions in China are taken from Zhou et al. (2018) and Cui

et al. (2024). The GAINS model uses electricity generation as an activity variable for this sector. For other non-Annex-I (developing) countries, the emission factor for SF_6 per unit of electricity generated is taken from the average of Annex-I countries (UNFCCC, 2023) and applied in a consistent manner to all regions. In recent years, several alternatives to SF_6 in both mid- and high-voltage electrical switch gear were developed. The GAINS model incorporated alternative substitutes for SF_6 in mid- and high-voltage electrical switch gear, including zero-GWP AIR, NOVEC-4710 with a GWP100 of 2100, and NOVEC-5110 with a GWP100 of 1 (Gschrey et al., 2022; Owens et al., 2021). Additionally, emissions can be reduced through recycling practices for used SF_6 switch gears, as mandated by F-gas Regulation (EC 842/2006) since 2010.

Magnesium production and casting

The casting and production of primary and secondary magnesium are recognized as significant sources of SF_6 atmospheric emissions. The gas is used as a shielding gas in magnesium foundries to protect the molten magnesium from reoxidizing whilst it is running to best casting ingots (IPCC, 2001). In this study, the GAINS model utilizes reported emissions for EU countries from the years 2005, 2010, 2015, and 2020 (UNFCCC, 2023). Activity data for non-EU countries on historic volumes of processed magnesium are taken from the United States Geological Survey (USGS, 2023) and the national communications to UNFCCC (UNFCCC, 2023). The GAINS model uses value added for the manufacturing industry as an activity variable for this sector. An emission factor of 1 kg SF_6 per ton of processed metal is taken from Schwarz and Leisewitz (1999) and Tohka (2005). According to Fang et al. (2013), SF_6 consumption factor of 1.65 kg SF_6 per ton of magnesium is employed specifically for magnesium processing in China. While the 2006 EU F-gas regulation only restricted SF_6 usage in die-casting operations, the bans on SF_6 usage in recycling magnesium die-casting alloys were introduced in the 2014 EU F-gas regulation (DEFRA, 2014). In the GAINS model, SF_6 emissions from magnesium production and casting can be substituted by using sulfur dioxide or the recently introduced sustainable cover gas NOVEC-612, which has a GWP100 of 1.

Soundproof windows

Some European countries used significant amounts of SF_6 in soundproof windows. From 2006, EC 842/2006 bans the use of SF_6 in soundproof windows. Soundproof windows have a relatively long lifetime, and it is therefore expected that the stock of SF_6 found in such windows in 2005 will be successively phased-out over a period of 25 years. The GAINS methodology to assess SF_6 emissions in soundproof windows is outlined in Purohit and Höglund-Isaksson (2017).

Other SF_6 sources

SF_6 has been used in several other applications including PV manufacturing, military applications, biomedical industry, fiber optic production, particle accelerators, and sports equipment. Activity data for these other sources of SF_6 emissions are taken from emissions reported by countries to the (UNFCCC, 2023). Since 2006, EC 842/2006 has banned SF_6 in sports equipment and tires, with GAINS assuming full EU compliance.

Spatial distribution

The spatial distribution of SF_6 emissions in Europe (EU27, Iceland, Norway, Switzerland, United Kingdom of Great Britain and Northern Ireland) follows 4081 electrical substation locations, based on ENTSO-E data from Wiegmans (2016). In absence of more detailed information about substation characteristics, an equal distribution among substations in each country was chosen and individual locations aggregated at 0.1° resolution. For the remaining regions differentiated in the GAINS model, emissions are allocated using a gridded population proxy from the Gridded Population of the World (GPW) Doxsey-Whitfield et al. (2015) and Global Human Settlement Layer (GHSL) (EC-JRC, 2015). The gridded population data is processed at its highest initial resolution, spatially allocated to a region, and aggregated to the output resolution (0.1° in this case). The distribution of emissions is subsequently based on the relative population share within a region.

References

Andrews, A., Crotwell, A., Crotwell, M., Handley, P., Higgs, J., Kofler, J., Lan, X., Legard, T., Madronich, M., McKain, K., Miller, J., Moglia, E., Mund, J., Neff, D., Newberger, T., Petron, G., Turnbull, J., Vimont, I., Wolter, S., and NOAA Global Monitoring Laboratory: NOAA Global Greenhouse Gas Reference Network Flask-Air PFP Sample Measurements of SF6 at Tall Tower and other Continental Sites, 2005-Present [Data set]., Version: 2022-11-01., NOAA GML., https://doi.org/10.15138/5R14-K382, 2022.

Arnold, T., Rennick, C., O'Doherty, S., Say, D., Young, D., Stavert, A., and Wenger, A.: Deriving Emissions related to Climate Change Network: CO2, CH4, N2O, SF6 and CO measurements from Heathfield Tall Tower, East Sussex. Centre for Environmental Data Analysis, https://catalogue.ceda.ac.uk/uuid/df502fe4715c4177ab5e4e367a99316b, last accessed: 2024-02-1, 2019.

CEDA: World Data Centre for Greenhouse Gases, https://archive.ceda.ac.uk//, last accessed: 2023-09-10, 2023.

Cui, Z., Li, Y., Xiao, S., Tian, S., Tang, J., Hao, Y., and Zhang, X.: Recent progresses, challenges and proposals on SF6 emission reduction approaches, Science of The Total Environment, p. 167347, https://doi.org/10.1016/j.scitotenv.2023.167347, 2024.

DEFRA: Magnesium smelting: bans on use of sulphur hexafluoride. Department for Environment, Food Rural Affairs and Environment Agency (DEFRA), UK, December, https://www.gov.uk/guidance/magnesium-smelting-bans-on-use-of-sulphur-hexafluoride, last accessed: 2024-02-15, 2014.

di Sarra, A., Hall, B. D., Dylag, C., Couret, C., Lunder, C., Sweeney, C., Sferlazzo, D., Say, D., Mondeel, D. J., Young, D., Dlugokencky, E., Cuevas, E., Meinhardt, F., Technos, G. E., Dutton, G. S., Lee, H., Nance, J. D., Arduini, J., Pitt, J., Tsuboi, K., Stanley, K., Gatti, L. V., Steinbacher, M., Vollmer, M., Krummel, P., Rivas, P., Weiss, R. F., Wang, R., Chiavarini, S., Piacentino, S., O'Doherty, S., Reimann, S., A. Montzka, S., Saito, T., and Lan, X.: All SF6 data contributed to WDCGG by GAW stations and mobiles by 2022-09-05, https://doi.org/10.50849/WDCGG_SF6_ALL_2022, 2022.

Dlugokencky, E., Crotwell, A., Mund, J., Crotwell, M., and Thoning, K.: Atmospheric Sulfur Hexafluoride Dry Air Mole Fractions from the NOAA GML Carbon Cycle Cooperative Global Air Sampling Network, 1997-2019, Version: 2020-07, https://doi.org/10.15138/p646-pa37, 2020.

Doxsey-Whitfield, E., MacManus, K., Adamo, S. B., Pistolesi, L., Squires, J., Borkovska, O., and Baptista, S. R.: Taking advantage of the improved availability of census data: a first look at the gridded population of the world, version 4, Papers in Applied Geography, 1, 226–234, https://doi.org/10.1080/23754931.2015.1014272, 2015.

Dutton, G. and Hall, B.: Global Atmospheric Sulfur hexaflouride Dry Air Mole Fractions from the NOAA GML Halocarbons in situ Network, 1998-2023, Version: 2023-04-13, https://doi.org/10.7289/V5X0659V, 2023.

D'Amelio, M. T., Gatti, L. V., Martins, E. A. J., Polakiewicz, L., Miller, J., Crotwell, A., and Tans, P.: Greenhouse gases study in the Amazonia atmosphere, https://www.researchgate.net/profile/Luciana-Gatti/publication/242072841_GREENHOUSE_GASES_STUDY_IN_THE_AMAZONIA_ATMOSPHERE/links/0f3175375e48855b32000000/GREENHOUSE-GASES-STUDY-IN-THE-AMAZONIA-ATMOSPHERE.pdf, last accessed: 2024-02-01, 2024.

EC-JRC: GHS-POP R2015A - GHS population grid, derived from GPW4, multitemporal (1975, 1990, 2000, 2015). European Commission, Joint Research Centre (JRC) [Dataset] PID:, http://data.europa.eu/89h/jrc-ghsl-ghs_pop_gpw4_globe_r2015a, 2015.

Elkins, J. and Dutton, G.: Nitrous oxide and sulfur hexafluoride [in 'State of the Climate in 2008']. Bull. Amer. Meteor. Soc, 90 S38-S39, 2008.

Elkins, J. W., Moore, F., Hintsa, E., Hurst, D., Hall, B., Montzka, S., Miller, B., Dutton, G., and Nance, D.: HATS Airborne Projects, www.esrl.noaa.gov/gmd/hats/airborne/, last accessed: 2024-02-1, 2020.

Fahey, D. W., Churnside, J. H., Elkins, J. W., Gasiewski, A. J., Rosenlof, K. H., Summers, S., Aslaksen, M., Jacobs, T. A., Sellars, J. D., Jennison, C. D., et al.: Altair unmanned aircraft system achieves demonstration goals, Eos, Transactions American Geophysical Union, 87, 197–201, https://doi.org/10.1029/2006EO200002, 2006.

Fang, X., Hu, X., Janssens-Maenhout, G., Wu, J., Han, J., Su, S., Zhang, J., and Hu, J.: Sulfur hexafluoride (SF6) emission estimates for China: an inventory for 1990–2010 and a projection to 2020, Environmental science & technology, 47, 3848–3855, https://doi.org/10.1021/es304348x, 2013.

Gambhir, A., Napp, T., Hawkes, A., Höglund-Isaksson, L., Winiwarter, W., Purohit, P., Wagner, F., Bernie, D., and Lowe, J.: The contribution of non-CO2 greenhouse gas mitigation to achieving long-term temperature goals, Energies, 10, 602, https://doi.org/10.3390/en10050602, 2017.

Gensch, I. V., Bunz, H., Baumgardner, D., Christensen, L. E., Fahey, D. W., Herman, R. L., Popp, P. J., Smith, J. B., Troy, R. F., Webster, C. R., et al.: Supersaturations, microphysics and nitric acid partitioning in a cold cirrus cloud observed during CR-AVE 2006: an observation–modelling intercomparison study, Environmental research letters, 3, 035 003, https://doi.org/10.1088/1748-9326/3/3/035003, 2008.

Gomez-Pelaez, A. and Ramos, R.: 4.1 Installation of a New Gas Chromatograph at Izaña GAW Station (Spain) to Measure CH4, N2O, and SF6, GAW Report No. 186, p. 55, https://citeseerx.ist.psu.edu/document?repid=rep1&type=pdf&doi=0f54fc63d0aaa54c6146cba55cc0ba7bbfbad00f#page=73, 2009.

Gschrey, B., Behringer, D., Kleinschmidt, J., Jörß, W., Liste, V. ., Ludig, S., Wissner, N., Birchby, D., Dubey, J., and Hekman, J.: Support contract for an Evaluation and Impact Assessment for amending Regulation (EU) No 517/2014 on fluorinated greenhouse gases, CLIMA.A2/ETU/2019/0016, Impact Assessment Final Report, March, 2022.

Guillevic, M., Vollmer, M. K., Wyss, S. A., Leuenberger, D., Ackermann, A., Pascale, C., Niederhauser, B., and Reimann, S.: Dynamic–gravimetric preparation of metrologically traceable primary calibration standards for halogenated greenhouse gases, Atmospheric Measurement Techniques, 11, 3351–3372, https://doi.org/10.5194/amt-11-3351-2018, 2018.

Hall, B., Dutton, G., Mondeel, D., Nance, J., Rigby, M., Butler, J., Moore, F., Hurst, D., and Elkins, J.: Improving measurements of SF 6 for the study of atmospheric transport and emissions, Atmospheric Measurement Techniques, 4, 2441–2451, https://doi.org/10.5194/amt-4-2441-2011, 2011.

IPCC/TEAP: IPCC/TEAP Special Report on Safeguarding the Ozone Layer and the Global Climate System: Issues Related to Hydrofluorocarbons and Perfluorocarbons, Intergovernmental Panel on Climate Change (IPCC) and Technology and Economic Assessment Panel (TEAP), Cambridge University Press, Cambridge, United Kingdom and New York, USA, 2005.

Jensen, E., Pan, L. L., Honomichl, S., Diskin, G. S., Krämer, M., Spelten, N., Günther, G., Hurst, D. F., Fujiwara, M., Vömel, H., et al.: Assessment of observational evidence for direct convective hydration of the lower stratosphere, Journal of Geophysical Research: Atmospheres, 125, e2020JD032 793, https://doi.org/10.1029/2020JD032793, 2020.

Jensen, E. J., Pfister, L., Jordan, D. E., Fahey, D. W., Newman, P. A., Thornberry, T., Rollins, A., Diskin, G., Bui, T. P., McGill, M., et al.: The NASA Airborne Tropical TRopopause EXperiment (ATTREX), SPARC Newsletter, 41, 15–24, 2013.

Kim, J., Li, S., Mühle, J., Stohl, A., Kim, S.-K., Park, S., Park, M.-K., Weiss, R. F., and Kim, K.-R.: Overview of the findings from measurements of halogenated compounds at Gosan (Jeju Island, Korea) quantifying emissions in East Asia, Journal of Integrative Environmental Sciences, 9, 71–80, https://doi.org/10.1080/1943815X.2012.696548, 2012.

Krummel, P., Montzka, S., Harth, C., Miller, B., Mühle, J., Dlugokencky, E., Salameh, P., Hall, B., O'Doherty, S., Steele, L., Dutton, G., Young, D., Nance, J., Langenfelds, R., Elkins, J., Loh, Z., Lunder, C., Fraser, P., Derek, N., Mitrevski, B., Weiss, R., and Prinn, R.: An update of comparisons of non-CO2 trace gas measurements between AGAGE and NOAA at common sites, Presenta-

tion at the 19th WMO/IAEA GGMT Meeting, 28-31 Aug 2017, Empa, Dübendorf, Switzerland, https://community.wmo.int/en/meetings/19th-wmoiaea-meeting-carbon-dioxide-other-greenhouse-gases-and-related-measurement-techniques-ggmt-2017, last accessed: 2024-02-01, 2017.

Lan, X., Mund, J., Crotwell, A., Crotwell, M., Moglia, E., Madronich, M., Neff, D., and Thoning, K.: Atmospheric Sulfur Hexafluoride Dry Air Mole Fractions from the NOAA GML Carbon Cycle Cooperative Global Air Sampling Network, 1997-2022, Version: 2023-08-28, https://doi.org/10.15138/p646-pa37, 2023.

Loeffel, S., Eichinger, R., Garny, H., Reddmann, T., Fritsch, F., Versick, S., Stiller, G., and Haenel, F.: The impact of sulfur hexafluoride (SF 6) sinks on age of air climatologies and trends, Atmospheric Chemistry and Physics, 22, 1175–1193, https://doi.org/10.5194/acp-22-1175-2022, 2022.

Maione, M., Giostra, U., Arduini, J., Furlani, F., Graziosi, F., Vullo, E. L., and Bonasoni, P.: Ten years of continuous observations of stratospheric ozone depleting gases at Monte Cimone (Italy)—Comments on the effectiveness of the Montreal Protocol from a regional perspective, Science of the total environment, 445, 155–164, https://doi.org/10.1016/j.scitotenv.2012.12.056, 2013.

McKain, K., Sweeney, C., Baier, B., Crotwell, A., Crotwell, M., Handley, P., Higgs, J., Legard, T.and Madronich, M., Miller, J. B., Moglia, E.and Mund, J. N. D., Newberger, T., Wolter, S., and Laboratory, N. G. M.: NOAA Global Greenhouse Gas Reference Network Flask-Air PFP Sample Measurements of CO2, CH4, CO, N2O, H2, SF6 and isotopic ratios collected from aircraft vertical profiles [Data set]. Version: 2022-12-01, https://doi.org/10.15138/39HR-9N34, 2022.

Newman, P., Fahey, D., and Global Hawk Pacific Experiment Science Team and others: The Global Hawk Pacific Mission (April-May, 2010), in: AGU Fall Meeting Abstracts, vol. 2010, pp. A53H–08, 2010.

NOAA Carbon Cycle Group ObsPack Team: Multi-laboratory compilation of atmospheric sulfure hexafluoride data for the period 1983-2017; obspacksf61v2.1.12018−08−17; NOAA Earth System Research Laboratory, Global Monitoring Division, https://doi.org/10.15138/g3ks7p, 2018.

NOAA ESRL: NOAA Earth System Research Laboratoriy: Sulfur Hexafluoride (SF6) WMO Scale, https://gml.noaa.gov/ccl/sf6_scale.html, last accessed: 2022-05-27, 2014.

O'Doherty, S., Say, D., Stanley, K., Young, D., Pitt, J., and Wenger, A.: Deriving Emissions related to Climate Change Network: CO2, CH4, N2O, SF6 and CO measurements from Bilsdale Tall Tower, North York Moors National Park. Centre for Environmental Data Analysis, https://catalogue.ceda.ac.uk/uuid/d2090552c8fe4c16a2fd7d616adc2d9f, last accessed: 2024-02-1, 2019.

Owens, J., Xiao, A., Bonk, J., DeLorme, M., and Zhang, A.: Recent development of two alternative gases to SF6 for high voltage electrical power applications, Energies, 14, 5051, https://doi.org/10.3390/en14165051, 2021.

Petropavlovskikh, I., Froidevaux, L., Shetter, R., Hall, S., Ullmann, K., Bhartia, P., Kroon, M., and Levelt, P.: In-flight validation of Aura MLS ozone with CAFS partial ozone columns, Journal of Geophysical Research: Atmospheres, 113, https://doi.org/10.1029/2007JD008690, 2008.

Popa, M., Gloor, M., Manning, A., Jordan, A., Schultz, U., Haensel, F., Seifert, T., and Heimann, M.: Measurements of greenhouse gases and related tracers at Bialystok tall tower station in Poland, Atmospheric Measurement Techniques, 3, 407–427, https://doi.org/10.5194/amt-3-407-2010, 2010.

Prinn, R. G., Weiss, R. F., Arduini, J., Arnold, T., DeWitt, H. L., Fraser, P. J., Ganesan, A. L., Gasore, J., Harth, C. M., Hermansen, O., Kim, J., Krummel, P. B., Li, S., Loh, Z. M., Lunder, C. R., Maione, M., Manning, A. J., Miller, B. R., Mitrevski, B., Mühle, J., O'Doherty, S., Park, S., Reimann, S., Rigby, M., Saito, T., Salameh, P. K., Schmidt, R., Simmonds, P. G., Steele, L. P., Vollmer, M. K., Wang, R. H., Yao,

B., Yokouchi, Y., Young, D., and Zhou, L.: History of chemically and radiatively important atmospheric gases from the Advanced Global Atmospheric Gases Experiment (AGAGE), Earth System Science Data, 10, 985–1018, https://doi.org/10.5194/essd-10-985-2018, 2018.

Purohit, P. and Höglund-Isaksson, L.: Global emissions of fluorinated greenhouse gases 2005–2050 with abatement potentials and costs, Atmospheric Chemistry and Physics, 17, 2795–2816, https://doi.org/10.5194/acp-17-2795-2017, 2017.

Rust, D., Katharopoulos, I., Vollmer, M. K., Henne, S., O'doherty, S., Say, D., Emmenegger, L., Zenobi, R., and Reimann, S.: Swiss halocarbon emissions for 2019 to 2020 assessed from regional atmospheric observations, Atmospheric Chemistry and Physics, 22, 2447–2466, https://doi.org/10.5194/acp-22-2447-2022, 2022.

Saikawa, E., Rigby, M., Prinn, R. G., Montzka, S. A., Miller, B. R., Kuijpers, L. J. M., Fraser, P. J. B., Vollmer, M. K., Saito, T., Yokouchi, Y., Harth, C. M., Mühle, J., Weiss, R. F., Salameh, P. K., Kim, J., Li, S., Park, S., Kim, K.-R., Young, D., O'Doherty, S., Simmonds, P. G., McCulloch, A., Krummel, P. B., Steele, L. P., Lunder, C., Hermansen, O., Maione, M., Arduini, J., Yao, B., Zhou, L. X., Wang, H. J., Elkins, J. W., and Hall, B.: Global and regional emission estimates for HCFC-22, Atmospheric Chemistry and Physics, 12, 10 033–10 050, https://doi.org/10.5194/acp-12-10033-2012, 2012.

Saito, T.: private communication, feb. 05, 2021.

Salawitch, R., Canty, T., Avery, M., Wennberg, P., Team, T. S., et al.: Chemistry Observations from TC4: Overview, in: AGU Spring Meeting Abstracts, vol. 2008, pp. A53B–07, 2008.

Schauffler, S., Atlas, E., Lueb, R., Hendershot, R., and Pope, L.: Whole Air Sampler measurements of organic halogens in the troposphere and lower stratosphere from aircraft and balloon platforms., in: EGU General Assembly Conference Abstracts, p. 2991, 2010.

Schuck, T. and Obersteiner, F.: IAGOS-CARIBIC whole air sampler data (2024.01.12) [Data set]. Zenodo., https://doi.org/10.5281/zenodo.10495039, 2024.

Schwarz, W. and Leisewitz, A.: Emissions and reduction potentials of hydrofluorocarbons, perfluorocarbons and sulphur hexafluoride in Germany, Öko-Recherche, Frankfurt, Report for the German Federal Environmental Agency (Umweltbundesamt, UBA, Berlin), https://www.oekorecherche.de/sites/default/files/publikationen/f-gases.pdf, last accessed: 2024-02-15, 1999.

Simmonds, P. G., Rigby, M., Manning, A. J., Park, S., Stanley, K. M., McCulloch, A., Henne, S., Graziosi, F., Maione, M., Arduini, J., Reimann, S., Vollmer, M. K., Mühle, J., O'Doherty, S., Young, D., Krummel, P. B., Fraser, P. J., Weiss, R. F., Salameh, P. K., Harth, C. M., Park, M.-K., Park, H., Arnold, T., Rennick, C., Steele, L. P., Mitrevski, B., Wang, R. H. J., and Prinn, R. G.: The Increasing Atmospheric Burden of the Greenhouse Gas Sulfur Hexafluoride (SF6), Atmospheric Chemistry and Physics, 20, 7271–7290, https://doi.org/10.5194/acp-20-7271-2020, 2020.

Stavert, A. R., O'doherty, S., Stanley, K., Young, D., Manning, A. J., Lunt, M. F., Rennick, C., and Arnold, T.: UK greenhouse gas measurements at two new tall towers for aiding emissions verification, Atmospheric Measurement Techniques, 12, 4495–4518, https://doi.org/710.5194/amt-12-4495-2019, 2019.

Stiller, G., Harrison, J. J., Haenel, F., Glatthor, N., and Kellmann, S.: MIPAS monthly zonal mean Age of Air data, based on MIPAS SF6 retrievals, processed at KIT-IMK, Karlsruhe, https://doi.org/10.5445/IR/1000139453, 2021.

Tohjima, Y., Machida, T., Utiyama, M., Katsumoto, M., Fujinuma, Y., and Maksyutov, S.: Analysis and presentation of in situ atmospheric methane measurements from Cape Ochi-ishi and Hateruma Island, Journal of Geophysical Research: Atmospheres, 107, ACH–8, https://doi.org/10.1029/2001JD001003, 2002.

Tohka, A.: The GAINS Model for Greenhouse Gases – Version 1.0: HFC, PFC and SF6, International Institute for Applied Systems Analysis (IIASA), Laxenburg, Austria, October, 2005.

Tørseth, K., Aas, W., Breivik, K., Fjæraa, A. M., Fiebig, M., Hjellbrekke, A.-G., Lund Myhre, C., Solberg, S., and Yttri, K. E.: Introduction to the European Monitoring and Evaluation Programme (EMEP) and observed atmospheric composition change during 1972–2009, Atmospheric Chemistry and Physics, 12, 5447–5481, https://doi.org/10.5194/acp-12-5447-2012, 2012.

UNFCCC: National Inventory Submissions 2023, https://unfccc.int/ghg-inventories-annex-i-parties/2023, 2023.

USGS: Magnesium Statistics and Information, United States Geological Survey (USGS), https://www.usgs.gov/centers/national-minerals-information-center/magnesium-statistics-and-information, 2023.

Waugh, D. and Hall, T.: Age of stratospheric air: Theory, observations, and models, Reviews of Geophysics, 40, 1–1, https://doi.org/10.1029/2000RG000101, 2002.

Wiegmans, B.: GridKit extract of ENTSO-E interactive map, Zenodo: Oldenburg, Germany, https://doi.org/10.5281/zenodo.55853, 2016.

Wofsy, S., Afshar, S., Allen, H., Apel, E., Asher, E., Barletta, B., Bent, J., Bian, H., Biggs, B., Blake, D., et al.: ATom: Merged atmospheric chemistry, trace gases, and aerosols, ORNL DAAC, Oak Ridge, Tennessee, USA, https://doi.org/10.3334/ORNLDAAC/1581, 2018.

Wofsy, S. C.: HIAPER Pole-to-Pole Observations (HIPPO): fine-grained, global-scale measurements of climatically important atmospheric gases and aerosols, Philosophical Transactions of the Royal Society A: Mathematical, Physical and Engineering Sciences, 369, 2073–2086, https://doi.org/10.1098/rsta.2010.0313, 2011.

Zellweger, C., Klausen, J., and Buchmann, B.: System and performance audit for surface ozone, carbon monoxide and methane at the global GAW station Zugspitze-Schneefernerhaus Germany, June, 2006. Dübendorf, Switzerland: EMPA. WCC-Empa Report 06/4, https://citeseerx.ist.psu.edu/document?repid=rep1&type=pdf&doi=49d2b76db4ad0b715ed94cb859feba895d81a4b1, last accessed: 2024-02-1, 2020.

Zhou, S., Teng, F., and Tong, Q.: Mitigating sulfur hexafluoride (SF6) emission from electrical equipment in China, Sustainability, 10, 2402, https://doi.org/10.3390/su10072402, 2018.

Bibliography

An, M., R. G. Prinn, L. M. Western, X. Zhao, B. Yao, J. Hu, A. L. Ganesan, J. Mühle, R. F. Weiss, P. B. Krummel, et al. "Sustained growth of sulfur hexafluoride emissions in China inferred from atmospheric observations." In: *Nature Communications* 15.1 (2024), p. 1997. DOI: 10.1038/s41467-024-46084-3.

Andersen, O., G. Gilpin, and A. S. Andrae. "Cradle-to-gate life cycle assessment of the dry etching step in the manufacturing of photovoltaic cells." In: *AIMS Energy* 2.4 (2014), pp. 410–423. DOI: 10.3934/energy.2014.4.410.

Annadate, S., S. Falasca, R. Cesari, U. Giostra, M. Maione, and J. Arduini. "A Sensitivity Study of a Bayesian Inversion Model Used to Estimate Emissions of Synthetic Greenhouse Gases at the European Scale." In: *Atmosphere* 15.1 (2023), p. 51. DOI: 10.3390/atmos15010051.

Arnold, D., C. Maurer, G. Wotawa, R. Draxler, K. Saito, and P. Seibert. "Influence of the meteorological input on the atmospheric transport modelling with FLEXPART of radionuclides from the Fukushima Daiichi nuclear accident." In: *Journal of Environmental Radioactivity* 139 (2015), pp. 212–225. DOI: 10.1016/j.jenvrad.2014.02.013.

Assael, M. J., I. Koini, K. Antoniadis, M. L. Huber, I. M. Abdulagatov, and R. A. Perkins. "Reference Correlation of the Thermal Conductivity of Sulfur Hexafluoride from the Triple Point to 1000 K and up to 150 MPa." In: *Journal of Physical and Chemical Reference Data* 41.2 (2012), pp. 023104–023104-9. DOI: 10.1063/1.4708620.

Baier, K., M. Duetsch, M. Mayer, L. Bakels, L. Haimberger, and A. Stohl. "The Role of Atmospheric Transport for El Niño-Southern Oscillation Teleconnections." In: *Geophysical Research Letters* 49.23 (2022), e2022GL100906. DOI: 10.1029/2022GL100906.

Bartos, S., J. Marks, R. Kantamaneni, and C. Laush. "Measured SF6 emissions from magnesium die casting operations." In: *Magnesium Technology, syf* (2003), pp. 23–29. URL: https://19january2021snapshot.epa.gov/sites/static/files/2016-02/documents/die-cast.pdf (visited on 03/27/2024).

Benjah-bmm27. *Sulfur-hexafluoride-2D-small*. Marked as public domain, details on Wikimedia Commons: https://commons.wikimedia.org/wiki/Template:PD-user. Wikimedia Commons, 2007. URL: https://commons.wikimedia.org/wiki/File:Sulfur-hexafluoride-2D-small.png (visited on 04/27/2024).

Berchet, A., I. Pison, F. Chevallier, P. Bousquet, S. Conil, M. Geever, T. Laurila, J. Lavrič, M. Lopez, J. Moncrieff, et al. "Towards better error statistics for atmospheric inversions of

methane surface fluxes." In: *Atmospheric Chemistry and Physics* 13.14 (2013), pp. 7115–7132. DOI: 10.5194/acp-13-7115-2013.

Berchet, A. et al. "The Community Inversion Framework v1.0: a unified system for atmospheric inversion studies." In: *Geoscientific Model Development* 14.8 (2021), pp. 5331–5354. DOI: 10.5194/gmd-14-5331-2021.

Bergamaschi, P., M. Corazza, U. Karstens, M. Athanassiadou, R. L. Thompson, I. Pison, A. J. Manning, P. Bousquet, A. Segers, A. Vermeulen, et al. "Top-down estimates of European CH 4 and N 2 O emissions based on four different inverse models." In: *Atmospheric Chemistry and Physics* 15.2 (2015), pp. 715–736. DOI: 10.5194/acp-15-715-2015.

Billen, P., B. Maes, M. Larrain, and J. Braet. "Replacing SF6 in electrical gas-insulated switchgear: technological alternatives and potential life cycle greenhouse gas savings in an EU-28 perspective." In: *Energies* 13.7 (2020), p. 1807. DOI: 10.3390/en13071807.

Brasseur, G. P. and D. J. Jacob. "Inverse Modeling for Atmospheric Chemistry." In: *Modeling of Atmospheric Chemistry*. Cambridge University Press, 2017, pp. 487–537. DOI: 10.1017/9781316544754.012.

Brinton, D. A. and C. P. Wilkinson. *Retinal Detachment: Priniciples and Practice*. Vol. 1. Oxford University Press, 2009, pp. 182–183.

Brunner, D., T. Arnold, S. Henne, A. Manning, R. L. Thompson, M. Maione, S. O'Doherty, and S. Reimann. "Comparison of four inverse modelling systems applied to the estimation of HFC-125, HFC-134a, and SF 6 emissions over Europe." In: *Atmospheric Chemistry and Physics* 17.17 (2017), pp. 10651–10674. DOI: 10.5194/acp-17-10651-2017.

Bullister, J. L., D. P. Wisegarver, and F. A. Menzia. "The solubility of sulfur hexafluoride in water and seawater." In: *Deep Sea Research Part I: Oceanographic Research Papers* 49.1 (2002), pp. 175–187. DOI: 10.1016/S0967-0637(01)00051-6.

Cai, M.-G., H.-X. Deng, P. Huang, H.-W. Ke, X.-H. Zheng, and L. Wen-Quan. "Simultaneous determination of chlorofluorocarbons and sulfur hexafluoride in seawater based on a purge and trap gas chromatographic system." In: *Chinese Journal of Analytical Chemistry* 44.7 (2016), pp. 1003–1008. DOI: 10.1016/S1872-2040(16)60941-6.

California State Legislature. *Assembly Bill 32 (AB 32): California's Global Warming Solutions Act*. 2006. URL: https://leginfo.legislature.ca.gov/faces/billTextClient.xhtml?bill_id=200520060AB32 (visited on 04/27/2024).

Camilli, G., G. Gordon, and R. Plump. "Gaseous Insulation for High-Voltage Transformers." In: *Transactions of the American Institute of Electrical Engineers. Part III: Power Apparatus and Systems* 71.1 (1952), pp. 348–357. DOI: 10.1109/AIEEPAS.1952.4498481.

Canadell, J. G., P. M. S. Monteiro, M. H. Costa, L. Cotrim da Cunha, P. M. Cox, A. V. Eliseev, S. Henson, M. Ishii, S. Jaccard, C. Koven, A. Lohila, P. K. Patra, S. Piao, J. Rogelj, S. Syampungani, S. Zaehle, and K. Zickfeld. "Global Carbon and other Biogeochemical Cycles and Feedbacks." In: *Climate Change 2021: The Physical Science Basis. Contribution*

of Working Group I to the Sixth Assessment Report of the Intergovernmental Panel on Climate Change. Ed. by V. Masson-Delmotte, P. Zhai, A. Pirani, S. L. Connors, C. Péan, S. Berger, N. Caud, Y. Chen, L. Goldfarb, M. I. Gomis, M. Huang, K. Leitzell, E. Lonnoy, J. B. R. Matthews, T. K. Maycock, T. Waterfield, O. Yelekçi, R. Yu, and B. Zhou. Cambridge, United Kingdom and New York, NY, USA: Cambridge University Press, 2021, pp. 673–816. DOI: 10.1017/9781009157896.007.

Cheng, J.-H., S. C. Bartos, W. M. Lee, S.-N. Li, et al. "SF6 usage and emission trends in the TFT-LCD industry." In: *International Journal of Greenhouse Gas Control* 17 (2013), pp. 106–110. DOI: 10.1016/j.ijggc.2013.04.003.

Chevallier, F., M. Remaud, C. W. O'Dell, D. Baker, P. Peylin, and A. Cozic. "Objective evaluation of surface-and satellite-driven carbon dioxide atmospheric inversions." In: *Atmospheric Chemistry and Physics* 19.22 (2019), pp. 14233–14251. DOI: 10.5194/acp-19-14233-2019.

Christensen, J. H. "The Danish Eulerian hemispheric model—A three-dimensional air pollution model used for the Arctic." In: *Atmospheric Environment* 31.24 (1997), pp. 4169–4191. DOI: 10.1016/S1352-2310(97)00264-1.

Christophorou, L. G., J. K. Olthoff, and D. S. Green. *Gases for electrical insulation and arc interruption: possible present and future alternatives to pure SF6; NIST Technical Note 1425*. US Department of Commerce, Technology Administration, National Institute of Standards and Technology, 1997. URL: https://19january2021snapshot.epa.gov/sites/static/files/2016-02/documents/new_report_final.pdf (visited on 04/28/2024).

Cleland, M. R. "Industrial applications of electron accelerators." In: *CAS - CERN Accelerator School and KVI: Specialised CAS Course on Small Accelerators* (2006), pp. 383–416. DOI: 10.5170/CERN-2006-012.383.

Cui, Z., Y. Li, S. Xiao, S. Tian, J. Tang, Y. Hao, and X. Zhang. "Recent progresses, challenges and proposals on SF6 emission reduction approaches." In: *Science of The Total Environment* (2024), p. 167347. DOI: 10.1016/j.scitotenv.2023.167347.

Danielsen, E. F. "Trajectories: Isobaric, isentropic and actual." In: *Journal of Atmospheric Sciences* 18.4 (1961), pp. 479–486. DOI: 10.1175/1520-0469(1961)018<0479:TIIAA>2.0.CO;2.

de Campos Velho, H. F., V. C. Barbosa, and S. Cocke. "Special issue on inverse problems in geosciences." In: *Inverse Problems in Science and Engineering* 21.3 (2013), pp. 355–356. DOI: 10.1080/17415977.2012.712532.

DeHope, W., K. Griffin, R. Kihara, M. Ong, and T. Ross. "An improved SF6 system for the FXR induction linac blumlein switches." In: *2007 IEEE Particle Accelerator Conference (PAC)*. IEEE. 2007, pp. 2361–2363. DOI: 10.1109/PAC.2007.4441250.

Dhakal, S., J. Minx, F. Toth, A. Abdel-Aziz, M. Figueroa Meza, K. Hubacek, I. Jonckheere, Y.-G. Kim, G. Nemet, S. Pachauri, X. Tan, and T. Wiedmann. "Emissions Trends and Drivers." In: *Climate Change 2022: Mitigation of Climate Change. Contribution of Working Group III to the Sixth Assessment Report of the Intergovernmental Panel on Climate Change*. Ed. by P. Shukla, J. Skea, R. Slade, A. Al Khourdajie, R. van Diemen, D. McCollum, M. Pathak, S. Some, P. Vyas, R. Fradera, M. Belkacemi, A. Hasija, G. Lisboa, S. Luz, and J. Malley. Cambridge, UK and New York, NY, USA: Cambridge University Press, 2022. DOI: 10.1017/9781009157926.004.

Dingy, I. *GIS 420kV*. Licensed under CC BY-SA 3.0. License details: https://creativecommons.org/licenses/by-sa/3.0/legalcode. Wikimedia Commons, 2007. URL: https://commons.wikimedia.org/wiki/File:GIS_420kV.jpg (visited on 04/27/2024).

Eastern Research Group, Inc. *Assessment of the Use of Sulfur Hexafluoride (SF6) Gas Insulated Switchgears (GIS) within the Offshore Wind*. 2023. URL: https://www.epa.gov/system/files/documents/2023-12/ocs-sf6.pdf (visited on 04/28/2024).

Eckhardt, S., I. Pisso, N. Evangeliou, C. G. Zwaaftink, A. Plach, J. R. McConnell, M. Sigl, M. Ruppel, C. Zdanowicz, S. Lim, et al. "Revised historical Northern Hemisphere black carbon emissions based on inverse modeling of ice core records." In: *Nature Communications* 14.1 (2023), p. 271. DOI: 10.1038/s41467-022-35660-0.

Eggleston, H., L. Buendia, K. Miwa, T. Ngara, and K. Tanabe. "2006 IPCC guidelines for national greenhouse gas inventories." In: (2006). URL: https://www.ipcc-nggip.iges.or.jp/meeting/pdfiles/Washington_Report.pdf (visited on 04/29/2024).

European Parliament and Council of the European Union. "Regulation (EC) No 842/2006 of the European Parliament and of the Council on certain fluorinated greenhouse gases." In: *Official Journal of the European Union* L 161 (2006), pp. 1–11. URL: https://eur-lex.europa.eu/legal-content/EN/TXT/PDF/?uri=CELEX:32006R0842 (visited on 03/31/2024).

– "Regulation (EU) No. 517/2014 of the European Parliament and of the Council on fluorinated greenhouse gases and repealing Regulation (EC) No. 842/2006." In: *Official Journal of the European Union* L 150 (2014), pp. 195–230. URL: https://faolex.fao.org/docs/pdf/eur133686.pdf (visited on 03/31/2024).

– *Regulation of the European Parlament and of the council on fluorinated greenhouse gases, amending Directive (EU) 2019/1937 and repealing Regulation (EU) No 517/2014*. 2024. URL: https://data.consilium.europa.eu/doc/document/PE-60-2023-INIT/en/pdf (visited on 03/31/2024).

Evangeliou, N., H. Grythe, Z. Klimont, C. Heyes, S. Eckhardt, S. Lopez-Aparicio, and A. Stohl. "Atmospheric transport is a major pathway of microplastics to remote regions." In: *Nature communications* 11.1 (2020), p. 3381. DOI: 10.1038/s41467-020-17201-9.

Ezhov, I., K. Scibilia, K. Franitza, F. Steinbauer, S. Shit, L. Zimmer, J. Lipkova, F. Kofler, J. C. Paetzold, L. Canalini, et al. "Learn-Morph-Infer: a new way of solving the inverse

problem for brain tumor modeling." In: *Medical Image Analysis* 83 (2023), p. 102672. DOI: 10.1016/j.media.2022.102672.

Fang, X., X. Hu, G. Janssens-Maenhout, J. Wu, J. Han, S. Su, J. Zhang, and J. Hu. "Sulfur hexafluoride (SF6) emission estimates for China: an inventory for 1990–2010 and a projection to 2020." In: *Environmental science & technology* 47.8 (2013), pp. 3848–3855. DOI: 10.1021/es304348x.

Fang, X., R. L. Thompson, T. Saito, Y. Yokouchi, J. Kim, S. Li, K. Kim, S. Park, F. Graziosi, and A. Stohl. "Sulfur hexafluoride (SF6) emissions in East Asia determined by inverse modeling." In: *Atmospheric Chemistry and Physics* 14.9 (2014), pp. 4779–4791. DOI: 10.5194/acp-14-4779-2014.

Fine, R. A. "Observations of CFCs and SF6 as ocean tracers." In: *Annual review of marine science* 3 (2011), pp. 173–195. DOI: 10.1146/annurev.marine.010908.163933.

Fletcher, S. and M. Zupanski. "A data assimilation method for log-normally distributed observational errors." In: *Quarterly Journal of the Royal Meteorological Society: A journal of the atmospheric sciences, applied meteorology and physical oceanography* 132.621 (2006), pp. 2505–2519. DOI: 10.1256/qj.05.222.

Fletcher, S. J., A. J. Kliewer, and A. S. Jones. "Quantification of optimal choices of parameters in lognormal variational data assimilation and their chaotic behavior." In: *Mathematical Geosciences* 51 (2019), pp. 187–207. DOI: 10.1007/s11004-018-9765-7.

Fornacon-Wood, I., H. Mistry, C. Johnson-Hart, C. Faivre-Finn, J. P. O'Connor, and G. J. Price. "Understanding the differences between Bayesian and frequentist statistics." In: *International journal of radiation oncology, biology, physics* 112.5 (2022), pp. 1076–1082. DOI: 10.1016/j.ijrobp.2021.12.011.

Gambhir, A., T. Napp, A. Hawkes, L. Höglund-Isaksson, W. Winiwarter, P. Purohit, F. Wagner, D. Bernie, and J. Lowe. "The contribution of non-CO2 greenhouse gas mitigation to achieving long-term temperature goals." In: *Energies* 10.5 (2017), p. 602. DOI: 10.3390/en10050602.

Ganesan, A., M. Rigby, A. Zammit-Mangion, A. Manning, R. Prinn, P. Fraser, C. Harth, K.-R. Kim, P. Krummel, S. Li, et al. "Characterization of uncertainties in atmospheric trace gas inversions using hierarchical Bayesian methods." In: *Atmospheric Chemistry and Physics* 14.8 (2014), pp. 3855–3864. DOI: 10.5194/acp-14-3855-2014.

Ganesan, A. L., M. Rigby, M. F. Lunt, R. J. Parker, H. Boesch, N. Goulding, T. Umezawa, A. Zahn, A. Chatterjee, R. G. Prinn, et al. "Atmospheric observations show accurate reporting and little growth in India's methane emissions." In: *Nature Communications* 8.1 (2017), p. 836. DOI: 10.1038/s41467-017-00994-7.

Ganshin, A., T. Oda, M. Saito, S. Maksyutov, V. Valsala, R. J. Andres, R. Fisher, D. Lowry, A. Lukyanov, H. Matsueda, et al. "A global coupled Eulerian-Lagrangian model and 1×1

km CO_2 surface flux dataset for high-resolution atmospheric CO_2 transport simulations." In: *Geoscientific Model Development* 5.1 (2012), pp. 231–243. DOI: 10.5194/gmd-5-231-2012.

German Environment Agency. *Submission under the United Nations Framework Convention on Climate Change and the Kyoto Protocol 2023 - National Inventory Report for the German Greenhouse Gas Inventory 1990 – 2021*. 2023. URL: https://www.umweltbundesamt.de/sites/default/files/medien/11850/publikationen/29_2023_cc_submission_under_the_united_nations_framework_convention.pdf (visited on 04/29/2024).

Giardini-Guidoni, A., R. Fantoni, R. Tiribelli, D. Vinciguerra, R. Camilloni, and G. Stefani. "Study of electronic properties of the SF6 molecule by (e, 2 e) spectroscopy." In: *The Journal of Chemical Physics* 71.8 (1979), pp. 3182–3188. DOI: 10.1063/1.325814.

Gouda, O. E., M. D. Ali, and A.-H. Ali-Hassan. "Comparasion between Oil Immersed and SF6 Gas Power Transformers Ratings." In: *TELKOMNIKA (Telecommunication Computing Electronics and Control)* 10.1 (2012), pp. 43–54. DOI: 10.12928/telkomnika.v10i1.797.

Graziosi, F., J. Arduini, F. Furlani, U. Giostra, L. J. Kuijpers, S. A. Montzka, B. R. Miller, S. J. O'Doherty, A. Stohl, P. Bonasoni, et al. "European emissions of HCFC-22 based on eleven years of high frequency atmospheric measurements and a Bayesian inversion method." In: *Atmospheric Environment* 112 (2015), pp. 196–207. DOI: 10.1016/j.atmosenv.2015.04.042.

Grell, G. A., S. E. Peckham, R. Schmitz, S. A. McKeen, G. Frost, W. C. Skamarock, and B. Eder. "Fully coupled "online" chemistry within the WRF model." In: *Atmospheric environment* 39.37 (2005), pp. 6957–6975. DOI: 10.5194/gmd-13-2379-2020.

Groot Zwaaftink, C. D., Ó. Arnalds, P. Dagsson-Waldhauserova, S. Eckhardt, J. M. Prospero, and A. Stohl. "Temporal and spatial variability of Icelandic dust emissions and atmospheric transport." In: *Atmospheric Chemistry and Physics* 17.17 (2017), pp. 10865–10878. DOI: 10.5194/acp-17-10865-2017.

Groot Zwaaftink, C. D., S. Henne, R. L. Thompson, E. J. Dlugokencky, T. Machida, J.-D. Paris, M. Sasakawa, A. Segers, C. Sweeney, and A. Stohl. "Three-dimensional methane distribution simulated with FLEXPART 8-CTM-1.1 constrained with observation data." In: *Geoscientific Model Development* 11.11 (2018), pp. 4469–4487. DOI: 10.5194/gmd-11-4469-2018.

Guo, L., Y. Yang, P. J. Fraser, G. J. Velders, Z. Liu, D. Cui, J. Quan, Z. Cai, B. Yao, J. Hu, et al. "Projected increases in emissions of high global warming potential fluorinated gases in China." In: *Communications Earth & Environment* 4.1 (2023), p. 205. DOI: /10.1038/s43247-023-00859-6.

Gupta, J., X. Olsthoorn, and E. Rotenberg. "The role of scientific uncertainty in compliance with the Kyoto Protocol to the Climate Change Convention." In: *Environmental Science & Policy* 6.6 (2003), pp. 475–486. DOI: 10.1016/j.envsci.2003.09.001.

Gurney, K. R., R. M. Law, A. S. Denning, P. J. Rayner, D. Baker, P. Bousquet, L. Bruhwiler, Y.-H. Chen, P. Ciais, S. Fan, et al. "TransCom 3 CO2 inversion intercomparison: 1. Annual mean control results and sensitivity to transport and prior flux information." In: *Tellus B: Chemical and Physical Meteorology* 55.2 (2003), pp. 555–579. DOI: 10.3402/tellusb.v55i2.16728.

Guzzi, R., T. Colombo, and P. Paci. "Inverse problems in systems biology: A critical review." In: *Systems biology* 1702 (2018), pp. 69–94. DOI: 10.1007/978-1-4939-7456-6_6.

Hanna, S. "Applications in air pollution modeling." In: *Atmospheric Turbulence and Air Pollution Modelling*. Atmospheric Sciences Library, vol 1, Springer, 1984, pp. 275–310. DOI: 10.1007/978-94-010-9112-1_7.

Harnisch, J. and A. Eisenhauer. "Natural CF4 and SF6 on Earth." In: *Geophysical Research Letters* 25.13 (1998), pp. 2401–2404. DOI: 10.1029/98GL01779.

Harrison, J. J. "New infrared absorption cross sections for the infrared limb sounding of sulfur hexafluoride (SF6)." In: *Journal of Quantitative Spectroscopy and Radiative Transfer* 254 (2020), p. 107202. DOI: 10.1016/j.jqsrt.2020.107202.

Heise, H., R. Kurte, P. Fischer, D. Klockow, and P. Janissek. "Gas analysis by infrared spectroscopy as a tool for electrical fault diagnostics in SF6 insulated equipment." In: *Fresenius' journal of analytical chemistry* 358 (1997), pp. 793–799. DOI: 10.1007/s002160050511.

Henne, S., D. Brunner, B. Oney, M. Leuenberger, W. Eugster, I. Bamberger, F. Meinhardt, M. Steinbacher, and L. Emmenegger. "Validation of the Swiss methane emission inventory by atmospheric observations and inverse modelling." In: *Atmospheric Chemistry and Physics* 16.6 (2016), pp. 3683–3710. DOI: 10.5194/acp-16-3683-2016.

Ho, D. T., P. Schlosser, and T. Caplow. "Determination of longitudinal dispersion coefficient and net advection in the tidal Hudson River with a large-scale, high resolution SF6 tracer release experiment." In: *Environmental science & technology* 36.15 (2002), pp. 3234–3241. DOI: https://doi.org/10.1021/es015814+.

Hodak, S. K., T. Supasai, B. Paosawatyanyong, K. Kamlangkla, and V. Pavarajarn. "Enhancement of the hydrophobicity of silk fabrics by SF6 plasma." In: *Applied Surface Science* 254.15 (2008), pp. 4744–4749. DOI: 10.1016/j.apsusc.2008.01.110.

Horowitz, J. L. "Ill-posed inverse problems in economics." In: *Annu. Rev. Econ.* 6.1 (2014), pp. 21–51. DOI: 10.1146/annurev-economics-080213-041213.

Hort, N., B. Wiese, H. Dieringa, and K. U. Kainer. "Magnesium melt protection." In: *Materials Science Forum*. Vol. 828. Trans Tech Publ. 2015, pp. 78–81. DOI: 10.4028/www.scientific.net/MSF.828-829.78.

Hu, L., D. Ottinger, S. Bogle, S. A. Montzka, P. L. DeCola, E. Dlugokencky, A. Andrews, K. Thoning, C. Sweeney, G. Dutton, et al. "Declining, seasonal-varying emissions of sulfur hexafluoride from the United States." In: *Atmospheric Chemistry and Physics* 23.2 (2023), pp. 1437–1448. DOI: 10.5194/acp-23-1437-2023.

IEEE. "IEEE Guide for Sulphur Hexafluoride (SF6) Gas Handling for High-Voltage (over 1000 Vac) Equipment." In: *IEEE Std C37.122.3-2011* (2012), pp. 1–69. DOI: 10.1109/IEEESTD.2012.6127885.

IPCC. "Summary for Policymakers." In: *Climate Change 2021: The Physical Science Basis. Contribution of Working Group I to the Sixth Assessment Report of the Intergovernmental Panel on Climate Change*. Ed. by V. Masson-Delmotte, P. Zhai, A. Pirani, S. Connors, C. Péan, S. Berger, N. Caud, Y. Chen, L. Goldfarb, M. Gomis, M. Huang, K. Leitzell, E. Lonnoy, J. Matthews, T. Maycock, T. Waterfield, O. Yelekçi, R. Yu, and B. Zhou. Cambridge, United Kingdom and New York, NY, USA: Cambridge University Press, 2021, 332. DOI: 10.1017/9781009157896.001.

– "Summary for Policymakers." In: *Climate Change 2022: Mitigation of Climate Change. Contribution of Working Group III to the Sixth Assessment Report of the Intergovernmental Panel on Climate Change*. Ed. by P. Shukla, J. Skea, R. Slade, A. Al Khourdajie, R. van Diemen, D. McCollum, M. Pathak, S. Some, P. Vyas, R. Fradera, M. Belkacemi, A. Hasija, G. Lisboa, S. Luz, and J. Malley. Cambridge, UK and New York, NY, USA: Cambridge University Press, 2022. DOI: 10.1017/9781009157926.001.

Jacob, D. J. *Introduction to atmospheric chemistry*. Princeton university press, 1999, p. 81.

Jähn, M., G. Kuhlmann, Q. Mu, J.-M. Haussaire, D. Ochsner, K. Osterried, V. Clément, and D. Brunner. "An online emission module for atmospheric chemistry transport models: implementation in COSMO-GHG v5. 6a and COSMO-ART v5. 1-3.1." In: *Geoscientific Model Development* 13.5 (2020), pp. 2379–2392. DOI: 10.1016/j.atmosenv.2005.04.027.

Jingmin, W. and W. Dong. "Compromises of Bali Roadmap." In: *Chinese Journal of Population Resources and Environment* 6.3 (2008), pp. 27–32. DOI: 10.1080/10042857.2008.10684879.

Jones, A., D. Thomson, M. Hort, and B. Devenish. "The UK Met Office's next-generation atmospheric dispersion model, NAME III." In: *Air pollution modeling and its application XVII*. Springer, 2007, pp. 580–589. DOI: 10.1007/978-0-387-68854-1_62.

Kaminski, T., P. J. Rayner, M. Heimann, and I. G. Enting. "On aggregation errors in atmospheric transport inversions." In: *Journal of Geophysical Research: Atmospheres* 106.D5 (2001), pp. 4703–4715. DOI: 10.1029/2000JD900581.

Katharopoulos, I. "Advances in Inverse Modelling for the Estimation of Greenhouse Gas Emissions." PhD thesis. ETH Zurich, 2022. DOI: 10.3929/ethz-b-000578641.

Katharopoulos, I., D. Rust, M. K. Vollmer, D. Brunner, S. Reimann, S. J. O'Doherty, D. Young, K. M. Stanley, T. Schuck, J. Arduini, et al. "Impact of transport model resolution

and a priori assumptions on inverse modeling of Swiss F-gas emissions." In: *Atmospheric Chemistry and Physics* 23.22 (2023), pp. 14159–14186. DOI: 10.5194/acp-23-14159-2023.

Keller, C. A., M. Hill, M. K. Vollmer, S. Henne, D. Brunner, S. Reimann, S. O'Doherty, J. Arduini, M. Maione, Z. Ferenczi, et al. "European emissions of halogenated greenhouse gases inferred from atmospheric measurements." In: *Environmental science & technology* 46.1 (2012), pp. 217–225. DOI: 10.1021/es202453j.

Kim, J., R. Thompson, H. Park, S. Bogle, J. Mühle, M.-K. Park, Y. Kim, C. M. Harth, P. K. Salameh, R. Schmidt, et al. "Emissions of tetrafluoromethane (CF4) and hexafluoroethane (C2F6) from East Asia: 2008 to 2019." In: *Journal of Geophysical Research: Atmospheres* 126.16 (2021), e2021JD034888. DOI: 10.1029/2021JD034888.

Klemm, W. and P. Henkel. "Über einige physikalische Eigenschaften von SF6, SeF6, TeF6 und CF4." In: *Zeitschrift für anorganische und allgemeine Chemie* 207.1 (1932), pp. 73–86. DOI: 10.1002/zaac.19322070107.

– "Das Brechungsvermögen einiger gasförmiger Fluoride." In: *Zeitschrift für anorganische und allgemeine Chemie* 213.1-2 (1933), pp. 115–125. DOI: 10.1002/zaac.19332130112.

Ko, M. K., N. D. Sze, W.-C. Wang, G. Shia, A. Goldman, F. J. Murcray, D. G. Murcray, and C. P. Rinsland. "Atmospheric sulfur hexafluoride: Sources, sinks and greenhouse warming." In: *Journal of Geophysical Research: Atmospheres* 98.D6 (1993), pp. 10499–10507. DOI: 10.1029/93JD00228.

Koch, E.-C. "Special materials in pyrotechnics: III. Application of lithium and its compounds in energetic systems." In: *Propellants, Explosives, Pyrotechnics: An International Journal Dealing with Scientific and Technological Aspects of Energetic Materials* 29.2 (2004), pp. 67–80. DOI: 10.1002/prep.200400032.

Koch, H. "Basic information on Gas Insulated Transmission lines (GIL)." In: *2008 IEEE Power and Energy Society General Meeting - Conversion and Delivery of Electrical Energy in the 21st Century*. 2008, pp. 1–4. DOI: 10.1109/PES.2008.4596485.

Koch, H., F. Goll, T. Magier, and K. Juhre. "Technical aspects of gas insulated transmission lines and application of new insulating gases." In: *IEEE Transactions on Dielectrics and Electrical Insulation* 25.4 (2018), pp. 1448–1453. DOI: 10.1109/TDEI.2018.007311.

Koch, H. J. *Gas insulated transmission lines (GIL)*. John Wiley & Sons, 2011, pp. 39–40.

Kovács, T., W. Feng, A. Totterdill, J. Plane, S. Dhomse, J. C. Gómez-Martín, G. P. Stiller, F. J. Haenel, C. Smith, P. M. Forster, et al. "Determination of the atmospheric lifetime and global warming potential of sulfur hexafluoride using a three-dimensional model." In: *Atmospheric Chemistry and Physics* 17.2 (2017), pp. 883–898. DOI: 10.5194/acp-17-883-2017.

Koyama, Y., S. Maksyutov, H. Mukai, K. Thoning, and P. Tans. "Simulation of variability in atmospheric carbon dioxide using a global coupled Eulerian–Lagrangian transport model." In: *Geoscientific Model Development* 4.2 (2011), pp. 317–324. DOI: 10.5194/gmd-4-317-2011.

Kunze, D., E. Binder, J. Türk, S. Pöhler, and J. Alter. "Gas-Insulated Transmission Lines—Underground Power Transmission Achieving a Maximum of Operational Safety and Reliability." In: *Proceedings of the International Conference on Insulated Power Cables (JICABLE'07)*. 2007. URL: http://www.jicable.org/2007/Actes/Session_A3/JIC07_A36.pdf (visited on 04/28/2024).

Lal, R. "Soil carbon sequestration impacts on global climate change and food security." In: *science* 304.5677 (2004), pp. 1623–1627. DOI: 10.1126/science.1097396.

Lan, X., K. Thoning, and E. Dlugokencky. *Trends in globally-averaged CH4, N2O, and SF6 determined from NOAA Global Monitoring Laboratory measurements. Version 2024-02*. 2024. DOI: 10.15138/P8XG-AA10. (Visited on 02/19/2024).

Lee, G., H. Choi, J. Kim, J. Mühle, M. Vojta, S. O'Doherty, P. B. Krummel, R. F. Weiss, A. Stohl, and S. Park. *Atmospheric observation-based SF6 emissions in East Asia: comparison of top-down and bottom-up estimates*. Forthcoming.

Lee, H. J., T.-J. Yoon, and Y. I. Yoon. "Synthesis of ultrasound contrast agents: characteristics and size distribution analysis (secondary publication)." In: *Ultrasonography* 36.4 (2017), p. 378. DOI: 10.14366/usg.17014.

Lee, H. M., M. B. Chang, and K. Y. Wu. "Abatement of sulfur hexafluoride emissions from the semiconductor manufacturing process by atmospheric-pressure plasmas." In: *Journal of the Air & Waste Management Association* 54.8 (2004), pp. 960–970. DOI: 10.1080/10473289.2004.10470963.

Leeds, W., T. Browne, and A. Strom. "The use of SF 6 for high-power arc quenching." In: *Electrical Engineering* 76.9 (1957), pp. 788–791. DOI: 10.1109/EE.1957.6442711.

Leip, A., U. Skiba, A. Vermeulen, and R. L. Thompson. "A complete rethink is needed on how greenhouse gas emissions are quantified for national reporting." In: *Atmospheric Environment* 174 (2017), pp. 237–240. DOI: 10.1016/j.atmosenv.2017.12.006.

Levin, I., T. Naegler, R. Heinz, D. Osusko, E. Cuevas, A. Engel, J. Ilmberger, R. L. Langenfelds, B. Neininger, C. v. Rohden, et al. "The global SF 6 source inferred from long-term high precision atmospheric measurements and its comparison with emission inventories." In: *Atmospheric Chemistry and Physics* 10.6 (2010), pp. 2655–2662. DOI: 10.5194/acp-10-2655-2010.

Levy, J. I., J. D. Spengler, D. Hlinka, D. Sullivan, and D. Moon. "Using CALPUFF to evaluate the impacts of power plant emissions in Illinois: model sensitivity and implications." In: *Atmospheric Environment* 36.6 (2002), pp. 1063–1075. DOI: 10.1016/S1352-2310(01)00493-9.

Lichter, K. E., J. R. Bloom, R.-D. Sheu, L. T. Zalavari, K. Leung, A. Collins, A. Witztum, and R. Chuter. "Tracking and Reducing SF6 Usage in Radiation Oncology: A Step Toward Net-Zero Health Care Emissions." In: *Practical Radiation Oncology* 13.6 (2023), e471–e474. DOI: 10.1016/j.prro.2023.06.003.

Lin, J. C. "Lagrangian Modeling of the Atmosphere: An Introduction." In: *Lagrangian Modeling of the Atmosphere*. Ed. by J. Lin, D. Brunner, C. Gerbig, A. Stohl, A. Luhar, and P. Webley. 2012. DOI: 10.1029/2012GM001376.

Locatelli, R., P. Bousquet, F. Chevallier, A. Fortems-Cheney, S. Szopa, M. Saunois, A. Agusti-Panareda, D. Bergmann, H. Bian, P. Cameron-Smith, et al. "Impact of transport model errors on the global and regional methane emissions estimated by inverse modelling." In: *Atmospheric Chemistry and Physics* 13.19 (2013), pp. 9917–9937. DOI: 10.5194/acp-13-9917-2013.

Lunt, M. F., M. Rigby, A. L. Ganesan, and A. J. Manning. "Estimation of trace gas fluxes with objectively determined basis functions using reversible-jump Markov chain Monte Carlo." In: *Geoscientific Model Development* 9.9 (2016), pp. 3213–3229. DOI: 10.5194/gmd-9-3213-2016.

Maione, M., F. Graziosi, J. Arduini, F. Furlani, U. Giostra, D. R. Blake, P. Bonasoni, X. Fang, S. A. Montzka, S. J. O'Doherty, et al. "Estimates of European emissions of methyl chloroform using a Bayesian inversion method." In: *Atmospheric Chemistry and Physics* 14.18 (2014), pp. 9755–9770. DOI: 10.5194/acp-14-9755-2014.

Maiss, M. and C. A. Brenninkmeijer. "Atmospheric SF6: trends, sources, and prospects." In: *Environmental Science & Technology* 32.20 (1998), pp. 3077–3086. DOI: 10.1021/es9802807.

Maiss, M., L. P. Steele, R. J. Francey, P. J. Fraser, R. L. Langenfelds, N. B. Trivett, and I. Levin. "Sulfur hexafluoride—A powerful new atmospheric tracer." In: *Atmospheric environment* 30.10-11 (1996), pp. 1621–1629. DOI: 10.1016/1352-2310(95)00425-4.

Manning, A., A. Redington, S. O'Doherty, D. Say, D. Young, T. Arnold, C. Rennick, M. Rigby, A. Wisher, and P. Simmonds. *Long-Term Atmospheric Measurement and Interpretation of Radiatively Active Trace Gases, Annual Report (September 2019 to August 2020)*. 2022. URL: https://assets.publishing.service.gov.uk/media/62d7b9bee90e071e7e59c97e/verification-uk-greenhouse-gas-emissions-using-atmospheric-observations-annual-report-2021.pdf (visited on 04/28/2024).

Manning, A. J., A. L. Redington, D. Say, S. O'Doherty, D. Young, P. G. Simmonds, M. K. Vollmer, J. Mühle, J. Arduini, G. Spain, et al. "Evidence of a recent decline in UK emissions of hydrofluorocarbons determined by the InTEM inverse model and atmospheric measurements." In: *Atmospheric Chemistry and Physics* 21.16 (2021), pp. 12739–12755. DOI: 10.5194/acp-21-12739-2021.

Martin, D., K. Petersson, and D. Shallcross. "The use of cyclic perfluoroalkanes and SF6 in atmospheric dispersion experiments." In: *Quarterly Journal of the Royal Meteorological Society* 137.661 (2011), pp. 2047–2063. DOI: 10.1002/qj.881.

Martinsson, J., G. Monteil, M. K. Sporre, A. M. Kaldal Hansen, A. Kristensson, K. Eriksson Stenström, E. Swietlicki, and M. Glasius. "Exploring sources of biogenic secondary organic aerosol compounds using chemical analysis and the FLEXPART model." In: *Atmospheric Chemistry and Physics* 17.18 (2017), pp. 11025–11040. DOI: 10.5194/acp-17-11025-2017.

Massachusetts. *310 CMR 7.72 Reducing Sulfur Hexafluoride Emissions from Gas-Insulated Switchgear*. 2021. URL: https://www.mass.gov/doc/310-cmr-772-final-sf6-regulation/download (visited on 04/28/2024).

McGrath, M. *Climate change: Electrical industry's 'dirty secret' boosts warming*. BBC, 13 September 2019. URL: https://www.bbc.com/news/science-environment-49567197?ref=WindEurope (visited on 04/27/2024).

McNider, R. T., M. D. Moran, and R. A. Pielke. "Influence of diurnal and inertial boundary-layer oscillations on long-range dispersion." In: *Atmospheric Environment (1967)* 22.11 (1988), pp. 2445–2462. DOI: 10.1016/0004-6981(88)90476-3.

Menut, L., B. Bessagnet, R. Briant, A. Cholakian, F. Couvidat, S. Mailler, R. Pennel, G. Siour, P. Tuccella, S. Turquety, et al. "The CHIMERE v2020r1 online chemistry-transport model." In: *Geoscientific Model Development* 14.11 (2021), pp. 6781–6811. DOI: 10.5194/gmd-14-6781-2021.

Michalak, A. M., A. Hirsch, L. Bruhwiler, K. R. Gurney, W. Peters, and P. P. Tans. "Maximum likelihood estimation of covariance parameters for Bayesian atmospheric trace gas surface flux inversions." In: *Journal of Geophysical Research: Atmospheres* 110.D24 (2005). DOI: 10.1029/2005JD005970.

Monteil, G. and M. Scholze. "Regional CO 2 inversions with LUMIA, the Lund University modular inversion algorithm, v1. 0." In: *Geoscientific Model Development* 14.6 (2021), pp. 3383–3406. DOI: 10.5194/gmd-14-3383-2021.

Morris, R. A., T. M. Miller, A. Viggiano, J. F. Paulson, S. Solomon, and G. Reid. "Effects of electron and ion reactions on atmospheric lifetimes of fully fluorinated compounds." In: *Journal of Geophysical Research: Atmospheres* 100.D1 (1995), pp. 1287–1294. DOI: 10.1029/94JD02399.

Myhre, G., D. Shindell, F.-M. Bréon, W. Collins, J. Fuglestvedt, J. Huang, D. Koch, J.-F. Lamarque, D. Lee, B. Mendoza, T. Nakajima, A. Robock, G. Stephens, T. Takemura, and H. Zhang. "Anthropogenic and natural radiative forcing." In: *Climate Change 2013: The Physical Science Basis. Contribution of Working Group I to the Fifth Assessment Report of the Intergovernmental Panel on Climate Change*. Ed. by T. F. Stocker, D. Qin, G.-K. Plattner, M. Tignor, S. K. Allen, J. Doschung, A. Nauels, Y. Xia, V. Bex, and

P. M. Midgley. Cambridge, UK: Cambridge University Press, 2013, pp. 659–740. DOI: 10.1017/CBO9781107415324.018.

Ni, J., S.-S. Liu, X.-P. Lang, Z. He, and G.-P. Yang. "Sulfur hexafluoride in the marine atmosphere and surface seawater of the Western Pacific and Eastern Indian Ocean." In: *Environmental Pollution* 335 (2023), p. 122266. DOI: 10.1016/j.envpol.2023.122266.

Nilsson, S., M. Jonas, M. Obersteiner, and D. G. Victor. "Verification: The gorilla in the struggle to slow global warming." In: *The Forestry Chronicle* 77.3 (2001), pp. 475–478. DOI: 10.5558/tfc77475-3.

Nisbet, E. and R. Weiss. "Top-down versus bottom-up." In: *Science* 328.5983 (2010), pp. 1241–1243. DOI: 10.1126/science.1189936.

Okofo, L. B., M.-G. Adonadaga, and M. Martienssen. "Groundwater age dating using multi-environmental tracers (SF6, CFC-11, CFC-12, δ18O, and δD) to investigate groundwater residence times and recharge processes in Northeastern Ghana." In: *Journal of Hydrology* 610 (2022), p. 127821. DOI: 10.1016/j.jhydrol.2022.127821.

Oney, B., N. Gruber, S. Henne, M. Leuenberger, and D. Brunner. "A CO-based method to determine the regional biospheric signal in atmospheric CO2." In: *Tellus B: Chemical and Physical Meteorology* 69.1 (2017), p. 1353388. DOI: 10.1080/16000889.2017.1353388.

Ottinger, D., M. Averyt, and D. Harris. "US consumption and supplies of sulphur hexafluoride reported under the greenhouse gas reporting program." In: *Journal of Integrative Environmental Sciences* 12 (2015), pp. 5–16. DOI: 10.1080/1943815X.2015.1092452.

Owens, J., A. Xiao, J. Bonk, M. DeLorme, and A. Zhang. "Recent development of two alternative gases to SF6 for high voltage electrical power applications." In: *Energies* 14.16 (2021), p. 5051. DOI: 10.3390/en14165051.

Özgönenel, O., D. Thomas, and Ü. Kurt. "SF6 gas-insulated 50-kVA distribution transformer design." In: *Turkish Journal of Electrical Engineering and Computer Sciences* 26.4 (2018), pp. 2140–2150. DOI: 10.3906/elk-1708-28.

Pan, Y., R. A. Birdsey, J. Fang, R. Houghton, P. E. Kauppi, W. A. Kurz, O. L. Phillips, A. Shvidenko, S. L. Lewis, J. G. Canadell, et al. "A large and persistent carbon sink in the world's forests." In: *Science* 333.6045 (2011), pp. 988–993. DOI: 10.1126/science.1201609.

Paris, J.-D., A. Stohl, P. Nédélec, M. Y. Arshinov, M. Panchenko, V. Shmargunov, K. S. Law, B. Belan, and P. Ciais. "Wildfire smoke in the Siberian Arctic in summer: source characterization and plume evolution from airborne measurements." In: *Atmospheric Chemistry and Physics* 9.23 (2009), pp. 9315–9327. DOI: 10.5194/acp-9-9315-2009.

Patra, P. K., S. Lal, B. Subbaraya, C. H. Jackman, and P. Rajaratnam. "Observed vertical profile of sulphur hexafluoride (SF6) and its atmospheric applications." In: *Journal of*

Geophysical Research: Atmospheres 102.D7 (1997), pp. 8855–8859. DOI: 10.1029/96JD03503.

Pedersen, P. H. *Ways of reducing consumption and emission of potent greenhouse gases (HFCs, PFCs and SF6)*. Nordic Council of Ministers, 2000, pp. 65–66.

Pisso, I., E. Sollum, H. Grythe, N. I. Kristiansen, M. Cassiani, S. Eckhardt, D. Arnold, D. Morton, R. L. Thompson, C. D. Groot Zwaaftink, et al. "The Lagrangian particle dispersion model FLEXPART version 10.4." In: *Geoscientific Model Development* 12.12 (2019), pp. 4955–4997. DOI: 10.5194/gmd-12-4955-2019.

Powell, R. L. "CFC phase-out: have we met the challenge?" In: *Journal of fluorine chemistry* 114.2 (2002), pp. 237–250. DOI: 10.1016/S0022-1139(02)00030-1.

Prideaux, E. B. R. "XXXV.—Some reactions and new compounds of fluorine." In: *Journal of the Chemical Society, Transactions* 89 (1906), pp. 316–332. DOI: 10.1039/CT9068900316.

Pugh, T., M. Cain, J. Methven, O. Wild, S. Arnold, E. Real, K. S. Law, K. Emmerson, S. Owen, J. Pyle, et al. "A Lagrangian model of air-mass photochemistry and mixing using a trajectory ensemble: the Cambridge Tropospheric Trajectory model of Chemistry And Transport (CiTTyCAT) version 4.2." In: *Geoscientific Model Development* 5.1 (2012), pp. 193–221. DOI: 10.5194/gmd-5-193-2012.

Purohit, P. private communication. 24.03. 2024.

Purohit, P. and L. Höglund-Isaksson. "Global emissions of fluorinated greenhouse gases 2005–2050 with abatement potentials and costs." In: *Atmospheric Chemistry and Physics* 17.4 (2017), pp. 2795–2816. DOI: 10.5194/acp-17-2795-2017.

Rabie, M. and C. M. Franck. "Assessment of eco-friendly gases for electrical insulation to replace the most potent industrial greenhouse gas SF6." In: *Environmental science & technology* 52.2 (2018), pp. 369–380. DOI: 10.1021/acs.est.7b03465.

Ramsden, A. E., A. L. Ganesan, L. M. Western, M. Rigby, A. J. Manning, A. Foulds, J. L. France, P. Barker, P. Levy, D. Say, et al. "Quantifying fossil fuel methane emissions using observations of atmospheric ethane and an uncertain emission ratio." In: *Atmospheric Chemistry and Physics* 22.6 (2022), pp. 3911–3929. DOI: 10.5194/acp-22-3911-2022.

Ravishankara, A., S. Solomon, A. A. Turnipseed, and R. Warren. "Atmospheric lifetimes of long-lived halogenated species." In: *Science* 259.5092 (1993), pp. 194–199. DOI: 10.1126/science.259.5092.194.

Ray, E. A., F. L. Moore, J. W. Elkins, K. H. Rosenlof, J. C. Laube, T. Röckmann, D. R. Marsh, and A. E. Andrews. "Quantification of the SF6 lifetime based on mesospheric loss measured in the stratospheric polar vortex." In: *Journal of Geophysical Research: Atmospheres* 122.8 (2017), pp. 4626–4638. DOI: 10.1002/2016JD026198.

Rigby, M., A. Manning, and R. Prinn. "Inversion of long-lived trace gas emissions using combined Eulerian and Lagrangian chemical transport models." In: *Atmospheric Chemistry and Physics* 11.18 (2011), pp. 9887–9898. DOI: 10.5194/acp-11-9887-2011.

Rigby, M., R. Prinn, S. O'Doherty, S. Montzka, A. McCulloch, C. Harth, J. Mühle, P. Salameh, R. Weiss, D. Young, et al. "Re-evaluation of the lifetimes of the major CFCs and CH_3CCl_3 using atmospheric trends." In: *Atmospheric Chemistry and Physics* 13.5 (2013), pp. 2691–2702. DOI: 10.5194/acp-13-2691-2013.

Rigby, M. et al. "History of atmospheric SF_6; from 1973 to 2008." en. In: *Atmospheric Chemistry and Physics* 10.21 (Nov. 2010), pp. 10305–10320. ISSN: 1680-7324. DOI: 10.5194/acp-10-10305-2010. URL: https://acp.copernicus.org/articles/10/10305/2010/ (visited on 04/16/2021).

Rödenbeck, C., C. Gerbig, K. Trusilova, and M. Heimann. "A two-step scheme for high-resolution regional atmospheric trace gas inversions based on independent models." In: *Atmospheric Chemistry and Physics* 9.14 (2009), pp. 5331–5342. DOI: 10.5194/acp-9-5331-2009.

Rößler, T., M. Albert, R. Terasa, and J. Bartha. "Alternative etching gases to SF6 for plasma enhanced chamber cleaning in silicon deposition systems." In: *Surface and Coatings Technology* 200.1-4 (2005), pp. 552–555. DOI: 10.1016/j.surfcoat.2005.02.183.

Ruckstuhl, A. F., S. Henne, S. Reimann, M. Steinbacher, M. K. Vollmer, S. O'Doherty, B. Buchmann, and C. Hueglin. "Robust extraction of baseline signal of atmospheric trace species using local regression." In: *Atmospheric Measurement Techniques* 5.11 (2012), pp. 2613–2624. DOI: 10.5194/amt-5-2613-2012.

Rypdal, K., F. Stordal, J. Fuglestvedt, and T. Berntsen. "Introducing top-down methods in assessing compliance with the Kyoto Protocol." In: *Climate Policy* 5.4 (2005), pp. 393–405. DOI: 10.1080/14693062.2005.9685565.

Rypdal, K. and W. Winiwarter. "Uncertainties in greenhouse gas emission inventories—evaluation, comparability and implications." In: *Environmental Science & Policy* 4.2-3 (2001), pp. 107–116. DOI: 10.1016/S1462-9011(00)00113-1.

Sabine, C. L., R. A. Feely, N. Gruber, R. M. Key, K. Lee, J. L. Bullister, R. Wanninkhof, C. Wong, D. W. Wallace, B. Tilbrook, et al. "The oceanic sink for anthropogenic CO2." In: *science* 305.5682 (2004), pp. 367–371. DOI: 10.1126/science.1097403.

Saikawa, E., M. Rigby, R. G. Prinn, S. A. Montzka, B. R. Miller, L. J. Kuijpers, P. J. Fraser, M. K. Vollmer, T. Saito, Y. Yokouchi, et al. "Global and regional emission estimates for HCFC-22." In: *Atmospheric Chemistry and Physics* 12.21 (2012), pp. 10033–10050. DOI: 10.5194/acp-12-10033-2012.

Saito, T., Y. Yokouchi, A. Stohl, S. Taguchi, and H. Mukai. "Large emissions of perfluorocarbons in East Asia deduced from continuous atmospheric measurements." In: *Environmental science & technology* 44.11 (2010), pp. 4089–4095. DOI: 10.1021/es1001488.

Say, D., A. J. Manning, L. M. Western, D. Young, A. Wisher, M. Rigby, S. Reimann, M. K. Vollmer, M. Maione, J. Arduini, P. B. Krummel, J. Mühle, C. M. Harth, B. Evans, R. F. Weiss, R. G. Prinn, and S. O'Doherty. "Global trends and European emissions of tetrafluoromethane (CF_4), hexafluoroethane (C_2F_6) and octafluoropropane (C_3F_8)." In: *Atmospheric Chemistry and Physics* 21.3 (2021), pp. 2149–2164. DOI: 10.5194/acp-21-2149-2021.

Say, D., A. L. Ganesan, M. F. Lunt, M. Rigby, S. O'doherty, C. Harth, A. J. Manning, P. B. Krummel, and S. Bauguitte. "Emissions of halocarbons from India inferred through atmospheric measurements." In: *Atmospheric Chemistry and Physics* 19.15 (2019), pp. 9865–9885. DOI: 10.5194/acp-19-9865-2019.

Schoenenberger, F., S. Henne, M. Hill, M. K. Vollmer, G. Kouvarakis, N. Mihalopoulos, S. O'Doherty, M. Maione, L. Emmenegger, T. Peter, et al. "Abundance and sources of atmospheric halocarbons in the Eastern Mediterranean." In: *Atmospheric Chemistry and Physics* 18.6 (2018), pp. 4069–4092. DOI: 10.5194/acp-18-4069-2018.

Schreiber, W. G., B. Eberle, S. Laukemper-Ostendorf, K. Markstaller, N. Weiler, A. Scholz, K. Bürger, C. P. Heussel, M. Thelen, and H.-U. Kauczor. "Dynamic 19F-MRI of pulmonary ventilation using sulfur hexafluoride (SF6) gas." In: *Magnetic Resonance in Medicine: An Official Journal of the International Society for Magnetic Resonance in Medicine* 45.4 (2001), pp. 605–613. DOI: 10.1002/mrm.1082.

Schumb, W. "Preparation and properties of sulfur hexafluoride." In: *Industrial & Engineering Chemistry* 39.3 (1947), pp. 421–423. DOI: 10.1021/ie50447a642.

Schwaab, K. "Emissions Reduction Potentials for SF6 in Germany." In: *Conference Paper (EPA): SF6 and the environment: Emission reduction strategies.* Citeseer. 2000. URL: https://citeseerx.ist.psu.edu/document?repid=rep1&type=pdf&doi=d885668be934608b9a54db7ac2dc9ecdcda6b26a (visited on 04/28/2024).

Schwarz, W. *Emissions, activity data, and emission factors of fluorinated greenhouse gases (F-Gases) in Germany 1995-2002, Research Report 201 41 261/01, UBA-FB 000811/e, Umweltbundesamt, Berlin*. 2005. URL: https://www.osti.gov/etdeweb/biblio/21154958 (visited on 04/28/2024).

Schwarz, W. and B. Gschrey. "Service contract to assess the feasibility of options to reduce emissions of SF6 from the EU non-ferrous metal industry and analyse their potential impacts." In: *Öko-Recherche, Frankfurt* (2009). URL: http://www.oekorecherche.de/sites/default/files/publikationen/sf6-nf-metal.pdf (visited on 04/28/2024).

Seibert, P. and A. Frank. "Source-receptor matrix calculation with a Lagrangian particle dispersion model in backward mode." In: *Atmospheric Chemistry and Physics* 4.1 (2004), pp. 51–63. DOI: 10.5194/acp-4-51-2004.

Sellitto, P., G. Salerno, S. Corradini, I. Xueref-Remy, A. Riandet, C. Bellon, S. Khaykin, G. Ancellet, S. Lolli, E. J. Welton, et al. "Volcanic emissions, plume dispersion, and downwind radiative impacts following Mount Etna series of eruptions of February 21–26,

2021." In: *Journal of Geophysical Research: Atmospheres* 128.6 (2023), e2021JD035974. DOI: 10.1029/2021JD035974.

Shadloo, M. S., G. Oger, and D. Le Touzé. "Smoothed particle hydrodynamics method for fluid flows, towards industrial applications: Motivations, current state, and challenges." In: *Computers & Fluids* 136 (2016), pp. 11–34. DOI: 10.1016/j.compfluid.2016.05.029.

Sheldon, D. J. and M. R. Crimmin. "Repurposing of F-gases: challenges and opportunities in fluorine chemistry." In: *Chemical Society Reviews* 51.12 (2022), pp. 4977–4995. DOI: 10.1039/d1cs01072g.

Shida, T. *The chemical bond: a fundamental quantum-mechanical picture*. Vol. 76. Springer Science & Business Media, 2013, pp. 187–188.

Shirai, T., Y. Yokouchi, S. Sugata, and S. Maksyutov. "HCFC-22 flux estimates over East Asia by inverse modeling from hourly observations at Hateruma monitoring station." In: *Journal of Geophysical Research: Atmospheres* 115.D15 (2010). DOI: 10.1029/2009JD012858.

Simmonds, P. G., M. Rigby, A. J. Manning, S. Park, K. M. Stanley, A. McCulloch, S. Henne, F. Graziosi, M. Maione, J. Arduini, et al. "The increasing atmospheric burden of the greenhouse gas sulfur hexafluoride (SF 6)." In: *Atmospheric Chemistry and Physics* 20.12 (2020), pp. 7271–7290. DOI: 10.5194/acp-20-7271-2020.

Simmonds, P. G., M. Rigby, A. McCulloch, S. O'Doherty, D. Young, J. Mühle, P. B. Krummel, P. Steele, P. J. Fraser, A. J. Manning, et al. "Changing trends and emissions of hydrochlorofluorocarbons (HCFCs) and their hydrofluorocarbon (HFCs) replacements." In: *Atmospheric Chemistry and Physics* 17.7 (2017), pp. 4641–4655. DOI: 10.5194/acp-17-4641-2017.

Simmonds, P. G., M. Rigby, A. McCulloch, M. K. Vollmer, S. Henne, J. Mühle, S. O'Doherty, A. J. Manning, P. B. Krummel, P. J. Fraser, et al. "Recent increases in the atmospheric growth rate and emissions of HFC-23 (CHF_3) and the link to HCFC-22 ($CHClF_2$) production." In: *Atmospheric Chemistry and Physics* 18.6 (2018), pp. 4153–4169. DOI: 10.5194/acp-18-4153-2018.

Smith, C., Z. Nicholls, K. Armour, W. Collins, P. Forster, M. Meinshausen, M. Palmer, and M. Watanabe. *The Earth's Energy Budget, Climate Feedbacks, and Climate Sensitivity Supplementary Material. In Climate Change 2021: The Physical Science Basis. Contribution of Working Group I to the Sixth Assessment Report of the Intergovernmental Panel on Climate Change [Masson-Delmotte, V., P. Zhai, A. Pirani, S.L. Connors, C. Péan, S. Berger, N. Caud, Y. Chen, L. Goldfarb, M.I. Gomis, M. Huang, K. Leitzell, E. Lonnoy, J.B.R. Matthews, T.K. Maycock, T. Waterfield, O. Yelekçi, R. Yu, and B. Zhou (eds.)]. Available from https://www.ipcc.ch*. 2021. URL: https://www.ipcc.ch/report/ar6/wg1/downloads/report/IPCC_AR6_WGI_Chapter07_SM.pdf (visited on 04/28/2024).

Solvay. *Sulphur Hexafluoride, technical report, Solvay Special Chemicals*. 2018. URL: https://www.solvay.com/sites/g/files/srpend221/files/2018-08/SF6-Sulphur-Hexafluoride_0.pdf (visited on 04/28/2024).

State of Maine. *An Act To Stop Perfluoroalkyl and Polyfluoroalkyl Substances Pollution*. Law LD 1503, 130th Legislature. 2021. URL: https://www.mainelegislature.org/legis/bills/getPDF.asp?paper=HP1113&item=5&snum=130 (visited on 04/28/2024).

Stein, A. F., R. R. Draxler, G. D. Rolph, B. J. Stunder, M. D. Cohen, and F. Ngan. "NOAA's HYSPLIT atmospheric transport and dispersion modeling system." In: *Bulletin of the American Meteorological Society* 96.12 (2015), pp. 2059–2077. DOI: 10.1175/BAMS-D-14-00110.1.

Stohl, A., J. Kim, S. Li, S. O'Doherty, B. Yao, Y. Yokouchi, and L. X. Zhou. "Hydrochlorofluorocarbon and hydrofluorocarbon emissions in East Asia determined by inverse modeling." English. In: *Atmospheric Chemistry and Physics* 10.8 (2010), pp. 3545–3560. DOI: 10.5194/acp-10-3545-2010.

Stohl, A., P. Seibert, J. Arduini, S. Eckhardt, P. Fraser, B. Greally, C. Lunder, M. Maione, J. Mühle, S. O'doherty, et al. "An analytical inversion method for determining regional and global emissions of greenhouse gases: Sensitivity studies and application to halocarbons." In: *Atmospheric Chemistry and Physics* 9.5 (2009), pp. 1597–1620. DOI: 10.5194/acp-9-1597-2009.

Stohl, A. "Computation, accuracy and applications of trajectories—A review and bibliography." In: *Atmospheric Environment* 32.6 (1998), pp. 947–966. DOI: 10.1016/S1352-2310(97)00457-3.

Stohl, A., C. Forster, A. Frank, P. Seibert, and G. Wotawa. "The Lagrangian particle dispersion model FLEXPART version 6.2." In: *Atmospheric Chemistry and Physics* 5.9 (2005), pp. 2461–2474. DOI: 10.5194/acp-5-2461-2005.

Stohl, A. and D. J. Thomson. "A density correction for Lagrangian particle dispersion models." In: *Boundary-Layer Meteorology* 90 (1999), pp. 155–167. DOI: 10.1023/A:1001741110696.

Stohl, A. and G. Wotawa. "A method for computing single trajectories representing boundary layer transport." In: *Atmospheric Environment* 29.22 (1995), pp. 3235–3238. DOI: doi.org/10.1016/1352-2310(95)00259-2.

Tanhua, T., K. A. Olsson, and E. Fogelqvist. "A first study of SF6 as a transient tracer in the Southern Ocean." In: *Deep Sea Research Part II: Topical Studies in Oceanography* 51.22-24 (2004), pp. 2683–2699. DOI: 10.1016/j.dsr2.2001.02.001.

Tarantola, A. "Inverse Problem Theory and Methods for Model Parameter Estimation." In: Society for Industrial and Applied Mathematics, 2005, pp. 1–67. DOI: 10.1137/1.9780898717921.

Thompson, R. L., M. Sasakawa, T. Machida, T. Aalto, D. Worthy, J. V. Lavric, C. Lund Myhre, and A. Stohl. "Methane fluxes in the high northern latitudes for 2005–2013 estimated using a Bayesian atmospheric inversion." In: *Atmospheric Chemistry and Physics* 17.5 (2017), pp. 3553–3572. DOI: 10.5194/acp-17-3553-2017.

Thompson, R. L. and A. Stohl. "FLEXINVERT: an atmospheric Bayesian inversion framework for determining surface fluxes of trace species using an optimized grid." In: *Geoscientific Model Development* 7.5 (2014), pp. 2223–2242. DOI: 10.5194/gmd-7-2223-2014.

Thomson, D. J. "Criteria for the selection of stochastic models of particle trajectories in turbulent flows." In: *Journal of Fluid Mechanics* 180 (1987), pp. 529–556. DOI: 10.1017/S0022112087001940.

Toda, K. "Structural features of gas insulated transformers." In: *IEEE/PES Transmission and Distribution Conference and Exhibition*. Vol. 1. 2002, pp. 508–510. DOI: 10.1109/TDC.2002.1178435.

Trusilova, K., C. Rödenbeck, C. Gerbig, and M. Heimann. "A new coupled system for global-to-regional downscaling of CO_2 concentration estimation." In: *Atmospheric Chemistry and Physics* 10.7 (2010), pp. 3205–3213. DOI: 10.5194/acp-10-3205-2010.

United Nations Framework Convention on Climate Change. *Kyoto Protocol to the United Nations Framework Convention on Climate Change*. U.N. Doc. FCCC/CP/1997/L.7/Add.1. 1997. URL: https://unfccc.int/sites/default/files/resource/docs/cop3/l07a01.pdf#page=24 (visited on 04/28/2024).

– *Bali Road Map*. 2007. URL: https://www.undp.org/sites/g/files/zskgke326/files/publications/Bali_Road_Map_Key_Issues_Under_Negotiation.pdf (visited on 04/28/2024).
– *Report of the Conference of the Parties on its fifteenth session, held in Copenhagen from 7 to 19 December 2009*. 2009. URL: https://unfccc.int/resource/docs/2009/cop15/eng/11a01.pdf (visited on 04/28/2024).
– *Paris Agreement. Conference of the Parties to the United Nations Framework Convention on Climate Change, 21st Session, December 2015, Paris,* 2015. URL: https://unfccc.int/files/meetings/paris_nov_2015/application/pdf/paris_agreement_english_.pdf (visited on 04/28/2024).

Velders, G. J., J. S. Daniel, S. A. Montzka, I. Vimont, M. Rigby, P. B. Krummel, J. Muhle, S. O'Doherty, R. G. Prinn, R. F. Weiss, et al. "Projections of hydrofluorocarbon (HFC) emissions and the resulting global warming based on recent trends in observed abundances and current policies." In: *Atmospheric Chemistry and Physics* 22.9 (2022), pp. 6087–6101. DOI: 10.5194/acp-22-6087-2022.

Vojta, M., A. Plach, S. Annadate, S. Park, G. Lee, P. Purohit, F. Lindl, X. Lan, J. Mühle, R. L. Thompson, and A. Stohl. "A global re-analysis of regionally resolved emissions and atmospheric mole fractions of SF_6 for the period 2005–2021." In: *EGUsphere* 2024 (2024), pp. 1–48. DOI: 10.5194/egusphere-2024-811.

Vojta, M., A. Plach, R. L. Thompson, and A. Stohl. "A comprehensive evaluation of the use of Lagrangian particle dispersion models for inverse modeling of greenhouse gas emissions." In: *Geoscientific Model Development* 15.22 (2022), pp. 8295–8323. DOI: 10.5194/gmd-15-8295-2022.

Vollmer, M. K., J. Mühle, C. M. Trudinger, M. Rigby, S. A. Montzka, C. M. Harth, B. R. Miller, S. Henne, P. B. Krummel, B. D. Hall, et al. "Atmospheric histories and global emissions of halons H-1211 (CBrClF2), H-1301 (CBrF3), and H-2402 (CBrF2CBrF2)." In: *Journal of Geophysical Research: Atmospheres* 121.7 (2016), pp. 3663–3686. DOI: 10.1002/2015JD024488.

Vollmer, M., L. Zhou, B. Greally, S. Henne, B. Yao, S. Reimann, F. Stordal, D. Cunnold, X. Zhang, M. Maione, et al. "Emissions of ozone-depleting halocarbons from China." In: *Geophysical Research Letters* 36.15 (2009). DOI: 10.1029/2009GL038659.

Wan, J., J. Hu, W. Bi, M. Yu, X. Xu, Y. Sun, Q. Zhou, Y. Hou, and X. Guan. "Study of the leakage tracer gas transport property in condenser: He and SF6." In: *Thermal Science* 00 (2024), pp. 11–11. DOI: 10.2298/TSCI230901011W.

Wang, Y., L. Li, and W. Yao. "Analysis and Discussion of SF6 Byproducts in Simulated Electric Equipment of Overheating Faults in Low Humidity." In: *2011 Asia-Pacific Power and Energy Engineering Conference*. IEEE. 2011, pp. 1–3. DOI: 10.1109/APPEEC.2011.5748656.

Wanninkhof, R., J. R. Ledwell, and W. S. Broecker. "Gas exchange-wind speed relation measured with sulfur hexafluoride on a lake." In: *Science* 227.4691 (1985), pp. 1224–1226. DOI: 10.1126/science.227.4691.1224.

Weiss, R. "Carbon dioxide in water and seawater: the solubility of a non-ideal gas." In: *Marine chemistry* 2.3 (1974), pp. 203–215. DOI: 10.1016/0304-4203(74)90015-2.

Weiss, R. F. and R. G. Prinn. "Quantifying greenhouse-gas emissions from atmospheric measurements: a critical reality check for climate legislation." In: *Philosophical Transactions of the Royal Society A: Mathematical, Physical and Engineering Sciences* 369.1943 (2011), pp. 1925–1942. DOI: 10.1098/rsta.2011.0006.

Weiss, R. F., A. Ravishankara, and P. A. Newman. "Huge gaps in detection networks plague emissions monitoring." In: *Nature* 595.7868 (2021), pp. 491–493. DOI: 10.1038/d41586-021-01967-z.

Wild, M., D. Folini, M. Z. Hakuba, C. Schär, S. I. Seneviratne, S. Kato, D. Rutan, C. Ammann, E. F. Wood, and G. König-Langlo. "The energy balance over land and oceans: an assessment based on direct observations and CMIP5 climate models." In: *Climate Dynamics* 44 (2015), pp. 3393–3429. DOI: 10.1007/s00382-014-2430-z.

WindEurope. *Wind energy and SF6 in perspective*. 25 September 2019. URL: https://windeurope.org/newsroom/news/wind-energy-and-sf6-in-perspective/ (visited on 04/28/2024).

Xu, C., T. Zhou, X. Chen, X. Li, and C. Kang. "Estimating of sulfur hexafluoride gas emission from electric equipments." In: *2011 1st International Conference on Electric Power Equipment-Switching Technology*. IEEE. 2011, pp. 299–303. DOI: 10.1109/ICEPE-ST.2011.6122993.

Yedinak, E., K. Lentijo, and I. C. Kizilyalli. "Eliminating SF6 from Switchgear." In: *Direct Current Fault Protection: Basic Concepts and Technology Advances*. Springer, 2023, pp. 409–427. DOI: 10.1007/978-3-031-26572-3_18.

Yeti-Hunter. *Sulfur hexafluoride tank*. Licensed under https://creativecommons.org/licenses/by-sa/4.0/legalcode. Wikimedia Commons, 2018. URL: https://commons.wikimedia.org/wiki/File:SF6_Speichertank.jpg (visited on 04/27/2024).

Zavattoni, L. "Conduction phenomena through gas and insulating solids in HVDC Gas Insulated Substations, and consequences on electric field distribution." PhD thesis. Université de Grenoble, 2014. URL: https://theses.hal.science/tel-01305949/file/ZAVATTONI_2014_diffusion.pdf (visited on 04/27/2024).

Zeng, J., H. Nakajima, T. Matsunaga, H. Mukai, K. Hiraki, and Y. Yokota. "Linking carbon dioxide variability at Hateruma station to East Asia emissions by Bayesian inversion." In: *Lagrangian Modeling of the Atmosphere, Geophys. Monograph Series*. Vol. 200. 2012, pp. 163–172. DOI: 10.1029/2012GM001245.

Zhao, C., A. E. Andrews, L. Bianco, J. Eluszkiewicz, A. Hirsch, C. MacDonald, T. Nehrkorn, and M. L. Fischer. "Atmospheric inverse estimates of methane emissions from Central California." In: *Journal of Geophysical Research: Atmospheres* 114 (2009), p. D16302. DOI: 10.1029/2008JD011671.

Zhou, S., F. Teng, and Q. Tong. "Mitigating sulfur hexafluoride (SF6) emission from electrical equipment in China." In: *Sustainability* 10.7 (2018), p. 2402. DOI: 10.3390/su10072402.

Zhu, C., Y. Kanaya, M. Takigawa, K. Ikeda, H. Tanimoto, F. Taketani, T. Miyakawa, H. Kobayashi, and I. Pisso. "FLEXPART v10. 1 simulation of source contributions to Arctic black carbon." In: *Atmospheric Chemistry and Physics* 20.3 (2020), pp. 1641–1656. DOI: 10.5194/acp-20-1641-2020.

Zille, A., M. R. Czerniak, and S. Raoux. "Other product manufacture and use." In: *2019 Refinement to the 2006 IPCC Guidelines for National Greenhouse Gas Inventories, Volume 3: Industrial Processes and Product Use*. Intergovernmental Panel on Climate Change Report, 2019. URL: https://www.ipcc-nggip.iges.or.jp/public/2019rf/pdf/3_Volume3/19R_V3_Ch08_Other_Product.pdf (visited on 04/28/2024).

Acknowledgment of tools for writing

The AI writing assistance tools "Grammarly" and the AI language model "ChatGPT (3.5)" have been utilized to correct grammatical and spelling errors, provide recommendations for improved writing, and suggest appropriate phrases.

Acknowledgment

Above all, I want to express my deepest gratitude to Andreas Stohl, my supervisor who guided me throughout the entire phase of my Ph.D. From the start, Andreas placed a lot of trust and confidence in me, fostering an environment where I felt valued and supported. Despite his huge workload, his door was always open for me and he dedicated a lot of time to my research, providing invaluable ideas and feedback, with passion and encouragement. Together with Martin Weißmann, Aiko Voigt, Leopold Haimberger, and Manfred Dorninger, they have built a great working place at the University of Vienna, with amazing people and a warm atmosphere, where I found a sense of belonging. This brings me to my dear colleges, who through time, also became friends. I want to thank the whole FLEXTEAM - Andreas Plach, Marina Dütsch, Lucie Bakels, Katharina Baier, Silvia Bucci, Michael Blaschek, Daria Tatsii, Seyed Omid Nabavi, Anjumol Raju, Ioanna Evangelou, Rakesh Subramanian, Saurabh Annadate and Andrey Skorokhod for their exceptional and selfless support within our close-knit community. I'm also very grateful to my office mates, Lukas Kugler, Kaushambi Jyoti, and Anne Martin for creating such a pleasant work environment. I also want to thank Dorian Spät, Tobias Necker, Philipp Griewank, Lukas Brunner, Maximilian Meindl, Magdalena Fritz, Federico Ambrogi, Blaž Gasparini, Johannes Hörner, Susanna Winkelbauer, Stefano Serafin, Sandy Chkeir, Markus Rosenberger, Ulrich Voggenberger, Vanessa Rieger, and Michael Mayer for the enjoyable moments we shared together, whether during lunch and coffee breaks, dinners, padel tennis matches, planking sessions, concerts, karaoke nights, or other memorable occasions. I'm also thankful to Melissa König, Herta Gassner, Stefanie Weinberger, Markus Ristic, and Vera Flasch for their great help, whenever I faced organizational challenges. I also want to thank Rona Thompson, Sabine Eckhardt and Christine Groot Zwaaftink for their technical support and for their great hospitality during my visit in Norway.

Further, I want to thank my girlfriend Sophie and my flatmates Anna, Martin, Maria, Antonio, Nuno, and Luis, who do not only provide the best home possible, but also a place where I could work during Corona times. A big thanks also goes to my friends Martin and Marie, who were a great support and whose hospitality make a highlight every week. Lastly, I want to thank my mother and my sister, who always stand by my side, and my father, who is always there when I turn on the music to start my working day.